

Role of Surface Roughness in Tribology: From Atomic to Macroscopic Scale

Vorgelegt von
Mast.-Ing.
Chunyan Yang
aus Hebei, China

Von der Fakultät V Verkehrs- und Maschinensysteme
der Technischen Universität Berlin
zur Erlangung des akademischen Grades
Doktor der Ingenieurwissenschaften
Dr.-Ing

genehmigte Dissertation

Promotionsausschluss
Vorsitzender: Prof. Dr. Ing. Henning Jürgen Meyer
Gutachter: Prof. Dr. rer. nat. Valentin Popov
Gutachter: Dr. Bo Nils Johan Persson

Tag der wissenschaftlichen Aussprache: 30.06.2008

Berlin 2008

D 83

This thesis was written at the institute
Quantum-Theorie der Materialien, Institut für Festkörperforschung (IFF),
Forschungszentrum Jülich GmbH, Jülich, Deutschland.

It is available online at the internet pages of the library of
Technische Universität Berlin.

Abstract

The practical importance of friction cannot be underestimated: from the creation of fires by rubbing sticks together, to the current efforts to build nano devices, friction has played an important role in the whole history of technology of mankind. Friction is a complex multiscale phenomenon that depends both on the atomic interactions inside the contacts, on the macroscopic elastic and plastic behavior of the solids in contact, and on the unavoidable, stochastic roughness characterizing real surfaces. Tribology, the science of friction, has developed much in recent years, but many questions are still open.

This thesis addresses the role of surface roughness in tribology from atomic to macroscopic scale with the aid of numerical calculations. We have studied several features of the contact between rough surfaces, such as the area of contact, the interfacial separation, the adhesive and frictional properties, and leakage of sealed fluids. We have also studied the wetting behavior of nanodroplets on randomly rough surfaces.

In order to study contact mechanics accurately it is necessary to consider an elastic solid whose thickness is comparable to the largest wavelength of the surface roughness. In principle, one should simulate a system with a very large amount of atoms, even for a relatively small system. A fully atomistic model is impracticable, and we have developed a multiscale molecular dynamics approach: the atomistic description is employed where necessary, at the nanocontacts and on the surfaces, while a coarse-grained picture allows us to simulate the correct long-range elastic response.

The area of contact between rough surfaces and the interfacial separation, with and without adhesion, have been analyzed. The real area of contact plays a crucial role in the friction, adhesion and wear. The interfacial separation is relevant to capillarity, leak-rate of seals and optical interference. Numerical simulations showed that at small squeezing pressure in the absence of adhesion, the area of contact depends linearly on the squeezing pressure, and the interfacial separation depends logarithmically on squeezing pressure.

The sliding of elastic solids in contact with both flat and the rough surfaces, has been studied. We found a strong dependence of sliding friction on the elastic modulus of solids, and this is one of the main origins of the instability while sliding. For elastically hard solids with planar surfaces with incommensurate surface structures, extremely low friction (superlubricity) has been observed, which increases very abruptly as the elastic modulus of the solids decreases. Even a relatively small surface roughness or a low concentration of adsorbates can eliminate the superlubricity.

The wetting behavior of nanodroplets on rough hydrophilic and hydrophobic surfaces has been studied. The problem is relevant for the fields of nano-electro-mechanics and of nano fluid dynamics, both of which are of great current interest. No contact angle hysteresis has been detected for nano-droplets on hydrophobic surfaces due to thermal fluctuations. The contact angle increases with the root-mean-square roughness of the surface and is almost independent of the fractal dimension of the surface. We have found that thermal fluctuation are very important at the nanoscale. On hydrophilic surfaces, however, thermal fluctuations do not remove the hysteresis of the contact angle.

Kurzfassung

Die Bedeutung der Reibung in unserem Alltag ist nicht zu unterschätzen. Vom Entfachen eines Feuers durch Aneinanderreiben von Stöckchen bis hin zu den heutigen Bemühungen, nanoelektromechanische Systeme herzustellen, hat die Reibung eine zentrale Rolle in der Technologieentwicklung der Menschheitsgeschichte gespielt. Reibung ist ein komplexes Phänomen, das sich auf vielen verschiedenen Längenskalen abspielt. Es hängt stark von den atomaren Wechselwirkungen innerhalb der Kontaktflächen, den makroskopischen elastischen und inelastischen Eigenschaften der Materialien sowie der unvermeidbaren stochastischen Rauigkeit realer Oberflächen ab. Trotz großer Fortschritte in der Tribologie – der Reibungswissenschaft – sind noch viele interessante Fragen offen.

Diese Arbeit befasst sich unter Zuhilfenahme numerischer Methoden mit der Rolle der Oberflächenrauigkeit in der Tribologie auf den verschiedenen Längenskalen, von der atomaren bis zur makroskopischen Größenordnung. Wir haben verschiedene Aspekte der Kontakte rauer Oberflächen untersucht, zum Beispiel Adhäsions- und Reibungseigenschaften sowie die Leckströmungen von Flüssigkeiten an einer Dichtung. Außerdem haben wir das Benetzungsverhalten von Nanotröpfchen auf stochastisch rauen Oberflächen betrachtet.

Für eine aussagekräftige Untersuchung der Mechanik des Kontaktes ist es notwendig, die Dicke des elastischen Materials vergleichbar mit der größten Wellenlänge der Oberflächenrauigkeit zu wählen. Obwohl man prinzipiell eine atomistische Beschreibung verwenden sollte, ist der numerische Aufwand bereits bei kleinen Systemen zu hoch. Deshalb haben wir eine Multiskalen-Molekulardynamik-Methode entwickelt, bei der wir eine atomistische Beschreibung nur in den kritischen Regionen, nämlich in den Nanokontakten und an der Oberfläche, verwenden; in den übrigen Gebiete wird die Physik der langreichweiten elastischen Response durch ein größeres Modell wiedergegeben.

Die Kontaktfläche und die Grenzflächenseparation werden als Funktion des auf das System ausgeübten Drucks ohne und mit Adhäsion analysiert. Die tatsächliche Kontaktfläche beeinflusst die Reibungs- und Hafteigenschaften und die Abnutzung entscheidend. Die Grenzflächenseparation ist dagegen verantwortlich für Effekte wie die Kapillarität, optische Interferenz und die Leckrate einer Abdichtung. Durch numerische Simulationen konnten wir zeigen, dass bei kleinem Druck und ohne anziehende Wechselwirkung die effektive Kontaktfläche linear vom angewandten Druck abhängt, während die Grenzflächenseparation logarithmisch von diesem abhängt.

Ferner haben wir das Gleiten von elastischen Materialien mit adhäsivem Kontakt bei glatten und rauen Oberflächen untersucht. Dabei haben wir eine starke Abhängigkeit der Gleitreibung vom Elastizitätsmodul festgestellt; dies ist eine der Hauptursachen der Gleitinstabilität. Bei elastisch harten Materialien mit glatten Oberflächen und inkommensurablen Gitterstrukturen beobachteten wir eine extrem niedrige Reibung (superlubricity), die bei sinkendem Elastizitätsmodul des Festkörpers abrupt ansteigt. Dieser Effekt wird allerdings schon durch eine kleine Oberflächenrauigkeit oder durch eine geringe Konzentration eines Adsorbats zerstört.

Des weiteren haben wir das Benetzungsverhalten von Nanotröpfchen auf rauen hydrophilen wie hydrophoben Oberflächen untersucht. Dieses Problem ist relevant in der Nanoelektromechanik und der Nanofluidodynamik, die beide von großem aktuellen Interesse sind. Aufgrund thermischer Fluktuationen wurde für Nanotröpfchen auf hydrophoben Oberflächen keine Berührungsinkel-Hysterese gefunden. Der Kontaktwinkel steigt mit der mittleren quadratischen Abweichung der Rauigkeit der Oberfläche und ist nahezu unabhängig von ihrer fraktalen Dimension. Wir konnten feststellen, dass thermische Fluktuationen auf der Nanoebene sehr wichtig sind. Auf hydrophilen Oberflächen ist die thermische Fluktuation allerdings nicht ausreichend, um die Hysterese des Kontaktwinkels zu beseitigen.

Contents

Abstract	I
Kurzfassung	III
1 Introduction	1
1.1 Overview of tribology	2
1.2 Surface roughness	3
1.2.1 Lessons from Nature	3
1.2.2 Modern applications	5
1.3 Surface roughness enters tribology	6
2 Multiscale Molecular Dynamics	9
2.1 Simulation method	9
2.1.1 Numerical integration algorithm	9
2.1.2 Interatomic potential and potential truncation	10
2.1.3 Periodic boundary condition	11
2.2 The ancestor of the “smartblock”	11
2.2.1 A lattice of atoms connected through springs	12
2.2.2 The springs	12
2.3 Elastic properties of a medium with cubic symmetry	13
2.3.1 The Poisson ratio of the Smartblock is zero	14
2.3.2 Anisotropy of the Smartblock	14
2.4 Going multiscale	16
3 Area of Contact between Randomly Rough Surfaces	19
3.1 Introduction	19
3.2 Multiscale molecular dynamics	21
3.2.1 Why use multiscale molecular dynamics?	21
3.2.2 Parameters and potential	23
3.2.3 Self affine fractal surfaces	24
3.3 Numerical results	25
3.3.1 Test cases: Hertz contact and complete contact	26
3.3.2 Contact mechanics without adhesion	30
3.3.3 Contact mechanics with adhesion	31
3.4 Discussion	32
3.5 Summary	37

4 Interfacial Separation from Small to Full Contact without adhesion	39
4.1 Introduction	39
4.2 Interfacial separation without adhesion	40
4.3 Molecular Dynamics	43
4.4 Numerical results	47
4.4.1 Contact area from small to full contact	47
4.4.2 Interfacial surface separation from small to full contact	50
4.5 Contact mechanics for a measured surface	54
4.6 Summary	58
5 Interfacial Separation and Contact Area with Adhesion	61
5.1 Background	61
5.2 Interfacial separation with adhesion	62
5.3 Molecular dynamics	62
5.4 Numerical results	63
5.4.1 Interfacial separation u vs. squeezing pressure p with adhesion	63
5.4.2 Probability distribution of u and p	63
5.4.3 Contact area comparison between MD and Theory	65
5.5 Summary	65
6 Theory of the Leak-rate of Seals	69
6.1 Introduction	69
6.2 Basic picture of leak-rate	70
6.3 Results	73
6.3.1 Numerical results	73
6.3.2 Molecular dynamics results	74
6.4 Improved analytical description	80
6.5 Comparison with experiment	81
6.6 Comment on the role of non-uniform pressure, rubber viscoelasticity and adhesion	82
6.7 Dynamical seals	83
6.8 A new experiment	87
6.9 Summary	87
7 How do Liquids Confined at the Nanoscale Influence Adhesion?	91
7.1 Motivation	91
7.2 Preparing the initial configuration	92
7.3 Numerical results	92
7.3.1 Confined liquid on flat surfaces	92
7.3.2 Confined liquid on rough surfaces	94
7.4 Contact hysteresis	98
7.5 Discussion	101
7.6 Summary	101
8 Effect of Surface Roughness and Adsorbates on Superlubricity	103
8.1 Introduction	103
8.2 Model	104
8.3 Numerical results	106
8.3.1 Influence of surface roughness on friction	107
8.3.2 Dependence of the friction on the load	111
8.3.3 Role of adsorbates	116

8.4 Summary	118
9 Nanodroplets on Rough Hydrophilic and Hydrophobic Surfaces	119
9.1 Introduction	119
9.2 Theoretical background	120
9.2.1 Flat surfaces	121
9.2.2 Rough surfaces: minimum free energy state	121
9.2.3 Rough surfaces: activation barriers and hysteresis	124
9.2.4 Cassie and Wenzel states for randomly rough surfaces	127
9.3 Simulation Method	128
9.3.1 Molecular dynamics model	128
9.3.2 Multiscale rough surfaces	131
9.4 Numerical results	132
9.4.1 Static contact angle on hydrophobic surface	132
9.4.2 Dynamic contact angle: Contact angle hysteresis	134
9.5 Discussion	139
9.6 Summary	140
10 Concluding Remarks	141
Acknowledgments	143
A Contact Mechanics Theories	145
A.1 Single asperity contact	145
A.1.1 Hertz theory	145
A.1.2 JKR theory	145
A.2 Multi asperities contact	147
A.2.1 Greenwood-Williamson theory	147
A.2.2 Bush-Gibson-Thomas theory	148
A.2.3 Persson theory	148
B Pressure Distribution between Randomly Rough Surfaces	151
C Distribution of Surface Slopes for Randomly Rough Surfaces	153
C.1 The surface area A and the average surface slope ξ	153
C.2 Surface slope probability distribution	154
C.3 Solution of the diffusion equation	155
C.4 Distribution function $P(s_0, \zeta)$	156
C.5 Surface area with slope below $\tan\theta$	156

Chapter 1

Introduction

If we put two solid objects with flat surfaces into contact we should expect a large adhesive energy due to the formation of chemical bonds between the atoms of the two surfaces. Even when the surfaces are chemically inert, the relatively weak van der Waals interaction, typically $\sim 10 - 100$ meV per atom, is enough to give rise to a large separation force. In addition, at least for commensurate surfaces, the friction preventing lateral sliding should be very large, all this without any glue, and without any external normal load, since the adhesive interaction of the surfaces in contact acts as a large normal load. Furthermore we should expect a perfect seal: the contact between flat surfaces allows no space for fluid to flow at the interface.

On the other hand we know from everyday's experience that apparently flat surfaces in contact usually behave in a completely different way, with negligible adhesion, a friction force proportional to the normal load, and weak sealing properties.

So, why do apparently flat surfaces not behave as expected? The explanation is simple: "flat" surfaces are not flat! Although they may seem flat macroscopically, a careful examination at smaller length-scale reveals a rough, random microscopic profile [1]. The real contact area can be many orders of magnitude smaller than the nominal one, and our arguments based on the adhesive energy per atom does not hold.

Recently much theoretical effort has been devoted to the study of the influence by roughness on contact mechanics adhesion, friction, wetting, and sealing [2–4]. Many questions remain unanswered and the available theories can derive large benefit from comparisons with numerical simulations, both in term of validation and of tuning and adjustment of the theory. It is of no surprise that several research groups have tackled these problems with various numerical techniques [5–7].

We have developed a novel approach to numerical simulations of contact mechanics problems for rough surfaces. Our method is based on Molecular Dynamics and allows us to simulate systems at atomic resolution. To manage large enough systems without having to deal with the huge number of atoms involved, we have designed a multiscale scheme borrowed from the finite element analysis techniques [5]. The smartblock model — this is the colloquial name that we use for our multiscale model — is described in Chapter 2. The subsequent chapters, from (3 to 9), show studies and simulations of five different topics involving randomly rough surfaces. Chapter 10 reports the final remarks and conclusions of my work. But before going into more details, let me introduce this fascinating topic with some hints about the role of roughness in tribology and in nature.

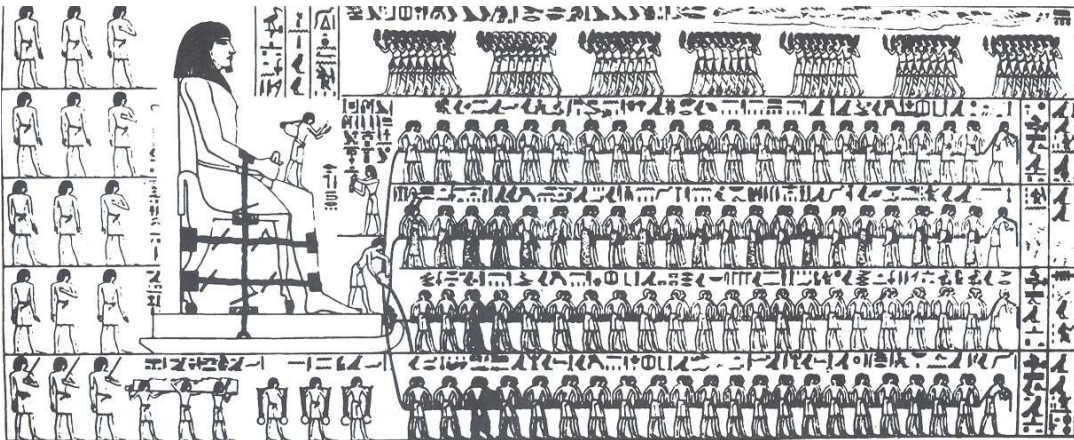


Figure 1.1: Egyptians using lubricant to reduce friction, and aid the movement of colossus. Adapted from Ref. [11].

1.1 Overview of tribology

Tribology is a multidisciplinary science dealing with friction, wear and lubrication. It affects many aspects of everyday life and has played a central role in technology. The word tribology, which is based upon the Greek word *tribos* (rubbing), appeared in 1966. The literal translation would be the “science of rubbing”. Tribological phenomena occur whenever two material bodies are brought together and translated with respect to each other. The goals of exploration of these phenomena, dating back from the creation of fire by rubbing sticks together to current efforts to make nanodevices, are to understand their physical and chemical origins, and to design ways and means for minimizing losses, e.g. energy dissipation and material degradation, which can cause huge economic loss [8,9].

Tribological phenomena occur in systems encompassing a broad spectrum of length scales, from common machine, instrument and tool elements, such as a ball bearing and its race groove, a pair of spur gear involute teeth, cams and shafts, components of polishing, machining and patterning instruments, to high density data storage devices, micro-machines and bio-tribological system, such as synovial joints and total joint replacements [10]. Common to all tribological systems is the importance of interfacial configuration. Thus, studies of the basic origins of tribological phenomena should focus on the investigation of contact mechanisms and on properties of interfaces between solids (both static and dynamic), interfacial structure and adhesion, flow, and rheology of confined liquid under shearing.

Our ancestors already knew how to reduce friction. Here is an example: In order to build monuments or stone blocks, they had to transport large stones. It is amazing that in 3500 BC they already knew that adding lubricants reduced friction, during the transportation of these heavy stones. Painting shown in Fig. 1.1 illustrates the use of sledge to transport heavy statues in Egypt (circa 1880 BC). In this transportation 172 slaves are being used to drag a large statue weighing about 60,000 kg along a wooden track. One man, standing on the sledge supporting the statue, can be seen pouring a liquid into the path of motion. He could be viewed as one of the earliest lubrication engineers [10]. Dowson has estimated that each man exerted a pull of about 80 kg. On this basis the total effort, which must at least equal the friction force, becomes 172×800 N. Thus, the coefficient of friction is about 0.23 [11]. A tomb in Egypt, dated several thousands of years BC, provides the evidence of the use of lubricants. A chariot in this tomb still contains

some of the original animal-fat lubricant in its wheel bearing.

Several thousand years ago our ancestors used a practical way to reduce friction. But there were no clear friction laws available at that time. The two basic laws of friction, that the frictional resistance is proportional to load and that it is independent of the area of the sliding surfaces, have been known since the work of Leonardo da Vinci (1452-1519). The two laws had been verified experimentally and were later rediscovered in 1699 by the French engineer Amontons [12]. These observations were verified by Coulomb in 1781, who made clear distinction between static friction, the force required to start sliding, and kinetic friction, the force required to maintain friction. The latter is usually appreciably lower than the former. Coulomb observed that the kinetic friction is often nearly independent of the speed of sliding. He also concluded that the friction was due to the interlocking of the surface asperities and represented in the main work of lifting the load over the summits of these asperities.

In reality, friction is a complex multiscale phenomenon that depends both on the atomic interactions inside the contacts and on the macroscopic elastic and plastic deformation that determine the morphology and stress distribution within these contacts. Understanding the atomistic mechanisms underlying tribological processes is fundamental to many basic and applied problems, such as wetting, capillarity, adhesion, lubrication, sealing, hardness, micro/nano indentation, atomic-scale probing, surface modification and manipulation [13, 14]. Exploring these phenomena in the nanoscale regime often requires both experimental probes and theoretical approaches. Sometimes it may be difficult or impossible to carry out useful experiments under extreme temperatures and pressures. But, a computer simulation of a material in, say, a shock wave, a high-temperature plasma, a nuclear reactor, a planetary core, could be perfectly feasible. Thus computer simulation provides a direct route from the microscopic details of a system, such as the masses of the atoms, the interactions between them, the molecular geometry, up to macroscopic properties of experimental interest, such as the equation of state, transport coefficients, structure parameters. In general it opens new avenues of investigation of the microscopic origins of material phenomena. This thesis will address some recent computational studies that are helping to unravel this complex interplay underlying tribology.

1.2 Surface roughness

Normally it is very difficult to prepare surfaces really flat. Even on carefully polished surfaces, hills and valleys are large compared with the size of a molecule. If two solids are placed in contact, the upper surface will be supported on the summits of the irregularities, and large areas of the surfaces will be separated by a distance which is great compared with the molecular range of action [9, 12]. Although the techniques of grinding and polishing have advanced recently, it remains difficult to prepare surfaces of appreciable size that are flat on the scale of order 100 Å, and most surfaces used in engineering practice have surface irregularities which are much greater.

1.2.1 Lessons from Nature

Some biological systems have anti-adhesive surfaces. Firstly, many plant leaves (such as the lotus leaf) are covered by a hydrophobic cuticle, which is composed of a mixture of large hydrocarbon molecules [16, 17]. Secondly, the surface has a unique roughness distribution. It has been reported that for some leaf surfaces, the roughness of the hydrophobic leaf surface decrease wettability, which is reflected in a larger contact angle of water droplets on such surfaces (see Fig. 1.2 and 1.3).



Figure 1.2: A droplet on a superhydrophobic surface: The droplet touches the leaf only at a few points and forms a ball. It completely rolls off at the slightest declination. Adapted from Ref. [15] with permission.

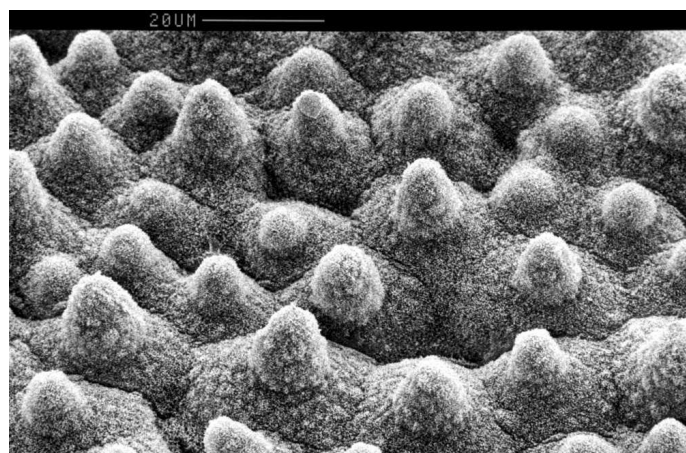


Figure 1.3: A leaf surface with roughness on several length scales optimized via nature selection for hydrophobicity and self-cleaning. Through the combination of micro-structure (cells) and nanostructure (wax crystals) the macroscopic water contact angle θ_0 is maximized. Adapted from Ref. [15] with permission.



Figure 1.4: A gecko climbing on a vertical glass wall.

Geckos are known for their amazing climbing ability. They can run up any wall, run across the ceiling, and stick to ceilings (see Fig. 1.4). They rely on the extreme miniaturization and multiplication of contact elements, and the soles of their feet are covered by about half a million sub-micrometer keratin hairs, called spatula. These spatulas make their feet, known as “gecko feet”, so sticky. Each hair is $30 - 130 \mu\text{m}$ long and is only one tenth the diameter of a human hair and contains hundreds of projections terminating in $0.2 - 0.5 \mu\text{m}$ plate-like structures. The foot typically has about 5000 hairs/mm^2 . Each hair produces a tiny force ($\approx 100 \text{ nN}$), primarily due to van der Waals attraction and possibly capillary interactions (meniscus contribution), and millions of hairs acting together create a large adhesive force of the order of 10 nN with a pad area of approximately 100 mm^2 , sufficient to keep geckos firmly on their feet, even when upside down on a glass ceiling [18]. The bond between hair and surface can be easily broken by “peeling” in the same way one removes a strip of adhesive tape, allowing geckos to run across ceilings.

1.2.2 Modern applications

Surface roughness has a huge influence on many important physical phenomena such as contact mechanics, sealing, adhesion and friction. Thus, for example, experiments have shown that a substrate with a root-mean-square(*rms*) roughness of the order $\sim 1 \mu\text{m}$ can completely remove the adhesion between a rubber ball and a substrate, while nanoscale roughness will remove the adhesion between most hard solids, e.g., metals and minerals; this is the reason why adhesion is usually not observed in most macroscopic phenomena [1]. Similarly, rubber friction on most surfaces of practical interest, e.g., road surfaces, is mainly due to the pulsating forces that act on the rubber surface as it slides over the substrate asperities.

There is an ever increasing trend toward device miniaturization and micro or nano-electromechanical (MEMS/NEMS) devices [19]. The central problems are bonding and sticking between the contacting surfaces [20], and the production of these has always been a tricky and risky task to bond parts of two wafer surfaces, while preventing another predefined area of the same wafer surfaces from sticking. However, in many MEMS fabrication processes, the wafer bonding and anti-sticking must be achieved at the same time in one processing step. Let us illustrate the importance of surface roughness on two modern

applications.

The first deals with surface roughness effects on direct wafer bonding¹. At room temperature the wafer bonding is due to relatively weak inter-atomic attraction forces, e.g., van der Waals interaction or hydrogen bonding, giving (for perfectly flat surfaces) an interfacial binding energy of order $6 \text{ meV}/\text{\AA}^2$. The surface roughness of the wafer is the most critical parameter determining the strength of the wafer bonding. In particular, when the surface roughness exceeds a critical value, the wafers will not bind at all, and this is in good agreement with the theory presented in Ref. [21]. Primary grade polished silicon wafer surfaces have *rms* roughness of order $\sim 0.1 \text{ nm}$ when they are measured over a surface area with $10\mu\text{m} \times 10\mu\text{m}$, and such surfaces bind spontaneously. However, when the surface roughness amplitude is of order $\sim 1 \text{ nm}$, the surfaces either bind weakly when they are squeezed together, or they do not bind at all, depending on the detailed nature of the surface roughness power spectrum.

The second application is anti-sticking via the formation of hydrophobic coatings on surfaces by creating the appropriate type of surface roughness. It involves copying Nature where many plant surfaces are highly hydrophobic as a result of the formation of special types of surface roughness. The surface roughness allows air to be trapped between the liquid and the substrate, while the liquid is suspended on the asperities. Since the area of real liquid-substrate contact is highly reduced, the contact angle of the drop is determined almost solely by the liquid surface tension, leading to a very large contact angle. New commercial products based on “Lotus effect”, such as self-cleaning paints, glass windows and car windshields, have been produced.

1.3 Surface roughness enters tribology

Computer simulations can provide essentially exact results for problems in statistical mechanics that would otherwise be soluble only by approximate methods. Computer simulation can be used to test theories, and these results compared with experiments. In the first place, it is a test of the underlying model used in computer simulation. If the model is a good one, one hopes to offer insights to experimentalist and assists in the interpretation of the results. Computer simulation has a dual role as a bridge that connects models and theoretical predictions on one hand, and which connects models and experimental results on the other. It can be also termed as “computer experiments” due to its connecting role [22, 23].

The scope of this thesis is to use theoretical and computational tools to study the role of surface roughness in tribology, including the area of real contact, interfacial separation, adhesion, friction, sealing and superhydrophobicity. The thesis is divided into ten chapters. In the first I give an overview of tribology and surface roughness and Chapter 2 describes multiscale molecular dynamics model we use. Chapters 3-5 deal with contact mechanics. The first two chapters consider contact mechanics without adhesion. The area of contact between two randomly rough surfaces is considered in the third chapter. At small load the real contact area varies linearly with the load, and at high load the contact area approaches approximately full contact, in good agreement with theories.

When two randomly rough surfaces are brought into contact, what is the distribution of interfacial separations? How does the interfacial separation depend on the load? This topic will be discussed in chapter 4, and in chapter 5 I will discuss what happens to the area of contact and interfacial separation when adhesion is included.

¹Wafer bonding is a convenient method to combine different materials. If the surfaces of applied wafers are sufficiently flat and clean, it is possible to bring them so close together that bonds will be formed.

Based on the contact mechanics theory developed in chapter 4, a theory of leak-rate seals will be presented in chapter 6. Molecular dynamics results will be presented, showing that when two elastic solids with randomly rough surfaces are squeezed together with increasing magnification or decreasing squeezing pressure, a non-contact channel will percolate when the relative projected contact area A/A_0 , is of order 0.4, in accordance with the percolation theory.

Everyday life tells us that liquids play an important role in sliding friction and adhesion. They behave as lubricants in human bodies, particularly in the joints. However, in many biological attachment systems, they act like adhesives, e.g. facilitating insects to move on ceilings or vertical walls. From previous chapters, we know how the real contact area and interfacial separation change with load, when two surfaces are brought into contact. The force required to separate these two surfaces, is usually called pull-off force. What happens if we put liquid in between? How does the amount of liquid influence adhesion? These questions will be addressed in chapter 7.

The sliding of elastic solids, in adhesive contact with flat and rough surfaces, is studied in chapter 8, where the dependence of the sliding friction on the elastic modulus is considered. For elastically hard solids, with planar surface and incommensurate surface structures, we observe extremely low friction (superlubricity), which increases abruptly as the elastic modulus decreases. We show that even a relatively small surface roughness, or a low concentration of adsorbates, may completely kill the superlubric state.

The wetting property of the lubricants is essential to lubrication. The behavior of liquid nanodroplets, on a rough hydrophobic and hydrophilic solid surface, will be studied in chapter 9. On hydrophobic surfaces, the contact angle of nanodroplets depends strongly on the root-mean-square (*rms*) roughness amplitude of the substrate, but is nearly independent of the fractal dimension of the surface, and there is negligible contact angle hysteresis. On hydrophilic surfaces, however, there is strong contact angle hysteresis, due to a higher energy barrier. These findings may be very important for the development of artificially bio-mimetic superhydrophobic surfaces.

Chapter 10 reports the final remarks and conclusions of my work.

The work contained in this thesis has led to the following publications:

1. C. Yang, U. Tartaglino and B.N.J. Persson, *A multiscale molecular dynamics approach to contact mechanics*, Eur. Phys. J. E 19 (2006) 47
2. C. Yang, U. Tartaglino and B.N.J. Persson, *Influence of surface roughness on superhydrophobicity*, Phys. Rev. Lett. 97 (2006) 116103
3. C. Yang, U. Tartaglino and B.N.J. Persson, *How do liquids confined on the nanoscale influence adhesion*, J. Phys. Condens. Matt. 18 (2006) 11521
4. C. Yang and B.N.J. Persson, *Molecular dynamics study of contact mechanics: contact area and interfacial separation from small to full contact*, Phys. Rev. Lett. 100 (2008) 024303
5. C. Yang, U. Tartaglino and B.N.J. Persson, *Nanodroplet on rough hydrophilic and hydrophobic surfaces*, Eur. Phys. J. E 25 (2008) 139
6. C. Yang and B.N.J. Persson, *Contact mechanics: contact area and interfacial separation from small contact to full contact*, J. Phys.: Condens. Matter 20 (2008) 215214
7. B.N.J. Persson and C. Yang, *Theory of leak-rate seals*, J. Phys.: Condens. Matter (in press, 2008)

8. C. Yang, B.N.J. Persson, J. Israelachvili and K. Rosenberg, *Contact mechanics with adhesion: interfacial separation and contact area*, submitted.

Book chapters:

1. B.N.J. Persson, G. Carbone, V.N. Samoilov, I.M. Sivebaek, U. Tartaglino, A.I. Volokitin and C. Yang, *Contact mechanics, friction, adhesion with application to quasicrystals*, 269, Fundamentals of friction and wear on the nanoscale, Ed. E. Gnecco and E. Meyer, Springer (2006).
2. U. Tartaglino, C. Yang and B.N.J. Persson, *A multicale molecular dynamics approach to contact mechanics and friction: from continuum mechanics to molecular dynamics*, 307, Fundamentals of friction and wear on the nanoscale, Ed. E. Gnecco and E. Meyer, Springer (2006).
3. V.N. Samoilov, C. Yang, U. Tartaglino and B.N.J. Persson, *The effect of surface roughness and adsorbates on superlubricity*, Chapter 8, Superlubricity, Ed. A. Erdemir and J.M. Martin, Elsevier (2007).

Chapter 2

Multiscale Molecular Dynamics

In present chapter I will present a detailed description of the main features of Molecular Dynamics(MD): molecular dynamics time integration algorithm, interatomic potential, potential truncation and periodic boundary condition. Section 2.2 describes the system without multiscale coarse-graining. Section 2.3 discusses its elastic properties, and section 2.4 shows the technical details to implement the multiscale description. In the next section I will introduce the basic ideas that drive the development of the model.

The need to simulate large elastic bodies in the contest of friction and adhesion brought our group to implement what we named “Smartblock” model. The description of the body is atomistic, and the atoms are treated within the conventional Molecular Dynamics. Only the outermost atoms can interact with external atoms, such as lubricant molecules or surfaces of other bodies.

The “Smartblock” correctly implements the elastic response of the system to external forces, over the widest range of wavelength compatible with the discrete structure of the atomistic description and the finite size of the sample.

The model is quite simple to understand and to implement. Moreover, the internal lattice structure of the block avoids the need of the list of neighbors and allows an efficient pipe lining of the computer instructions, thus the calculation is much less computationally demanding than the analogous one with the typical realistic potentials. The model allows an easy tuning of the elastic parameters of the medium. Furthermore a coarse-grained multiscale description is trivially implemented, allowing the simulations of quite thick bodies.

On the other hand there is no attempt to describe other properties such as plastic deformation, dislocations, cracks, atomistic diffusion, structural changes and phase transitions.

2.1 Simulation method

2.1.1 Numerical integration algorithm

Nowadays one of the most attractive, simple and numerically stable integration schemes for Newton’s equation of motion is the velocity Verlet algorithm. Based on Taylor expansion of the coordinates $\mathbf{r}(t)$, we can calculate the position $\mathbf{r}(t + \delta t)$ at time $t + \delta t$:

$$\mathbf{r}(t + \delta t) = \mathbf{r}(t) + \sum_n \frac{(\delta t)^n}{n!} \frac{d^n \mathbf{r}(t)}{dt^n}$$

If we add the corresponding equation for $\mathbf{r}(t - \delta t)$ and neglect the terms of order $(\delta t)^4$ and higher, a simple expression for the calculation of the particle position after a single

time step is obtained:

$$\mathbf{r}(t + \delta t) = 2\mathbf{r}(t) - \mathbf{r}(t - \delta t) + (\delta t)^2 \frac{\mathbf{f}(t)}{m}$$

where m is an atomic mass and $\mathbf{f}(t)$ is the force experienced by this atom at time t . The velocities can be calculated at time t from the following expression:

$$\dot{\mathbf{r}}(t) = \frac{1}{2\delta t}(\mathbf{r}(t + \delta t) - \mathbf{r}(t - \delta t))$$

The described integration scheme is known as Verlet algorithm. A slight modification is the velocity scheme Verlet which calculates the velocities at time $t + \delta t$ using the velocities obtained at time $t + \frac{\delta t}{2}$:

$$\begin{aligned}\mathbf{v}(t + \frac{\delta t}{2}) &= \mathbf{v}(t) + \frac{\delta t}{2} \frac{\mathbf{f}(t)}{m} \\ \mathbf{r}(t + \delta t) &= \mathbf{r}(t) + \delta t \mathbf{v}(t) + \frac{(\delta t)^2}{2} \frac{\mathbf{f}(t)}{m} + O(\delta t^4)\end{aligned}$$

Finally new velocities at time $t + \delta t$ are estimated as:

$$\mathbf{v}(t + \delta t) = \mathbf{v}(t) + \frac{\delta t}{2m} [\mathbf{f}(t + \delta t) + \mathbf{f}(t)] + O(\delta t^3)$$

The modified velocity Verlet for Langevin and damping dynamics was developed by Ermak [23]. In his approximation the forces $\mathbf{f}(t)$ remain almost constant over the time step δt . The algorithm for zero stochastic forces was implemented by Ref. [24]:

$$\begin{aligned}\mathbf{r}(t + \delta t) &= \mathbf{r}(t) + c_1 \delta t \mathbf{v}(t) + c_2 \delta t^2 \frac{\mathbf{f}(t)}{m} + O(\delta t^4) \\ \mathbf{v}(t + \delta t) &= c_0 \mathbf{v}(t) + c_1 \delta t \frac{\mathbf{f}(t)}{m} + O(\delta t^3)\end{aligned}$$

where $c_0 = e^{-\gamma \delta t}$, $c_1 = (\gamma \delta t)^{-1}(1 - c_0)$, $c_2 = (\gamma \delta t)^{-1}(1 - c_1)$ and γ is a friction coefficient. The structure relaxation near the minimum of the potential energy is performed by “smart minimization”, i.e. if $\mathbf{v}(t) \cdot \mathbf{f}(t) < 0$ the velocity is set zero.

2.1.2 Interatomic potential and potential truncation

The atoms at the interface between block and substrate interact with potential

$$U(r) = 4\epsilon \left[\left(\frac{r_0}{r} \right)^{12} - \alpha \left(\frac{r_0}{r} \right)^6 \right] \quad (2.1)$$

where r is the distance between a pair of atoms. When $\alpha = 1$, Eq. 2.1 becomes the standard Lennard-Jones potential. In this case the parameter ϵ is the binding energy between two atoms at the separation $r = 2^{1/6}r_0$. We can estimate the interfacial binding energy (when $\alpha = 1$) per unit area with $\Delta\gamma = 4\epsilon/a^2$. For example, if $r_0 = 3.28 \text{ \AA}$ and $\epsilon = 18.6 \text{ meV}$, the interfacial binding energy per unit area is $\Delta\gamma \approx 11 \text{ meV}/\text{\AA}^2$. When we study contact mechanics without adhesion we put $\alpha = 0$.

The potential in Eq. 2.1 has an infinite range. In practical applications, it is customary to establish a cutoff radius R_c and disregard the interactions between atoms separated by more than R_c . This results in simpler programs and enormous savings of computer resources, because the number of atomic pairs separated by a distance r grows as r^2 and becomes quickly huge. A simple truncation of the potential creates a new problem though:

whenever a particle pair crosses the cutoff distance, the energy makes a little jump. A large number of these events is likely to spoil energy conservation in a simulation. To avoid this problem, the potential is often shifted in order to vanish at the cutoff radius [25]. In our simulations, we apply the LJ potential when $r < R_c$, where $R_c = 3.5r_0$. When $R_c < r < R_c + r_0/2$, we use an interpolated third order of polynomial equation to connect it to zero. The two functions have the same value and the first derivative in R_c , in order to make the potential have a smooth transition from the cutoff distance to where the potential becomes zero.

When we study lubrication and liquid droplets property, we include the octane molecules C₈H₁₈ between block and substrate. The octane molecules are treated with the united atom model: every molecule comprises eight particles corresponding to the groups CH₂ and CH₃. The optimized potential for liquid simulation (OPLS) [26, 27] is employed. The atoms of the two walls interact through Lennard-Jones potential with $r_0 = 3.28 \text{ \AA}$.

2.1.3 Periodic boundary condition

No matter how large the simulated system is, its number of atoms N would be negligible compared with the number of atoms contained in a macroscopic piece of matter (of the order of 10²³), and the ratio between the number of surface atoms and the total number of atoms would be much larger than in reality, causing surface effects to be much more important than what they should.

A solution to this problem is to use *periodic boundary conditions*(PBC). When using PBC, particles are enclosed in a box, and we can imagine that this box is replicated to infinity by rigid translation in all three Cartesian directions, completely filling the space. In other words, if one of our particles is located at position \mathbf{r} in the box, we assume that this particle really represents an infinite set of particles located at

$$\mathbf{r} + l\mathbf{a} + m\mathbf{b} + n\mathbf{c}, (l, m, n = -\infty, \infty)$$

where l, m, n are integers, we have indicated with $\mathbf{a}, \mathbf{b}, \mathbf{c}$ the vectors corresponding to the edges of the box. All these “image” particles move together, and in fact only one of them is represented in the computer program.

The key point is that now each particle i in the box should be thought as interacting not only with other particles j in the box, but also with their images in nearby boxes. That is, interactions can go through box boundaries. In fact, one can easily see that (a) we have virtually eliminated surface effects from our system, and (b) the position of the box boundaries has no effect. Apparently, the number of interacting pairs increases enormously as an effect of PBC. In practice, this is not true because potentials usually have a short interaction range. The *minimum image criterion* discussed in Ref. [28] simplifies things further, minimizing the additional complexity introduced in a program by PBC.

2.2 The ancestor of the “smartblock”

In 2000 Persson and Ballone published a paper [29] where they introduced a simple and effective model to study the boundary lubrication between elastic walls. For each wall only the outermost layer of atoms was considered. These atoms were able to interact with the lubricant or with the atoms of the other wall with Lennard-Jones potentials. The walls’ atoms were connected to a rigid surface through special springs which exert an elastic reaction not only to elongation, but also to lateral bending. The walls’ atoms are coupled with their in-plane neighbors with similar springs.

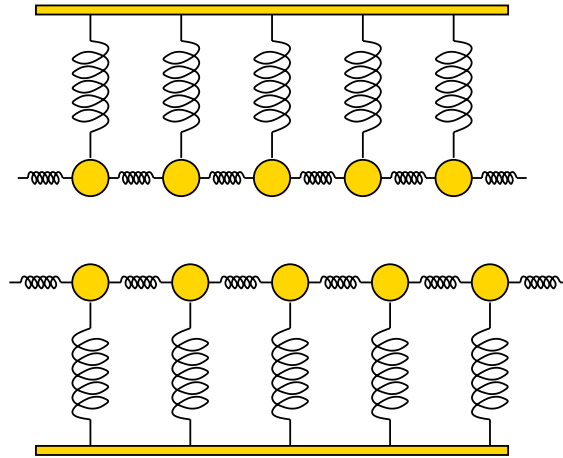


Figure 2.1: The model of Persson and Ballone with long range elasticity. Side view.

The simple model of Persson and Ballone catches two essential features: Firstly the walls are not rigid, differently from previous models adopted for simulations on boundary lubrication [30], but they take into account properly the elastic energy stored during compression or stretching, which is an essential ingredient for the study of the squeeze-out process. Secondly the shear rigidity is also properly described. Both the Young modulus and the shear modulus can be independently tuned via the choice of the elastic constants of the springs.

2.2.1 A lattice of atoms connected through springs

The model of Persson and Ballone works well when long range elastic deformation is considered, i.e., when the field of displacements varies gently at the interface. When there are abrupt changes of the profile, for instance when the displacement at the interface comprises short wavelength Fourier components, then the model reveals its limitations. The lack of internal degrees of freedom does not allow a proper description of the elastic fields inside the bulk. In particular the elastic lateral coupling within the bulk, responsible of the exponential damping of the short wavelengths strain fields, here is absent.

The solution to overcome this limitation is straightforward: we explicitly introduce many layers of atoms, placed on the points of a simple cubic lattice, and coupled with springs to their nearest neighbors.

2.2.2 The springs

The “springs”, as in the previous model, are special, since they can resist to lateral bending. The force due to a vertical spring connecting two consecutive atoms 1 and 2 along the z axis is given by the formulas below, where a is the lattice spacing, that is the equilibrium length of the spring.

$$F_x = -k_b \Delta x = -k_b(x_2 - x_1) \quad (2.2)$$

$$F_y = -k_b \Delta y = -k_b(y_2 - y_1) \quad (2.3)$$

$$F_z = -k(\Delta z - a) = -k[z_2 - (z_1 + a)] \quad (2.4)$$

Analogous formulas hold for the springs parallel to the x and to the y axes. The two elastic constants of the spring, namely k and k_b , are related to the Young modulus Y and

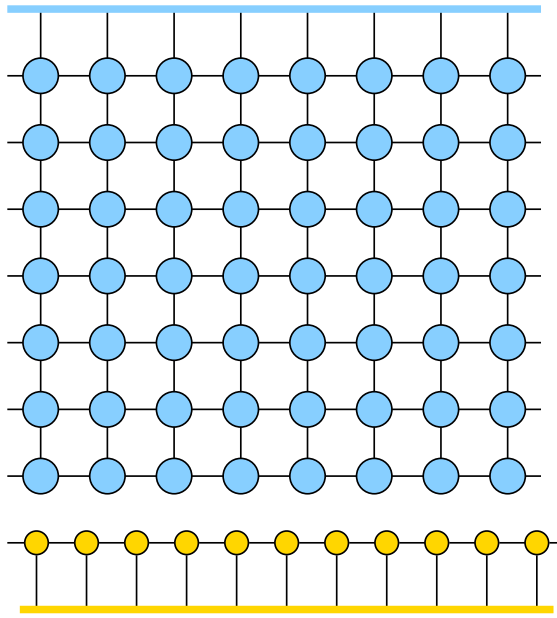


Figure 2.2: Side view of the block. The system is replaced by a simple cubic grid of atoms connected through springs, to take care of the internal degrees of freedom. Periodic boundary conditions are used along the x and y directions.

the shear modulus G respectively:

$$k = Ya$$

$$k_b = Ga$$

We observe that in the special case $k_b = k$ the force acting on particle 2 due to the spring connecting 1 with 2 becomes the one of a usual spring with length 0 and with equilibrium position coinciding with the equilibrium position of particle 2 relative to particle 1. While the force exerted by particle 2 onto particle 1 is centered on the equilibrium position of particle 1 with relative to particle 2. We observe also that a true spring connecting the particles 1 and 2 would have a completely different behavior, giving rise to forces along the line between the two particles.

The “springs” introduced in the model do not conserve the total angular momentum, since the forces are not in the direction of the springs. This is of no surprise: each spring predicts its own orientation parallel to one of the three Cartesian axes, thus the system is not invariant for rotation.

2.3 Elastic properties of a medium with cubic symmetry

The Smartblock is made of simple cubic lattice, thus it has the symmetric properties of a cubic system. In particular the system is not isotropic and it is described by 3 independent elastic constants, instead of 2 like for isotropic elastic media [31]. That means that we can choose, for example, the Young modulus Y (along the axes), the Poisson ratio ν , and the shear modulus G . In isotropic media the latter parameter follows from the first two through the relation $G = Y/[2(1 + \nu)]$ [32]

Following [33] we can write the relations between stress and strain for the cubic system in the following way:

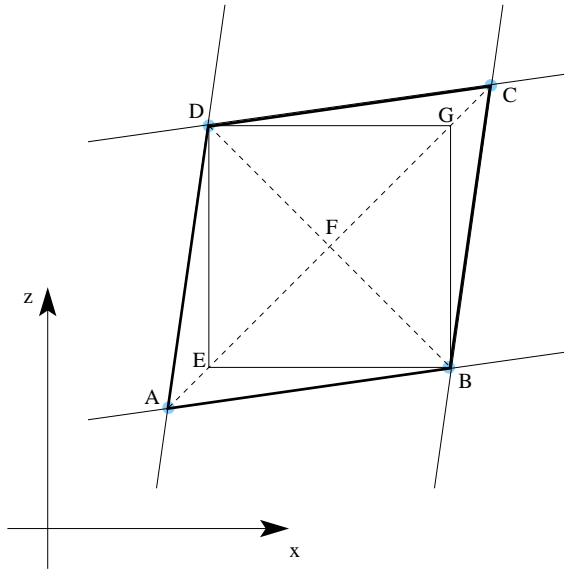


Figure 2.3: The grid of atoms under uniform strain along the diagonal \overline{AC} $\{x = z, y = 0\}$. There is no strain along the orthogonal directions, that is along the y axis and the \overline{BD} diagonal.

$$\begin{pmatrix} \sigma_{xx} \\ \sigma_{yy} \\ \sigma_{zz} \\ \sigma_{yz} \\ \sigma_{zx} \\ \sigma_{xy} \end{pmatrix} = \begin{pmatrix} c_{11} & c_{12} & c_{12} & 0 & 0 & 0 \\ c_{12} & c_{11} & c_{12} & 0 & 0 & 0 \\ c_{12} & c_{12} & c_{11} & 0 & 0 & 0 \\ 0 & 0 & 0 & c_{44} & 0 & 0 \\ 0 & 0 & 0 & 0 & c_{44} & 0 \\ 0 & 0 & 0 & 0 & 0 & c_{44} \end{pmatrix} \begin{pmatrix} \epsilon_{xx} \\ \epsilon_{yy} \\ \epsilon_{zz} \\ \epsilon_{yz} \\ \epsilon_{zx} \\ \epsilon_{xy} \end{pmatrix} \quad (2.5)$$

The three elastic moduli c_{11} , c_{12} and c_{44} are given by

$$c_{11} = \frac{1 - \nu}{(1 + \nu)(1 - 2\nu)} Y$$

$$c_{12} = \frac{\nu}{(1 + \nu)(1 - 2\nu)} Y$$

$$c_{44} = 2G$$

In many texts the matrix notation of equation 2.5 is often defined in a slightly different way, using the shear strains $\gamma_{xy} = 2\epsilon_{xy}$, $\gamma_{yz} = 2\epsilon_{yz}$, and $\gamma_{zx} = 2\epsilon_{zx}$ in place of the off-diagonal terms of the strain tensors. Thus the definition of c_{44} differs by a factor 0.5.

2.3.1 The Poisson ratio of the Smartblock is zero

The Smartblock always has vanishing Poisson ratio, no matter what are the choices of the elastic constants k and k_b . Indeed any compression parallel to one axis does not give rise to lateral expansion or to compressive stress along the other axes.

2.3.2 Anisotropy of the Smartblock

To better understand the anisotropic behavior of the smartblock, let us consider an uniaxial strain along a direction not parallel with the axes, such as the [101] crystalline

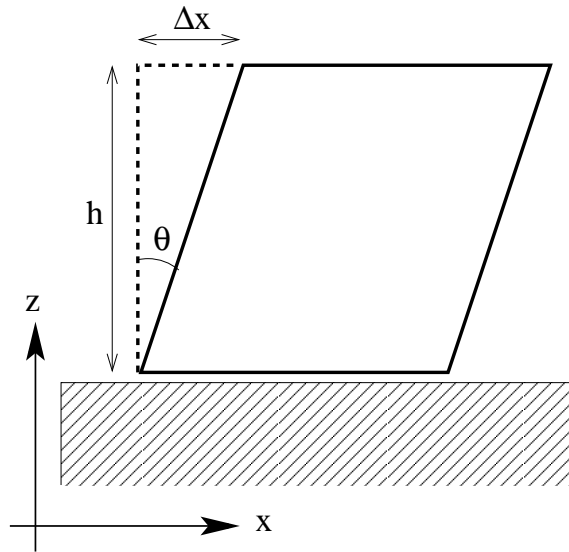


Figure 2.4: Elastic block under shear strain. The strain tensor has component $\epsilon_{xz} = \Delta x/2h \approx \theta/2$

orientation as shown in figure 2.3. Let the strain along \overline{AC} be ε and the strain along \overline{BD} be zero. We want to calculate the components of the stress tensor. The lattice spacing a is the length of the relaxed cell: $a = \overline{EB} = \overline{BG}$. We have $\overline{FC} = (1 + \varepsilon)a/\sqrt{2}$, thus the deformations of the strings \overline{BC} and \overline{DC} are $\Delta x = \Delta z = \varepsilon a/2$; $\Delta y = 0$. The springs parallel to the y axis, i.e., orthogonal to the plane of the figure, are not deformed.

The calculation of the stress between atomic planes orthogonal to \overline{AC} is straightforward. The force on atom C due to atoms B and D is directed towards A and has modulus $(\sqrt{2}/2)\varepsilon a(k + k_b)$. The area per atom in the considered atomic planes is $\sqrt{2}a^2$. Thus the stress along \overline{AC} is $\varepsilon(k + k_b)/(2a)$. The same strain applied along one of the main axes would lead to the stress $\varepsilon k/a$. **In order to get the same stress along different directions we must choose $k_b = k$.** It is easy to see that with this choice the stress along \overline{BD} vanishes, as it has to be for a system with Poisson ratio $\nu = 0$.

The shear modulus of the smartblock is $G = k_b/a$, thus in the case of the isotropic smartblock ($k = k_b$) it coincides with the Young modulus. This is puzzling, since isotropic elastic materials must have the shear modulus $G = Y/[2(1 + \nu)]$, hence G must be half of Y when the Poisson ratio is null. This discrepancy has to do with the broken rotational invariance of the model. Consider the shear stress sketched in figure 2.4: the shear $\theta \approx \Delta x/h$ is twice the off-diagonal component ϵ_{xz} of the strain tensor. Indeed only the symmetric part of the gradient of the displacement $\frac{1}{2}(\frac{\partial u_x}{\partial z} + \frac{\partial u_z}{\partial x}) \approx \theta/2$ contributes to the strain. The antisymmetric part $\frac{1}{2}(\frac{\partial u_x}{\partial z} - \frac{\partial u_z}{\partial x})$ corresponds to an average rotation of $\theta/2$. On the other hand the smartblock reacts to any attempt to rotate it in a similar way as when a shear strain is applied. Therefore an isotropic smartblock should have a shear modulus twice bigger than that of an isotropic elastic medium. Conversely, **when the smartblock has to behave as close as possible to isotropic elastic media, the best choice of the shear modulus is anyway $G = Y/[2(1 + \nu)] = Y/2$, so that the proper force field is obtained for small deformations.**

2.4 Going multiscale

In some circumstances [5,6] it is useful to simulate quite large and thick samples. Moreover high resolution up to the atomic level is needed in part of the sample, typically at the interface. The solution to avoid excessive computational times is a multiscale approach: high resolution is achieved where it is needed, but a coarse grained description is employed when it is feasible. The coarse graining can happen more times, and to various degrees of resolution, so that a multilevel description of the system comprising many hierarchies is implemented.

The grid structure of the smartblock allows a simple procedure to achieve a multiscale description: groups of atoms can be replaced by single, bigger atoms, and the elastic constants of the springs are redefined to guarantee the same elastic response. In many calculations performed by our group we used to replace a cube of $2 \times 2 \times 2$ particles with a single particle, repeating this merging procedure every two layers. More generally any change of resolution involves merging together a box made of $m_x \times m_y \times m_z$ particles. The three numbers m_x , m_y and m_z are called *merging factors* along the three axes.

The equilibrium position of the new particle is in the center of mass of the group of particles merged together. Its mass is $m_x m_y m_z$ times the mass of the original particles, so that the density does not change. In fact the masses are only important to study the kinetic, but they do not influence the static equilibrium configuration.

The three merging factors can be chosen independently. The easiest way to calculate the new springs' elastic constants is to consider the merging only along one of the axes. Fig. 2.5 sketches the case $m_z = 2$, $m_x = m_y = 1$ (no change of lattice spacing along x and y). Along the direction of merging the new spring constants for elongation and bending are $k' = k/m_z$ and $k'_b = k_b/m_z$ respectively. The longer springs get proportionally smaller elastic constants, as it happens when springs are connected in series. In the two directions orthogonal to each spring, m_z (old) springs are replaced by a single one in parallel configuration, so the elastic constants increase proportionally: $k' = m_x k$, $k'_b = m_x k_b$. Below is the general formula giving the new elastic constants of the springs along the z axis, with arbitrary merging factors:

$$k' = \frac{m_x m_y}{m_z} k; \quad k'_b = \frac{m_x m_y}{m_z} k_b \quad (2.6)$$

Analogous formulas hold for the springs parallel to the x and y axes.

To get the whole picture we have to characterize the springs at the interface between the two lattices, e.g., the ones crossing the dashed line in figure 2.5. When the merging is in the direction z orthogonal to the interface, the answer is easy: both elastic constants k and k_b get multiplied by the factor $2/(1 + m_z)$. Actually their length is $\frac{1}{2}(m_z + 1)a_z$, a_z being the old lattice spacing along z . Each of these interface springs can be thought as half a spring of the old grid connected with half a spring of the new grid.

When the merging is along a direction orthogonal to the interface between the two grids, as sketched in figure 2.6, then the spring constants do not change, but the forces between the particles are calculated taking into account the in-plane shift between the atoms of the two grids. Each interface particle of the upper lattice interacts with $m_x \times m_y$ particles of the lower lattice. The equations (2.2) and (2.3) are modified: $F_x = -k_b(\Delta x + x\text{-shift})$, $F_y = -k_b(\Delta y + y\text{-shift})$. The two in-plane shifts depend on the pair of particle considered.

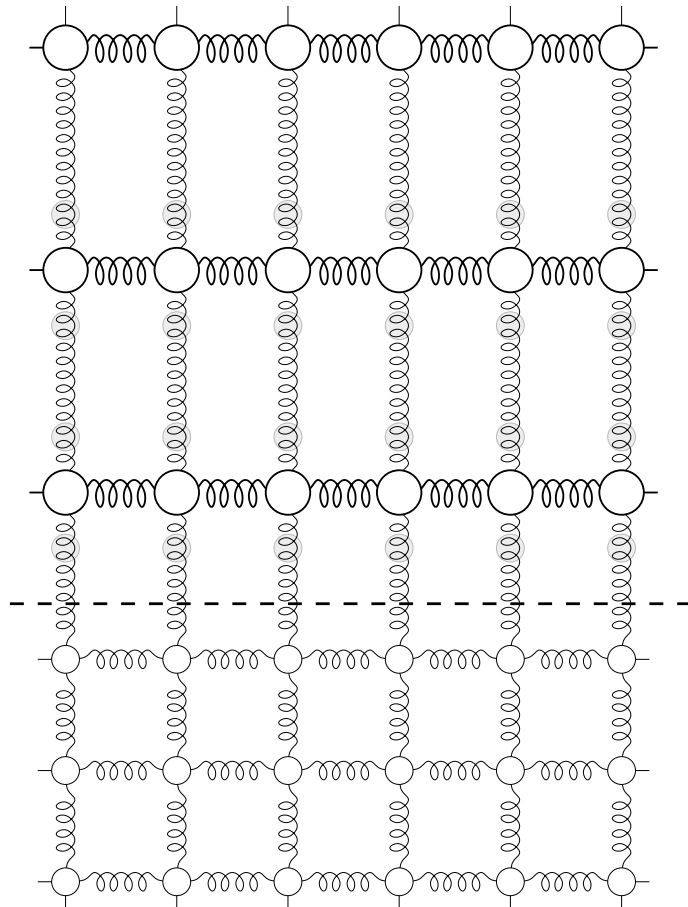


Figure 2.5: The grid of particles is coarse grained by replacing two atoms with a single one. Merging factors $m_x = m_y = 1$, $m_z = 2$. Masses, equilibrium positions and spring constants are changed accordingly.

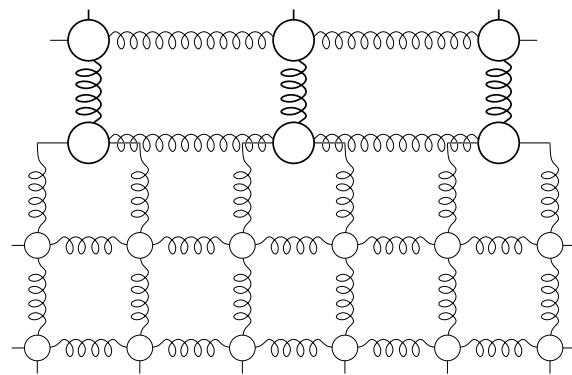


Figure 2.6: Change of lattice spacing along a direction parallel to the interface between the two grids.

Chapter 3

Area of Contact between Randomly Rough Surfaces

It is very difficult to prepare surfaces which are really flat. Even on highly polished surfaces, there are hills and valleys, which are large compared with the size of a molecule. If two solids are placed in contact, the upper surface will be supported on the summits of irregularities, and large areas of the surfaces will be separated by a distance which is great compared with the molecular range of action.

In this chapter I will use our multiscale molecular dynamics approach to study contact mechanics, which can be used also when the surfaces have roughness on many different length scales, e.g. for self-affine fractal surfaces. As an illustration, the contact between randomly rough surfaces is considered. Results show that the contact area varies linearly with the load for small load. The contact morphology and the pressure distribution, at different magnifications, are shown both with and without adhesion. The calculations are compared with analytical contact mechanics models based on continuum mechanics. All the numerical calculations in this chapter are based on the condition of small load, that is, the real contact area is much smaller than the nominal contact area.

3.1 Introduction

Adhesion and friction between solid surfaces are common phenomena in nature and of extreme importance in biology and technology. Most surfaces of solids have roughness on many different length scales [34, 35], and it is usually necessary to consider many decades in length scale when describing the contact between solids [1]. This makes it very hard to describe accurately the contact mechanics between macroscopic solids using computer simulation methods, e.g., atomistic molecular dynamics, or finite element calculations based on continuum mechanics.

Consider a solid with a nominally flat surface. Let x, y, z be a coordinate system with the x, y plane parallel to the surface plane. Assume that $z = h(\mathbf{x})$ describes the surface height profile, where $\mathbf{x} = (x, y)$ is the position vector within the surface plane. The most important property characterizing a randomly rough surface is the surface roughness power spectrum $C(\mathbf{q})$ defined by [1, 2]

$$C(\mathbf{q}) = \frac{1}{(2\pi)^2} \int d^2x \langle h(\mathbf{x})h(\mathbf{0}) \rangle e^{i\mathbf{q}\cdot\mathbf{x}}. \quad (3.1)$$

Here $\langle \dots \rangle$ stands for ensemble average and we have assumed that $h(\mathbf{x})$ is measured from the average surface plane so that $\langle h \rangle = 0$. In what follows we will assume that the

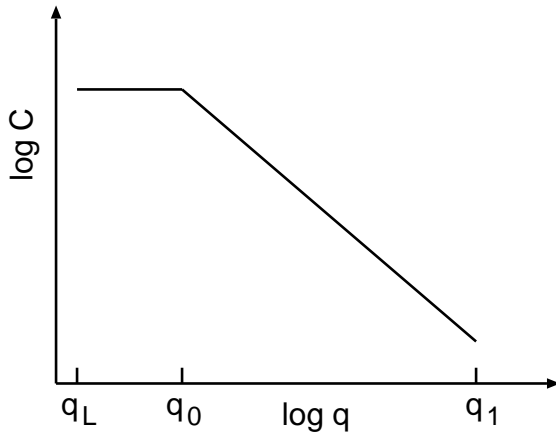


Figure 3.1: Surface roughness power spectrum of a surface which is self affine fractal for $q_0 < q < q_1$. The long-distance roll-off wave vector q_0 and the short distance cut-off wave vector q_1 depends on the system under consideration. The slope of the $\log C - \log q$ relation for $q > q_0$ determines the fractal exponent of the surface. The lateral size L of the surface (or of the studied surface region) determines the smallest possible wave vector $q_L = 2\pi/L$.

statistical properties of the surface are isotropic, in which case $C(q)$ will only depend on the magnitude $q = |\mathbf{q}|$ of the wave vector \mathbf{q} .

Many surfaces tend to be nearly self-affine fractal. A self-affine fractal surface has the property that if part of the surface is magnified, with a magnification which in general is appropriately different in the perpendicular direction to the surface as compared to the lateral directions, then the surface “looks the same”, i.e., the statistical properties of the surface are invariant under the scale transformation [1]. For a self-affine surface the power spectrum has the power-law behavior

$$C(q) \sim q^{-2(H+1)},$$

where the Hurst exponent H is related to the fractal dimension D_f of the surface via $H = 3 - D_f$. Of course, for real surfaces this relation only holds in some finite wave vector region $q_0 < q < q_1$, and in a typical case $C(q)$ has the form shown in Fig. 3.1. Note that in many cases there is a roll-off wave-vector q_0 below which $C(q)$ is approximately constant.

Let us consider the contact between an elastic solid with a flat surface and a hard randomly rough substrate. Fig. 3.1 shows the contact between the solids at increasing magnification ζ . At low magnification ($\zeta = 1$) it looks as if complete contact occurs between the solids at the caps of many macro asperities. but when the magnification is increased, smaller length scale roughness is detected, and it is observed that only partial contact occurs at the asperity caps. In fact, if there were no short distance cut-off, the true contact area would vanish. In reality, however, a short distance cut-off will always exist since the shortest possible length is an atomic distance. In many cases, the local pressure at asperity contact regions at high magnification becomes so high that the material yields plastically before reaching the atomic dimension. In these cases the size of the real contact area will be determined mainly by the yield stress of the solid.

The magnification ζ refers to some (arbitrary) chosen reference length scale. This could be, e.g., the lateral size L of the nominal contact area in which case $\zeta = L/\lambda$, where λ is the shortest wavelength roughness which can be resolved at magnification ζ . In this chapter I will instead use the roll-off wavelength $\lambda_0 = 2\pi/q_0$ as the reference length so that $\zeta = \lambda_0/\lambda$.

Recently, a very general contact mechanics theory has been developed in order to describe rubber friction on rough substrate. It can be applied to both stationary and sliding contact for viscoelastic solids (which includes elastic solids as a special case) [2]. For elastic solids the theory can also be applied when the adhesive interaction is taken into account [4]. In contrast to earlier contact mechanics theories, the theory presented in Ref. [2, 4] is particularly accurate close to complete contact, as would be the case for, e.g., rubber on smooth surfaces. The basic idea behind the theory is to study the contact at different magnification (more details can be found in Appendix A). In particular, the theory describes the change in the stress distribution $P(\sigma, \zeta)$ as the magnifications ζ increases. Here

$$P(\sigma, \zeta) = \langle \delta(\sigma - \sigma(\mathbf{x}, \zeta)) \rangle \quad (3.2)$$

is the stress distribution at the interface when the surface roughness with wavelength smaller than $\lambda = \lambda_0/\zeta$ has been removed. In (3.2), $\langle \dots \rangle$ stands for ensemble average, and $\sigma(\mathbf{x}, \zeta)$ is the stress orthogonal to the interface smeared over a distance $\lambda = \lambda_0/\zeta$. It is clear that as the magnification ζ increases, the distribution $P(\sigma, \zeta)$ will be broader and broader and the theory describes this in detail. The (normalized) area of real contact (projected on the xy -plane) at the magnification ζ can be written as

$$\frac{A(\zeta)}{A_0} = \int_{0^+}^{\infty} d\sigma P(\sigma, \zeta). \quad (3.3)$$

where the lower integration limit 0^+ indicates that the delta function at the origin $\sigma = 0$ (arising from the non-contact area) should be excluded from the integral. The rubber friction theory described in Ref. [2] depends on the function $A(\zeta)/A_0$ for *all magnifications*. This just reflects the fact that the friction force results from the viscoelastic deformations of the rubber on all length scales, and when evaluating the contribution to the friction from the viscoelastic deformations on the length scale λ , it is necessary to know the contact between the rubber and the substrate at the magnification $\zeta = \lambda_0/\lambda$. Thus, not only the area of real (atomic) contact is of great interest, but also many important applications require the whole function $A(\zeta)$, and the pressure distribution $P(\sigma, \zeta)$.

In order to accurately reproduce the contact mechanics between elastic solids, it is in general necessary to consider solid blocks which extend a similar distance in the direction normal to the nominal contact area as the linear size of the contact area. This leads to an enormous number of atoms or dynamical variables already for relatively small systems. In this chapter we develop a multiscale approach to contact mechanics where the number of dynamical variables scales like $\sim N^2$ rather than as $\sim N^3$, where $N \times N$ is the number of atoms in the nominal contact area. As an application we consider the contact mechanics between randomly rough surfaces both with and without adhesion, and compare the results with analytical contact mechanics theories.

3.2 Multiscale molecular dynamics

3.2.1 Why use multiscale molecular dynamics?

Let us discuss the minimum block-size necessary in a computer simulation for an accurate description of the contact mechanics between two semi-infinite elastic solids with nominal flat surfaces. Assume that the surface roughness power spectrum has a roll-off wave-vector $q = q_0$ corresponding to the roll-off wavelength $\lambda_0 = 2\pi/q_0$. In this case the minimum block must extend $L_x \approx \lambda_0$ and $L_y \approx \lambda_0$ along the x and y -directions. Furthermore, the block must extend at least a distance $L_z \approx \lambda_0$ in the direction perpendicular to the nominal contact area. The latter follows from the fact that a periodic stress distribution

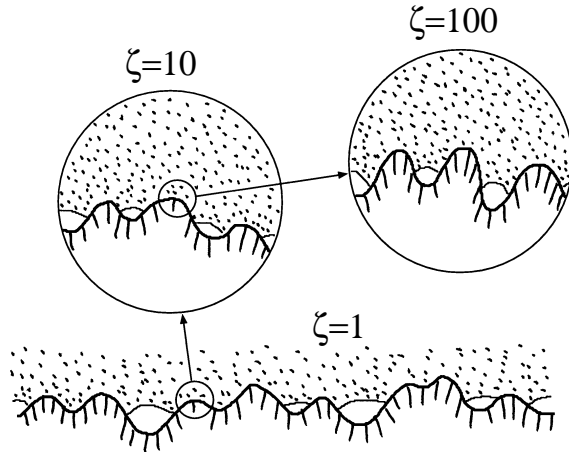


Figure 3.2: A rubber block (dotted area) in adhesive contact with a hard rough substrate (dashed area). The substrate has roughness on many different length scales and the rubber makes partial contact with the substrate on all length scales. When a contact area is studied at low magnification ($\zeta = 1$) it appears as if complete contact occurs in the macro asperity contact regions, but when the magnification is increased it is observed that in reality only partial contact occurs.

with wavelength λ , acting on the surface of a semi-infinite elastic solid, gives rise to a deformation field which extends a distance $\sim \lambda$ into the solid. Thus, the minimum block is a cube with the side $L = \lambda_0$.

As an example, if λ_0 corresponds to 1000 atomic spacings, one must at least consider a block with 1000×1000 atoms within the xy -contact plane, i.e., one would need to study the elastic deformation in a cubic block with at least 10^9 atoms. However, it is possible to drastically reduce the number of dynamical variables without loss of accuracy if one notes that an interfacial roughness with wavelength λ will give rise to a deformation field in the block which extends a distance λ into the solid, and which varies spatially over a typical length scale λ . Thus when we study the deformation a distance z into the block we do not need to describe the solid on the atomistic level, but we can coarse-grain the solid by replacing groups of atoms with bigger “atoms” as indicated schematically in Fig. 3.3. If there are $N \times N$ atoms in the nominal contact area one need $n \approx \ln N$ “atomic” layers in the z -direction. Moreover the number of atoms in each layer decreases in a geometric progression every time the coarse graining procedure is applied, so that the total number of particles is of order N^2 instead of N^3 . This results in a huge reduction in the computation time for large systems. This multiscale approach may be implemented in various ways, and in chapter 2 we have outlined the procedure we have used in this chapter which we refer to as the *smartblock*. Another implementation similar to our approach can be found in Ref. [36].

The smartblock model should accurately describe the deformations in the solids as long as the deformations vary slowly enough with time. However, the model cannot accurately describe the propagation of short wavelength phonons. This is, in fact, true with all forms of Hamiltonian multiscale descriptions of solids, because of the energy conservation together and the unavoidable loss of information in the coarse grained region. In principle it should be possible to prevent the back reflection of short wavelength phonons by describing the coarse grained region as a continuum, where the numerical calculation can be carried on through a Finite Element scheme. [37–40] This indeed would require no

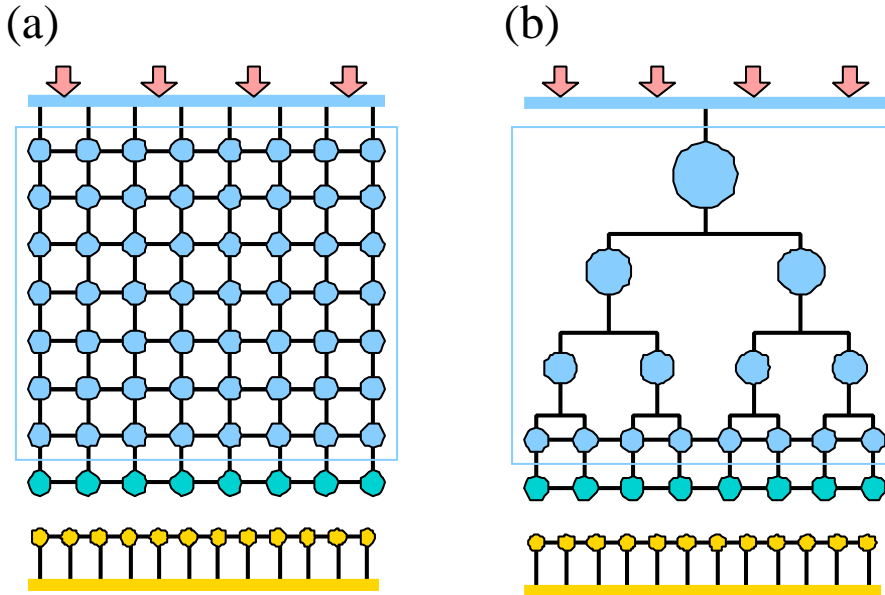


Figure 3.3: Schematic structure of the model. (a) The fully atomistic model. (b) The multiscale *smartblock* model, where the solid in (a) is coarse grained by replacing groups of atoms with bigger ‘‘atoms’’.

coarse graining at all in the region treated with molecular dynamics, and a proper choice of the matching conditions between the atomistic and the continuum region. However, with respect to contact mechanics and adhesion the back reflection of short wavelength phonons is not an important limitation. With respect to sliding friction it may be a more severe limitation in some cases.

Fig. 3.3 illustrates a case where the block is in the form of a cube with atomically flat surfaces. It is possible to obtain curved surfaces of nearly arbitrary shape by ‘‘gluing’’ the upper surface of the block to a hard curved surface profile. This was described in detail in Ref. [2]. The elastic modulus and the shear modulus of the solid can be fixed at any value by proper choice of the elongation and bending spring constants for the springs between the atoms (see Ref. [2] and chapter 2). The upper surface of the smartblock can be moved with arbitrary velocity in any direction, or an external force of arbitrary magnitude can be applied to the upper surface of the smartblock. The sliding friction problems are studied in chapter 8, where the upper surface of the smartblock is connected to a spring which is pulled in some prescribed way. The computer code also allows for various lubricant fluids between the solid surfaces of the block and the substrate. Thus the present model is extremely flexible and can be used to study many interesting adhesion and friction phenomena (see the following chapters).

3.2.2 Parameters and potential

Note that with respect to contact mechanics, when the slopes of the surfaces are small, i.e. when the surfaces are almost horizontal, one of the two surfaces can be considered flat, while the profile of the other surface has to be replaced by the difference of the two original profiles [41]. Thus, if the substrate has the profile $z = h_1(\mathbf{x})$ and the block has the profile $z = h_2(\mathbf{x})$, then one can replace the actual system with a fictive one where the block has a smooth surface while the substrate profile is $h(\mathbf{x}) = h_2(\mathbf{x}) - h_1(\mathbf{x})$. Furthermore, if the

original solids have the elastic modulus E_1 and E_2 , and the Poisson ratio ν_1 and ν_2 , then the substrate in the fictive system can be treated as rigid and the block as elastic with the elastic modulus E and Poisson ratio ν chosen so that $(1-\nu^2)/E = (1-\nu_1^2)/E_1 + (1-\nu_2^2)/E_2$.

The results presented below have been obtained for a rigid and rough substrate. The atoms in the bottom layer of the block form a simple square lattice with lattice constant a . The lateral dimensions $L_x = N_x a$ and $L_y = N_y a$. For the block, $N_x = 400$ and $N_y = 400$. Periodic boundary conditions are applied in the xy plane. The lateral size of the block is equal to that of substrate, but we use a different lattice constant $b \approx a/\phi$, where $\phi = (1+\sqrt{5})/2$ is the golden mean, in order to avoid the formation of commensurate structures at the interface. The mass of a block atom is 197 a.m.u. and the lattice constant of the block is $a = 2.6$ Å. We consider solid blocks with two different Young's moduli: a hard solid with $E = 77.2$ GPa, like in gold, and a soft one with 0.5 GPa. The corresponding shear moduli were $G = 27$ GPa and 0.18 GPa, respectively.

The atoms at the interface between the block and the substrate interact with the potential

$$U(r) = 4\epsilon \left[\left(\frac{r_0}{r} \right)^{12} - \alpha \left(\frac{r_0}{r} \right)^6 \right] \quad (3.4)$$

where r is the distance between a pair of atoms. When $\alpha = 1$, Eq. 3.4 is the standard Lennard-Jones potential. The parameter ϵ is the binding energy between two atoms at the separation $r = 2^{1/6}r_0$. When we study contact mechanics without adhesion we put $\alpha = 0$. In the calculations presented below we have used $r_0 = 3.28$ Å and $\epsilon = 18.6$ meV, which (when $\alpha = 1$) gives an interfacial binding energy (per unit area) [42] $\Delta\gamma \approx 4\epsilon/a^2 \approx 11$ meV/Å².

3.2.3 Self affine fractal surfaces

Self affine fractal surfaces, generated as outlined in Ref. [1], have been used in the following calculations. Thus, the surface height is written as

$$h(\mathbf{x}) = \sum_{\mathbf{q}} B(\mathbf{q}) e^{i[\mathbf{q} \cdot \mathbf{x} + \phi(\mathbf{q})]} \quad (3.5)$$

where, since $h(\mathbf{x})$ is real, $B(-\mathbf{q}) = B(\mathbf{q})$ and $\phi(-\mathbf{q}) = -\phi(\mathbf{q})$. If $\phi(\mathbf{q})$ are independent random variables, uniformly distributed in the interval $[0, 2\pi]$, then one can easily show that higher order correlation functions involving $h(\mathbf{x})$ can be decomposed into a product of pair correlations, which implies that the height probability distribution $P_h = \langle \delta(h - h(\mathbf{x})) \rangle$ is Gaussian [1]. However, such surfaces can have *arbitrary surface roughness power spectrum*. To prove this, substitute (3.5) into (3.1) and use that

$$\langle e^{i\phi(\mathbf{q}')} e^{i\phi(\mathbf{q}'')} \rangle = \delta_{\mathbf{q}', -\mathbf{q}''}$$

gives

$$\begin{aligned} C(\mathbf{q}) &= \frac{1}{(2\pi)^2} \int d^2x \sum_{\mathbf{q}'} |B(\mathbf{q}')|^2 e^{i(\mathbf{q}-\mathbf{q}') \cdot \mathbf{x}} \\ &= \sum_{\mathbf{q}'} |B(\mathbf{q}')|^2 \delta(\mathbf{q} - \mathbf{q}') \end{aligned}$$

Replacing

$$\sum_{\mathbf{q}} \rightarrow \frac{A_0}{(2\pi)^2} \int d^2q,$$

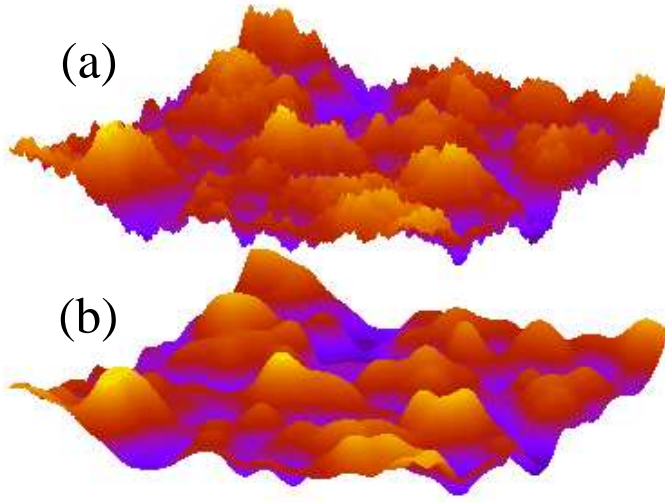


Figure 3.4: (a) Fractal surface with the large wave-vector cut-off $q_1 = 2\pi/b \approx 216q_0$. (b) The same surface as in (a) but at lower resolution with $q_1 = 4q_0$. For a square $1040 \text{ \AA} \times 1040 \text{ \AA}$ surface area. The fractal dimension $D_f = 2.2$ and the root-mean-square roughness amplitude is 10 \AA .

where A_0 is the nominal surface area, gives

$$C(\mathbf{q}) = \frac{A_0}{(2\pi)^2} |B(\mathbf{q})|^2.$$

Thus, if we choose

$$B(\mathbf{q}) = (2\pi/L)[C(\mathbf{q})]^{1/2}, \quad (3.6)$$

where $L = A_0^{1/2}$, then the surface roughness profile (3.5) has the surface roughness power density $C(\mathbf{q})$. If we assume that the statistical properties of the rough surface are isotropic, then $C(\mathbf{q}) = C(q)$ is a function of the magnitude $q = |\mathbf{q}|$, but not of the direction of \mathbf{q} . The following numerical calculations use randomly rough surfaces as substrates generated using (3.5) and (3.6) and assuming that the surface roughness power spectra have the form shown in Fig. 3.1, with the fractal dimension $D_f = 2.2$ and the roll-off wave-vector $q_0 = 3q_L$, where $q_L = 2\pi/L_x$. We have chosen $q_0 = 3q_L$ rather than $q_0 = q_L$ since the former value gives some self-averaging and less noisy numerical results. We also used $q_1 = 2\pi/b \approx 216q_0$ (topography (a) in Fig. 3.4) and some surfaces with several smaller values for q_1 (Fig. 3.4 (b) shows the topography when $q_1 = 4q_0$), corresponding to lower magnification (see Sec. 3.3).

3.3 Numerical results

In this section I illustrate our multiscale molecular dynamics (MD) approach by some applications. The MD results are compared with two known contact mechanics results from continuum mechanics. Next I discuss contact mechanics for randomly rough surfaces both with and without adhesion.

3.3.1 Test cases: Hertz contact and complete contact

In 1881 Hertz presented an exact solution for the contact between two perfectly elastic solids with local quadratic profiles. The results were derived using the elastic continuum model and neglecting the adhesion between the solids. In addition, Hertz assumed that the interfacial friction vanishes so that no shear stress can develop at the interface between the solids. When a spherical asperity is squeezed against a flat surface a circular contact area (radius r_H) is formed, where the pressure decreases continuously from the center $r = 0$ to the periphery $r = r_H$ of the contact according to

$$\sigma = \sigma_H \left[1 - \left(\frac{r}{r_H} \right)^2 \right]^{1/2}. \quad (3.7)$$

Let us compare the prediction of our atomistic model with the Hertz theory. We use the Lennard-Jones potential with $\alpha = 0$, i.e. without the attractive term. In Fig. 3.5 we compare the Hertz contact pressure (green line) with our numerical data (red data points). The numerical data were obtained for a rigid spherical tip squeezed against a flat elastic surface. Note that the pressure obtained from the MD calculation has a tail beyond the Hertz contact radius r_H . Similar “pressure tails” were recently observed in molecular dynamics simulations by Luan and Robbins [43]. The tail reflects the non-zero extent of the atom-atom interaction potential. The deviation between the molecular dynamics results and the continuum mechanics results should decrease continuously as the size of the system increases.

At the atomic level there is no unique way to define when two solids are in contact, and one may use several different criteria. One method is based on the force acting between the atoms at the interface and works best when the adhesive interaction is neglected. Thus, when two surfaces approach each other, the repulsive force between the atoms increases. We may define contact when the repulsive force is above some critical value. When adhesion is included the interaction between the wall atoms becomes more long-ranged and it is less obvious how to define contact based on a force criterion, and we find it more convenient to use a criteria based on the nearest neighbor distance between atoms on the two surfaces. Thus, when the separation between two opposing surface atoms is less than some critical value, contact is defined to occur. However, we have found that neither of these two criteria gives fully satisfactory results. The reason is that if the critical force or the critical distance used to define when contact occurs is determined by fitting the Hertz pressure profile (3.7) to the numerical data as in Fig. 3.5, then the resulting values depend on the radius of curvature of the asperity. For example, for the Hertz contact in Fig. 3.5 the contact area deduced from the atomistic MD calculation agrees with the Hertz theory if we choose the cut-off pressure $p_c \approx 0.7$ GPa. However, if the radius of curvature of the asperity is 10 times smaller ($R = 104$ Å) then, for the same penetration, the cut-off would be $p_c \approx 2.5$ GPa, i.e., more than three times larger. On the other hand randomly rough surfaces have a wide distribution of curvatures and it is not clear how to choose the optimum cut-off distance or force. In this chapter we have therefore used another way of determining the contact area which turned out to be more unique. We will now describe this method.

Let us consider the pressure distribution $P(\sigma, \zeta)$ at the interface. For Hertz contact we get the pressure distribution

$$P(\sigma) = \frac{1}{A_0} \int_{A_0} d^2x \delta(\sigma - \sigma(x)) \quad (3.8)$$

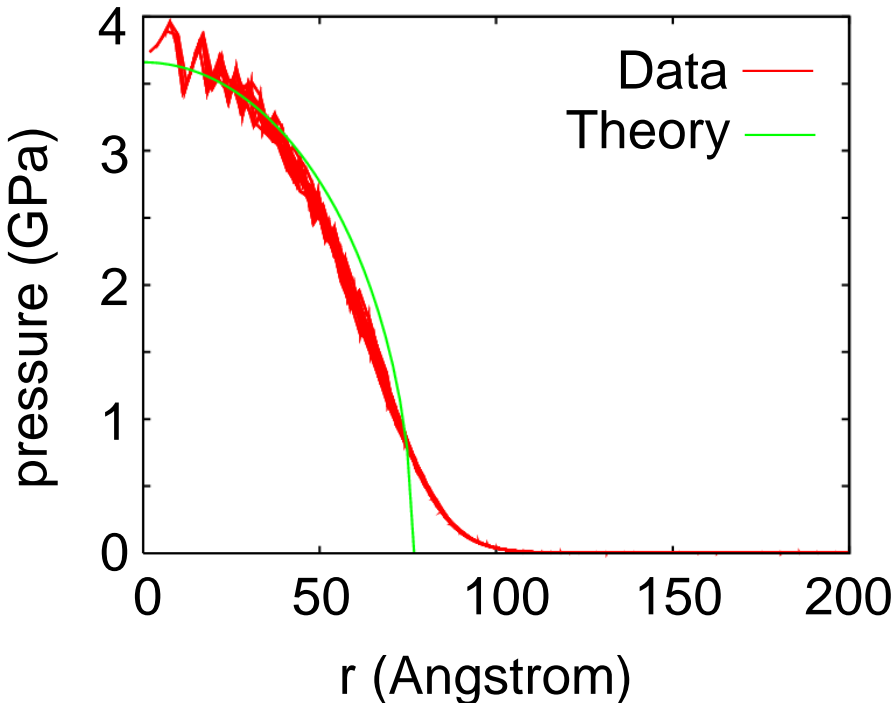


Figure 3.5: The pressure in the contact region between a spherical tip and a flat elastic surface. We show the simulation data and the theoretical Hertz result. The spherical tip has the radius of curvature $R = 1040 \text{ \AA}$ and the loading force $4.6 \times 10^{-7} \text{ N}$.

Using $\sigma(\mathbf{x})$ from (3.7) for $r < r_H$ and $\sigma(\mathbf{x}) = 0$ for $r > r_H$ gives

$$P(\sigma) = \left(1 - \frac{A}{A_0}\right) \delta(\sigma) + \frac{2\sigma}{\sigma_H^2} \frac{A}{A_0} \quad (3.9)$$

where $A = \pi r_H^2$ is the Hertz contact area. In Fig. 3.6 we show the pressure distribution in the contact region between a hard spherical tip and an elastic solid with a flat surface. The red curve shows the simulation data, while the green curve is the theoretical Hertz result obtained by a suitable choice of A in Eq. 3.9. Note that while the Hertz solution and the atomic MD simulation results agree very well for large pressure, there is a fundamental difference for small pressure. Thus, for the Hertz solution, for small pressure $\sigma \rightarrow 0$, $P(\sigma) \sim \sigma$, while in the atomistic model $P(\sigma)$ increase monotonically as $\sigma \rightarrow 0$. This difference is due to the long-range interaction between the solid walls in the atomistic model, which is absent in the Hertz model. When the long range wall-wall interaction is taken into account the delta function at $\sigma = 0$ in the Hertz solution (3.9) will broaden, resulting in a $P(\sigma)$ which (for the small systems considered here) will decay monotonically with increasing σ as observed for the atomistic model. Note that this effect is of exactly the same origin as the “pressure tail” for $r > r_H$ in Fig. 3.5.

The fact that $P(\sigma, \zeta)$ vanishes linearly with σ as $\sigma \rightarrow 0$ is an exact result in continuum mechanics with contact interaction (no long range wall-wall interaction), and is valid not only for the Hertz contact case, but also holds in general [44]. However, as explained above, this effect will never be observed in the atomistic model if the wall-wall interaction is long-ranged.

Note that the contact area A can be determined directly by fitting the analytical expression for $P(\sigma)$ for the Hertz contact (Eq. 3.9) to the numerical MD results for large

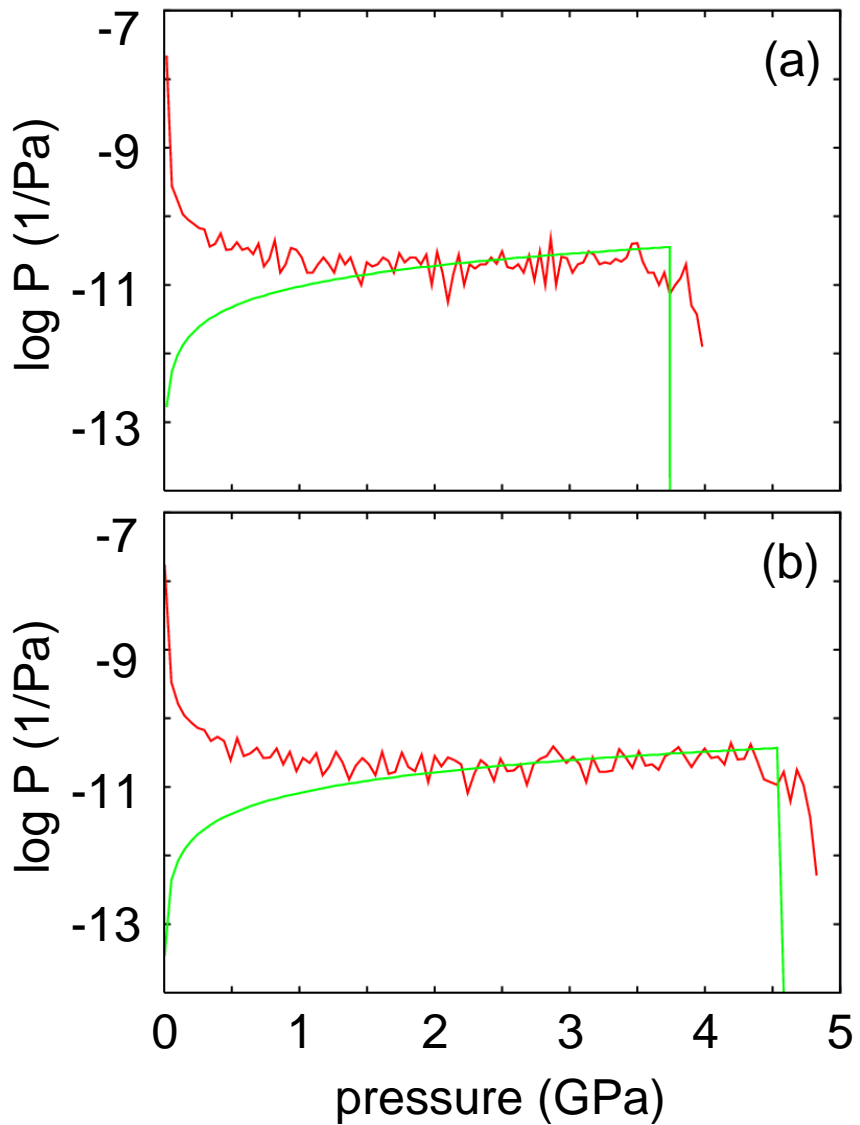


Figure 3.6: The pressure distribution in the contact region between a spherical tip and a flat surface. We show the simulation data (red curves) and the theoretical Hertz result (green curves). Loading force in (a) is 4.6×10^{-7} N and in (b) 7.3×10^{-7} N.

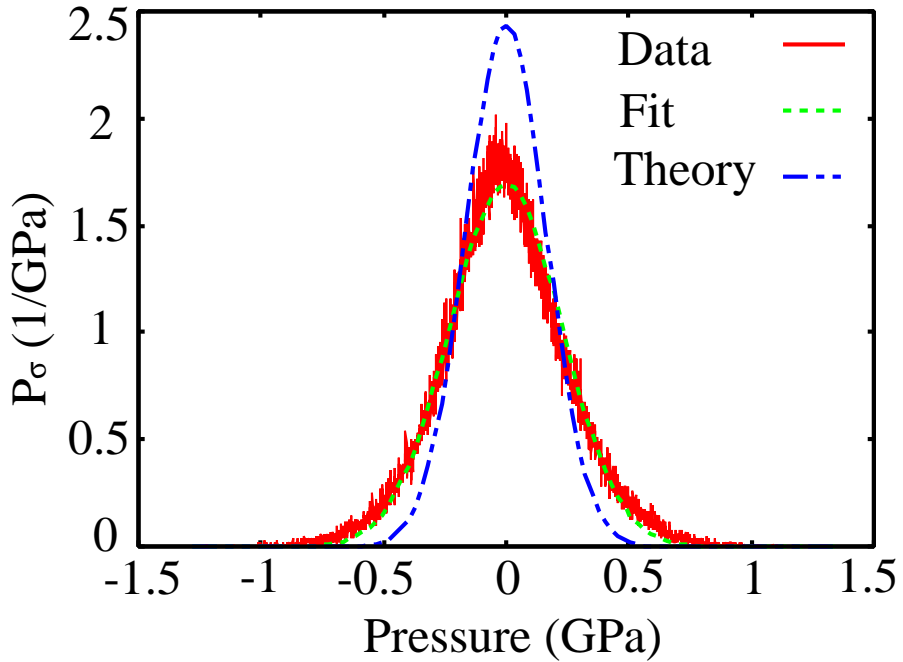


Figure 3.7: The normalized pressure distribution $P(\sigma)$ at the interface between an elastic block (elastic modulus $E = 0.5$ GPa) with a flat surface and a rigid randomly rough substrate. Because of adhesion complete contact occurs at the interface. The red curve is the simulation result and the green line is the Gaussian fit to the simulation data with the root-mean-square width $\sigma_{\text{rms}} = 0.229$ GPa. The blue line is the theoretical Gaussian distribution obtained using continuum mechanics (see Appendix B). The theoretical rms width $\sigma_{\text{rms}} = 0.164$ GPa.

enough pressures (see Fig. 3.6). In the present case, for $F_N = 4.6 \times 10^{-7}$ N (Fig. 3.6(a)) this gives a contact area $A = \pi r_H^2$ which is nearly identical to the one deduced from the fit in Fig. 3.5. A similar procedure can be used to determine the contact area between randomly rough surfaces using the following analytical expression derived from the contact mechanics theory of Persson (see Eq. A.21 in Appendix A). Where σ_0 is the nominal contact stress, and where the fitting parameter $G = G(\zeta)$ can be related to the contact area using Eq. 3.3. Thus, if $A/A_0 \ll 1$ we have $G = (\sigma_0^2/\pi)(A/A_0)^{-2}$. We have found (see below) that this expression for $P(\sigma, \zeta)$ can fit the numerical MD data very well (lending support for the accuracy of the Persson theory), and we have used this method to determine the contact area as a function of the squeezing force for randomly rough substrates.

Let us consider the pressure distribution at the interface between a rigid randomly rough substrate and a flat elastic surface when the solids are in complete contact. Complete contact can result either by squeezing the solids together by high enough force, or if the adhesive interaction between the solids is high enough (or the elastic modulus small enough). However, when complete contact occurs the pressure distribution is the same.

For an elastic solid with a flat surface in perfect contact with a hard randomly rough surface, continuum mechanics predicts a Gaussian pressure distribution of the form (see Appendix B):

$$P(\sigma) = \frac{1}{(2\pi)^{1/2}\sigma_{\text{rms}}} e^{-(\sigma-\sigma_0)^2/2\sigma_{\text{rms}}^2}$$

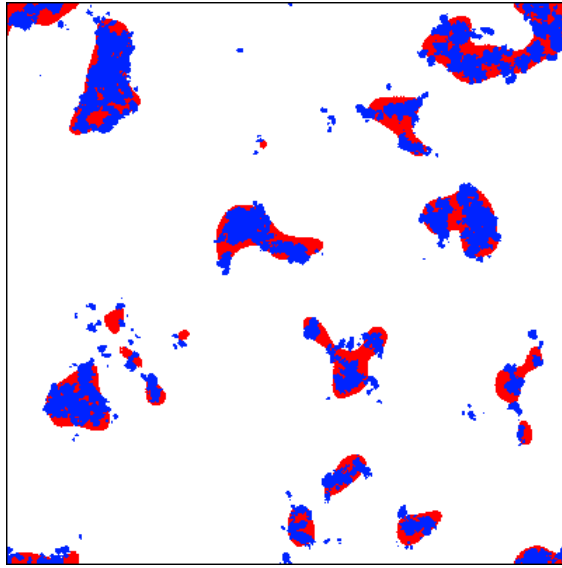


Figure 3.8: Contact morphology for two different magnifications. The red color denotes contact regions for the low magnification $\zeta = 4$, while the blue color corresponds to the contact regions for the high magnification $\zeta = 216$.

where the root-mean-square width σ_{rms} is determined by the power spectrum [6]:

$$\sigma_{\text{rms}}^2 = \langle \sigma^2 \rangle = \frac{\pi}{2} \frac{E^2}{(1 - \nu^2)^2} \int_{q_0}^{q_1} dq q^3 C(q)$$

In Fig. 3.7 we compare the theoretical pressure distribution (blue curve) with the pressure distribution obtained from the atomistic model for the case where the complete contact results from the adhesive interaction between the solids. The MD data are well fitted by a Gaussian curve, but the width of the curve is slightly larger than expected from the continuum mechanics theory $\sigma_{\text{rms}}(\text{MD}) = 0.229$ GPa while $\sigma_{\text{rms}}(\text{theory}) = 0.164$ GPa. The randomly rough surface used in the MD calculation is self affine fractal the whole way down to the atomic distance, and one can therefore not expect the continuum mechanics result for $P(\sigma)$, which assumes “smooth” surface roughness, to agree perfectly with the MD result.

3.3.2 Contact mechanics without adhesion

Here we study contact mechanics without adhesion as obtained with $\alpha = 0$ in Eq. 3.4, corresponding to purely repulsive interaction between the walls. Fig. 3.8 shows the contact morphologies at different magnifications ζ for the same load. The red and blue color indicate the contact area at low ($\zeta = 4$) and high ($\zeta = 216$) magnification, respectively. Note that with increasing magnification the contact area decreases, and the boundary line of the contact islands becomes rougher. In Ref. [45] and [5] it has been shown that the statistical properties of the contact regions exhibit power-law scaling behavior. At low magnification ($\zeta = 4$) it looks as if complete contact occurs between the solids at asperity contact regions. However, when the magnification is increased, smaller length scale roughness is detected and it is observed that only partial contact occurs at the asperities. In fact, if there were no short distance cut-off in the surface roughness, the true contact area would eventually vanish. But in reality a short distance cut-off always exists, e.g. the interatomic distance.

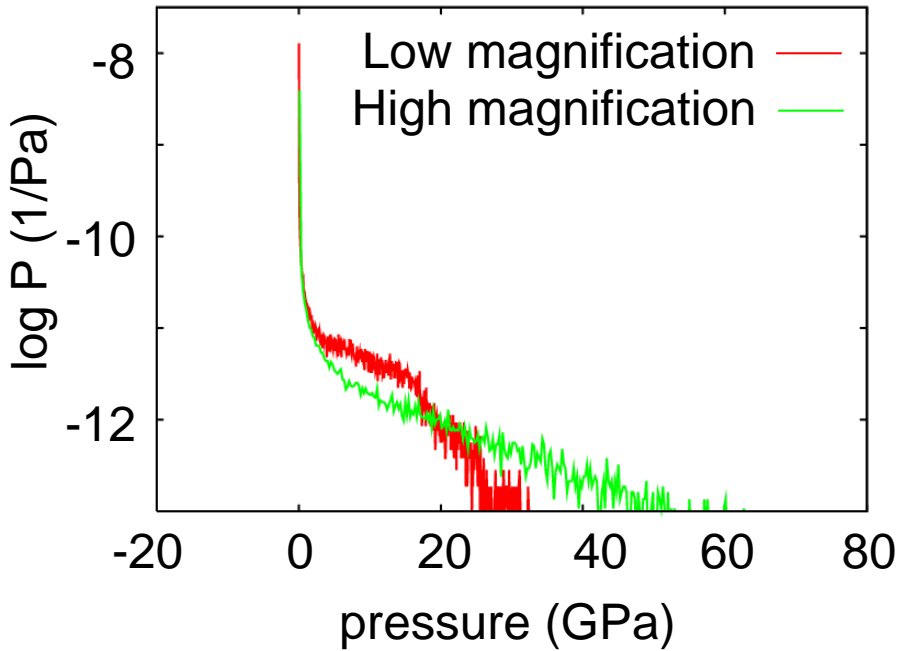


Figure 3.9: The pressure distribution in the contact area for two different magnifications. The red line corresponds to the pressure distribution for low magnification $\zeta = 4$, while the green line is for high magnification $\zeta = 216$.

Fig. 3.9 shows the pressure distribution in the contact area for two different magnifications. When we study contact on shorter and shorter length scale, which corresponds to increasing magnification ζ , the pressure distribution becomes broader and broader.

Fig. 3.10 shows that the contact area varies (approximately) linearly with the load for the small load at two different magnifications $\zeta = 4$ and 32. The contact area was determined as described in Sec. 3.3.1 by fitting the pressure distribution to a function of the form (A.21). The pressure distributions and the fitting functions are shown in Fig. 3.11 and 3.12 for $\zeta = 4$ and 32, respectively. The slope of the lines in Fig. 3.10 is only a factor 1.14 larger than predicted by the contact theory of Persson (see Sec. 3.4).

In Fig. 3.13 we show the variation of the contact area with the nominal squeezing pressure for the highest magnification case $\zeta = 216$. In this case we have defined contact to occur when the separation between the surfaces is below some critical value $r_c = 4.3615 \text{ \AA}$. In contrast to the definition used above, this definition does not give a strict linear dependence of the contact area on the load for small load as found above when the contact area is defined using the stress distribution.

3.3.3 Contact mechanics with adhesion

In this section we include the adhesive interaction i.e. we put $\alpha = 1$ in Eq. 3.4. Fig. 3.14 presents the contact morphology both with and without the adhesion at the highest magnification ($\zeta = 216$). The regions with blue color denotes the contact area without adhesion. The red color region denotes the *additional* contact area when adhesion is included. The contact area with adhesion is, of course, larger than that without adhesion since the attractive adhesional interaction will effectively increase the external load [46–48].

Fig. 3.15 shows the pressure distribution $P(\sigma, \zeta)$ at high magnification with and with-

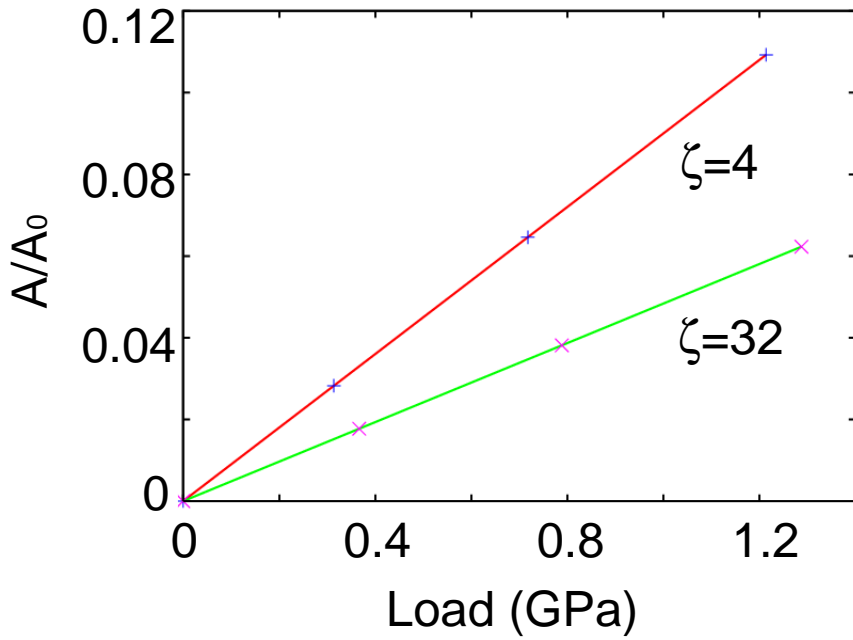


Figure 3.10: The relative contact area A/A_0 , as a function of applied stress F_N/A_0 . Results are presented for two different magnifications $\zeta = \lambda_0/\lambda = 4$ and 32. The fractal dimension is $D_f = 2.2$.

out adhesion. When adhesion is neglected (corresponding to the $\alpha = 0$ in 3.4), the pressure is positive in the contact area and $P(\sigma, \zeta) = 0$ for $\sigma < 0$. When the adhesive interaction is included, the stress becomes tensile close to the edges of every contact region and $P(\sigma, \zeta)$ is in general finite also for $\sigma < 0$.

3.4 Discussion

Several analytical theories [2,4,49], based on continuum mechanics, have been developed to describe the contact between elastic bodies both with and without the adhesive interaction. Here we will compare the results presented above with the predictions of some of these theories (see Appendix A). For small squeezing pressure F_N the Persson theory predicts a linear dependence of the area of real contact on the load. For very high squeezing pressure $\sigma_0 \gg G^{1/2}$ complete contact will occur at the interface. In this case the second term on the rhs in Eq. A.21 of Appendix A can be neglected, so the pressure distribution is a Gaussian centered at σ_0 and with the root-mean-square width $\sigma_{\text{rms}} = (2G)^{1/2}$. This result is exact (see Appendix B). Thus, the theory of Persson is expected to give a good description of the contact mechanics for all squeezing pressure (see chapter 4). All other analytical contact mechanics theories are only valid when the squeezing pressure is so small that the area of real contact is (nearly) proportional to F_N . But in many important applications, e.g., in the context of rubber friction and rubber adhesion, the area of real contact for smooth surfaces is often close to the nominal contact area.

The standard theory of Greenwood and Williamson [50] describes the contact between rough surfaces (in the absence of adhesion), where the asperities are approximated by spherical cups with equal radius of curvature but with Gaussian distributed heights. In this theory the area of real contact depends (slightly) non-linearly on the load for small

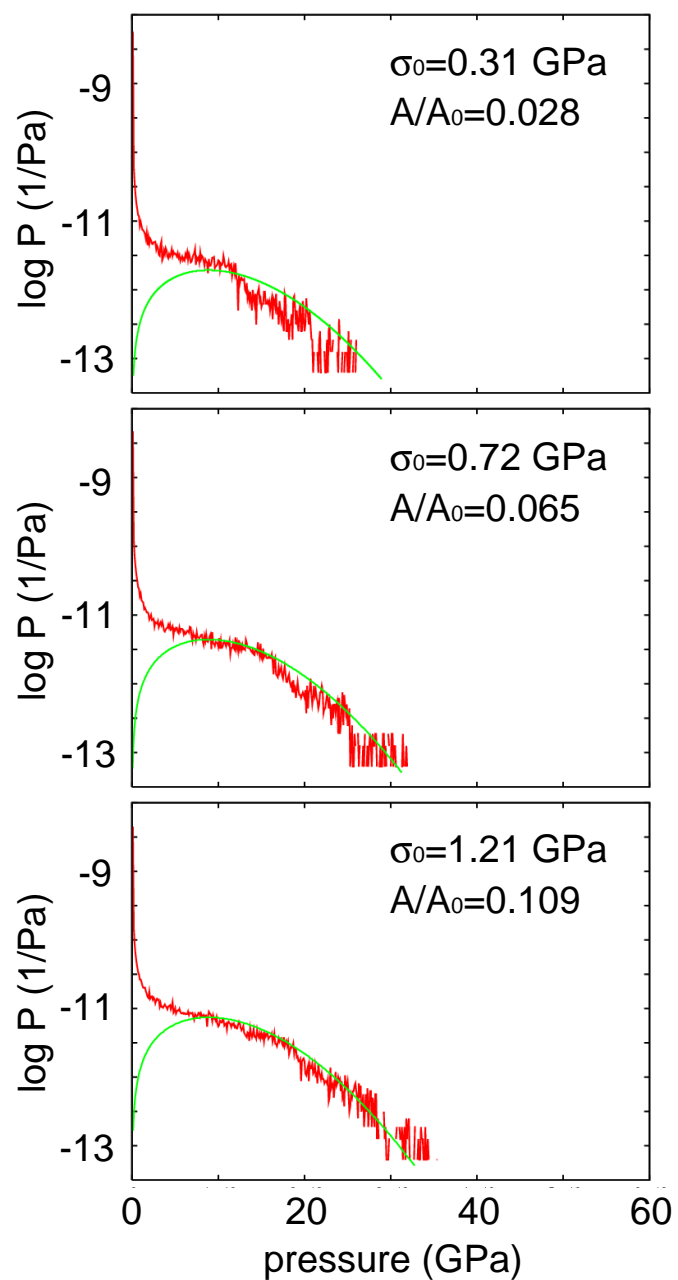


Figure 3.11: The stress distribution for $\zeta = 4$ for three different nominal pressure.

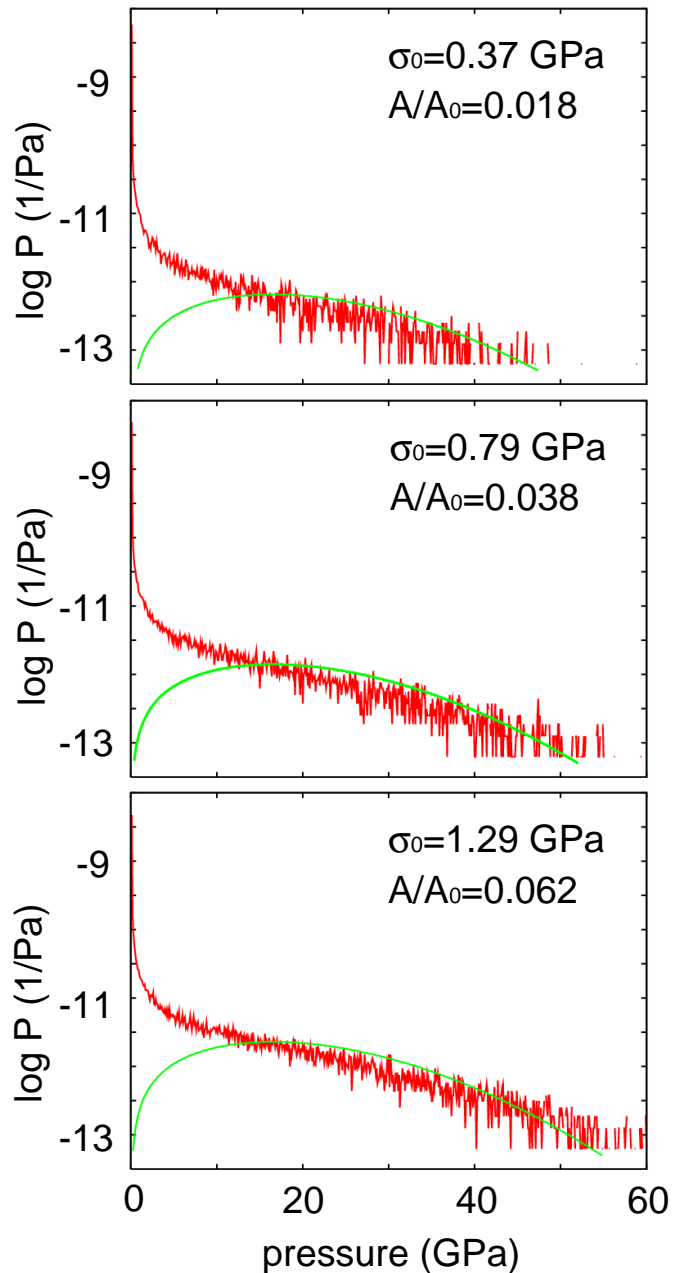


Figure 3.12: The stress distribution for $\zeta = 32$ for three different nominal pressure.

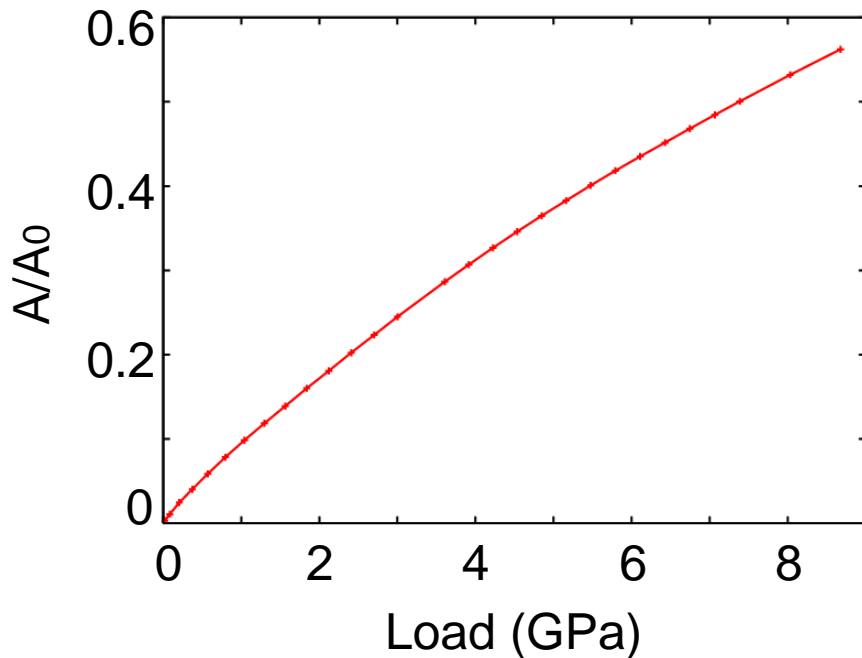


Figure 3.13: The relative contact area A/A_0 , as a function of applied stress F_N/A_0 . Results are presented for the highest magnification $\zeta = 216$. Contact is defined when the separation between the surfaces is below a critical value. The fractal dimension is $D_f = 2.2$.

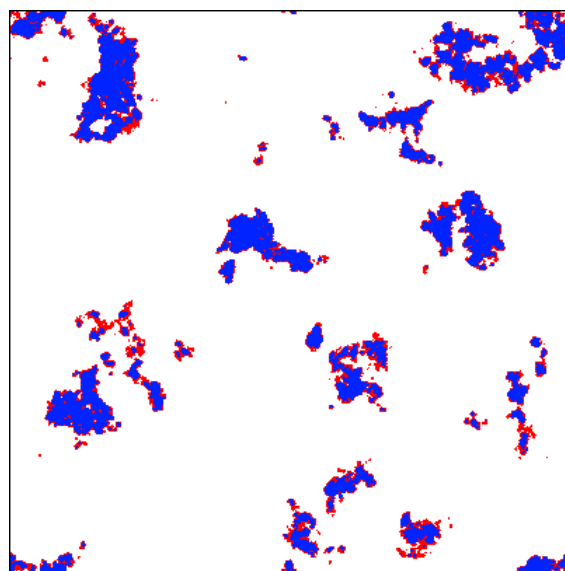


Figure 3.14: Contact morphology with adhesion and without adhesion. The blue color region denotes the contact without adhesion. The red color region denote the *additional* contact area when the adhesive interaction is included.

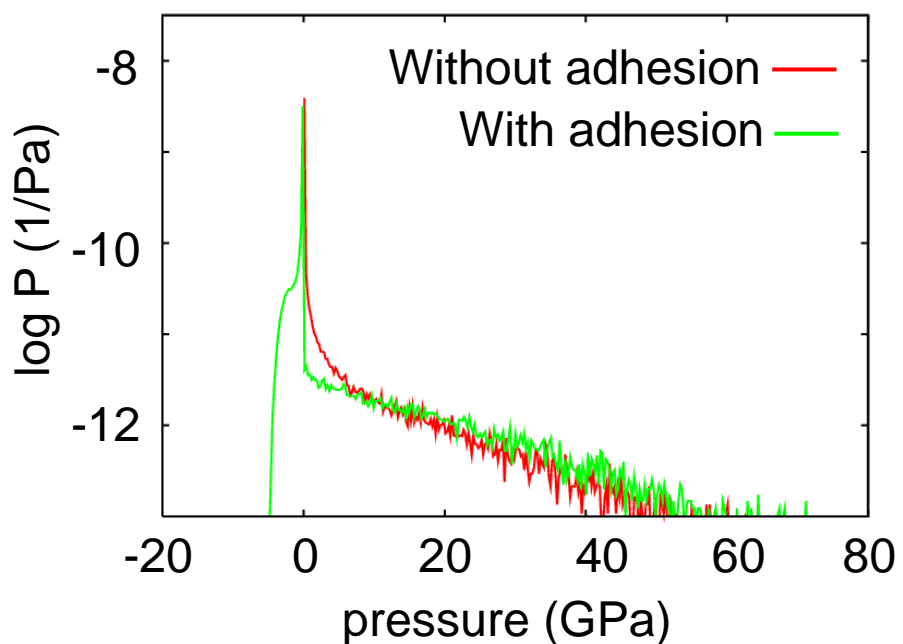


Figure 3.15: The pressure distribution with and without adhesion. The red curve denotes the pressure distribution with adhesion while the green curve is without adhesion.

load, and can therefore not be directly compared with the Persson result (A.26). Bush et al [49] developed a more general and accurate contact theory. They assumed that the rough surface consists of a mean plane with hills and valleys randomly distributed on it. The summits of these hills are approximated by paraboloids, whose distributions and principal curvatures are obtained from the random precess theory. As a result of more random nature of the surface, Bush et al found that at small load the area of contact depends linearly on the load according to (A.26) but with $\kappa = (2\pi)^{1/2}$. Thus the contact area of Persson's theory is a factor of $2/\pi$ smaller than that predicted by Bush. Both the theory of Greenwood and Williamson and the theory of Bush et al assume that the asperity contact regions are independent (no elastic coupling). However, as discussed in [44], for real surfaces (which always have surface roughness on many different length scales) this will never be the case even at a very low nominal contact pressure, which may be the origin of difference of $2/\pi$ between Persson's theory and Bush's theory.

Hyun et al performed a finite-element analysis of contact between elastic self-affine fractal surfaces [5]. The simulations were done for rough elastic surface contacting a perfectly rigid flat surface. They found that the contact area varies linearly with the load for small load. The factor κ was found to be between the results of the Bush and Persson theories for all fractal dimensions D_f . For $D_f = 2.2$ (corresponding to $H = 0.8$) they found that κ was only $\sim 13\%$ larger than predicted by the Persson theory.

The red curves in Fig. 3.16 shows the pressure distribution from the simulations for several different values of the magnification $\zeta = q_1/q_0 = 4, 8, 32$ and 216, neglecting the adhesion. In the simulations the nominal squeezing pressure $\sigma_0 = 800$ MPa. The best fit (green curves in Fig. 3.16) of the pressure distribution (A.21) to the numerical results is obtained if $G^{-1/2}$ is taken to be a factor 1.14 larger than predicted by the Persson theory [Eq. A.21], corresponding to a contact area which is 14% larger than predicted by the analytical theory, in good agreement with the results obtained by Hyun et al.

Our simulations show that the contact area varies linearly with the load for small load, see Fig. 3.10. Figs. 3.10 and 3.16 show that the slope $\alpha(\zeta)$ of the line $A = \alpha(\zeta)F$ decreases with increasing magnification ζ , as predicted by the analytical theory [44, 45]. Thus, while $A/A_0 = 0.072$ for $\zeta = 4$ we get $A/A_0 = 0.038$ for $\zeta = 32$, which both are 14% larger than predicted by Eq. A.24.

3.5 Summary

In summary, I have studied the contact between surfaces which are rough on many different length scales, i.e. self-affine fractal surface, the contact morphologies both at high and low magnification, with and without adhesion. In atomistic models it is non-trivial on how to define the area of real contact between two solids. Our study shows that the area of real contact is best defined by studying the interfacial pressure distribution, and fitting it to an analytical expression. The numerical results are consistent with the theoretical results that the contact area varies linearly with the load for small load, where the proportionality constant depends on the magnification L/λ . For randomly rough surfaces with the fractal dimension $D_f = 2.2$ (which is typical for many real surfaces, e.g., produced by fracture or by blasting with small particles) we have found that for small load (where the contact area is proportional to the load) this numerical study gives an area of atomic contact which is about $\sim 14\%$ larger than predicted by the analytical theory of Persson. Since the Persson's theory is exact in the limit of complete contact, it is likely that the Persson theory is even better for higher squeezing pressure, which will be discussed in next chapter.

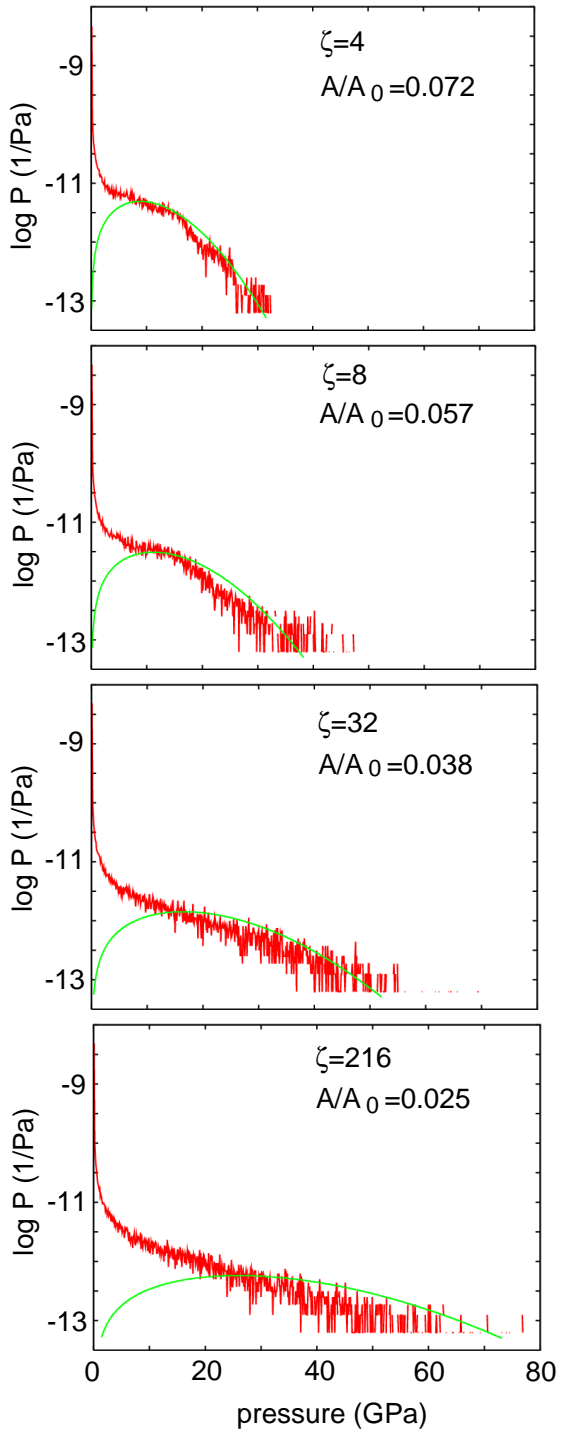


Figure 3.16: The pressure distribution at four different magnifications $\zeta = q_1/q_0 = 4, 8, 32$ and 216 for the squeezing pressure $\sigma_0 = 800$ MPa. The red curves is the pressure distribution obtained from the computer simulation, while the green curves is from the analytical theory assuming that $G^{-1/2}$, and hence the relative contact area, is a factor of 1.14 larger than predicted by the analytical theory, Eq. A.21.

Chapter 4

Interfacial Separation from Small to Full Contact without adhesion

In this chapter I will present a molecular dynamics study of the contact between a rigid solid with a randomly rough surface and an elastic block with a flat surface. The numerical calculation has been mainly focused on the contact area and the interfacial separation *from small contact (low load) to full contact (high load)*. For small load the contact area varies linearly with the load, and the interfacial separation depends logarithmically on the load. For high load the contact area approaches the nominal contact area (i.e., complete contact), and the interfacial separation approaches zero. The “correction factor” has been introduced to describe the small difference between the analytical and numerical results. The present results may be very important for soft solids, e.g., rubber, or for very smooth surfaces, where complete contact can be reached at moderate high loads without plastic deformation of the solids.

4.1 Introduction

What happens at the atomic and molecular level when surfaces come into contact with each other? And how do these events relate to macroscopic properties and observations? These questions, which center on the phenomena of adhesion and friction, pose challenges not only in engineering but also in many areas of physical and biological sciences [51]. Finding correlations and models that connect the atomic and macroscopic worlds usually is not easy. However, recently I have surprisingly found that the pressure distribution obtained from molecular dynamics calculations is in a good agreement with the prediction based on continuum contact mechanics, and in particular with the analytical contact mechanics theory of Persson [2, 4, 52].

When two elastic solids with rough surfaces are squeezed together, the solids will in general not make contact everywhere in the apparent contact area, but only on top of asperities [45]. The separation $u(\mathbf{x})$ between the surfaces will vary in a nearly random way with the lateral coordinate $\mathbf{x} = (x, y)$ in the apparent contact area. When the applied squeezing pressure increases, the contact area A will increase and the average surface separation $\bar{u} = \langle u(\mathbf{x}) \rangle$ will decrease, but in most situations it is not possible to squeeze the solids into perfect contact corresponding to $\bar{u} = 0$. The area of real contact, and the space between two solids has a tremendous influence on many important processes [52].

Most studies of contact mechanics have been focused on small load where the contact area depends linearly on the load [7, 49, 50, 53, 54]. However, for soft solids, such as rubber or gelatin, and for smooth surfaces nearly full contact may occur at the interface, and

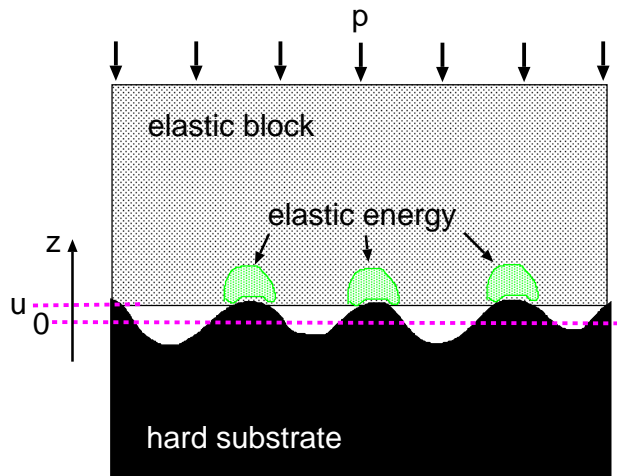


Figure 4.1: An elastic block squeezed against a rigid rough substrate. The separation between the average plane of the substrate and the average plane of the lower surface of the block is denoted by u . Elastic energy is stored in the block in the vicinity of the asperity contact regions.

it is of great interest to study how the contact area, the interfacial surface separation and stress distribution vary with the load from small load (where the contact area varies linearly with the load), to high load (where the contact is (nearly) complete). Here I will present such a study using molecular dynamics, and compare the numerical results with the prediction of the analytical contact mechanics theory of Persson.

4.2 Interfacial separation without adhesion

The space between two solids has a tremendous influence on many important processes, e.g., heat transfer [55], contact resistivity [56], lubrication [9], sealing [57] and optical interference [58]. Persson has recently presented a simple theory for the (average) separation \bar{u} as a function of the squeezing pressure p [52]. The theory shows that for randomly rough surfaces at low squeezing pressures $p \sim \exp(-\bar{u}/u_0)$ where the reference length u_0 depends on the nature of the surface roughness but is independent of p , in good agreement with experiments [58].

Consider an elastic block with a flat surface squeezed against a hard rough substrate surface, see Fig. 4.1. The separation between the average surface plane of the block and the average surface plane of the substrate is denoted by \bar{u} with $\bar{u} \geq 0$. When the applied squeezing force p increases, the separation between the surfaces at the interface will decrease, and Now consider $p = p(\bar{u})$ as a function of \bar{u} . The elastic energy $U_{\text{el}}(\bar{u})$ stored in the substrate asperity–elastic block contact regions must equal the work done by the external pressure p in displacing the lower surface of the block towards the substrate, i.e.,

$$\int_{\bar{u}}^{\infty} du' A_0 p(u') = U_{\text{el}}(\bar{u}) \quad (4.1)$$

or

$$p(\bar{u}) = -\frac{1}{A_0} \frac{dU_{\text{el}}}{d\bar{u}} \quad (4.2)$$

where A_0 is the nominal contact area. Eq. 4.2 is exact, and shows that if the dependence of the surface separation u on the squeezing pressure p is known, e.g., from finite element calculations or molecular dynamics, one can obtain the elastic energy U_{el} stored in the asperity contact regions [6]. This is an important result as $U_{\text{el}}(\bar{u})$ is relevant for many important applications.

Theory shows that for low squeezing pressure, the area of real contact A varies linearly with the squeezing force pA_0 , and that the interfacial stress distribution, and the size-distribution of contact spots, are independent of the squeezing pressure [59, 60]. That is, with increasing p existing contact areas grow and new contact areas form in such a way that in the thermodynamic limit (infinite-sized system) the quantities referred to above remain unchanged. It follows immediately that for small load *the elastic energy stored in the asperity contact region will increase linearly with the load*, i.e., $U_{\text{el}}(\bar{u}) = u_0 A_0 p(\bar{u})$, where u_0 is a characteristic length which depends on the surface roughness (see below) but is independent of the squeezing pressure p . Thus, for small pressures Eq. 4.2 takes the form

$$p(\bar{u}) = -u_0 \frac{dp}{d\bar{u}}$$

or

$$p(\bar{u}) \sim e^{-\bar{u}/u_0}, \quad (4.3)$$

in good agreement with experimental data for the contact between elastic solids when the adhesive interaction between the solids can be neglected [58]. We note that the result (4.3) differs drastically from the prediction of the Bush et al theory [49], and that of Greenwood and Williamson theory (GW) [50], which for low squeezing pressures (for randomly rough surfaces with Gaussian height distribution) predict $p(\bar{u}) \sim \bar{u}^{-a} \exp(-b\bar{u}^2)$, where $a = 1$ in the Bush et al theory and $a = 5/2$ in the GW theory. Thus *these theories do not correctly describe the interfacial spacing between contacting solids*. This is not surprising because these approaches assume a rigid substrate surface covered with flexible asperities. In reality, the bulk of the solids whose surfaces are in contact is not rigid. Furthermore, there exist a hierarchy of asperities on many length scales, all of which can distort.

The elastic energy U_{el} has been studied in Ref. [4] and [60]. Here let us use

$$U_{\text{el}} \approx A_0 E^* \frac{\pi}{2} \int_{q_0}^{q_1} dq q^2 W(q, p) C(q), \quad (4.4)$$

where $E^* = E/(1 - \nu^2)$ and

$$W(q, p) = P_p(q) \left[\gamma + (1 - \gamma) P_p^2(q) \right], \quad (4.5)$$

where $P_p(q)$ is given by Eq. A.24:

$$P_p(q) = \operatorname{erf} \left(\frac{p}{2G^{1/2}(\zeta)} \right) \quad (4.6)$$

For complete contact (infinite squeezing pressure) $P_p = 1$ and thus $W(q, p) = 1$ and in this limit (4.4) is exact. For small squeezing pressure $W(q, p) \approx \gamma P_p$. The parameter γ is of order ≈ 0.4 (see below), and takes into account that the elastic energy stored in the contact region (per unit surface area) in general is less than the average elastic energy (per unit surface area) for perfect contact (see Ref. [60]). The particular way to interpolate between the limits $W(q, p) = 1$ for complete contact and $W(q, p) = \gamma P_p$ for very small contact using (4.5) was designed to give good agreement between the interfacial separation calculated using (4.2), and the interfacial separation obtained from Molecular Dynamics (MD) and Finite Element Method (FEM) (see Sec. /refchap4:numerical.separation and 4.5).

Let us write (4.6) as [2, 44]

$$P_p(q) = \frac{2}{\sqrt{\pi}} \int_0^{s(q)p} dx e^{-x^2}, \quad (4.7)$$

where $s(q) = w(q)/E^*$ with

$$w(q) = \left(\pi \int_{q_0}^q dq' q'^3 C(q') \right)^{-1/2}.$$

Using (4.7) gives

$$\frac{\partial P_p}{\partial \bar{u}} = \frac{2}{\sqrt{\pi}} s \frac{dp}{d\bar{u}} e^{-s^2 p^2}, \quad (4.8)$$

Substituting (4.4) and (4.5) in (4.2), and using (4.8) gives

$$\begin{aligned} p(\bar{u}) &= -\sqrt{\pi} \int_{q_0}^{q_1} dq q^2 C(q) w(q) [\gamma + 3(1-\gamma) P_p^2(q)] \\ &\quad \times e^{-[w(q)p/E^*]^2} \frac{dp}{d\bar{u}} \end{aligned}$$

or

$$\begin{aligned} d\bar{u} &= -\sqrt{\pi} \int_{q_0}^{q_1} dq q^2 C(q) w(q) [\gamma + 3(1-\gamma) P_p^2(q)] \\ &\quad \times e^{-[w(q)p/E^*]^2} \frac{dp}{p} \end{aligned}$$

Integrating this from $\bar{u} = 0$ (complete contact, corresponding to $p = \infty$) to \bar{u} gives

$$\begin{aligned} \bar{u} &= \sqrt{\pi} \int_{q_0}^{q_1} dq q^2 C(q) w(q) \\ &\quad \times \int_p^\infty dp' \frac{1}{p'} [\gamma + 3(1-\gamma) P^2(q, p')] e^{-[w(q)p'/E^*]^2}, \end{aligned} \quad (4.9)$$

Now consider the limiting case of very low squeezing pressure. If one introduces $x = w(q)p'/E^*$ the last integral in (4.9) becomes

$$J = \int_{pw(q)/E^*}^\infty dx \frac{1}{x} [\gamma + 3(1-\gamma) P^2(x)] e^{-x^2},$$

where

$$P(x) = \frac{2}{\sqrt{\pi}} \int_0^x dx' e^{-x'^2}.$$

Performing a partial integration gives

$$\begin{aligned} J &= \left[\log x [\gamma + 3(1-\gamma) P^2(x)] e^{-x^2} \right]_{pw(q)/E^*}^\infty \\ &\quad - \int_{pw(q)/E^*}^\infty dx \log x (6(1-\gamma) P(x) P'(x) \\ &\quad + [\gamma + 3(1-\gamma) P^2(x)] (-2x)) e^{-x^2}. \end{aligned}$$

The leading contributions to J as $p \rightarrow 0$ is

$$J = -\gamma \log \left(\frac{pw(q)}{E^*} \right) - \int_0^\infty dx \log x (6(1-\gamma) P(x) P'(x)$$

$$+ \left[\gamma + 3(1 - \gamma)P^2(x) \right] (-2x) e^{-x^2} = -\gamma \log \left(\frac{pw(q)}{\epsilon E^*} \right). \quad (4.10)$$

where

$$\begin{aligned} \epsilon = \exp & \left[- \int_0^\infty dx \log x \left(6 \frac{1 - \gamma}{\gamma} P(x) P'(x) \right. \right. \\ & \left. \left. + \left[1 + 3 \frac{1 - \gamma}{\gamma} P^2(x) \right] (-2x) \right) e^{-x^2} \right]. \end{aligned} \quad (4.11)$$

Using (4.11) one gets $\epsilon = 4.047$. Note that ϵ depends on $P_p(q)$ for all pressures from small relative contact area ($P \ll 1$) to complete contact corresponding to $P = 1$. Thus, although the slope of the linear relation between u and $\log p$, which holds for very small p , only depends on $P_p(q)$ for very small p (where the relative contact area is proportional to p), the lateral position of the line *does* depend on the whole function $P_p(q)$ [or $P(x)$]. For this reason it is important to accurately describe how U_{el} depends on $P_p(q)$ for all p , even if one is only interested in the relation between \bar{u} and p for very small p . The physical reason for this is simple: even for arbitrarily small applied nominal stress p , the stress (at high enough magnification) in the area of contact will be very high, which may result in (nearly) complete contact in the asperity contact regions.

Substituting (4.10) in (4.9) gives [61]

$$\begin{aligned} \bar{u} &= -\sqrt{\pi} \int_{q_0}^{q_1} dq q^2 C(q) w(q) \gamma \log \left(\frac{pw(q)}{\epsilon E^*} \right) \\ &= -u_0 [\log p - \log(\beta E^*)] \end{aligned}$$

or

$$p = \beta E^* e^{-\bar{u}/u_0} \quad (4.12)$$

where

$$u_0 = \sqrt{\pi} \gamma \int_{q_0}^{q_1} dq q^2 C(q) w(q) \quad (4.13)$$

and

$$\beta = \epsilon \exp \left[- \frac{\int_{q_0}^{q_1} dq q^2 C(q) w(q) \log[w(q)]}{\int_{q_0}^{q_1} dq q^2 C(q) w(q)} \right] \quad (4.14)$$

The relation (4.3) between p and \bar{u} for the special case of self-affine fractal surfaces was studied in Ref. [52] using $W(q, p) = \gamma P_p(q)$ in the expression for the elastic energy.

4.3 Molecular Dynamics

I have performed Molecular Dynamics(MD) to study the contact area and the interfacial separation from small contact to full contact. We are interested in surfaces with random roughness with wavelength components in some finite range $\lambda_1 < \lambda < \lambda_0$, where λ_0 typically is similar to (but smaller than) the lateral size of the nominal contact area. In order to accurately reproduce the contact mechanics between elastic blocks, it is necessary to consider solid blocks which extends at least a distance $\sim \lambda_0$ in the direction normal to the nominal contact area. (Note the lower part of the system has been called substrate while the upper part is called block.) This leads to an enormous number of atoms or dynamical variables even for a small system. In order to avoid this trouble we have developed a multiscale MD approach (see chapter 2). This approach has been described in detail in Ref. [6] and is only summarized here. The system has lateral dimension $L_x = N_x a$ and

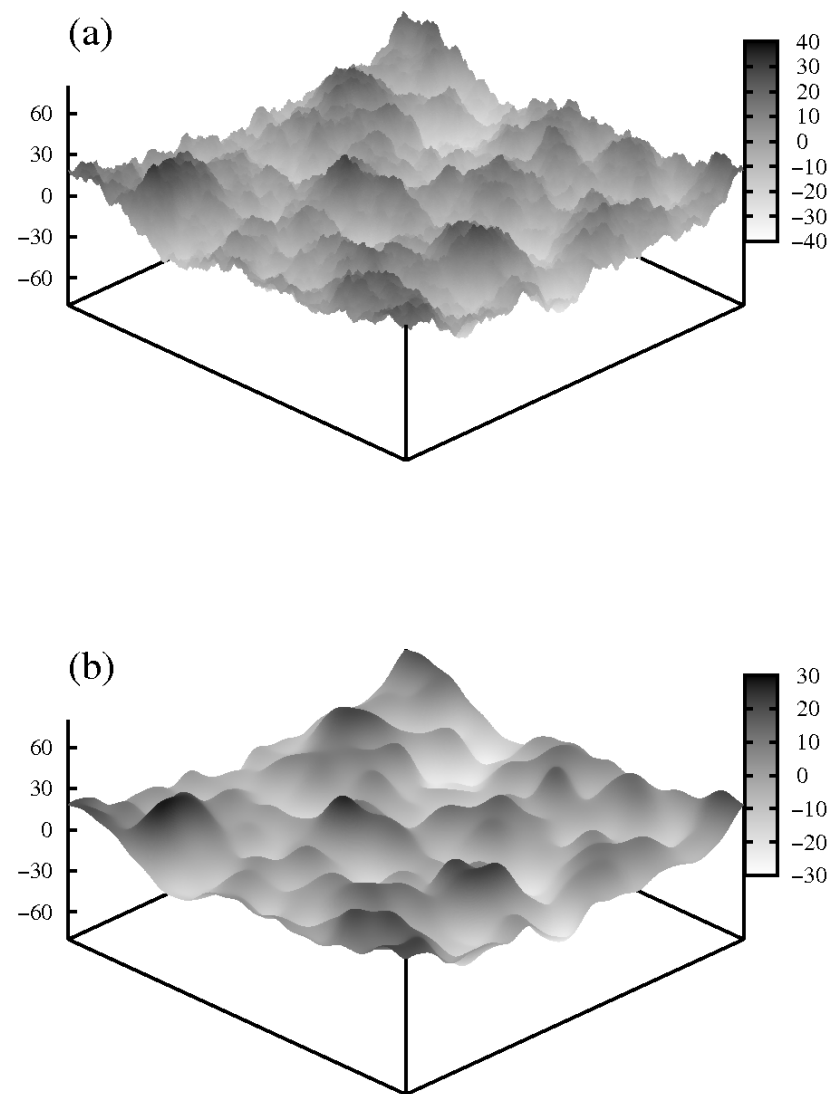


Figure 4.2: Surface height profile of a mathematically generated self affine fractal surface ($104 \times 104 \text{ nm}^2$ square surface area) with the root mean square roughness 1 nm. (a) high magnification ($\zeta = 216$), (b) low magnification ($\zeta = 4$)

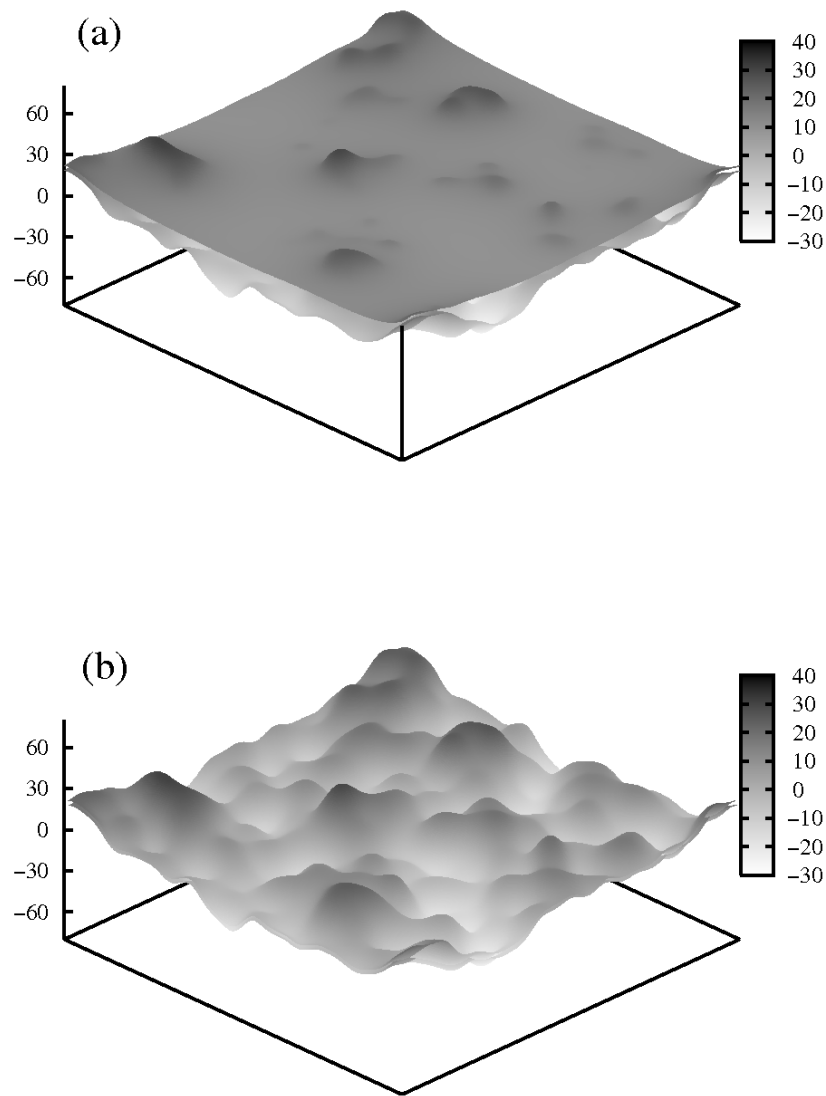


Figure 4.3: 3D images of contacting regions with both substrate and block, at low magnification $\zeta = 4$ under different load (a) $\sigma_0/E^* = 0.0129$ and $A/A_0 = 0.1089$, (b) $\sigma_0/E = 0.26$ and $A/A_0 = 0.9527$. Note $E^* = E/(1 - \nu^2)$ is an effective modulus.

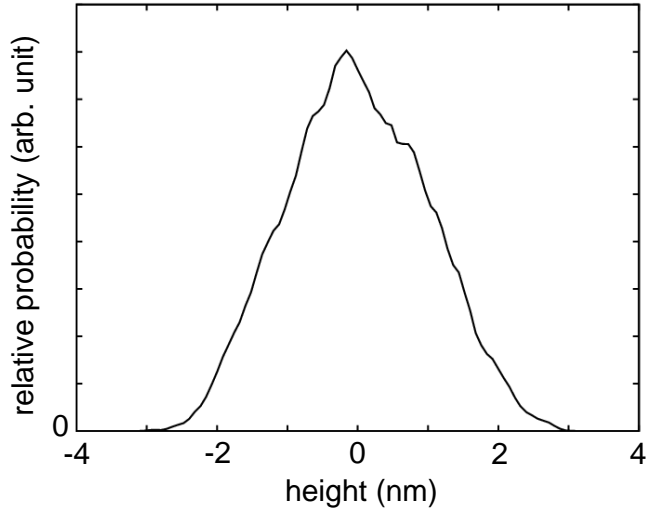


Figure 4.4: The probability distribution P_h of surface height h for the mathematically generated surface shown in Fig. 4.2. For a square area $104 \times 104 \text{ nm}^2$ with lattice constant $a = 1.605 \text{ \AA}$.

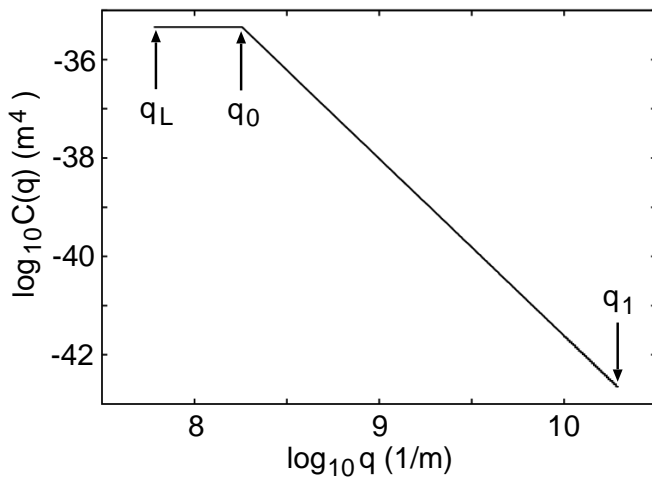


Figure 4.5: Surface roughness power spectra $C(q)$ of the mathematically generated substrate surface studied in Ref. [1] and below. For a self affine fractal surface with the fractal dimension $D_f = 2.2$ and $q_L = 6.04 \times 10^7 \text{ m}^{-1}$, $q_0 = 1.81 \times 10^8 \text{ m}^{-1}$, and $q_1 = 3.9 \times 10^{10} \text{ m}^{-1}$, and the root mean square roughness amplitude $h_{\text{rms}} = 1 \text{ nm}$.

$L_y = N_y a$, where a is the lattice space of the block. Periodic boundary condition has been used in xy plane. For the block $N_x = N_y = 400$, while the lattice space of the substrate $b \approx a/\phi$, where $\phi = (1 + \sqrt{5})/2$ is the golden mean, in order to avoid the formation of commensurate structures at the interface. The mass of the block atoms is 197 a.m.u. and the $a = 2.6$ Å. The elastic modulus and Poisson ratio of the block is $E = 77.2$ GPa and $\nu = 0.42$, respectively.

The atoms at the interface between the block and substrate interact with the repulsive potential $U(r) = \epsilon (r_0/r)^{12}$, where r is the distance between a pair of atoms. We use $r_0 = 3.28$ Å and $\epsilon = 74.4$ meV. In the MD-model calculations there is no unique way of how to define the separation \bar{u} between the solid walls (see Ref. [6] for a discussion of this point). We have used the same definition as in Ref. [6] $\bar{u} = d - d_c$, where d is the separation between the average z coordinate of the bottom layer of the block atoms and the average plane of the substrate. d_c is the critical atom-atom separation to define contact on atomic scale. Thus, $\bar{u} = 0$ corresponds to the separation $d_c = 4.3615$ Å between planes through the center of mass of the interfacial atoms of the block and the substrate.

4.4 Numerical results

4.4.1 Contact area from small to full contact

From the molecular dynamics simulation one can calculate the interfacial stress distribution. In order to obtain the contact area I follow the procedure outlined in Ref. [6] and fit the numerical results to the theoretically predicted stress distribution

$$P(\sigma, \zeta) = \frac{1}{2(\pi\tilde{G})^{1/2}} \left(e^{-(\sigma-p)^2/4\tilde{G}} - e^{-(\sigma+p)^2/4\tilde{G}} \right) \quad (4.15)$$

where $\tilde{G}(p, \zeta)$ depends on the nominal squeezing pressure p and the magnification ζ (but which is independent of σ), and which has been chosen to get the best agreement with numerical data. In Fig. 4.6 I have shown the good agreement between the numerical pressure distribution and the analytical function (4.15) for $\zeta = 4$ under three different nominal pressure. When \tilde{G} is known one can calculate the relative contact area using

$$\frac{A}{A_0} = \int_0^\infty d\sigma P(\sigma, \zeta). \quad (4.16)$$

In Fig. 4.7 the result for A/A_0 has been shown as a function of normalized pressure p/E^* .

The fitted $\tilde{G}(p, \zeta)$ can now be compared to theory. Thus, the theory of Persson predicts $\tilde{G} = G$ where

$$G = \frac{\pi}{4} \left(\frac{E}{1 - \nu^2} \right)^2 \int_{q_L}^{\zeta q_0} dq q^3 C(q). \quad (4.17)$$

In Fig. 4.8 the ratio $r = \tilde{G}/G$ has been shown which is referred to as the correction factor. Note that r increases from ≈ 0.51 to 1 as the squeezing pressure p increases from zero to infinity (i.e., the normalized contact area A/A_0 increases from zero to 1). Since the contact area for small load is proportional to $\sim 1/\sqrt{G}$ it follows that the MD simulation for small load predicts a contact area which is about $\sim 30\%$ larger than that predicted by the theory. This is slightly larger than what has been found in earlier numerical simulations. Thus, the finite element calculations of Hyun and Robbins [62] and the Green's function molecular dynamics study of Campana and Müser [7] gives $r \approx 0.64$, corresponding to a contact area which is about $\sim 20\%$ larger than that predicted by the Persson theory. Similarly, the study of Höning [63] gives $r \approx 0.56$ for small load. However, none of the

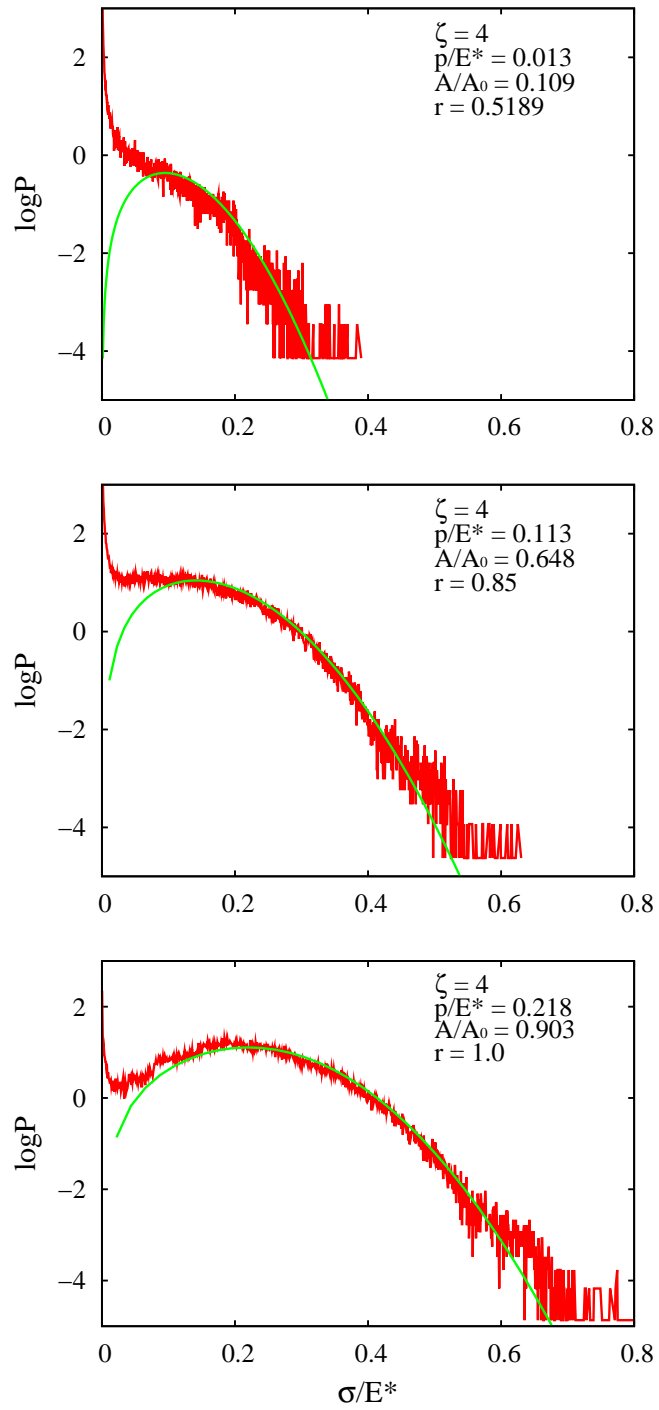


Figure 4.6: The pressure distribution for $\zeta = 4$ for three different nominal pressure. Properly choosing the correction factor makes the calculation results in good agreement with Persson's contact mechanics theory.

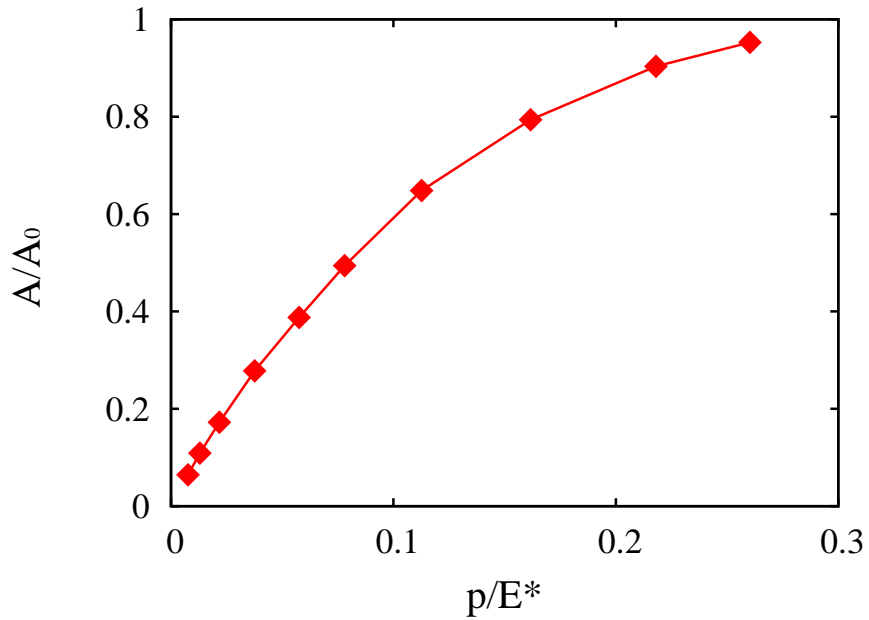


Figure 4.7: Contact area ratio A/A_0 calculated from (A.24), as a function of normalized pressure p/E^* .

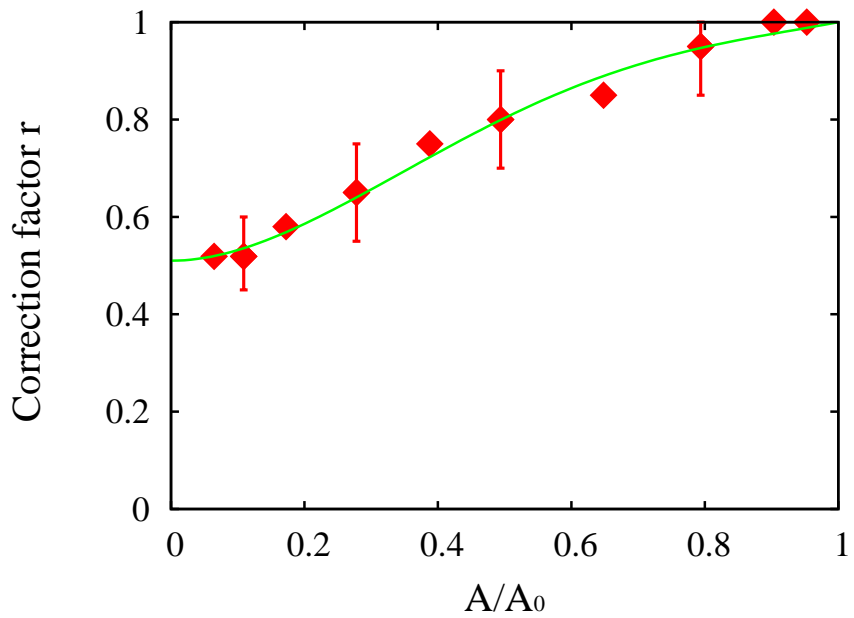


Figure 4.8: Correction factor r as a function of the contact area ratio A/A_0 . The points are simulation results, which have been fitted by the function $f(x) = a + bx^2 + cx^3 + dx^4$ under the condition $d = 1 - a - b - c$ (solid line). The corresponding coefficients a, b, c are 0.51, 2.5, -3.3 respectively.

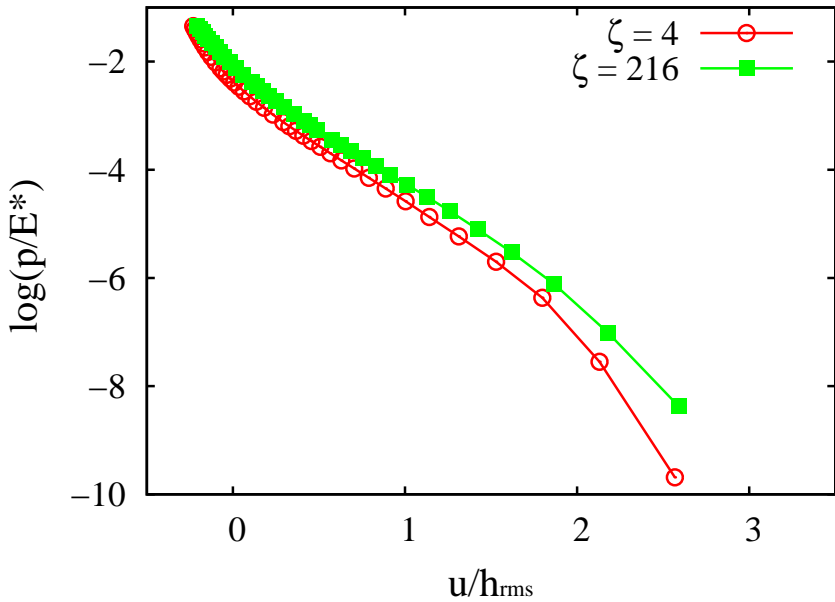


Figure 4.9: An elastic block squeezed against a rigid rough substrate. The (natural) logarithm of the normalized average pressure p/E^* , as a function of the normalized separation between the average plane of the substrate and the average plane of the lower surface of the block and the average plane of the lower surface of the block denoted by \bar{u}/h_{rms} .

computer simulations can be considered as perfectly converged, and the difference between theory and fully converged computer simulations may be smaller than that indicated by the numbers given above. Thus, most of the numerical studies reported use rather few grid points within the shortest wavelength roughness, which result in an overestimation of the contact area [53]. In the simulations for $\zeta = 4$ there are many atoms within the shortest substrate roughness wavelength, but the surface roughness extends over less than one decade in length scale.

Finally, I note that while the pressure distribution for low magnification ($\zeta = 4$) is in good agreement with Persson's theory, for the highest magnification ($\zeta = 216$) this is not the case because only one atom (or of order one atom) occurs within the shortest wavelength roughness of the substrate (which is roughly given by the substrate lattice constant). In the latter case one observes that the stress probability distribution for high normal stress falls off roughly exponentially rather than like a Gaussian. This has also been observed in earlier (non-converged) finite element calculations [5]. It is clear that this limiting case cannot be described by the elastic continuum model, which is the basis for all analytical contact mechanics theories.

4.4.2 Interfacial surface separation from small to full contact

The (natural) logarithm of the normalized average pressure p/E , as a function of the normalized separation \bar{u}/h_{rms} between the average plane of the substrate and the average plane of the lower surface of the block, has been shown in Fig. 4.9. It shows results for the magnification $\zeta = 4$ (open circles) and $\zeta = 216$ (solid squares). In this figure $\bar{u} = 0$ corresponds to the separation 4.3615 Å between the plane through the center of the atoms of the top layer of substrate atoms and bottom layer of block atoms. Since the

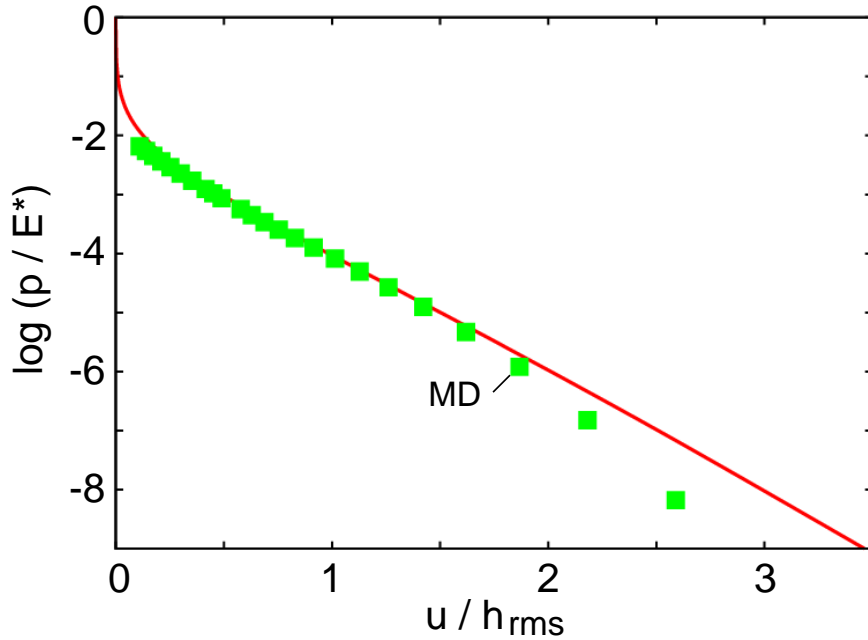


Figure 4.10: The relation between the (natural) logarithm of the squeezing pressure p (normalized by E^*) and the interfacial separation \bar{u} (normalized by the root-mean-square roughness amplitude h_{rms}) for an elastic solid squeezed against a rigid surface with the power spectra shown in Fig. 4.2. $\gamma = 0.42$ has been used in the calculations.

atoms interact with a long-range repulsive $\sim r^{-12}$ pair potential, it is possible to squeeze the surfaces closer to each other than what corresponds to $\bar{u} = 0$. This explains why simulation data points occur also for $\bar{u} < 0$. The theory described in Sec.4.2 assumes a contact interaction potential so that $\bar{u} \geq 0$, and therefore can not be compared with the MD simulations for very small (and negative) \bar{u} .

The MD results from Fig. 4.9 (solid squares) have been compared with the theoretical prediction calculated from (4.9) using the same surface roughness power spectra (and other parameters) as in the MD-calculation (see Fig. 4.10). The theory is in good agreement with the numerical data for $0.2 < \bar{u}/h_{rms} < 2$. For $\bar{u}/h_{rms} < 0.2$ the two curves differ because of the reason discussed above, i.e., the “soft” potential used in the MD simulation allows the block and substrate atoms to approach each other beyond $\bar{u} = 0$, while in the analytical theory a contact potential is assumed where the repulsive potential is infinite for $\bar{u} < 0$ and zero for $\bar{u} > 0$. The difference between the theory and the MD results for $\bar{u}/h_{rms} > 2$ is due to a finite size effect. That is, since the MD calculations uses a very small system, the highest asperities are only $\sim 3h_{rms}$ above the average plane (see the height distribution in Fig. 4.4), and for large \bar{u} very few contact spots will occur, and in particular for $\bar{u} > 3h_{rms}$ no contact occurs and p must vanish. In the analytical theory the system is assumed infinitely large so that even for a Gaussian distribution of asperity height there will always be (infinitely) many infinitely high asperities and contact will occur at arbitrary large separation \bar{u} , and the asymptotic relation $\bar{u} \sim \log p$ will hold for arbitrarily large \bar{u} (or small squeezing pressures p).

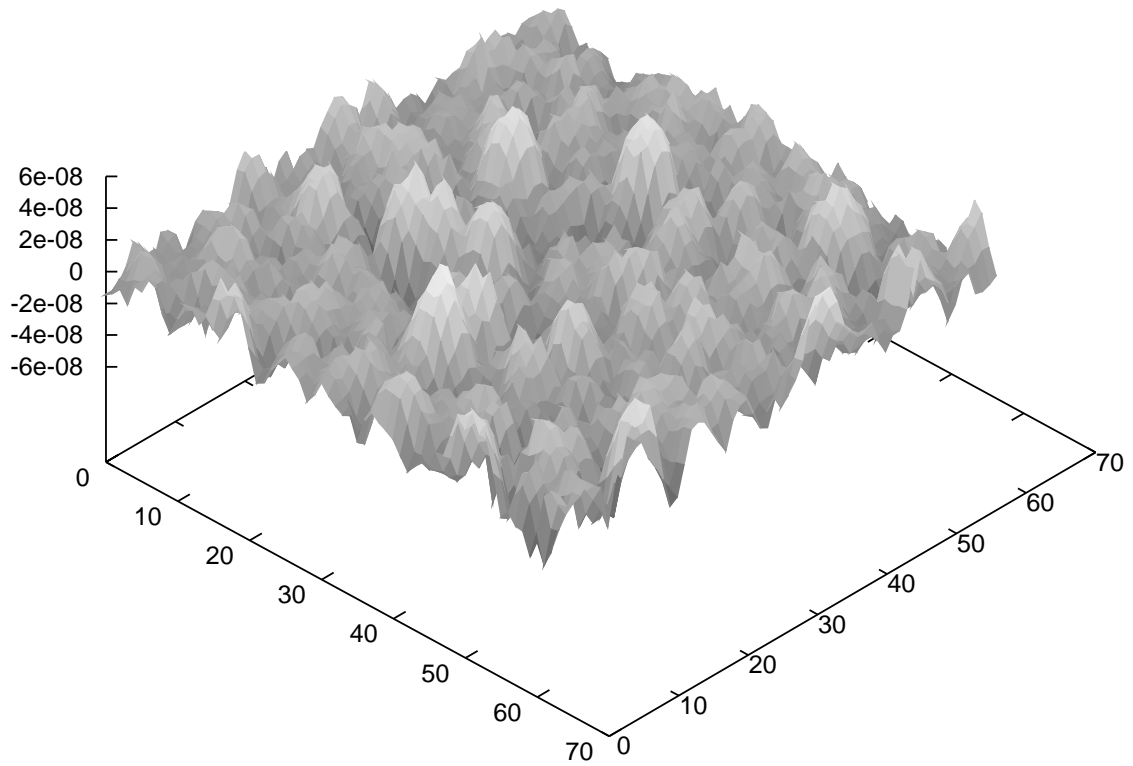


Figure 4.11: Surface height profile of a polymer surface, with the root mean square roughness 14 nm, measured over a $10 \times 10 \mu\text{m}^2$ square surface area.

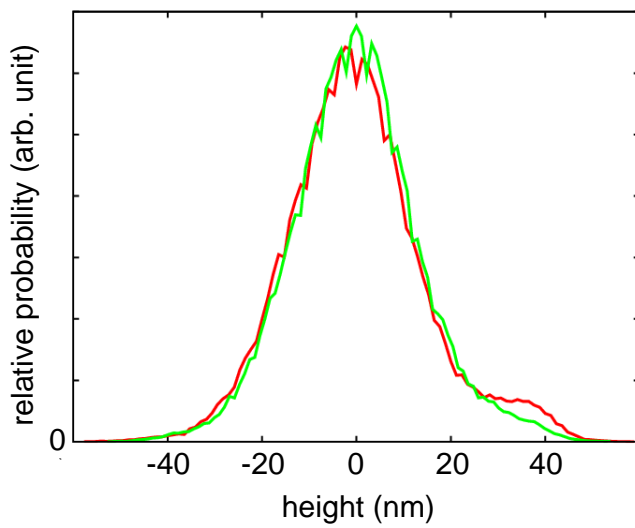


Figure 4.12: The probability distribution P_h of surface height h for the polymer film in Fig. 4.11. The two curves correspond to height profile data measured at two different square surface areas, each $10 \times 10 \mu\text{m}^2$.

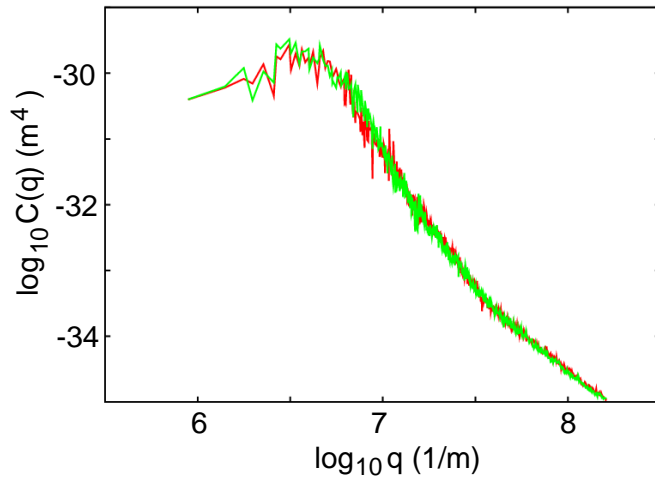


Figure 4.13: Surface roughness power spectra $C(q)$ of the polymer film in Fig. 4.11. The two curves correspond to height profile data measured at two different square surface areas, each $10 \times 10 \mu\text{m}^2$. The height probability distribution for the same surface areas is shown in Fig. 4.12.

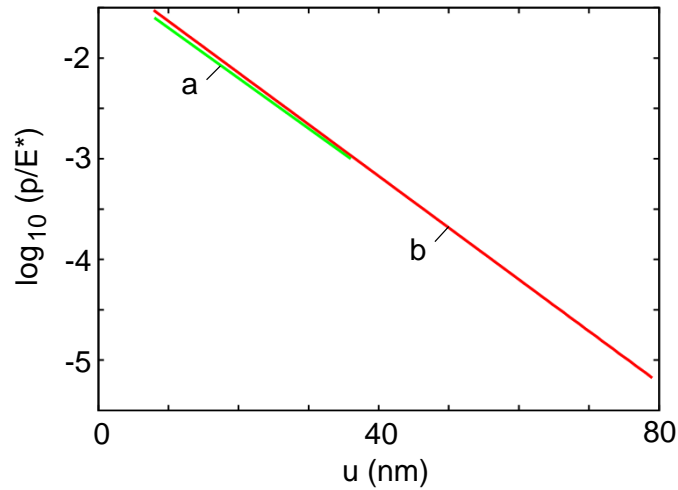


Figure 4.14: The relation between the logarithm (with 10 as basis) of the squeezing pressure p (normalized by E^*) and the interfacial separation \bar{u} (in nm) for an elastic solid squeezed against a rigid surface with the power spectra shown in Fig. 4.11 (but multiplied by a factor of two). The line **a** is the result of the Finite Element calculation of Pei et al, while the line **b** is the prediction of the theory. $\gamma = 0.38$ has been used in the calculations.

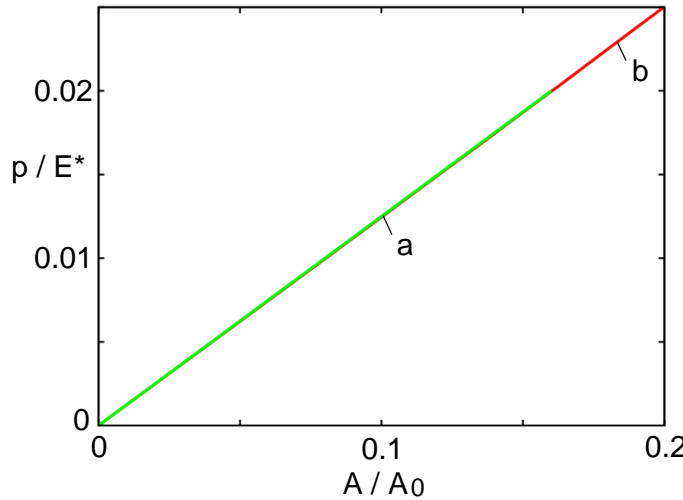


Figure 4.15: The relation between the relative contact area, A/A_0 , and the normalized squeezing pressure, p/E^* , for an elastic solid squeezed against a rigid surface with the power spectra shown in Fig. 4.14 (but multiplied by a factor of two). The line **a** is the result of the Finite Element calculation of Pei et al, while the line **b** is the prediction of the theory where A/A_0 is scaled by a factor of 1.29, corresponding to the correction factor $r \approx 0.6$.

4.5 Contact mechanics for a measured surface

Pei et al [53] have performed a Finite Element Method (FEM) computer simulation of the contact mechanics for a polymer surface, using the measured surface topography [58] as input, squeezed against a flat surface. Here I would like to compare the FEM results with the analytical results of Persson.

The surface height profile of a polymer surface studied in Ref. [58] with the root mean square roughness 14 nm, has been shown in In Fig. 4.11. The probability distribution of surface height P_h for two different square $10 \times 10 \mu\text{m}^2$ surface areas on the polymer film is shown in Fig. 4.12. These two surface areas was used in the FEM calculation by Pei et al as the upper and lower surface. It is remarkable that in spite of the fact that the height distributions are not perfect Gaussian (in particular one surface exhibits a “bump” in the height distribution on the outer side of the height profile), Pei et al obtained a nearly perfect linear relation between $\log p$ and \bar{u} . This result indicates that even in the present case the area of real contact is proportional to the load (see below) and the statistical properties of the contact regions do not change with the load for small load. The surface roughness power spectra of the two surfaces are shown in Fig. 4.13, and are almost identical in spite of the difference which occurs in the height distribution P_h .

Fig. 4.14 shows the relation between the logarithm (with 10 as basis) of the squeezing pressure p (normalized by E^*) and the interfacial separation \bar{u} (in nm) for an elastic solid squeezed against a rigid surface with the power spectra given by the sum of the two power spectra shown in Fig. 4.11. The line **a** is the result of the FEM calculation of Pei et al, and shows that for large separation $p \sim \exp(-\bar{u}/\gamma h_{\text{rms}})$ with $\gamma \approx 0.4$, which is consistent with our analytical results (see line **b** in Fig. 4.14).

Fig. 4.15 shows the relation between the relative contact area, A/A_0 , and the normalized squeezing pressure, p/E^* , for an elastic solid squeezed against a rigid surface with the power spectra shown in Fig. 4.11 (but multiplied by a factor of two). The line **a** is the

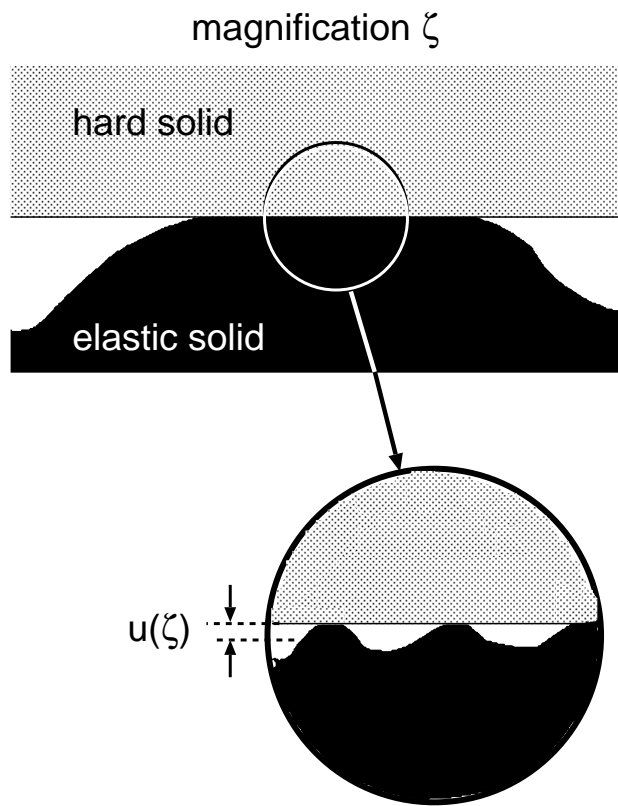


Figure 4.16: An asperity contact region observed at the magnification ζ . It appears that complete contact occur in the asperity contact region, but upon increasing the magnification it is observed that the solids are separated by the average distance $\bar{u}(\zeta)$.

result of the FEM calculation of Pei et al, while the line **b** is the prediction of the theory where A/A_0 is scaled by a factor of 1.29.

The good agreement between the FEM calculations and the analytical theory found above indicates that the contact mechanics results are robust and not very sensitive to many details such as the assumption of perfectly random surfaces, which is unlikely to be exactly obeyed for the polymer surfaces, the surface topography of which was used in the FEM calculations. (In order to address to what extent a measured surface is randomly rough one would need to calculate higher order correlation functions, and show that odd order functions in the height coordinate vanish (or are very small), and that even order height correlation functions can be decomposed into a sum of pair correlation functions. No such study for “real” measured surface profiles has yet been found.)

Note that the observation of an effective exponential repulsion has important implications for tribology, colloid science, powder technology, and materials science [58]. For example, the density or volume of granular materials has long been known to have a logarithmic dependence on the externally applied isotropic pressure or stress, as found, for example, in the compression stage during processing of ceramic materials [64]. Recent work on the confinement of nanoparticles have also indicated an exponential force upon compression [65], suggesting that this relationship could be prevalent among quite different types of heterogeneous surfaces.

Finally, let us consider the distribution of interfacial separations [66]

$$P_u = \langle \delta(u - u(\mathbf{x})) \rangle \quad (4.18)$$

where $\langle \dots \rangle$ stands for ensemble average (which often is equivalent to average over the surface area). This function is shown in Fig. 4.17 for three different loads and two different magnifications. Note that the distributions of interfacial separations observed at low and high magnifications are similar for $u > 5 \text{ \AA}$. This result is expected since mainly the long-wavelength, large amplitude roughness will determine the separation between the surfaces when the separation is large. The quantity P_u has many important applications. For example, for lubricated contact at low sliding velocity, one may estimate the contribution from shearing the liquid film to the (nominal) frictional stress using

$$\tau \approx \eta v \int_{u_c}^{\infty} du \frac{P_u}{u}$$

where η is the viscosity and v the sliding velocity, and where u_c is a cut-off separation of order nanometer (continuum fluid dynamics is not valid for liquid films thinner than a few nanometers). Another important application is for estimating the fluid leaking through sealing.

Another distribution \bar{P}_u of interfacial separations, which differs from (4.18), by using instead of $u(\mathbf{x})$ another function which involves some average over the spatial coordinate, has been defined as follows: The probability to find the surface separation $u < u_1(\zeta)$ is

$$\Psi(u) = A(\zeta)/A_0 = P(\zeta)$$

where $\zeta = \zeta(u)$ is the solution to $u = u_1(\zeta)$ [note that $u_1(\zeta)$ is a monotonically decreasing function of ζ so there exist a unique solution $\zeta = \zeta(u)$ to $u = u_1(\zeta)$]. The probability distribution

$$\bar{P}_u = \frac{d\Psi(u)}{du} = \frac{P'(\zeta)}{u'_1(\zeta)}|_{\zeta=\zeta(u)}$$

We can also write

$$\bar{P}_u = - \int d\zeta \frac{A'(\zeta)}{A_0} \delta[u - u_1(\zeta)] \quad (4.19)$$

It is convenient to change integration variable to μ defined by $\zeta = \exp(-\mu)$ and consider A and u_1 as function of μ . This gives

$$\bar{P}_u = - \int d\mu \frac{A'(\mu)}{A_0} \delta[u - u_1(\mu)] \quad (4.20)$$

In Fig. 4.18, P_u and \bar{P}_u have been shown for the surface shown in Fig. 4.2, and for the squeezing pressure 1.3 GPa. The result for P_u was obtained from the MD-simulations, while \bar{P}_u was obtained from the analytical theory presented above. As expected the distribution \bar{P}_u is more narrow than P_u [since it involves u_1 which is already an average of $u(\mathbf{x})$], but it is easy to show that average of u is the same for both P and \bar{P} and equal to the average separation between the surfaces. Thus

$$\int du u \bar{P}_u = - \int d\zeta \frac{A'(\zeta)}{A_0} u_1(\zeta)$$

Substituting (25) in this equation gives

$$\int du u \bar{P}_u = - \frac{1}{A_0} \int_{\zeta_0}^{\zeta_1} d\zeta \frac{d}{d\zeta} [A(\zeta) \bar{u}(\zeta)] = \bar{u}(\zeta_0)$$

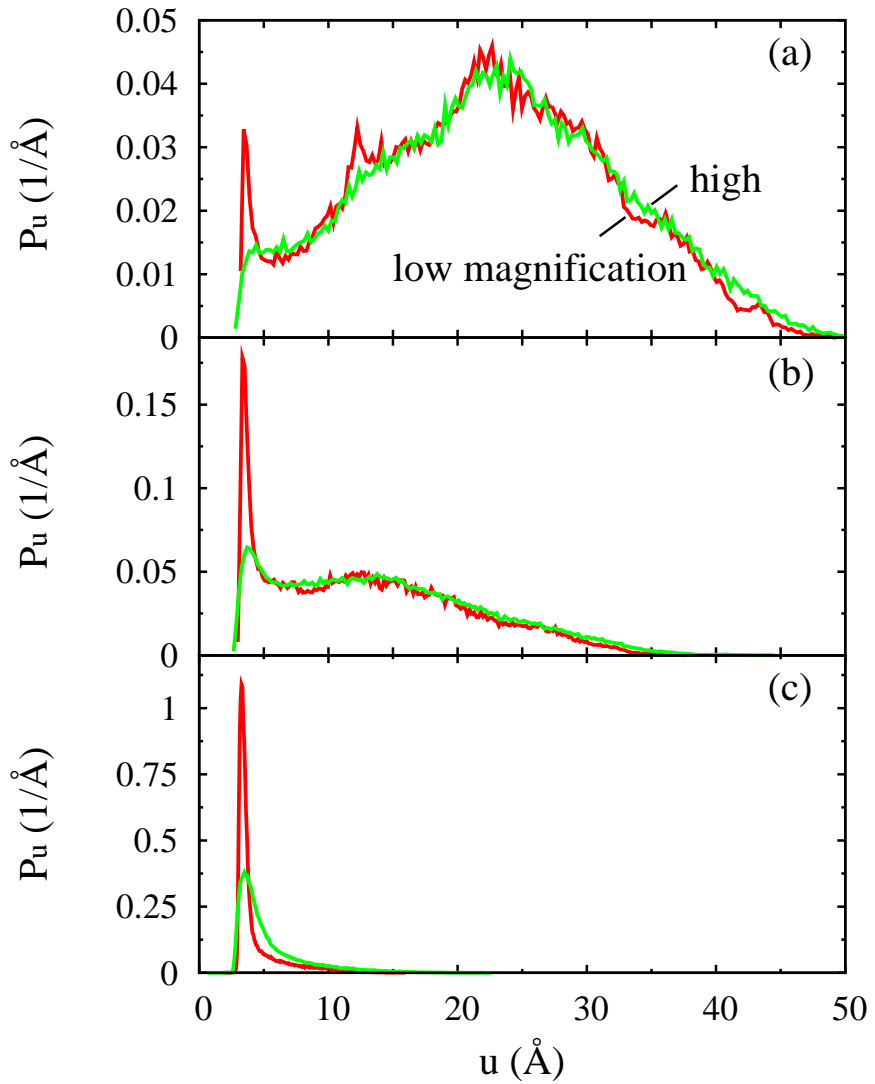


Figure 4.17: Probability distribution of interfacial separation under different pressure (a) $p/E^* \approx 0.002$, (b) $p/E^* \approx 0.013$, (c) $p/E^* \approx 0.113$, at low and high magnifications respectively. For low pressure, the interfacial separation probability distribution on low and high magnification is similar for $u > 5 \text{\AA}$. This result is expected since mainly the long-wavelength, large amplitude roughness will determine the separation between the surfaces when the separation is large.

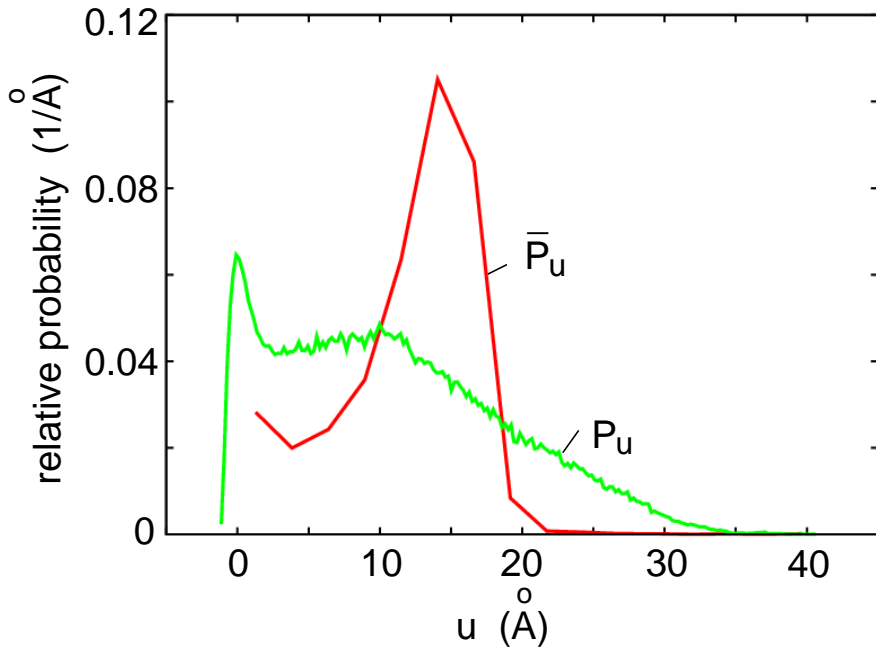


Figure 4.18: The probability distributions P_u and \bar{P}_u defined in the text, for the surface shown in Fig. 4.2 and for the squeezing pressure 1.3 GPa. The distribution \bar{P}_u has a delta function at $u = 0$ with the weight $A(\zeta_1)/A_0 \approx 0.047$.

where I have used that $\bar{u}(\zeta_1) = 0$ and that $A(\zeta_0) = A_0$ (note: ζ_0 is the lowest magnification usually chosen as unity). Since $\bar{u}(\zeta_0)$ equals the average separation between the surfaces which has been proved by our statement. Note that \bar{P}_u has a delta function at $u = 0$ with the weight $A(\zeta_1)/A_0$. Using this fact it is easy to show that distribution \bar{P}_u has the zero order moment equal to unity:

$$\int du \bar{P}_u = 1$$

Thus, the zero order and first order moments of P_u and \bar{P}_u are the same, but higher order moments will differ.

4.6 Summary

Our recently developed multiscale molecular dynamics approach [6], has been used to study real contact area and interfacial separation from small contact to full contact. The real contact area rises linearly with the load for small load. Here I have found that, at low magnification where the atomistic nature of the solids becomes unimportant, the MD results match very well with Persson's theory, especially when the contact approaches full contact. The "correction factor" r has been introduced to describe the deviation between the Persson theory and the MD calculation.

The interfacial separation as a function of squeezing pressure has been derived theoretically. For non-adhesive interaction and small applied pressure, $p \sim e^{-\bar{u}/u_0}$ is in good agreement with experimental observation. This relation has been tested with MD simulations and they match quite well with each other. As a conclusion, Persson theory can be considered as a model connecting the atomic and macroscopic world, excluding the extreme case when there is only one or a few atoms on the asperities. The present re-

sults may be of great importance for soft solids, e.g. rubber-like material, or very smooth surfaces.

Chapter 5

Interfacial Separation and Contact Area with Adhesion

Contact mechanics between solid surfaces is the basis for understanding many tribological processes such as friction, wear and sealing. The two most important properties are the area of real contact and the interfacial separation between the solid surfaces. The current chapter studies the adhesive contact between rough surfaces. The molecular dynamics calculations are compared with the theory, which turns out to be in good agreement with each other.

For non-adhesive contact and small squeezing pressure, the average interfacial separation depends logarithmically on the squeezing pressure [61], and the (projected) contact area depends linearly on the squeezing pressure. Based on the work in chapter 4, here the relations between average interfacial separation and squeezing pressure, and between contact area and squeezing pressure, are extended to the case with adhesion included. This chapter has been organized as follows. Section 5.2 deals with theory with adhesion, which is based on the theory in Ref. [61]. Section 5.3 deals with the Molecular Dynamics (MD) model. The numerical results will be presented in section 5.4. The summary will be given in section 5.5.

5.1 Background

With the rapid development of micro/nano electromechanical devices in last decade, surface forces play more and more important role, due to the increase of ratio between the number of atoms on the surface and that in the volume. When we bring two surfaces together, there is much evidence that attractive forces act between them. Such forces explain qualitatively that a mechanical load is required to separate two solid bodies placed in intimate contact [46]. This load, required to separate two surfaces, is referred to separation force (or adhesion force). Everything in the world has two-sided effects. Of course there is no exception for adhesion. On one hand, adhesion can help the Gecko walk on the ceilings or run on the vertical wall. On the other hand, adhesion can lead to the failure especially on micro or nano devices, e.g. the micro-sized cantilever beam. If it is too long or too thin, the free energy minimum state makes the cantilever beam partly bound to the flat substrate which leads to the failure of the device. However, if the surface roughness of the substrate is increased, the micro-sized the cantilever will stabilize due to the decrease of binding energy.

In reality most surfaces are not atomically flat. Even if a surface appears flat at low magnification, when the surface at higher magnification is studied, one usually observes

surface roughness. Similarly, when two solids with nominally smooth surfaces are brought into contact they will in general not make contact everywhere, but at high enough magnification there are many non-contact regions. The study of the interfacial separation is essential for describing, e.g., sealing or optical interference.

5.2 Interfacial separation with adhesion

Consider the (average) interfacial separation \bar{u} as a function of the squeezing pressure $p = F_N/A_0$. Note that as p increases, \bar{u} will decrease and consider $p = p(\bar{u})$ as a function of \bar{u} . Energy conservation gives [1]

$$\int_{\bar{u}}^{\infty} du \, p(u) A_0 = U \quad (5.1)$$

where $U = U_{\text{el}} + U_{\text{ad}}$ is the sum of the elastic energy U_{el} stored at the interface and the adhesional energy $U_{\text{ad}} = -\Delta\gamma A^*(\zeta_1)$ (see Appendix A). For the elastic energy U_{el} we use [61]

$$U_{\text{el}} \approx A_0 E^* \frac{\pi}{2} \int_{q_0}^{q_1} dq \, q^2 W(q, p) C(q), \quad (5.2)$$

where q_0 and q_1 are the smallest and the largest surface roughness wave vectors, and [61]

$$W(q, p) = P_p(q) \left[\beta + (1 - \beta) P_p^2(q) \right],$$

where $\beta = 0.4$. The equations given above are solved as described in Ref. [4].

From (5.1) one gets

$$p(\bar{u}) = -\frac{1}{A_0} \frac{dU(\bar{u})}{d\bar{u}}$$

Now consider U as a function of p and write

$$p(\bar{u}) = -\frac{1}{A_0} \frac{dU}{dp} \frac{dp}{d\bar{u}}$$

or

$$d\bar{u} = -\frac{1}{A_0 p} \frac{dU}{dp} dp$$

Integrating from $u = 0$ (corresponding to $p = \infty$) to u (corresponding to the pressure p) gives

$$\bar{u} = \frac{1}{A_0} \int_p^{\infty} dp \, \frac{1}{p} \frac{dU}{dp}$$

which is very convenient for numerical calculations.

5.3 Molecular dynamics

The MD system has lateral dimension $L_x = N_x a$ and $L_y = N_y a$, where a is the lattice spacing of the block. In order to accurately study contact mechanics between elastic solids, it is necessary to consider that the thickness of the block is of the same order of the lateral size of the longest wavelength roughness on the substrate. Thus, we have developed a multiscale MD approach to study contact mechanics [6]. Periodic boundary condition has been used in xy plane. For the block $N_x = N_y = 400$, while the lattice space of the substrate $b \approx a/\phi$, where $\phi = (1 + \sqrt{5})/2$ is the golden mean, in order to avoid the formation of commensurate structures at the interface. The mass of the block

atoms is 197 a.m.u. and the $a = 2.6 \text{ \AA}$. The elastic modulus and Poisson ratio of the block is $E = 77.2 \text{ GPa}$ and $\nu = 0.42$, respectively. The effective elastic modulus has been defined $E^* = E/(1 - \nu^2)$. For self-affine fractal surfaces, the power spectrum has power-law behavior $C(q) \sim q^{-2(H+1)}$, where the Hurst exponent H is related to the fractal dimension D_f of the surface via $H = 3 - D_f$. For real surfaces this relation holds only for a finite wave vector region $q_0 < q < q_1$, where $q_L = 2\pi/L$, $q_0 = 3q_L$, $q_1 = \zeta q_0$ and ζ . Note that in many cases, there is a roll-off wave vector q_0 below which $C(q)$ is approximately constant. In MD simulations, the substrate is fractal with fractal dimension $D_f = 2.2$ and root-mean-square roughness $h_{rms} = 10 \text{ \AA}$.

The atoms at the interface between block and substrate interact with the potential

$$U(r) = 4\epsilon \left[\left(\frac{r_0}{r} \right)^{12} - \left(\frac{r_0}{r} \right)^6 \right] \quad (5.3)$$

where r is the distance between the pair of atoms. The parameter ϵ is the binding energy between two atoms at separation $r = 2^{1/6}r_0$. In the calculations presented below I have used the $r_0 = 3.28 \text{ \AA}$ and $\epsilon = \epsilon_0 = 18.6 \text{ meV}$, $\epsilon = 4\epsilon_0$ and $\epsilon = 8\epsilon_0$. By comparing the total energy for the surfaces separated with the case where the surfaces are in contact at equilibrium (at zero external load) I obtain $\Delta\gamma = 0.69 \text{ J/m}^2$ for the case $\epsilon = \epsilon_0$, and 4 and 8 times higher interfacial binding energy for the other two cases.

Now let us discuss how to define contact on the atomic scale, when adhesion is included. In the absence of adhesion I have found that studying the interfacial stress distribution gives the most accurate way of deducing the area of real contact [6]. When adhesion is included a cut-off length r_c has been used to define contact. It is clear from the force-distance curve that the only distinctive point is the maximum tensile stress [67]. We regard the solids as in contact when the stress increases with separation, and separated when the stress decreases with separation (see Fig. 5.1). In our case, the critical wall-wall distance is $r_c = 3.68 \text{ \AA}$.

5.4 Numerical results

5.4.1 Interfacial separation u vs. squeezing pressure p with adhesion

The (natural) logarithm of the squeezing pressure p (in units of $E^* = E/(1 - \nu^2)$), as a function of the interfacial separation \bar{u} in units of the root-mean-square roughness amplitude h_{rms} , has been shown in Fig. 5.2. The most right-hand curve is for the case of no adhesion, which has been discussed in chapter 4. Now let us introduce adhesion. ϵ_0 is the strength of adhesion. One can easily see from Fig. 5.2 that for the same squeezing pressure, the stronger the adhesion, the smaller interfacial separation. As is well known, that the adhesion can bring two surfaces closer. E.g., if one continues the curve for $8\epsilon_0$, it may become vertical. Thus, when adhesion is included, the logarithmic relation, between interfacial separation and squeezing pressure, does not hold. The theoretical result (solid lines) agrees very well with the molecular dynamics calculations (square symbols).

5.4.2 Probability distribution of u and p

In Fig. 5.3 the probability distribution of perpendicular stress at the interface has been shown for several values of the adhesion (a), and for $\epsilon = 8\epsilon_0$ for three different applied stress (b). Note that when the adhesion increases, the maximum of the tensile stress increases roughly proportional to ϵ . In fact, one expects $\sigma_c \sim \epsilon/a$, where a is of order a bond length. At the same time the maximum repulsive pressure increases but weaker

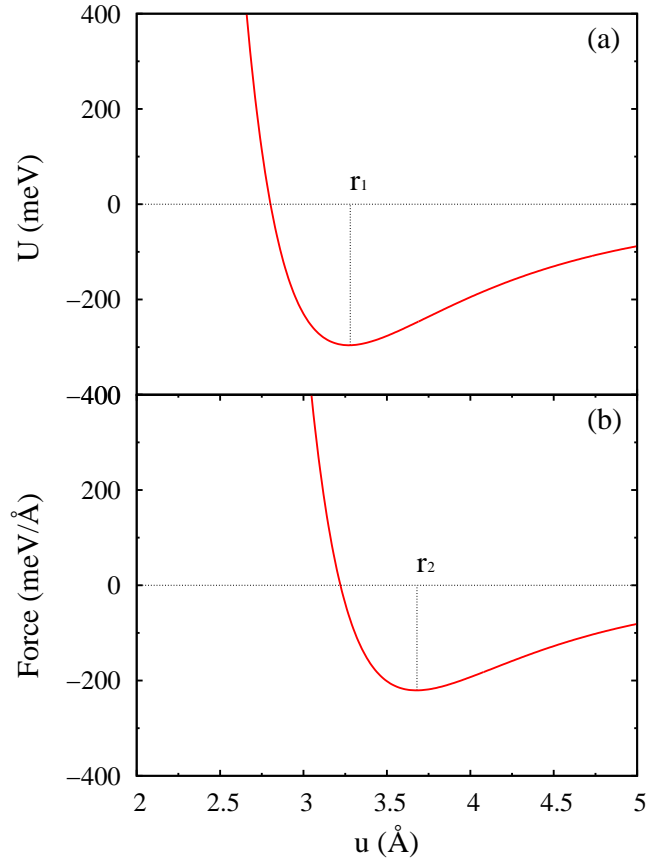


Figure 5.1: Lennard-Jones potential as a function of distance r in (a). From force-distance curve (b), one can see that the only distinctive point is the maximum tensile stress at r_2 .

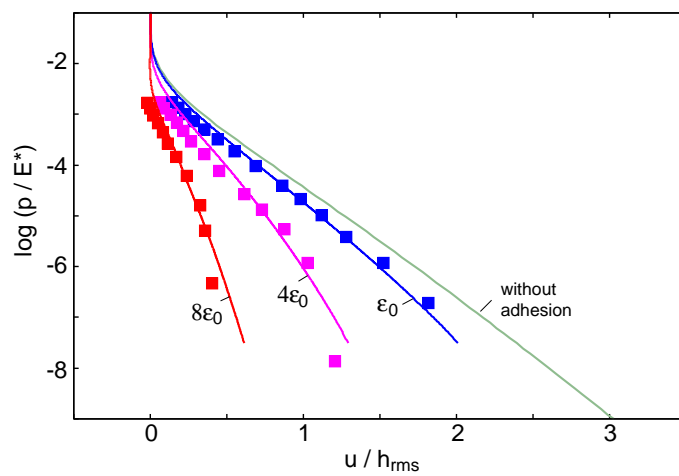


Figure 5.2: Molecular dynamics (square symbols) and theoretical (solid lines) results for the (natural) logarithm of the squeezing pressure p (in units of $E^* = E/(1-\nu^2)$) as a function of the interfacial separation \bar{u} in units of the root-mean-square roughness amplitude h_{rms} .

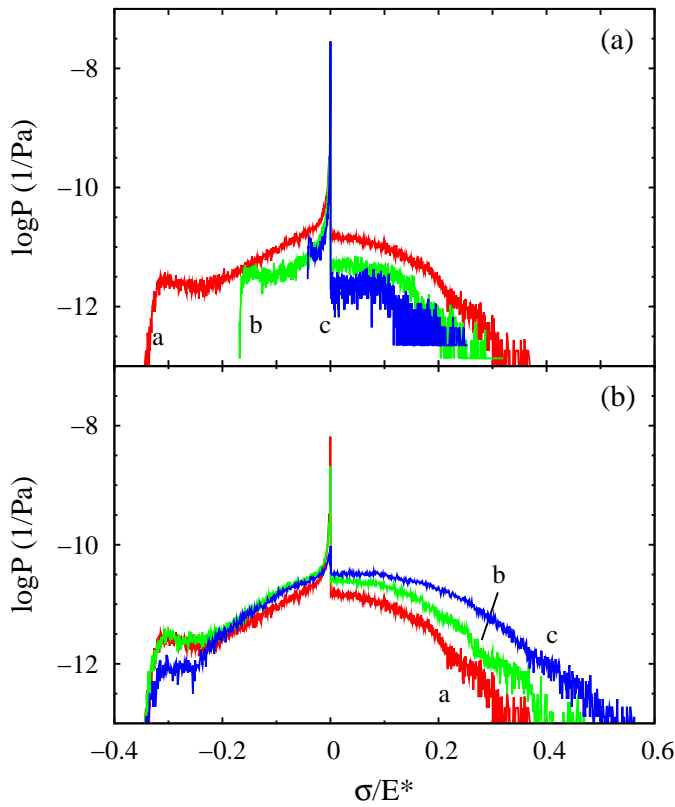


Figure 5.3: The logarithm (with 10 as basis) of the probability distribution of normal stress σ (where σ is in unit of E^*) for (a) three different adhesion parameters $\epsilon = 8\epsilon_0, 4\epsilon_0, \epsilon_0$ referred to as a,b,c respectively, and (b) with $8\epsilon_0$ for three different pressure $p/E^* = -0.00532, 0.00832, 0.06265$ denoted as a,b, and c respectively.

than linear. The increase in repulsive stress is, of course, due to the additional load which acts on the block.

The probability distribution of interfacial separations are shown in Fig. 5.4. When the adhesion increases, the surfaces are pulled closer together and the distribution of separations becomes more narrow. Similarly, when the applied pressure decreases, the separation between the walls decreases.

5.4.3 Contact area comparison between MD and Theory

The molecular dynamics simulations (square symbols) have been compared with the theory (solid lines) in Fig. 5.5, for the relative contact area A/A_0 as a function of the squeezing pressure. The result above shows that the theory gives a good description of adhesive contact mechanics between randomly rough surfaces, although the contact area from MD simulation is slightly bigger than that predicted by the theory.

5.5 Summary

The relation, between the interfacial separation and the squeezing pressure, both without and with adhesion, has been studied. For non-adhesive contact, the theory is in good agreement with MD simulations and FEM calculations. For adhesive contact, both theory

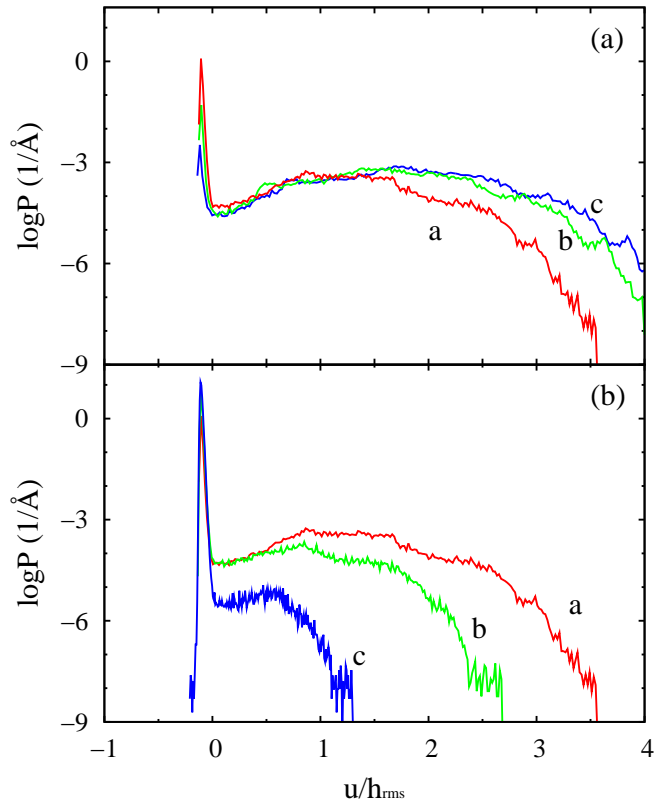


Figure 5.4: The logarithm (with 10 as basis) of the probability distribution of interfacial separations u (where u is in units of the root-mean-square roughness amplitude h_{rms}) for (a) three different adhesion parameters $\epsilon = 8\epsilon_0$, $4\epsilon_0$ and ϵ_0 , referred to as a, b and c respectively, and (b) with $8\epsilon_0$ for three different pressures $p/E^* = -0.00532$, 0.00832 , 0.06265 denoted by a,b, and c respectively.

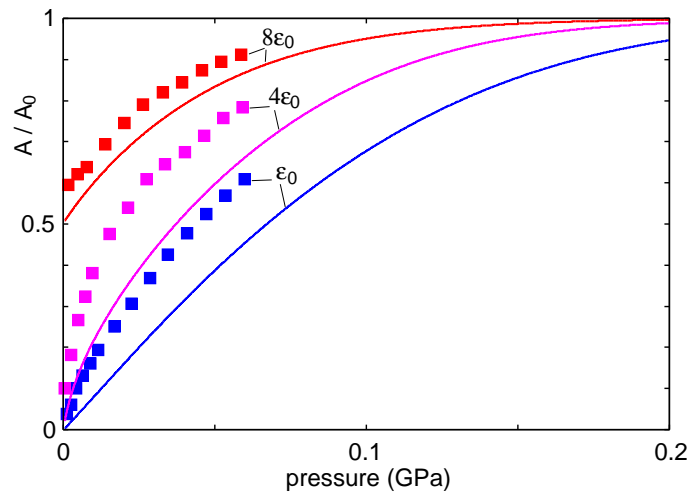


Figure 5.5: Molecular dynamics (square symbols) and theoretical (solid lines) results for the relative contact area A/A_0 as a function of the squeezing pressure (in GPa). In the calculation (solid lines) $\Delta\gamma = 0.7$, 2.8 and 5.6 J/m^2 have been used for the curves indicated by ϵ_0 , $4\epsilon_0$ and $8\epsilon_0$, respectively.

and experiment predict absolute slope bigger, between the interfacial separation and the log-scale pressure, than the one for non-adhesive contact. In adhesive contact, however, the absolute slope that the theory predicts is smaller than the one observed in the experiment by Benz et al. [58]. This discrepancy might be due to plastic yield occurring in the real experiments, but further investigations are still needed.

Chapter 6

Theory of the Leak-rate of Seals

Seals are extremely useful tools to prevent fluid leakage. However, the exact mechanism of roughness induced leakage is not well understood. A theory of the leak-rate of seals has been presented in this chapter, which is based on percolation theory and a recently developed contact mechanics theory. Both static and dynamics seals have been studied. I also present molecular dynamics results which show that when two elastic solids with randomly rough surfaces are squeezed together, as a function of increasing magnification or decreasing squeezing pressure, a non-contact channel will percolate when the (relative) projected contact area, A/A_0 , is of order 0.4, in accordance with percolation theory. A simple experiment has been suggested, which can be used to test the theory.

6.1 Introduction

A seal is a tool for closing a gap or making a joint fluid tight [68]. Seals play a crucial role in many modern engineering devices, and the failure of seals may result in catastrophic events, such as the Challenger disaster. In spite of its apparent simplicity, it is still not possible to predict theoretically the leak-rate and (for dynamic seals) the friction forces [69] for seals. The main problem is the influence of surface roughness on the contact mechanics at the seal-substrate interface. Most surfaces of engineering interest have surface roughness on a wide range of length scales [1], e.g, from cm to nm, which will influence the leak rate and friction of seals, and accounting for the whole range of surface roughness is impossible using standard numerical methods, such as the Finite Element Method.

In this chapter, the role of surface roughness on seals is analyzed. I will use a recently developed contact mechanics theory [2, 4, 44, 52, 60, 61] to calculate the leak-rate of static seals. We assume that purely elastic deformation occurs in the solids, which is the case for rubber seals. For metal seals, strong plastic deformation often occurs in the contact region.

The theory developed below is based on studying the interface between the rubber and the hard counter surface (usually a metal) at different magnifications ζ . At low magnification the surfaces appear flat and the contact between them appears to be complete (i.e., no leak channels can be observed). However, when the magnification is increased, surface roughness will be observed at the interface, and, in general, non-contact regions. As the magnification increases, more and more (short-wavelength) roughness will be observed, and the (apparent) contact area $A(\zeta)$ between the solids will decrease. At high enough magnification, for $\zeta = \zeta_c$, a non-contact (percolation) channel will appear, through which fluid will flow, from the high pressure side (pressure P_a) to the low pressure side (pressure P_b), see Fig. 6.1. We denote the most narrow passage between the two surfaces along the percolation path as the critical constriction. When the magnification increases further,

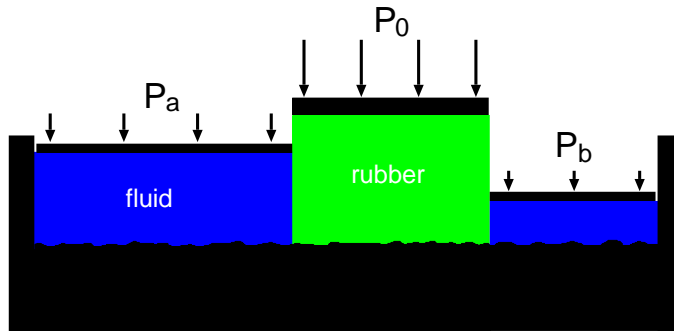


Figure 6.1: Rubber seal (schematic). The liquid on the left-hand-side is under the hydrostatic pressure P_a and the liquid to the right under the pressure P_b (usually, P_b is the atmospheric pressure). The pressure difference $\Delta P = P_a - P_b$ results in liquid flow at the interface between the rubber seal and the rough substrate surface. The volume of liquid flow per unit time is denoted by \dot{Q} , and depends on the squeezing pressure P_0 acting on the rubber seal.

more percolation channels will be observed, but these channels will have more narrow constrictions than those for the first channel which appears at the percolation threshold ($\zeta = \zeta_c$).

The picture described above for the leakage of seals has already been presented by Persson [1, 70]. However, recent development in contact mechanics now allows us to present a more accurate analysis of the leakage process. In this chapter the theory of Ref. [70] has been extended, and numerical results have been presented for the size of the critical constriction and for the leak-rate.

Sec. 6.2 describes the basic picture used to calculate the leak-rate of static seals. Sec. 6.3 presents numerical results for the size of the critical constriction and for the leak-rate, and Molecular Dynamics results which illustrate how the contact between the two solids changes as the magnification ζ increases. I find that the percolation channel is formed when $\zeta = \zeta_c$, where $A(\zeta_c)/A_0 \approx 0.4$, in accordance with percolation theory [71]. Sec. 6.4 deals with improvement of the theoretical picture of how to understand static seals. The theory has been compared with experimental data in Sec. 6.5. Some comments related to the non-uniform seal are presented in Sec. 6.6. pressure distribution, the role of adhesion and rubber viscoelasticity. Dynamical (linear reciprocal motion) seals at low sliding velocities is discussed in Sec. 6.7. In Sec. 6.8 a simple experiment is suggested to test the theory. The summary is in sec. 6.9.

6.2 Basic picture of leak-rate

We first briefly review the basic picture on which our calculations of the leak-rate are based [70]. Assume that the nominal contact region between the rubber and the hard countersurface is rectangular with area $L_x \times L_y$, see Fig. 6.2. We assume that the high pressure fluid region is for $x < 0$ and the low pressure region for $x > L_x$. We now divide the contact region into squares with the side $L_x = L$ and the area $A_0 = L^2$ (this assumes that $N = L_y/L_x$ is an integer, but this restriction does not affect the final result). Now, let us study the contact between the two solids within one of the squares as the magnification ζ changes. Define $\zeta = L/\lambda$, where λ is the resolution. I study how the apparent contact area (projected on the xy -plane), $A(\zeta)$, between the two solids depends on the magnification ζ .

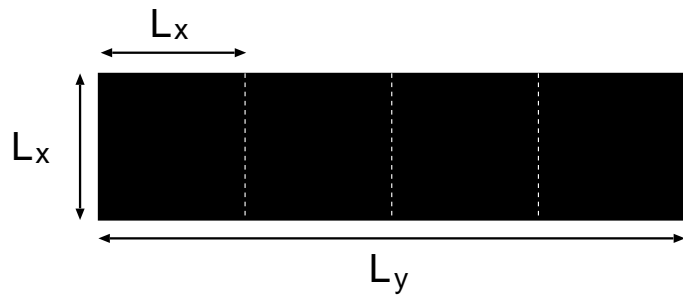


Figure 6.2: The rubber-countersurface apparent contact area is rectangular $L_x \times L_y$. We “divide” it into $N = L_y/L_x$ square areas with side $L = L_x$ and area $A_0 = L^2$.

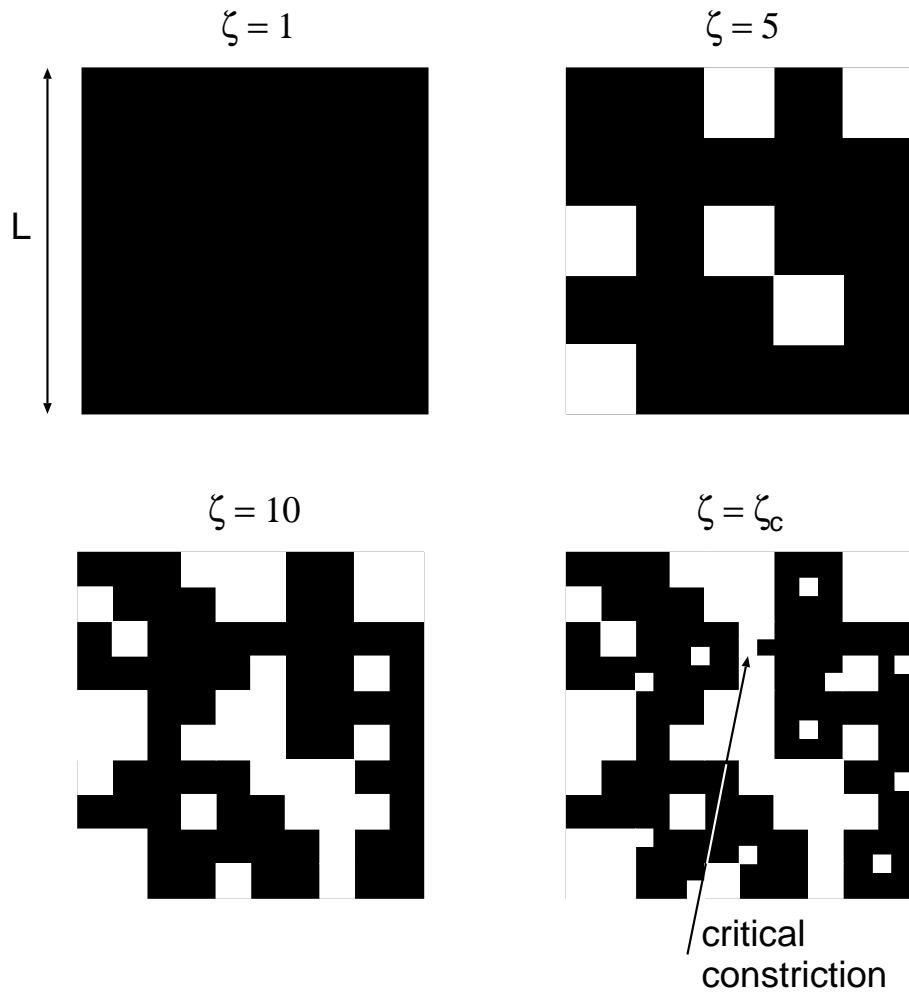


Figure 6.3: The contact region at different magnifications (schematic). Note that at the point where the non-contact area (white area) percolate $A(\zeta_c) \approx 0.4A_0$, while there appear to be complete contact between the surfaces at the lowest magnification $\zeta = 1$: $A(1) = A_0$.

At the lowest magnification one can not observe any surface roughness, and the contact between the solids appears to be complete i.e., $A(1) = A_0$. As the magnification increases, some interfacial roughness will be observed, and the (apparent) contact area will decrease, see Fig. 6.3. At high enough magnification, say $\zeta = \zeta_c$, a percolating path of non-contact area will be observed for the first time, see Fig. 6.3. The most narrow constriction along the percolation path will have the lateral size $\lambda_c = L/\zeta_c$ and the surface separation at this point is denoted by $u_c = u_1(\zeta_c)$ and is given by a recently developed contact mechanics theory (see below). As the magnification continues increasing, we will find more percolating channels between the surfaces, but these will have more narrow constrictions than the first channel which appears at $\zeta = \zeta_c$, and for the moment the contribution to the leak-rate from these channels (see also Sec. 6.4) will be neglected. Thus, in this chapter we will assume that the leak-rate is determined by the critical constriction.

A first rough estimate of the leak-rate is obtained by assuming that all the leakage occurs through the critical percolation channel, and that the whole pressure drop $\Delta P = P_a - P_b$ (where P_a and P_b is the pressure to the left and right of the seal) occurs over the critical constriction [of width and length $\lambda_c \approx L/\zeta_c$ and height $u_c = u_1(\zeta_c)$]. Thus for an incompressible Newtonian fluid, the volume-flow per unit time through the critical constriction will be

$$\dot{Q} = M \Delta P \quad (6.1)$$

where

$$M = \alpha \frac{u_1^3(\zeta_c)}{12\eta} \quad (6.2)$$

where η is the fluid viscosity. Laminar flow and $u_c \ll \lambda_c$ have been assumed in deriving (6.1), which are always satisfied in practice. No-slip boundary condition is assumed on the solid walls. This assumption is not always satisfied at the micro or nano scale, yet it is likely to be a good approximation in the present case owing to surface roughness occurring at length-scale shorter than the size of the critical constriction. In deriving 6.2 a factor α has been introduced, which depends on the exact shape of the critical constriction, but which is expected to be of order unity. Since there are $N = L_y/L_x$ square areas in the rubber-countersurface (apparent) contact area, we get the total leak-rate

$$\dot{Q} = \frac{L_y}{L_x} M \Delta P. \quad (6.3)$$

To complete the theory one has to calculate the separation $u_c = u_1(\zeta_c)$ of the surfaces at the critical constriction. We first determine the critical magnification ζ_c by assuming that the apparent relative contact area at this point is given by site percolation theory. Thus, the relative contact area $A(\zeta)/A_0 \approx 1 - p_c$, where p_c is the so called site percolation threshold [71]. For an infinite-sized systems $p_c \approx 0.696$ for a hexagonal lattice and 0.593 for a square lattice [71]. For finite sized systems the percolation will, on the average, occur for (slightly) smaller values of p , and fluctuations in the percolation threshold will occur between different realization of the same physical system. This problem will be addressed later (see Sec. 6.3) but for now let us take $p_c \approx 0.6$ so that $A(\zeta_c)/A_0 \approx 0.4$ will determine the critical magnification $\zeta = \zeta_c$.

Let us define $u_1(\zeta)$ to be the (average) height separating the surfaces which appear to come into contact when the magnification decreases from ζ to $\zeta - \Delta\zeta$, where $\Delta\zeta$ is a small (infinitesimal) change in the magnification. $u_1(\zeta)$ is a monotonically decreasing function of ζ , and can be calculated from the average interfacial separation $\bar{u}(\zeta)$ and $A(\zeta)$ using (see Ref. [61])

$$u_1(\zeta) = \bar{u}(\zeta) + \bar{u}'(\zeta) A(\zeta) / A'(\zeta).$$

The quantity $\bar{u}(\zeta)$ is the average separation between the surfaces in the apparent contact regions observed at the magnification ζ , see Fig. 4.16. It can be calculated from [61]

$$\begin{aligned}\bar{u}(\zeta) &= \sqrt{\pi} \int_{\zeta q_0}^{q_1} dq \ q^2 C(q) w(q) \\ &\times \int_{p(\zeta)}^{\infty} dp' \ \frac{1}{p'} \left[\gamma + 3(1 - \gamma) P^2(q, p', \zeta) \right] e^{-[w(q, \zeta)p'/E^*]^2},\end{aligned}$$

where $\gamma \approx 0.4$ and where

$$p(\zeta) = P_0 A_0 / A(\zeta)$$

and

$$w(q, \zeta) = \left(\pi \int_{\zeta q_0}^q dq' \ q'^3 C(q') \right)^{-1/2}.$$

The function $P(q, p, \zeta)$ is given by

$$P(q, p, \zeta) = \frac{2}{\sqrt{\pi}} \int_0^{s(q, \zeta)p} dx \ e^{-x^2},$$

where $s(q, \zeta) = w(q, \zeta)/E^*$.

The contact has been studied between the solids at increasing magnification. In an apparent contact area observed at the magnification ζ , the substrate has the root mean square roughness amplitude [2, 70]

$$h_{\text{rms}}^2(\zeta) = 2\pi \int_{\zeta q_0}^{q_1} dq \ q C(q). \quad (6.4)$$

When the apparent contact area has been studied at increasing magnification, the contact pressure $p(\zeta)$ will increase and the surface roughness amplitude $h_{\text{rms}}(\zeta)$ will decrease. Thus, the average separation $\bar{u}(\zeta)$, between the surfaces in the (apparent) contact regions observed at the magnification ζ , will decrease with increasing magnification.

6.3 Results

6.3.1 Numerical results

The numerical results have been presented to illustrate the theory developed above. Assume a rubber block with a flat surface, squeezed by the nominal pressure P_0 against a hard solid with a randomly rough surface which self affine fractal has been assumed. Thus the surface roughness power spectrum for $q_0 < q < q_1$:

$$C(q) = C_0 q^{-2(1+H)}$$

where

$$C_0 = \frac{H}{\pi} \langle h^2 \rangle \left[q_0^{-2H} - q_1^{-2H} \right]^{-1} \approx \frac{H}{\pi} \langle h^2 \rangle q_0^{-2H}$$

where q_0 and q_1 are the long-distance and short-distance cut-off wavevectors, respectively.

The rubber has the Young's modulus $E = 10$ MPa (as is typical for the low-frequency modulus of rubber used for seals) and Poisson ratio $\nu = 0.5$. The pressure difference in the fluid between the two sides of the seals is assumed to be $\Delta P = 0.01$ MPa, as long as ΔP is small compared to the pressure in the rubber-substrate nominal contact area, the leak-rate for other sealed pressure can be obtained using direct scaling (see Eq. 6.3). If this condition is not satisfied, i.e. $\Delta P \leq P_0$, it is necessary to account for the fluid

pressure in solving the contact mechanics problem. This can be done in an (approximate) mean-field type of approach by assuming that the rubber-contact area is determined by the squeezing pressure $P_0 - p_{fluid}(x)$, where $p_{fluid}(x)$ is the average local fluid pressure in the nominal rubber-substrate contact area. In the numerical calculations $L_y/L_x = 1$ and the leak-rate for other values of L_y/L_x can be obtained by using direct scaling (see Eq. 6.3). The fluid is assumed to be an incompressible Newtonian fluid with the viscosity $\eta = 0.001 \text{ Ns/m}^2$. We will study how the lateral size λ_c and the height u_c of the critical constriction depends on the fractal dimension $D_f = 3 - H$ and on the root-mean-square roughness amplitude h_{rms} of the rough surface. We also present results on how the volume flow of fluid through the seals depends on D_f and h_{rms} . The randomly rough surfaces have the cut-off wavevectors $q_0 = 1.0 \times 10^4 \text{ m}^{-1}$ and $q_1 = 7.8 \times 10^9 \text{ m}^{-1}$. We vary the applied squeezing pressure P_0 from 0.05 MPa to 1 MPa.

Let us first vary the rms roughness amplitude. In Fig. 6.4 we show the lateral size $\lambda_c = \lambda(\zeta_c)$ and in Fig. 6.5 the height (interfacial separation) u_c of the critical constriction, as a function of the applied normal (or squeezing) pressure P_0 . Results are shown for self affine fractal surfaces with the Hurst exponent $H = 0.8$ (or fractal dimension $D_f = 2.2$), and for surfaces with the root-mean-square roughness (rms) 1, 2, 4 and 6 μm . As expected, the size of the critical constriction increases when the roughness increases. In Fig. 6.6, the volume per unit time of fluid leaking through the seals has been shown as a function of the applied normal (or squeezing) pressure P_0 . Note the extremely strong decrease in \dot{Q} with increasing squeezing pressure and also its strong dependence on the rms roughness amplitude.

In Figs. 6.7, 6.8 and 6.9 we show the analogous results while varying the Hurst exponent $H = 0.9, 0.8, 0.7$ and 0.6 for $h_{rms} = 2 \mu\text{m}$. Note that when H decreases for a fixed h_{rms} , the short wavelength roughness increases while the long wavelength roughness is almost unchanged.

In Fig. 6.10, the interfacial separation $u_1(\zeta_c)$ and the rms-roughness $h_{rms}(\zeta_c)$ in the critical constriction, have been shown as a function of the applied normal (or squeezing) pressure P_0 . Results are shown for a self affine fractal surface with the Hurst exponent $H = 0.8$ (or fractal dimension $D_f = 2.2$), and with the root-mean-square roughness (rms) 6 μm . Note that the difference between $h_{rms}(\zeta_c)$ and $u_1(\zeta_c)$ is relatively small. We have found that this is the case also for the other parameters used in the study above.

6.3.2 Molecular dynamics results

The multiscale molecular dynamics model has been described in Ref. [6], but I review it briefly here. In what follows I denote the lower solid as *substrate*, the upper solid as *block*. We are concerned with the contact between a randomly rough and rigid substrate, and an elastic block, without adhesion. We are interested in surfaces with random roughness with wave-vector components in the finite range $q_1 > q > q_L$ (see Fig. 6.11), where $q_L = 2\pi/L$, L is the lateral size of the system. In order to accurately study contact mechanics between elastic solids, it is necessary to consider a solid block which extends a distance $\sim L$ in the direction normal to the nominal contact area. This requires huge number of atoms or dynamical variables even for small systems. Therefore, we have developed a multiscale molecular dynamics approach to study contact mechanics, to avoid this trouble [6]. The lateral size of the system is $L = 1040 \text{ \AA}$. $L_x = N_x a$ and $L_y = N_y a$, where $a = 2.6 \text{ \AA}$ is the lattice space of the block, $N_x = N_y = 400$ for the block. The elastic modulus and Poisson ratio are $E = 77.2 \text{ GPa}$ and $\nu = 0.42$. The lattice space of the substrate is $b \approx a/\phi$, where $\phi = (1 + \sqrt{5})/2$ is the golden mean, in order to achieve (nearly) incommensurate structures at the interface.

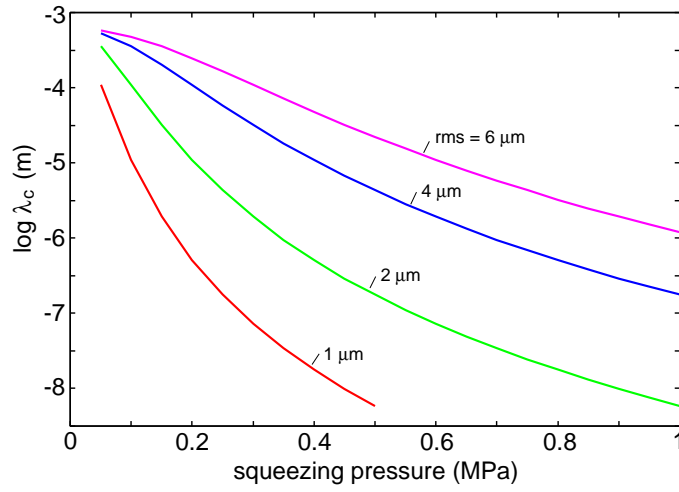


Figure 6.4: The lateral size $\lambda_c = \lambda(\zeta_c)$ of the critical constriction of the percolation channel, as a function of the applied normal (or squeezing) pressure P_0 . Results are shown for self affine fractal surfaces with the Hurst exponent $H = 0.8$ (or fractal dimension $D_f = 2.2$), and for surfaces with the root-mean-square roughness (rms) 1, 2, 4 and 6 μm .

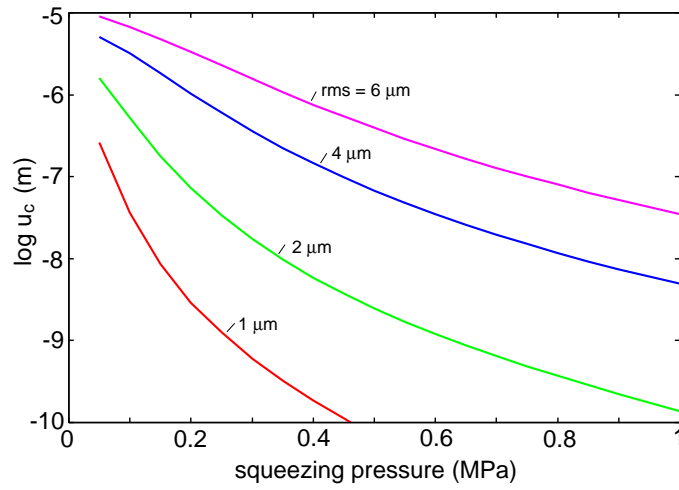


Figure 6.5: The interfacial separation $u_c = u_1(\zeta_c)$ at the critical constriction of the percolation channel, as a function of the applied normal (or squeezing) pressure P_0 . Results are shown for self affine fractal surfaces with the Hurst exponent $H = 0.8$ (or fractal dimension $D_f = 2.2$), and for surfaces with the root-mean-square roughness (rms) 1, 2, 4 and 6 μm .

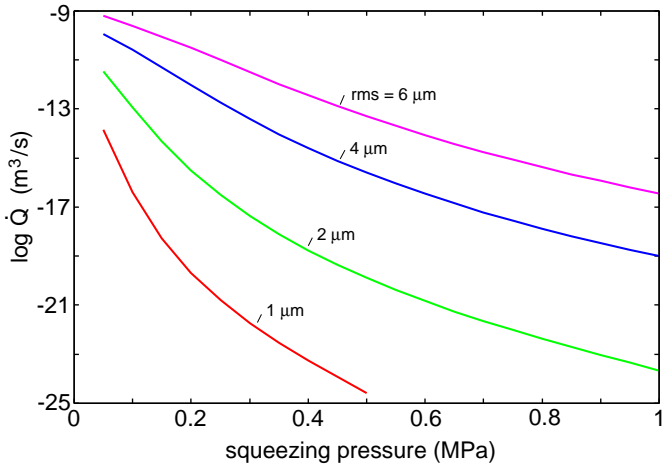


Figure 6.6: The volume per unit time, \dot{Q} , of fluid leaking through the seals as a function of the applied normal (or squeezing) pressure P_0 . Results are shown for self affine fractal surfaces with the Hurst exponent $H = 0.8$ (or fractal dimension $D_f = 2.2$), and for surfaces with the root-mean-square roughness (rms) 1, 2, 4 and 6 μm . The fluid pressure difference between the two sides is $\Delta P = 0.01$ MPa and the fluid viscosity $\mu = 10^{-3}$ Ns/m² (water).

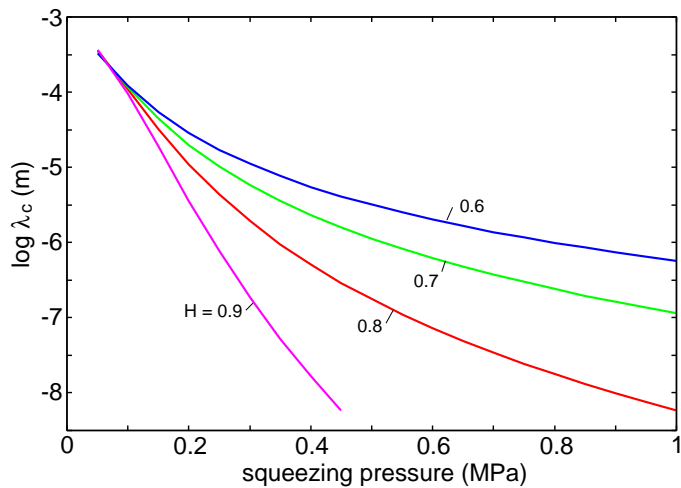


Figure 6.7: The lateral size $\lambda_c = \lambda(\zeta_c)$ of the critical constriction of the percolation channel, as a function of the applied normal (or squeezing) pressure P_0 . Results are shown for self affine fractal surfaces with the root-mean-square roughness (rms) 2 μm and for the Hurst exponent $H = 0.9, 0.8, 0.7$ and 0.6.

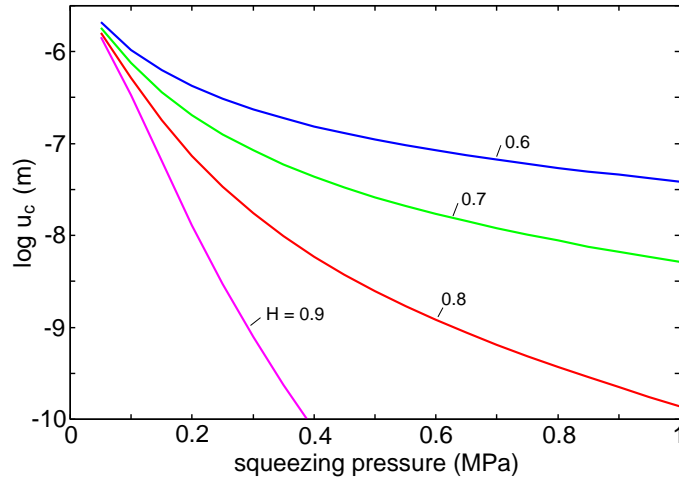


Figure 6.8: The interfacial separation $u_c = u_1(\zeta_c)$ at the critical constriction of the percolation channel, as a function of the applied normal (or squeezing) pressure P_0 . Results are shown for self affine fractal surfaces with the root-mean-square roughness (rms) $2 \mu\text{m}$ and for the Hurst exponents $H = 0.9, 0.8, 0.7$ and 0.6 .

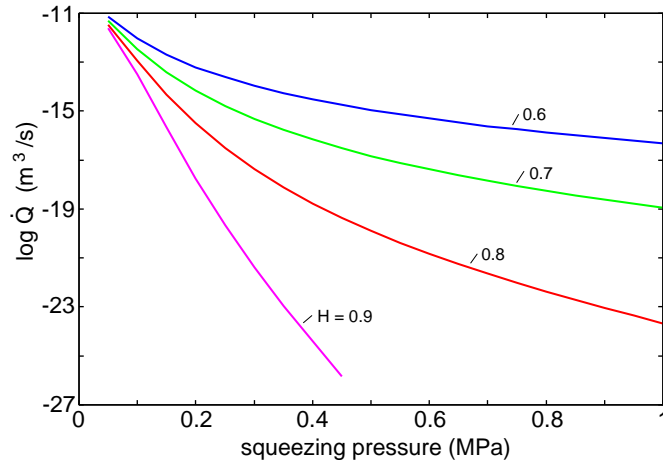


Figure 6.9: The volume per unit time, \dot{Q} , of fluid leaking through the seal as a function of the applied normal (or squeezing) pressure P_0 . Results are shown for self affine fractal surfaces with the root-mean-square roughness (rms) $2 \mu\text{m}$ and for the Hurst exponent $H = 0.9, 0.8, 0.7$ and 0.6 . The fluid pressure difference between the two sides is $\Delta P = 0.01 \text{ MPa}$ and the fluid viscosity $\mu = 10^{-3} \text{ Ns/m}^2$ (water).

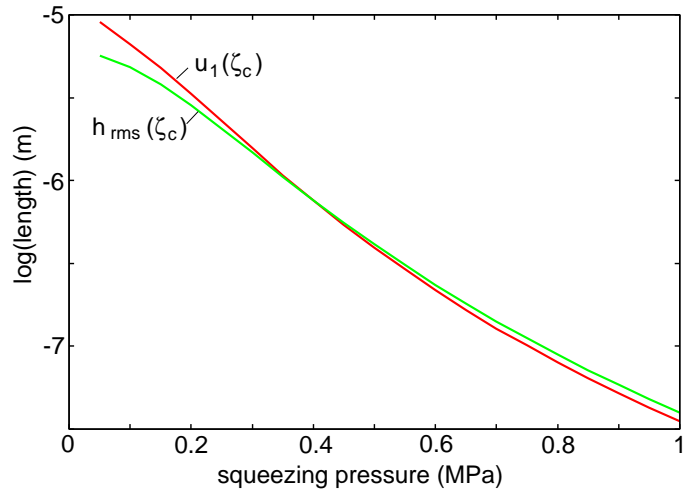


Figure 6.10: The interfacial separation $u_c = u_1(\zeta_c)$ and the rms-roughness $h_{\text{rms}}(\zeta_c)$ in the critical constriction of the percolation channel, as a function of the applied normal (or squeezing) pressure P_0 . Results are shown for self-affine fractal surfaces with the Hurst exponent $H = 0.8$ (or fractal dimension $D_f = 2.2$), and with the root-mean-square roughness (rms) $6 \mu\text{m}$.

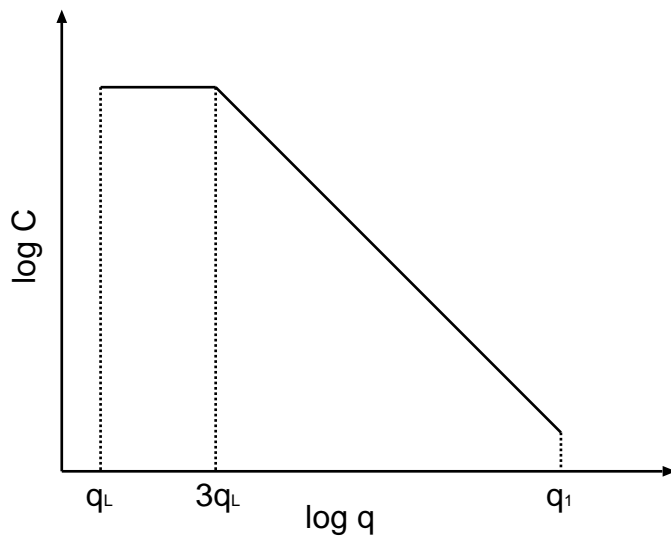


Figure 6.11: Surface roughness power spectrum of a surface which is self-affine fractal for $q_1 > q > 3q_L$. The slope $\log C - \log q$ relation for $q > 3q_L$ determines the fractal exponent of the surface. The lateral size L of the surface determines the smallest wave-vector $q_L = 2\pi/L$.

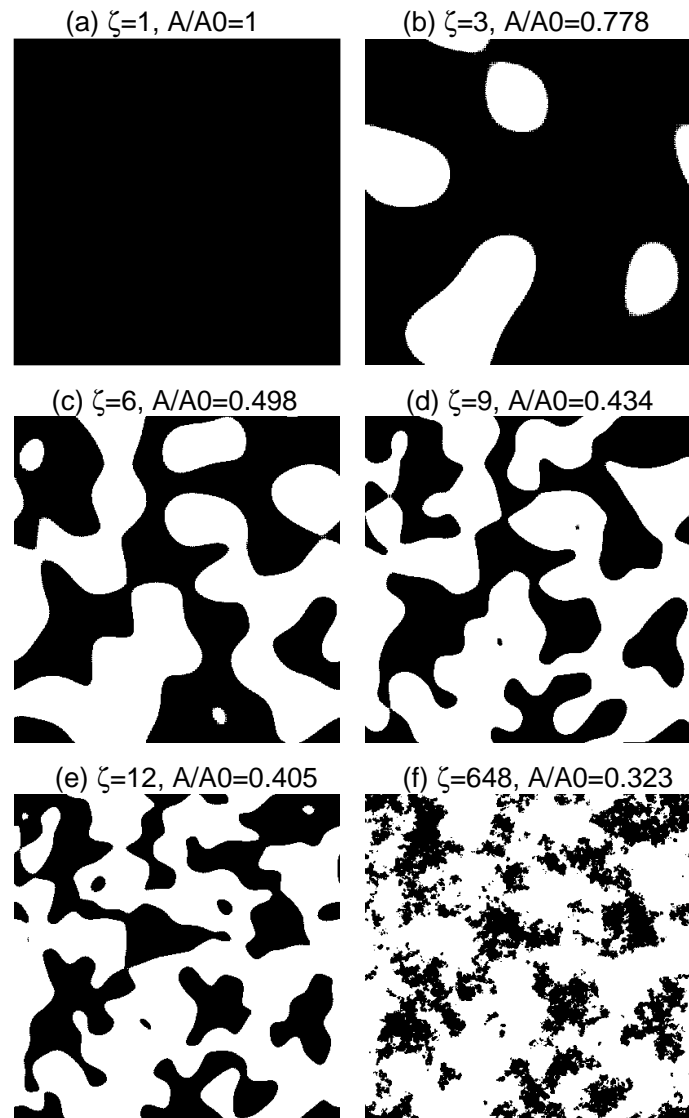


Figure 6.12: The contact regions at different magnifications $\zeta = 1, 3, 6, 9, 12, 648$, are shown in (a)-(f) respectively. The pressure is $p \approx 4.1$ GPa. When the magnification is increased from 9 to 12, the non-contact region percolate.

For self-affine fractal surfaces, the power spectrum has power-law behavior $C(q) \sim q^{-2(H+1)}$, where the Hurst exponent H is related to fractal dimension D_f of the surface via $H = 3 - D_f$. For real surfaces this relation holds only for a finite wave vector region $q_1 < q < q_0$, where $q_1 = 2\pi/b$, q_0 is roll-off wave-vector $q_0 = 3q_L$ (see Fig. 6.11). The randomly rough surfaces have been generated as described in Ref. [1,6], which have root-mean-square roughness $h_{rms} = 10 \text{ \AA}$ and fractal dimension $D_f = 2.2$. The roll-off wave-vector $q_0 = 3q_L$, where $q_L = 2\pi/L$ and $L = 1040 \text{ \AA}$. In this section I define the magnification $\zeta = q/q_L$.

The atoms at the interface between block and substrate interact with repulsive potential $U(r) = \epsilon(r_0/r)^{12}$, where r is the distance between a pair of atoms, $r_0 = 3.28 \text{ \AA}$ and $\epsilon = 74.4 \text{ meV}$. In molecular dynamics simulations there is no unique definition of contact (see Ref. [6]). Here the critical distance d_c has been used to define contact. If the separation between two atoms is smaller than d_c , it has been denoted as contact, otherwise non-contact. Here $d_c = 4.36 \text{ \AA}$.

Fig. 6.12 shows the block-substrate contact region at different magnifications $\zeta = 1, 3, 6, 9, 12, 648$. Note that when the magnification is increased from 9 to 12, the non-contact region percolates. The percolation occurs when the normalized projected contact area $A/A_0 \approx 0.4$, in good agreement with percolation theory [71].

6.4 Improved analytical description

In Sec. 6.2 we have assumed that all the fluid flow occurs through a single constriction referred to as the critical constriction. In reality, fluid flow will also occur in other flow channels even if they have more narrow constrictions. In this section let us assume that there are a finite concentration of critical or near critical constrictions, which correspond to all constrictions which appear when the magnification changes in some narrow interval around the critical value ζ_c , e.g., in such a way that $A(\zeta)/A_0$ changes by, say, ± 0.03 . Since it is very close to the percolation threshold, assumption has been made that the size of all the (nearly critical) constrictions remains the same. In a more accurate treatment one would instead introduce a distribution of sizes of constrictions. In Fig. 6.13(a) the dots correspond to the critical or near critical constrictions along percolation channels (solid lines). One expects the (nearly critical) constrictions to be nearly randomly distributed in the apparent contact area, and that the channels, of which they are part, to have all possible directions as indicated by the lines in Fig. 6.13(a). Here let us consider a simplified version of (a) where the (nearly critical) constrictions form a more ordered arrangement as in Fig. 6.13(b). In reality, the dots and the lines should be (nearly) randomly distributed as in 6.13(a), but this is likely to have only minor effects on what follows.

On the average fluid will only flow in the x -direction. Thus, in a first approximation one may assume that no fluid flows along the (transverse) channels pointing (mainly) in the y -direction in Fig. 6.13(b). Let a be the (average) distance between two nearby critical constrictions. Thus we expect $n = L_x/a$ constrictions along a percolation channel (in the figure $n = 3$). If \dot{Q}_1 denotes the fluid volume per unit time flowing along one percolation channel, then one has

$$\dot{Q}_1 = M(P_a - P_1) = M(P_1 - P_2) = \dots = M(P_n - P_b). \quad (6.5)$$

From (6.5) one gets

$$\dot{Q}_1 = \frac{M}{n}(P_a - P_b)$$

As expected, the amount of fluid flowing in the channel is reduced when the number of constriction increases. However, there will be roughly L_y/a percolation channels so the

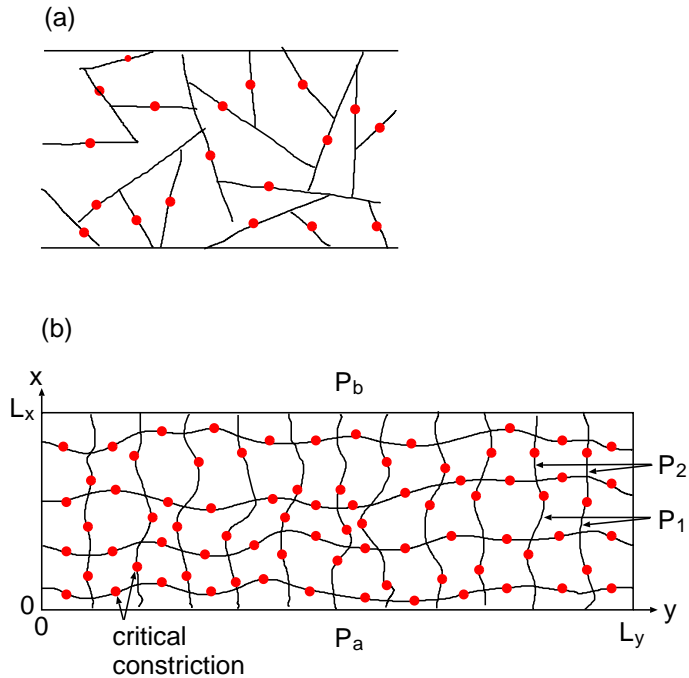


Figure 6.13: The solid lines denote non-contact channels and the dots critical or near critical constrictions. In reality the constrictions and channels are nearly randomly distributed as in (a) [see also Fig. 6.12(e)] but in the model calculation the more ordered structure has been shown in (b).

total fluid flow will be

$$\dot{Q} = \frac{L_y}{L_x} M(P_a - P_b) \quad (6.6)$$

which is identical to the result obtained in Sec. 6.2. This analysis is very rough, and a more detailed analysis will result in some modifications of the leak-rate, but (6.6) should be very useful as a first rough estimate of the leak-rate. Note that the present treatment will result in a more gradual changes in the liquid pressure in the apparent contact region, from the initial high pressure value P_a (entrance side) to the low pressure value P_b (exit side).

6.5 Comparison with experiment

We have not found any results in the literature about leak-rates of seals for well characterized systems. However, we have found some results which are in qualitative agreement with our theory. For example, leak-rates observed for both rubber and steel seals tend to decrease very fast (roughly exponentially) with increasing contact force. Thus, in Ref. [72] the leak-rate for a rubber seal decreased by 6 order of magnitude as the load increased by a factor of 10. A similar sharp drop in the leak-rate with increasing contact force has been observed for seals made from steel [73]. However, in the latter case some plastic deformation is likely to occur in the contact region. In both cases the nominal pressure may change less than the change in the load, due to an increase in the nominal contact area with increasing load. A detailed analysis of the experimental data is not possible as the surface topography was not studied in detail. In Sec. 6.8 a simple experiment has been proposed which can be used to test the theory.

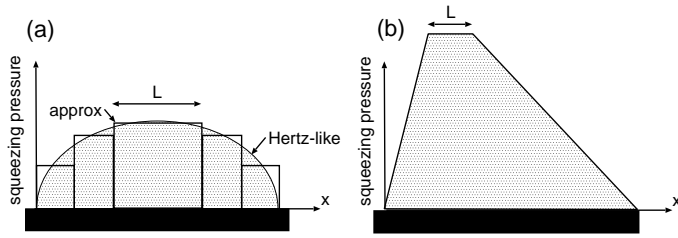


Figure 6.14: Nominal contact pressure distribution $P_0(x)$ (curve bounding the dotted area) for (a) O-ring seal and (b) lip seal. In (a) the curve denoted by “approx” is an approximation to the continuous Hertz-like curve.

The present theory implies that most of the fluid leakage occurs through the critical or nearly critical constrictions in the percolating channels at the interface between the two solids. Since the constrictions are very small they can be easily clogged up by dirt particles in the fluid. This results in leak-rates which decreases with increasing time as the microscopic gaps get clogged up. This has recently been observed for metal seals [73]. In fact, by using specially prepared fluids with immersed particles having a narrow distribution of particle diameters, it should be possible to determine (approximately) the size (or rather the height) of the critical constriction.

6.6 Comment on the role of non-uniform pressure, rubber viscoelasticity and adhesion

In the study above assumption has been made that the normal (squeezing) pressure is constant in the nominal rubber-countersurface contact region. In reality, this is (almost) never the case. Thus, in rubber O-ring applications one expects a pressure distribution which is Herzian-like, as indicated in Fig. 6.14(a). In (dynamical) rubber seals for linear reciprocal motion, the pressure distribution is asymmetric, with a much steeper increase in the pressure when going from the high-pressure (P_a) fluid side towards the center of the seal, as compared going from the low-pressure (P_b) fluid side toward the center of the seal, see Fig. 6.14(b). (The reason for this asymmetry does not interest us here.) The theory developed above can be applied approximately to these cases too. Thus in case (a) (e.g., rubber O-ring seals) one may approximate the actual Herzian-like pressure profile with a sum of step functions as indicated in Fig. 6.14(a). Since the seal-action is so strongly dependent on the squeezing pressure (see Figs. 6.6 and 6.9), it is enough to include the central step region (with width L) in the analysis. Since there is no unique way to determine the width L there will be some (small) uncertainty in the analysis, but this is not important in most practical cases. Similarly, for the lip-seal [Fig. 6.14(b)] during stationary condition it is enough to include the region (width L) where the normal pressure is maximal.

In the study above assumption has been made that the rubber behaves as a purely elastic solid. In reality, rubber-materials are viscoelastic. One consequence of this is stress relaxation. For example, after a rubber O-ring has been deformed to fit into the “cavity” where it is placed, the stress exerted on the solid walls will decrease with increasing time. Since rubber materials have a very wide distribution of relaxation times, the stress can

continue to decrease even one year after installation. Thus, after very long time the pressure in the rubber-countersurface contact region may be so low that the seal fails (note: we found earlier that the leak-rate depends extremely sensitively on the normal pressure). Stress relaxation can be easily taken into account in the analysis above by using the relaxation modulus $E(t)$ (where t is time) measured in the laboratory using standard methods.

Now let us comment on the role of adhesion in rubber seals. Note that if the fluid is an oil, the effective adhesion between the rubber and the hard countersurface may vanish or nearly vanish, as observed in some experiments [74]. If the fluid is not an oil (e.g., water) some effective adhesive interaction may remain. In particular, if the fluid is a gas then the effective adhesion may be similar to that in the normal atmosphere. However, even in this case the adhesive interaction between the solids may have a negligible influence on the leak-rate. The reason for this is that adhesion mainly operates at very short length scales, corresponding to high magnification $\zeta > \zeta_{\text{ad}}$, while the leak-rate is mainly determined by the contact mechanics at the point where the first percolation channel appears, corresponding to the magnification ζ_c . If $\zeta_c \ll \zeta_{\text{ad}}$ the adhesive interaction will have a negligible influence on the leak-rate. This is illustrated in Fig. 6.15 by a numerical calculation with the theory of Ref. [4].

Fig. 6.15 shows the relative contact area $A(\zeta)/A_0$ as a function of the logarithm of the magnification ζ . Note that at the magnification ζ_c , where the non-contact area first percolates, the adhesional interaction has no influence on the contact area. The adhesional interaction will manifest itself only for $\zeta > \zeta_{\text{ad}}$, where the adhesional interaction increases the contact area as compared to the case without the adhesional interaction included. The results in Fig. 6.15 is for rubber block in contact with a hard solid with a self-affine fractal surface with the root-mean-square roughness $h_{\text{rms}} = 6 \mu\text{m}$, the Hurst exponent $H = 0.8$, and for the squeezing pressure $P_0 = 0.2 \text{ MPa}$.

Finally I note that if there is very little fluid at the interface strong capillary adhesion may occur between the surfaces. This is known to be of great importance in, e.g., the context of rubber wiper blades. This topic has been discussed in detail in Ref. [75, 76]

6.7 Dynamical seals

The theory presented above is for static seals. Here we give some comments related to dynamical seals [77]. The leak-rate for linear reciprocal seals at very low sliding velocity has been estimated. Assumption has been made that the roughness mainly occurs on the rubber surface and the hard countersurface has been treated as perfectly flat. Thus, as the rubber slides along the countersurface the contact mechanics does not change, e.g., the percolation channel will be time-independent in the reference frame moving with the rubber. Consider the system in the reference frame where the rubber is stationary while the hard countersurface moves from left to right with the velocity v_0 . The rubber is assumed to be below the countersurface, see Fig. 6.16. The high pressure fluid region (pressure P_a) occupies $x < 0$ while the low pressure region (pressure P_b) occupies $x > L$.

Assume a Newtonian fluid and stationary and laminar flow. The basic equations for the fluid flow are

$$\nabla p = \eta \nabla^2 \mathbf{v}, \quad \nabla \cdot \mathbf{v} = 0,$$

where $p(\mathbf{x})$ and $\mathbf{v}(\mathbf{x})$ are the fluid pressure and the fluid flow velocity, respectively. Now consider the fluid flows in the percolation channel. Let s be the length-coordinate along the percolation channel. Since in general the $\lambda(s) \gg u(s)$, where $\lambda(s)$ is the width and $u(s)$ the height of the channel at the point s along the channel, one can write the velocity

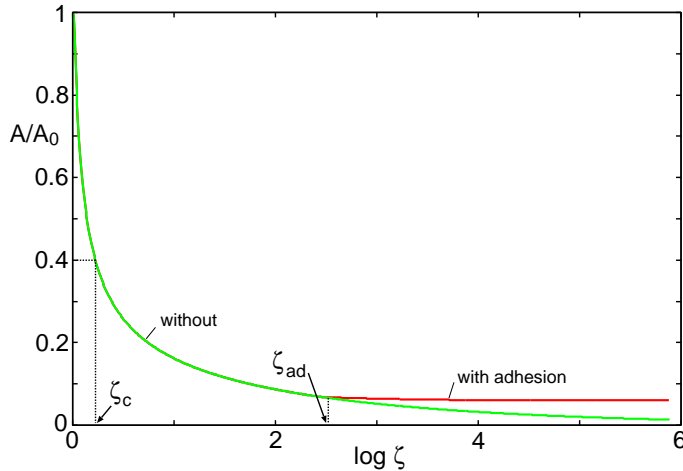


Figure 6.15: The relative contact area $A(\zeta)/A_0$ as a function of the logarithm of the magnification ζ . Note that at the magnification ζ_c , where the non-contact area first percolate, the adhesional interaction has no influence on the contact area. The adhesional interaction will manifest itself only for $\zeta > \zeta_{ad}$, where the adhesional interaction increases the contact area as compared to the case without the adhesional interaction included. For rubber block in contact with a hard solid with a self-affine fractal surface with the root-mean-square roughness $h_{rms} = 6 \mu\text{m}$, the Hurst exponent $H = 0.8$. The squeezing pressure $P_0 = 0.2 \text{ MPa}$ and, for the curve “with adhesion”, with the interfacial binding energy per unit area $\Delta\gamma = 0.05 \text{ J/m}^2$.

as $\mathbf{v}(\mathbf{x}) = \hat{s}v(s, z)$ where

$$v(s, z) \approx \frac{1}{2\eta} \frac{dp}{ds} z(z - u(s)) + v_0 \hat{x} \cdot \hat{s} \frac{z}{u(s)}$$

The volume flow per unit time through any cross section of the channel is assumed to be the same, and equal to \dot{Q} which gives

$$\begin{aligned} \dot{Q} &= \lambda(s) \int_0^{u(s)} dz v(s) = \\ &\lambda(s) \left(-\frac{u^3(s)}{12\eta} \frac{dp}{ds} + v_0 \hat{x} \cdot \hat{s} \frac{u(s)}{2} \right) \end{aligned}$$

or

$$\frac{dp}{ds} = \frac{6\eta}{u^2(s)} v_0 \hat{x} \cdot \hat{s} - \frac{12\eta \dot{Q}}{\lambda(s) u^3(s)}$$

Integrating this equation gives

$$p(l_a) = P_a + \int_0^{l_a} ds \left[\frac{6\eta}{u^2(s)} v_0 \hat{x} \cdot \hat{s} - \frac{12\eta \dot{Q}}{\lambda(s) u^3(s)} \right] \quad (6.7)$$

where l_a is the length of the percolation channel. Let $\tilde{P}(u)$ be the probability to find the surfaces separated by the height u along the percolation channel. Note that $\lambda(s)$ also can (at least locally) be considered as a function of u , which is denoted by $\lambda(u)$ for simplicity. Thus one can write (6.7) as

$$p(l_a) = P_a + 6L_a \eta v_0 \int_{u_c}^{\infty} du \frac{\tilde{P}(u)}{u^2} - 12l_a \eta \dot{Q} \int_{u_c}^{\infty} du \frac{\tilde{P}(u)}{\lambda(u)u^3} \quad (6.8)$$

where L_a is the length of the percolation path projected on the x -axis. In Ref. [61] we have shown how it is possible to calculate the distribution \bar{P}_u of heights u between two surfaces in elastic contact. Let us assume that (note: $u > u_c$)

$$\tilde{P}(u) \approx \frac{\bar{P}_u}{\int_{u_c}^{\infty} du' \bar{P}_{u'}}$$

Let us write (6.8) as

$$p(l_a) = P'_a = P_a + B_a v_0 - C_a \dot{Q} \quad (6.9)$$

where

$$B_a = 6L_a \eta \int_{u_c}^{\infty} du \frac{\tilde{P}(u)}{u^2} \quad (6.10)$$

and

$$C_a = 12l_a \eta \int_{u_c}^{\infty} du \frac{\tilde{P}(u)}{\lambda(u)u^3} \quad (6.11)$$

Similarly, one gets¹

$$p(l_b) = P'_b = P_b - B_b v_0 - C_b \dot{Q} \quad (6.12)$$

Thus in this case (6.1) takes the form

$$\begin{aligned} \dot{Q} &= M(P'_a - P'_b) = \\ &M(P_a - P_b) + M(B_a + B_b)v_0 - M(C_a - C_b)\dot{Q} \end{aligned}$$

or

$$\dot{Q} = M \frac{\Delta P + (B_a + B_b)v_0}{1 - M(C_a - C_b)} \quad (6.13)$$

The factor $M(C_a - C_b)$ in the denominator of this expression is independent of v_0 and assumption has been made that it is negligible compared to unity, and neglect it. One interesting application of (6.13) is to wiper blade. Here $\Delta P = 0$ so that (6.13) takes the form

$$\dot{Q} = M(B_a + B_b)v_0 \quad (6.14)$$

Substituting (6.2) and (6.10) (and a similar expression for B_b) in (6.14) gives

¹ Assume that no cavitation occurs at the exit of the critical constriction. Cavitation may occur if the local pressure at the exit of the critical constriction is negative, but in this chapter let us assume so low sliding velocity v_0 that this is not the case. If cavitation occurs $p(l_b) \approx 0$, or, more accurately, $p(l_b)$ is equal or close to the vapor pressure of the fluid or of gases dissolved in the fluid. Note that the transition from boundary or mixed lubrication to hydrodynamic lubrication probably involves cavitation at the exit of many narrow constrictions, since otherwise the total load supported by the fluid film will be very small. It would be very interesting to study this problem theoretically, since the transition from boundary lubrication to hydrodynamic lubrication is not well understood.

$$\dot{Q} = L_y u_c^3 v_0 \frac{\alpha}{2} \int_{u_c}^{\infty} du \frac{\tilde{P}(u)}{u^2} \quad (6.15)$$

where the extra factor L_y/L_x has been included to take into account the number of square seal units. During the time t the leak-volume is $\dot{Q}t$. Define the average thickness d of the leak-film as $d = \dot{Q}t/(L_y v_0 t)$. From (6.15) one gets

$$d = \beta u_c \quad (6.16)$$

$$\beta = \frac{\alpha}{2} \int_{u_c}^{\infty} du u_c^2 \frac{\tilde{P}(u)}{u^2} \quad (6.17)$$

The integral I in β has been calculated for some typical cases², and found that $I \approx 0.1 - 0.2$ so we expect $\beta \approx 0.1$.

In the treatment above assumption has been made that the contact between the rubber and the hard countersurface does not depend on the pressure in the fluid, which is a good approximation as long as the fluid pressure $p(\mathbf{x}) \ll P_0$. However, as the sliding velocity increases, the fluid pressure in some regions at the interface will increase which will tend to increase the separation between the two surfaces. At very high sliding velocity, hydrodynamic lubrication will prevail and the surfaces are completely separated by a thin fluid film. However, even at much lower sliding velocity the hydrodynamic pressure buildup may strongly increase the leak rate. In particular, the pressure at the critical constriction will tend to increase the separation between the surfaces and hence increase the leak-rate. We will not study this effect here but just estimate when this effect becomes important. Let p_c be the pressure at the critical constriction. If p_c acts over the area λ_c^2 it will locally increase the separation between the surfaces by the amount³ $\Delta u \approx \lambda_c p_c/E$. Thus, the pressure at the critical constriction must be much smaller than $E u_c / \lambda_c$ in order for the pressure-induced effect to be negligible. Note that

$$p_c \approx 6L\eta v_0 \int_{u_c}^{\infty} du \frac{\tilde{P}(u)}{u^2}$$

so the present study is limited to sliding velocities

$$v_0 \ll \frac{E u_c^3}{6L\eta\lambda_c} \left(\int_{u_c}^{\infty} du u_c^2 \frac{\tilde{P}(u)}{u^2} \right)^{-1} \approx \frac{E u_c^3}{L\eta\lambda_c} \quad (6.18)$$

where the integral typically is of order ~ 0.15 . Thus, for example, if in a wiper blade application, after some use the rubber blades typically develop (because of wear) a surface roughness with a rms amplitude of several micrometer. If the rms roughness is $2 \mu\text{m}$ (and the Hurst exponent $H = 0.8$), the nominal pressure $\sim 0.2 \text{ MPa}$, and if $E \approx 10 \text{ MPa}$ one gets from Fig. 6.5 and 6.4 $u_c \approx 0.1 \mu\text{m}$ and $\lambda_c \approx 10 \mu\text{m}$. If $L \approx 0.1 \text{ mm}$ and (for water) $\eta \approx 10^{-3} \text{ Pa} \cdot \text{s}$ we get that the slip velocity must be at most $\sim 1 \text{ cm/s}$ in order for (6.18) to be valid. According to (6.16) the (average) film thickness of the water layer would be of order $0.01 \mu\text{m}$.

²Two calculations have been done: For a self affine fractal surface with the rms roughness of $h_{\text{rms}} = 2 \mu\text{m}$ and the squeezing pressure $P_0 = 0.18 \text{ MPa}$ we got $B \approx 0.11$ (and $u_c \approx 0.1 \mu\text{m}$ and $\lambda_c \approx 16 \mu\text{m}$) and for $h_{\text{rms}} = 4 \mu\text{m}$ and $P_0 = 0.2 \text{ MPa}$ we got $B \approx 0.21$ (and $u_c \approx 1 \mu\text{m}$ and $\lambda_c \approx 109 \mu\text{m}$).

³The fluid pressure along the percolation channel increases towards the critical constriction. Thus, the elastic deformation of the rubber at the critical constriction is determined not just by the pressure at the constriction but also by the pressure acting on the rubber along the percolation path. If one assumes a strait percolation path and that the pressure along the percolation path $p(x) = p_c x/L$ then one can easily show that $\Delta u \approx \ln(L/\lambda_c) \lambda_c p_c / E$ but the additional logarithmic factor is never very large and does not change our qualitative conclusion.

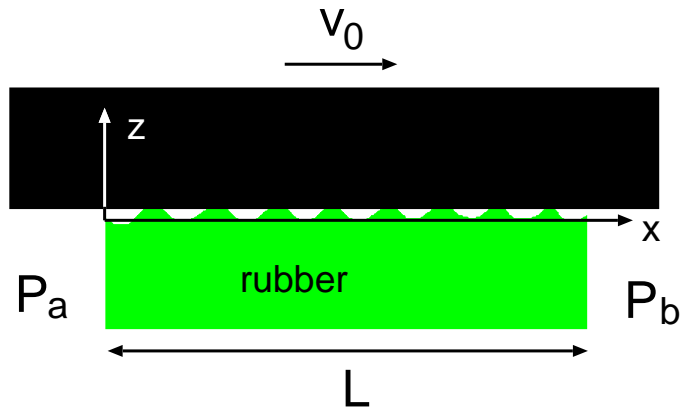


Figure 6.16: A rubber block with a rough surface in contact with a hard smooth counter-surface (upper block) which moves relative to the rubber block with the velocity v_0 .

6.8 A new experiment

Very few studies of leak rates of seals with well characterized surfaces have been published. Here let us suggest a very simple experiment which could be used to test the theory presented in Sec. 6.2. A set-up for measuring the leak-rate of seals has been shown in Fig. 6.17. A glass (or PMMA) cylinder with a rubber ring (with rectangular cross-section) glued to one end is squeezed against a hard substrate with well-defined surface roughness. The cylinder is filled with a fluid, e.g., water, and the leak-rate of the fluid at the rubber-countersurface is detected by the change in the height of the fluid in the cylinder. In this case the pressure difference $\Delta P = P_a - P_b = \rho g H$, where g is the gravitation constant, ρ the fluid density and H the height of the fluid column. With $H \approx 1$ m we get typically $\Delta P \approx 0.01$ MPa. With the diameter of the glass cylinder of order a few cm, the condition $P_0 \gg \Delta P$ (which is necessary in order to be able to neglect the influence on the contact mechanics from the fluid pressure at the rubber-countersurface) is satisfied already for loads (at the upper surface of the cylinder) of order kg.

6.9 Summary

A theory of the leak-rate of seals, based on percolation theory and a recently developed contact mechanics theory, has been presented. Both static and dynamics seals have been studied. Numerical results are presented for the leak-rate \dot{Q} , and for the lateral size λ_c and the height u_c of the critical constriction. Results with self-affine fractal surfaces are presented on how \dot{Q} , λ_c and u_c depend on the root-mean-square roughness amplitude and the fractal dimension $D_f = 3 - H$ (where H is the Hurst exponent), and on the squeezing pressure P_0 with which the rubber is squeezed against the rough countersurface.

I have also presented molecular dynamics results which show that when two elastic solids with randomly rough surfaces are squeezed together, as a function of increasing magnification or decreasing squeezing pressure, a non-contact channel will percolate when relative projected contact area, A/A_0 , is about 0.4, in accordance with percolation theory. Finally, a simple experiment has been suggested which can be used to test the theory.

The theory presented in this chapter is very rough, but I believe that it captures the most important physics, and that the presented approach can be improved and extended in various ways.

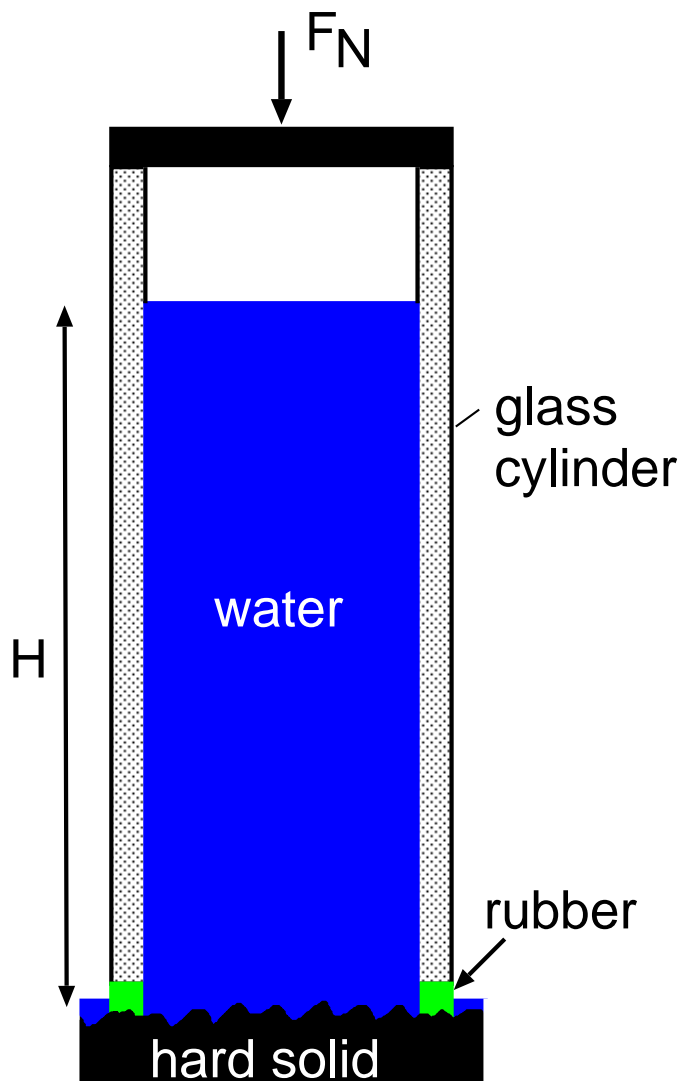


Figure 6.17: A simple experimental set-up for measuring the leak-rate of seals. A glass (or PMMA) cylinder with a rubber ring glued to one end is squeezed against a hard substrate with well-defined surface roughness. The cylinder is filled with a fluid, e.g., water, and the leak-rate of the fluid at the rubber-countersurface is detected by the change in the height of the fluid in the cylinder. In this case the pressure difference $\Delta P = P_a - P_b = \rho g H$, where g is the gravitation constant, ρ the fluid density and H the height of the fluid column. With $H \approx 1$ m we get typically $\Delta P \approx 0.01$ MPa.

Acknowledgments: I thank Ed Widder (Federal Mogul Sealing Systems) and Matthias Schmidt (IFAS, RWTH Aachen University) for useful correspondence related to seals.

Chapter 7

How do Liquids Confined at the Nanoscale Influence Adhesion?

Liquids play an important role in adhesion and sliding friction. They behave as lubricants in human bodies especially in the joints. However, in many biological attachment systems they act like adhesives, e.g. facilitating insects to move on ceilings or vertical walls. In this chapter I will use molecular dynamics to study how liquids confined at the nanoscale influence the adhesion between solid bodies with smooth and rough surfaces. It turns out that a monolayer of liquid may strongly affect the adhesion.

7.1 Motivation

Knowing the behavior of liquids confined to small volumes between contacting surfaces is essential for the understanding a vast array of common problems in science, such as biological interactions [2, 78, 79], crack propagation [80], molecular tribology and adhesion [9, 42, 81, 82]. Ultra-thin confined films can have two completely opposite effects. On one hand, the confined liquid may behave like a lubricant to reduce adhesion and friction. For instance, when bones meet at a joint, they need a liquid in-between to prevent scraping against each other. The liquid is called a synovial liquid [83], which is made mainly of water and water-based long chain polymers. Many internal organs in humans and other animals are separated by thin lubricant films. Examples include the cerebrospinal liquid in the brain [84], the pleural liquid in lungs [85] and water based liquid in eyes. On the other hand, in some applications liquids behave like adhesives, e.g. in some biological attachment systems. Thus, for example, insects can secret a liquid to enhance adhesion in order to walk on ceilings or vertical walls [78]. Geckos can also walk on the ceilings due to their hierarchical hair structure which makes their adhesion pads elastically soft on all relevant length scales [18]. Recently scientists found that water monolayer-films, which always occur on hydrophilic (water-loving) surfaces in the normal atmosphere, enhance Gecko adhesion [86, 87] to hydrophilic surfaces.

The influence of thin liquid layers on the effective adhesion between solids is well-known to most of us from our every-day experience, e.g., when separating two (slightly wet) microscopy cover glass surfaces, or two gauge blocks (steel blocks with very smooth surfaces). At the micro or nano-scale the increased adhesion resulting from the formation of water capillary bridges is one of the most severe problem in the production of micro-electro-mechanical systems (MEMS) [88]. In general, wetting liquids tend to increase the adhesion between solids with surface roughness, but at present it is not known exactly for which liquid coverage the pull-off force is maximal [42, 89]. There are also many unsolved

questions related to the influence of liquids on adhesion in biological systems, e.g., how is it possible for a Gecko to move on a vertical stone wall during raining, and how do cells (in liquids) adhere to solids walls?

In this chapter I show that small amounts of confined liquid between smooth and randomly rough surfaces can influence adhesion. Using liquids that interact weakly and strongly with the walls (hydrophobic [90] and hydrophilic walls), I demonstrate that sometimes the liquid acts like a lubricant, as in some biological systems, such as in the eyes, and sometimes it behaves like a glue, as the insects' secretions when they walk on ceilings or vertical walls.

7.2 Preparing the initial configuration

Consider an elastic block approaching a hard substrate covered with alkane molecules. The surfaces of the two walls are described as a square grid of atoms, with lattice constants $a = 2.6 \text{ \AA}$ for the elastic block and $b = 1.6 \text{ \AA}$ for the rigid substrate. The difference in the lattice constant is to avoid the pinning due to a perfect match of the crystal structures. A recently developed Multiscale Molecular Dynamics [6] description let us properly describe the elastic response of the block without simulating too many atoms in the bulk. The Young modulus of the block is $E = 100 \text{ GPa}$ and the Poisson ratio is $\nu = 0.3$.

Both atomically flat and rough substrates have been studied. The profile of the rough substrate is self affine fractal with root-mean-square (rms) amplitude 3 \AA and fractal dimension $D_f = 2.2$; it is prepared following the recipe in Refs. [1, 6].

The liquid between the walls is octane C_8H_{18} and the simulations are carried out at room temperature, $T = 300 \text{ K}$, well above the melting point of octane $T_m = 216 \text{ K}$. The octane molecules are treated with the United Atom model: every molecule comprises 8 particles corresponding to the groups CH_2 and CH_3 . The Optimized Potential for Liquid Simulation (OPLS) [26, 27] is employed. The atoms of the two walls interact through the Lennard-Jones potential, with parameters $\sigma = 3.28 \text{ \AA}$ and $\epsilon = 40 \text{ meV}$. The interaction between the walls' atoms and the groups CH_2 and CH_3 of the octane molecules are also given by the Lennard-Jones potential with $\sigma = 3.28 \text{ \AA}$, but two different interaction energies are considered: the *strong adsorbate interaction* with $\epsilon = 40 \text{ meV}$, and the *weak adsorbate interaction* with $\epsilon = 5 \text{ meV}$.

7.3 Numerical results

7.3.1 Confined liquid on flat surfaces

In the simulations I first bring the elastic block into contact with the substrate, and then pull up the block slowly until the two surfaces separate. In the process of detachment the interaction between the lubricated walls is attractive, and the adhesive force reaches a maximum at a given distance, which depends on the amount of liquid, and then it decreases. Fig. 7.1(a) shows the maximum pulling force per unit area (pull-off stress), as a function of liquid coverage θ , for the case of two flat walls. The corresponding distance between the walls when the pulling force is maximum is plotted in figure 7.1(b).

Note that the direct interaction between the block and the substrate is negligible when the surfaces are separated by one adsorbate monolayer. The pull-off stress is maximum for clean and smooth surfaces since there is strong interaction between the wall atoms (Lennard-Jones parameter $\epsilon = 40 \text{ meV}$). The pull-off stress rapidly decreases with increasing amount of liquid between the surfaces. For $\theta < 1$, the boundary line of an island

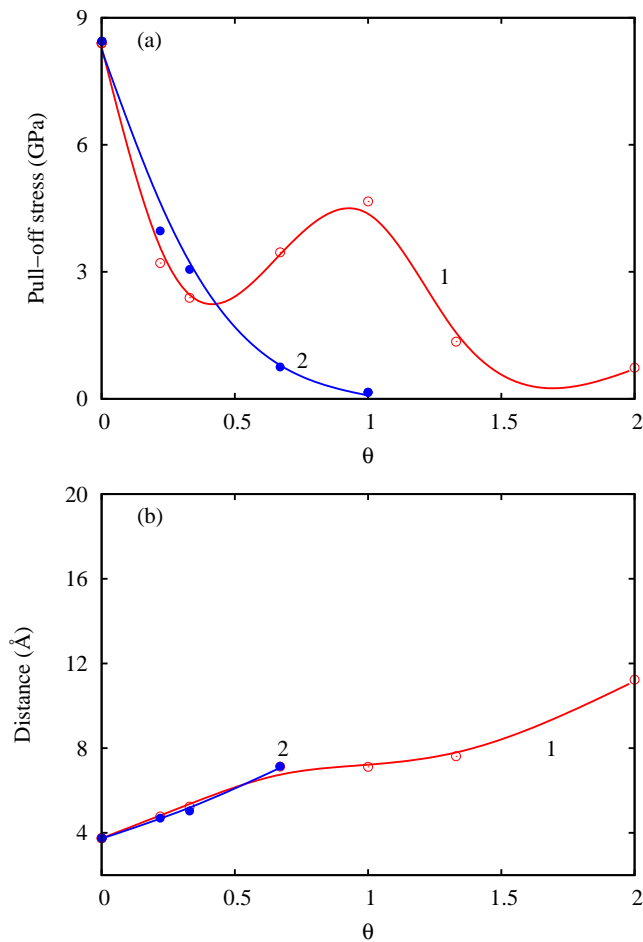


Figure 7.1: Pull-off on a flat substrate for strong adsorbate interaction (curve 1) and for weak adsorbate interaction (curve 2). (a): the maximum pull-off stress as a function of the liquid coverage θ . (b): the separation between the walls where the stress is maximum as a function of θ . Continuous lines: fit with smoothing cubic splines.

of lubricant molecules can be considered as a crack edge, as shown in Fig. 7.2. During pull-off high stress concentration occurs at the crack tip, and the interfacial crack propagation starts at the crack edge, resulting in the strong decrease in the pull-off force observed in the simulations for $\theta < 1$.

Fig. 7.2 shows the side view of the system before and after detachment when the coverage is $\theta = 1/4$. For the strong interaction between liquid and walls [(a) and (b)] not all molecules are trapped in one island. For the weak adsorbate interaction [(c) and (d)] the liquid molecules experience smaller lateral energy barriers, and for $\theta < 1$ they get squeezed into a single large island, thus less elastic energy is stored at the block-substrate interface in this case, resulting, at low liquid coverage, in a (slightly) stronger adhesion (or pull-off force) for the weak adsorbate interaction as compared to the case of strong interaction. This is of course a kinetic effect, and for an infinitely large system the liquid will always form finite clusters, whose size depends on the squeezing procedure. But as a general rule the stronger interaction will give rise to smaller islands, so that for the same preparation the stronger adsorbate interaction will lead to a slightly lower adhesion. Notice that after the detachment of the two walls the liquid sticks all to the substrate: indeed its adhesion energy to the substrate is larger because of the larger substrate atom density compared to that of the upper block.

For the weak adsorbate interaction the pull-off stress decreases monotonically with increasing C_8H_{18} coverage. On the other hand the strong adhesive interaction causes an increase of the pull-off stress up to a maximum for the coverage $\theta = 1$ corresponding to a complete monolayer. The physical reason for this phenomenon is that at $\theta = 1$ the liquid completely covers the atomically smooth surface and no crack-like defects occur at the interface; moreover the stored elastic energy at the interface is minimal. Thus the adhesion reaches a local maximum.

7.3.2 Confined liquid on rough surfaces

For the rough (self-affine fractal) substrate, the pull-off stress as a function of θ is showed in Fig. 7.3. In this case the monolayer coverage corresponds to $\theta \approx 1.3$ i.e., the roughness increases the substrate surface area by about 30%. For the strong adsorbate interaction, the adhesion decreases with increasing liquid coverage up to $\theta \approx 0.2$ due to molecules trapped in the asperity contact regions, which effectively enhances the substrate surface roughness. For $\theta > 0.2$ the pull-off force increases due to the formation of capillary bridges (see Fig. 7.5 (c)). For the weak adsorbate interaction, due to the strong wall-wall interaction and weak liquid-wall interaction, the liquid molecules are squeezed away from the asperity contact regions into the valleys [see Fig. 7.4 (c),(d) and Fig. 7.7], which results in nearly constant pull-off force for $\theta < 1$ (see curve 2 in Fig. 7.3). Due to the hydrophobic interaction between the liquid and the blocks, no capillary bridge forms, and as θ increases beyond 1 the pull-off force decreases towards zero.

For the strong adsorbate interaction the lateral corrugation of the molecule-substrate interaction potential is so high that liquid molecules are trapped in the asperity contact regions. This is illustrated in Fig. 7.4 (a) and (b) (side-view snapshots). The trapped molecules increase the elastic energy stored at the interface and reduce the effective wall-wall binding energy. Thus, for $\theta < 0.67$ the pull-off stress for the strong adsorbate interaction is smaller than that for the weak interaction, as it is shown in Fig. 7.3(a). For the rough substrate with strong adsorbate interaction the pull-off stress reaches a maximum at $\theta \approx 1.3$ (see curve 1 in Fig. 7.3). During pull-off some liquid molecules are pulled out of the valleys (or cavities), and form nano-size capillary bridges in the asperity regions of the rough substrate (see Fig. 7.5), which results in an effective wall-wall interaction

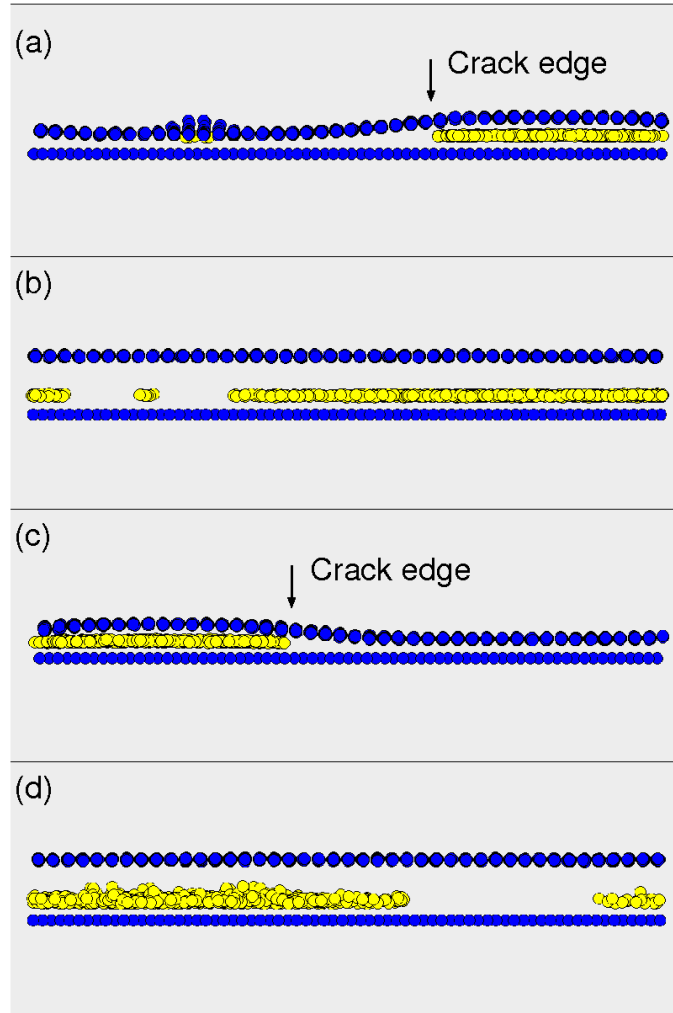


Figure 7.2: Side view of the system with coverage $\theta \approx 1/4$ during the pull-off. The light balls represent the CH_2 and CH_3 groups of the octane molecules. The dark balls are the atoms of the walls' surfaces. (a) Strong adsorbate interaction between the liquid and the walls; the separation happens by crack propagation. (b) After the detachment the block returns to its undeformed state. (c) and (d) during and after the detachment for the case of weak adsorbate interaction. The behavior is the same as in the previous case.

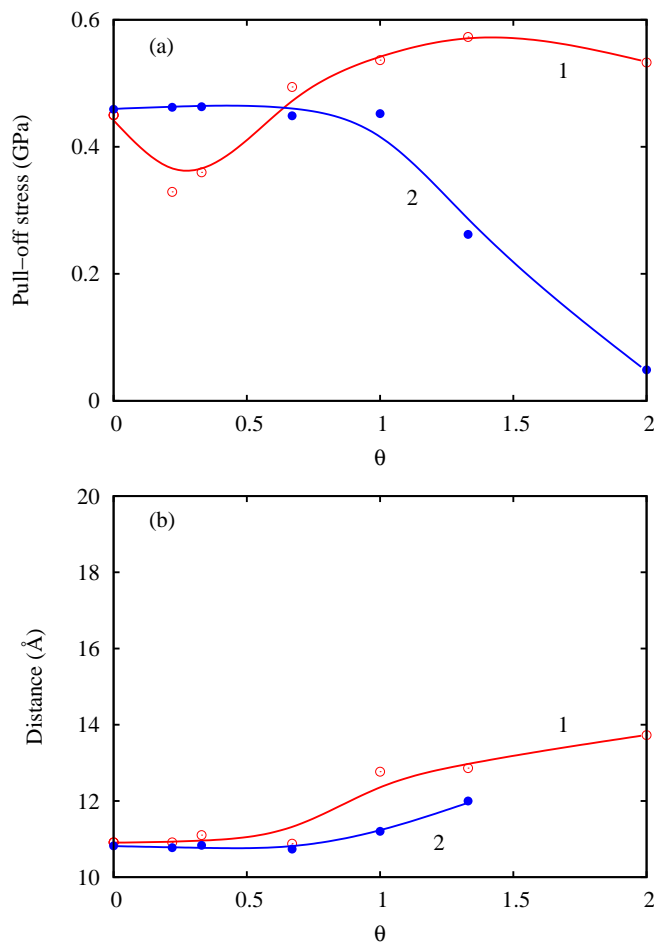


Figure 7.3: Pull-off on a rough substrate for strong adsorbate interaction (curve 1) and for weak adsorbate interaction (curve 2). (a): the maximum pull-off stress as a function of the liquid coverage θ . (b): the walls distance where the stress is maximum as a function of θ . Continuous lines: fit with smoothing cubic splines.

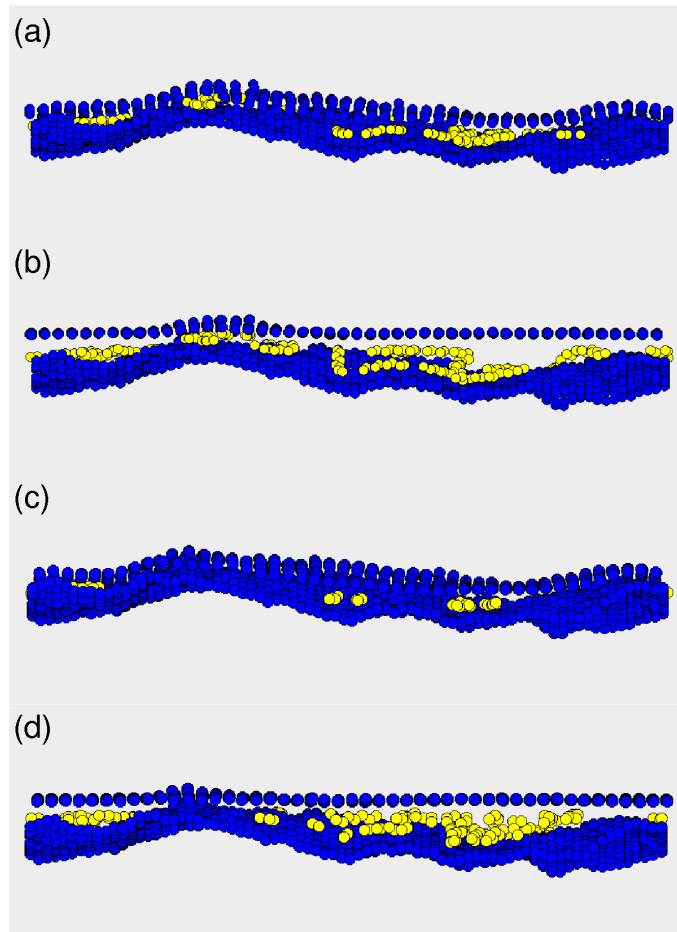


Figure 7.4: Side view of the contact for coverage $\theta = 1/4$ on a rough substrate. The pictures show only the atoms in a 29 Å thick slice including the highest asperity. (a) Strong adsorbate interaction; initial state. (b) Strong adsorbate interaction; maximum pull-off force. (c) Weak adsorbate interaction; initial state. (d) Weak adsorbate interaction; maximum pull-off force.

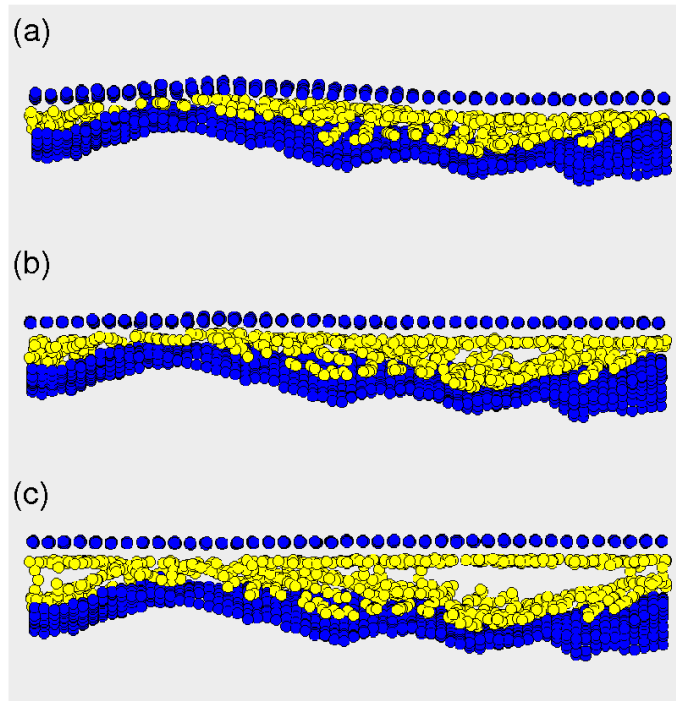


Figure 7.5: Side view of some atoms for the strong interacting adsorbate at coverage $\theta = 1.3$ on a rough substrate, including the highest asperity. The system evolves in time from (a) to (b) and then to (c) during the pulling phase.

which is more long ranged than when the wall-liquid interaction is weak. For the weak adsorbate interaction case (see Fig. 7.6) the liquid does not wet the surface of the block (hydrophobic interaction) and no capillary bridges form, and for $\theta > 1$ the pull-off stress is much smaller than that for the strong adsorbate interaction.

7.4 Contact hysteresis

The force-distance curves for the rough substrate with $\theta \approx 0.25$ and $\theta \approx 1.3$, are shown in Fig. 7.8 and 7.9 respectively, both for the strong (a) and weak (b) adsorbate interaction. Note that for the weak adsorbate interaction there is nearly no hysteresis. For the strong adsorbate interaction large hysteresis is observed, and several abrupt changes in the pressure can be observed during squeezing, which correspond to the squeeze-out of some lubricant molecules from some asperity contact regions.

The breaking of the bonds between two macroscopic solids during pull-off is usually due to interfacial crack propagation, and the macroscopic pull-off *force* is determined by the *energy* (per unit of created surface area) $G(v)$ to propagate the crack at the velocity v , or, equivalently the effective work of adhesion $\gamma_{\text{eff}}(v)$. For very small solid objects the bond-breaking may occur more uniformly over the contact area and the standard picture described above no longer holds (see Ref. [91]). Thus, the results presented in this study may be directly relevant for adhesion involving small (micro- or nano-) sized solid objects, while the pull-off force for macroscopic objects may be more related to the work of adhesion during retraction, which can be obtained from pressure-distance plots such as those presented in Fig. 7.8 and 7.9 but not studied in detail in this chapter.

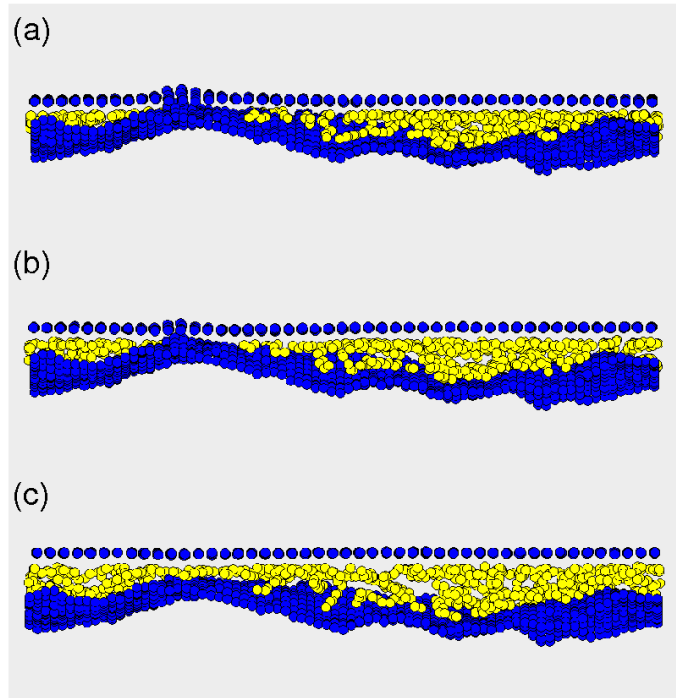


Figure 7.6: Side view of some atoms for the weak interacting adsorbate at coverage $\theta = 1.3$ on a rough substrate, including the highest asperity. The system evolves in time from (a) to (b) and then to (c) during the pulling phase.

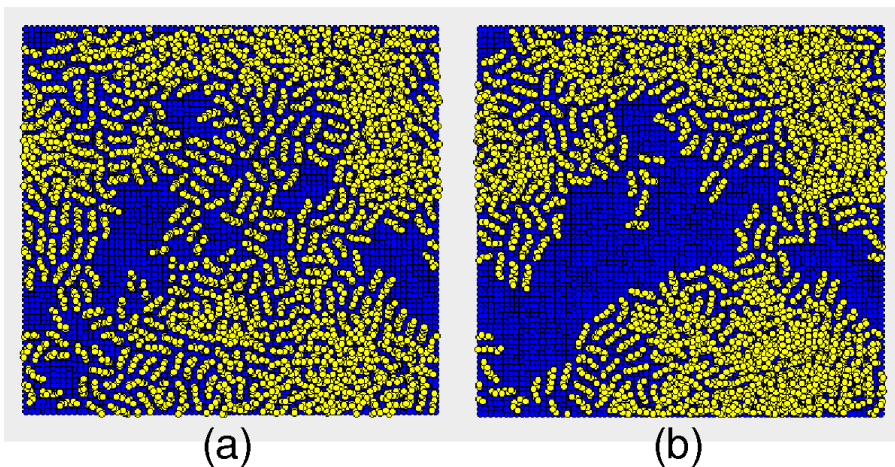


Figure 7.7: Top view snapshots of the liquid on a rough substrate for $\theta \approx 1.3$, with (a) strong interaction and (b) weak interaction between liquid and walls. These images correspond to the side views shown in Fig. 7.5(a) and Fig. 7.6(a) respectively.

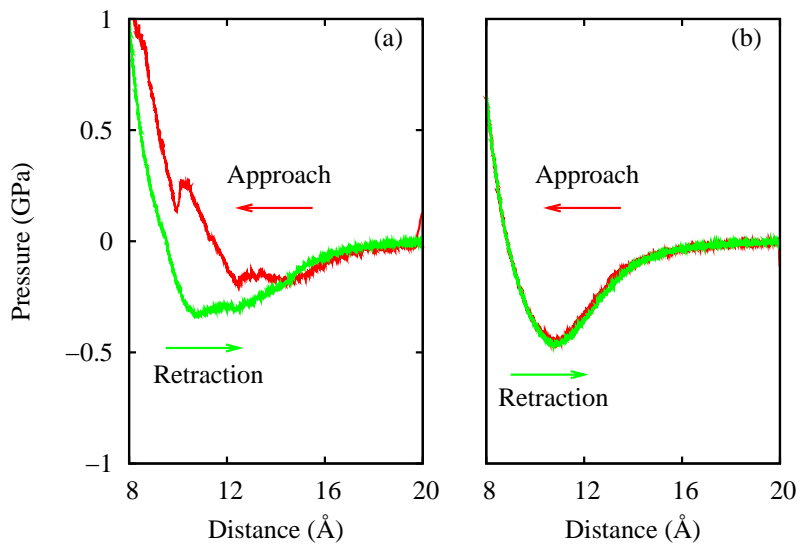


Figure 7.8: The average pressure as a function of the distance between the block and the rough substrate, with $\theta \approx 1/4$ monolayer of C_8H_{18} . (a) Strong interaction. (b) Weak interaction

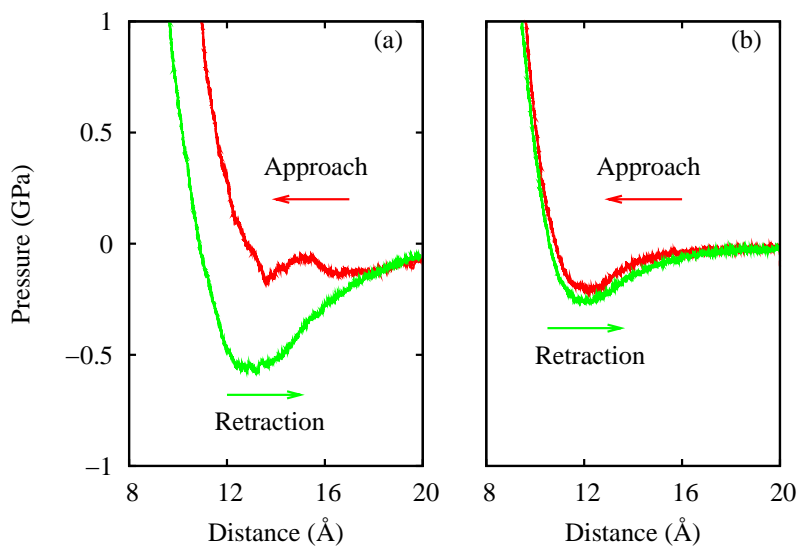


Figure 7.9: Average pressure as a function of the distance between the block and the rough substrate, with $\theta \approx 1.3$ monolayer of C_8H_{18} . (a) Strong interaction. (b) Weak interaction

7.5 Discussion

Very recently Huber et al [86, 87] have studied the influence of humidity on the nanoscale adhesion of individual Gecko spatulae to smooth glass surfaces. The hierarchical gecko foot structure consists of fiber or hair-like structures, and each fiber ends with a ~ 100 nm wide plate-like structure which is only a few nanometer thick at its thinnest place. The plates can easily bend to make contact even to very rough substrates [92]. Huber et al observed that the pull-off force on hydrophilic glass increased monotonically with increasing humidity. At the highest humidity the water film was ~ 0.2 nm thick which corresponds roughly to a water monolayer. This is consistent with our numerical results for rough surfaces and hydrophilic materials, which shows that the pull-off force increases with increasing θ as θ increases from 0.2 to monolayer coverage (see Fig. 7.3). As the glass surface used in the experiments by Huber et al was very smooth, the dominant surface roughness may be that of the bottom surface of the plate-like structure of the spatula. When one spatula is completely submerged under water the pull-off force decreases by a factor ~ 6 as compared to humid condition.

7.6 Summary

In summary, I have studied how molecularly thin liquid layers affect the adhesion between the solids both with smooth and rough surfaces. For strong interaction between the liquid and walls, the pull-off force exhibits a local *maximum* at monolayer coverage. For the weak interaction, the pull-off force decreases continuously with increasing liquid coverage, especially when $\theta > 1$ for rough substrate. It is clear that a fundamental understanding, of the influence of liquid on adhesion at the micro- or nanoscale, is central to a large number of biological and “high-tech” engineering applications.



Chapter 8

Effect of Surface Roughness and Adsorbates on Superlubricity

In this chapter I will address the sliding of elastic solids in adhesive contact with flat and rough surfaces. The dependence of the sliding friction on the elastic modulus of the solids has been considered. For elastically hard solids with planar surfaces with incommensurate surface structures, extremely low friction (superlubricity) has been observed, which very abruptly increases as the elastic modulus decreases. Results show that even a relatively small surface roughness or a low concentration of adsorbates can eliminate the superlubricity state.

8.1 Introduction

Friction between solid surfaces is a very important phenomenon for biology and technology [9] and it is very common in nature. Static friction always involves the coexistence of different metastable configurations at microscopic level. When one surface slides on the other at low speed, first there is a loading phase during which the actual configuration stores elastic energy. Then, when the stored energy is large enough, an instability arises [93–95]: the system jumps abruptly to another configuration and releases elastic energy into irregular heat motion. The exact way of how the energy is dissipated does not influence the sliding friction force, provided that the dissipation is fast enough to happen before the next sliding event.

There are many possible origins of elastic instabilities, e.g., they may involve individual molecules or, more likely, groups of molecules or “patches” at the interface, which have been named stress domains [96–99]. As a result the overall motion may not exhibit any stick and slip behavior at macroscopic level, since the local rearrangements can occur at different times in an incoherent manner. Moreover, at least at zero temperature, the friction force does not vanish in the limit of sliding speed $v \rightarrow 0$, but it tends to reach some finite value which depends on the average energy stored during the loading events.

On the other hand, a system without instabilities cannot present a non-vanishing kinetic friction as $v \rightarrow 0$: if for any sliding distance there exists only one stable configuration, the energy stored at the interface is a single-valued function of the relative sliding distance. Thus when sliding occurs slowly the process has to be reversible, i.e., with negligible friction.

If the structure of the two contacting surfaces does not match, the formation of pinned states is hindered: when some groups of atoms are in registry with the other surface, occupying a local energy minimum, some other groups of atoms cannot adjust to the local

energy-minimum configuration without a deformation of the solids. In this case there is a competition between two energies: the lateral corrugation of the interaction potential between the walls, and the elastic energy to deform the solid so that every surface patch adjusts into a local minimum. If the latter prevails, the system is pinned and static friction appears. Otherwise, if the solid is sufficiently stiff, local domains do not show any instability and can overcome reversibly the local barriers. The overall effect is a motion with no static friction, since when some domains move uphill some other regions move downhill, so that the total energy is constant. This absence of instabilities due to a mismatch of the two surfaces' structures has been named *superlubricity* [100], although a more appropriate name would have been *structural lubricity* [101].

It is well known that elastically hard solids tend to exhibit smaller sliding friction than (elastically) soft materials [102]. One extreme example is diamond which under normal circumstances exhibits very low kinetic friction coefficient, of the order of 0.01, when diamond is sliding on diamond. This can be explained by the nearly absence of elastic instabilities because of the elastic hardness of the material.

Recently, superlubricity has been observed during sliding of graphite on graphite: in the experiment described in Ref. [103] a tungsten tip with a graphite flake attached to it is slid on an atomically flat graphite surface. When the flake is in registry with the substrate stick-slip motion and large friction are observed. When the flake is rotated out of registry, the forces felt by the different atoms start to cancel each other out, causing the friction force to nearly vanish, and the contact to become superlubric.

Graphite and many other layered materials are excellently dry lubricants. The most likely reason for this is that the solid walls of the sliding objects get coated by graphite flakes or layers with different orientation so a large fraction of the graphite-graphite contacts will be in the superlubric state. This will lead to a strong reduction in the average friction. However, the coated solid walls are unlikely to be perfectly flat and clean, and it is important to address how surface roughness and adsorbates influence the superlubric state. Here I show that even a relatively small surface roughness or low adsorbate coverage can eliminate the superlubric state [104].

8.2 Model

The results presented below have been obtained for an elastically flat block sliding on a rigid substrate. Both flat and rough substrates are considered. The atoms in the bottom layer of the block form a simple square lattice with lattice constant a . The lateral dimensions $L_x = N_x a$ and $L_y = N_y a$. For the block, $N_x = N_y = 48$. Periodic boundary conditions are applied in the xy plane. A recently developed multiscale molecular dynamics model has been used, where the block extends in the vertical z -direction a similar distance as along the x -direction [6] (see also [53]).

The lateral size of the block is equal to that of the substrate, but for the latter a different lattice constant $b \approx a/\phi$ is used, where $\phi = (1 + \sqrt{5})/2$ is the golden mean, in order to hinder the formation of commensurate structures at the interface. For the substrate, $N_x = N_y = 78$. The mass of a block atom is 197 a.m.u. and the lattice spacing of the block is $a = 2.6$ Å. The lattice spacing of the substrate is $b = 1.6$ Å. Solid blocks with different Young's moduli from $E = 0.2$ GPa up to 1000 GPa are considered in this chapter. The Poisson ratio of the block is $\nu = 0.3$.

Many surfaces tend to be nearly self-affine fractal. A self-affine fractal surface has the property that if part of the surface is magnified, with a magnification which in general is appropriately different in the perpendicular direction to the surface as compared to the lateral directions, then the surface "looks the same", i.e., the statistical properties of the

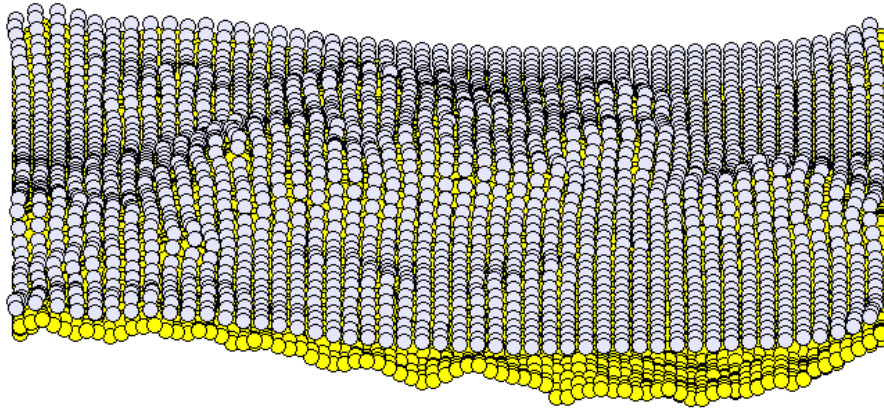


Figure 8.1: The contact between an elastic block with a flat surface and a rough *rigid* substrate. Only the interfacial layers of atoms are shown. The elastic modulus of the block is $E = 100$ GPa. The substrate is self-affine fractal with the root-mean-square roughness 3 \AA , fractal dimension $D_f = 2.2$. The applied pressure $p = 10$ GPa.

surface are invariant under this scale transformation [1, 6]. For a self-affine surface the power spectrum has the power-law behavior

$$C(q) \sim q^{-2(H+1)}, \quad (8.1)$$

where the Hurst exponent H is related to the fractal dimension D_f of the surface via $H = 3 - D_f$. Of course, for real surfaces this relation only holds in some finite wave vector region $q_0 < q < q_1$, and in a typical case $C(q)$ has a roll-off wavevector q_0 below which $C(q)$ is approximately constant.

In these calculations I have used self-affine fractal surfaces generated as outlined in Ref. [1], with the fractal dimension $D_f = 2.2$ and the roll-off wavevector $q_0 = 3q_L$, where $q_L = 2\pi/L_x$. $q_0 = 3q_L$ rather than $q_0 = q_L$ has been chosen since the former value gives some self-averaging and less noisy numerical results. Note $q_1 = 2\pi/b = 78q_0$.

The atoms at the interface between the block and the substrate interact with the Lennard-Jones potential

$$U(r) = 4\epsilon \left[\left(\frac{r_0}{r} \right)^{12} - \left(\frac{r_0}{r} \right)^6 \right], \quad (8.2)$$

where r is the distance between a pair of atoms. In the calculations presented below I have used $r_0 = 3.28 \text{ \AA}$ and $\epsilon = 40 \text{ meV}$, which gives an interfacial binding energy (per unit area) $\Delta\gamma \approx 4\epsilon/a^2 \approx 24 \text{ meV/\AA}^2$.

As an illustration, the contact between a flatly elastic block (top) and a randomly rough *rigid* substrate (bottom) has been shown in Fig. 8.1. Only the interfacial block and substrate atoms are shown. Note the non-contact regions occur in the “deep” valleys of the substrate.

In all results presented below the upper surface of the block moves with the velocity $v = 0.1 \text{ m/s}$, and the (nominal) squeezing pressure p , if not stated otherwise, is one tenth of the elastic modulus E of the block, i.e., $p = 0.1E$. Some test calculations for $v = 1 \text{ m/s}$ have been done (not shown), which show very similar results as for $v = 0.1 \text{ m/s}$. In fact, neglecting heating effects, one does not expect any strong dependence of the friction force on the velocity, as long as it is much smaller than the sound velocity (typically 1000 m/s), and much higher than the velocities that thermally activated creep motion

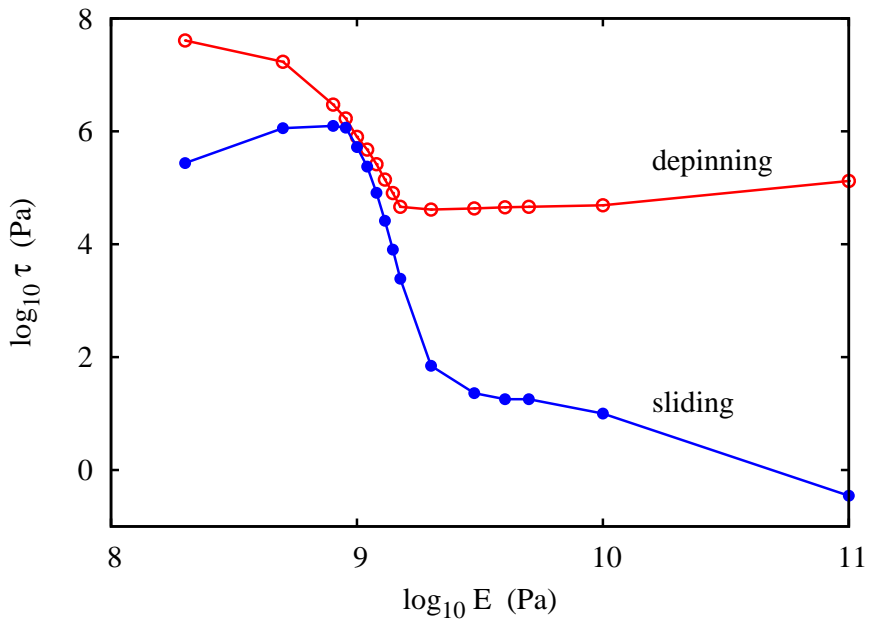


Figure 8.2: The shear stress at depinning (static friction) and during sliding (kinetic friction) as a function of the elastic modulus E of the block, for the flat substrate. In the calculation the squeezing pressure $p = 0.1E$ and the sliding velocity $v = 0.1$ m/s.

becomes important (usually a few $\mu\text{m}/\text{s}$). Furthermore, the sliding direction does not play a significant role since the commensurability ratio $8/13$ is the same along the x and y directions. For the (randomly) rough surfaces some test calculations have been done that the sliding direction is reversed which shows that the friction force changes by at most 20%. This is a finite-size effect: for an infinite system sliding along the positive or negative x -axis cannot change the friction force.

The reason for choosing p proportional to E is twofold. Firstly, solids with elastic modulus which varies over several orders of magnitude are considered, and it is not possible to use a constant p as this would result in unphysical large variations in the elastic deformation of the block. Secondly, if two elastic solids are squeezed together with a given load, then as long as the area of real contact is small compared to the nominal contact area, the pressure in the contact areas will be proportional to the elastic modulus of the solids [2].

The system is kept at low temperature by a viscous friction (a Langevin thermostat at $T = 0$ K) applied only to the topmost layers of block atoms, which are far away from the interface. On the time-scale of our simulations no significant variation in the frictional shear force has been observed, which could be attributed to a (slow) heating up of the system.

8.3 Numerical results

Firstly we study the sliding of clean smooth and rough surfaces for elastic solids with different elastic modulus and surface roughness. Secondly we study the influence of adsorbed molecules on the sliding friction. Results show that already a small surface roughness or less than a monolayer of adsorbed molecules may strongly increase the friction.

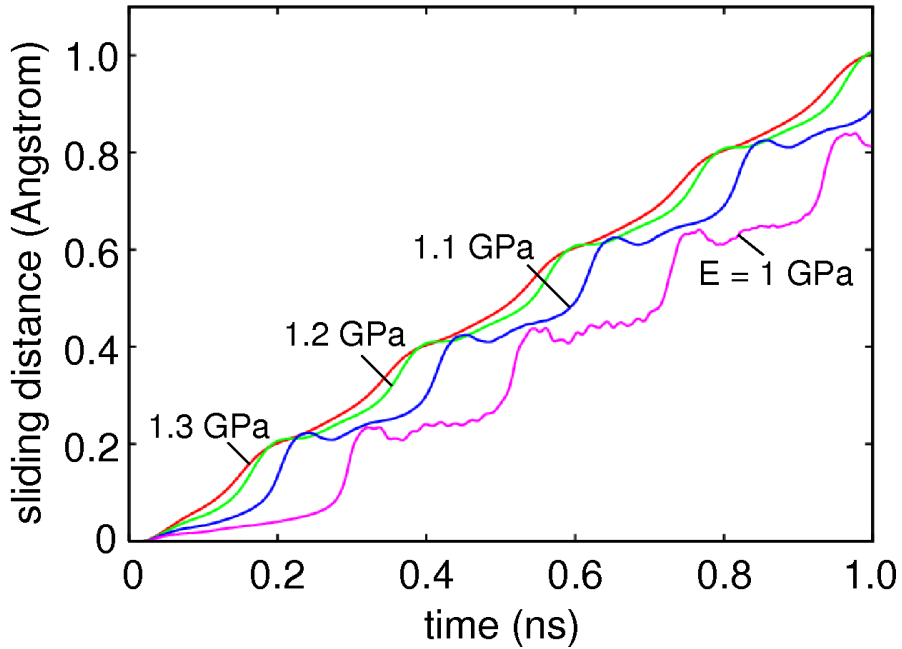


Figure 8.3: The average displacement of the interface block atoms (in the sliding direction) as a function of time, for the flat substrate. The elastic modulus of the block is $E = 1, 1.1, 1.2$ and 1.3 GPa. The transition from high friction (stick-slip) to superlubricity (steady sliding) is demonstrated clearly.

8.3.1 Influence of surface roughness on friction

Let us first assume that both the block and the substrate have atomically smooth surfaces. Fig. 8.2 shows the shear stress as a function of the elastic modulus E of the block. Note the relatively abrupt decrease in the friction when the elastic modulus changes from $E_1 \approx 0.7$ GPa to $E_2 \approx 2$ GPa. For $E > E_2$ practically no instabilities occur and the friction is extremely small, while for $E < E_1$ relatively strong elastic instabilities occur at the sliding interface, and the friction is high. For $E = 0.2$ GPa the static friction $\mu_s > 2$. This calculation illustrates that the transition from high friction to *superlubricity* can be very abrupt; in the present case an increase in the elastic modulus by only a factor of 3 (from 0.7 to 2.1 GPa) decreases the kinetic friction by a factor of $\sim 10^5$.

The variation of the shear stress as a function of time has been studied when the elastic modulus of the block equals (a) $E = 0.8$ GPa and (b) $E = 2$ GPa. When the elastic modulus of the solid is above the superlubric threshold as in case (b), no significantly elastic instabilities occur; the stress is a periodic function of time, with the period corresponding to the displacement 0.2 Å. For softer solids, when strong elastic instabilities occur during sliding as in case (a), the shear stress is less regular (and the arrangement of the interfacial block atoms more disordered) than for the stiffer solid, and the (average) period is *longer* than 0.2 Å.

The remarkable abruptness of the superlubric transition is illustrated in Fig. 8.3, which shows the average displacement of the interface block atoms (in the sliding direction) as a function of time, for the flat substrate. Note that onset of stick-slip as the elastic modulus of the block decreases from $E = 1.3$ GPa (upper curve) to 1 GPa (lower curve).

The regular pattern with period 0.2 Å has a simple geometrical explanation related to the commensurability ratio $8/13$ along the sliding direction: in the ground state each

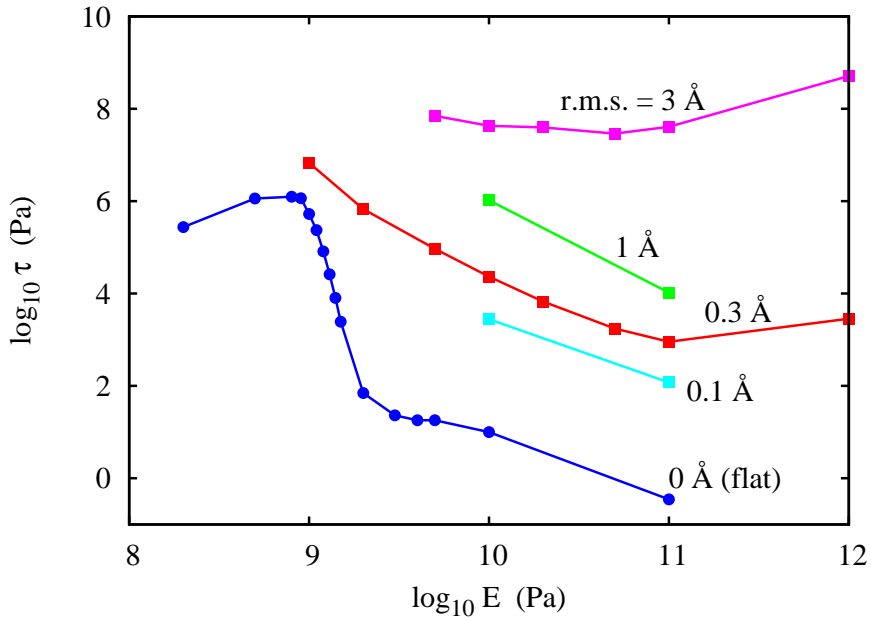


Figure 8.4: The shear stress for an elastic block sliding on rough substrates, as a function of the elastic modulus E of the block. The curves from top to bottom correspond to the root-mean-square roughness amplitudes of the fractal substrate 3, 1, 0.3, 0.1 Å and 0 (flat substrate).

block's atom has 8 allowed positions within the cell b of the substrate. Hence there are 8 equivalent configurations within a sliding distance $b = 1.6$ Å.

Let us now consider the influence of surface roughness on the sliding dynamics. The average shear stress for an elastic block sliding on a rough substrate, as a function of the elastic modulus E of the block, has been shown in Fig. 8.4. For the substrate with the largest roughness, no superlubric state can be observed for any elastic modulus up to $E = 10^{12}$ Pa.

Our results are in agreement with the theoretical predictions of Sokoloff [105]: roughness on multiple length scales can induce a transition from a *weak pinning regime* to a *strong pinning regime*. The main difference between our model and that of Sokoloff is that the latter assumes purely repulsive interactions between the atoms, while here the attractive part of the Lennard-Jones potential gives rise to an adhesive pressure p_{ad} which will contribute to the effective load. Since in our case $p_{ad} \approx 10$ GPa, the shear stress is almost independent of the external load.

The shear stress as a function of time for different elastic moduli has been shown in Fig. 8.5. Note that in addition to major slip events, several small slip events occur in all cases. These events correspond to local slip at some asperity contact regions before the major slip involving the whole contact area. In all cases, the time dependence of the shear stress remains periodic with the period 2.6 Å, which corresponds to the lattice spacing of the block. At the current sliding speed $v = 0.1$ m/s the kinetic friction force is smaller for the stiffer solid even if the load is larger: although the maximum shear stress achieved before sliding is quite big in such case, the average shear stress is small and part of the elastic energy stored in the loading phase is not dissipated, but it is given back to the system. For the elastically softer blocks ($E = 20$ and 5 GPa), the stress-noise increases after each major slip event; this is caused by the elastic waves (heat motion) excited during

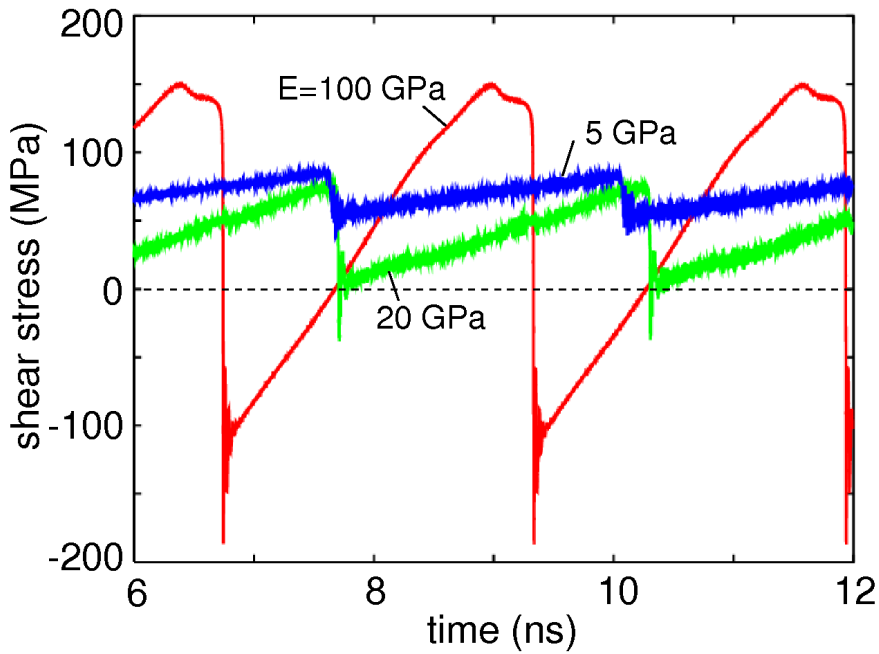


Figure 8.5: The shear stress as a function of time for the rough substrate with the root-mean-square roughness amplitude 3 \AA . The elastic modulus of the block is $E = 100, 20$ and 5 GPa .

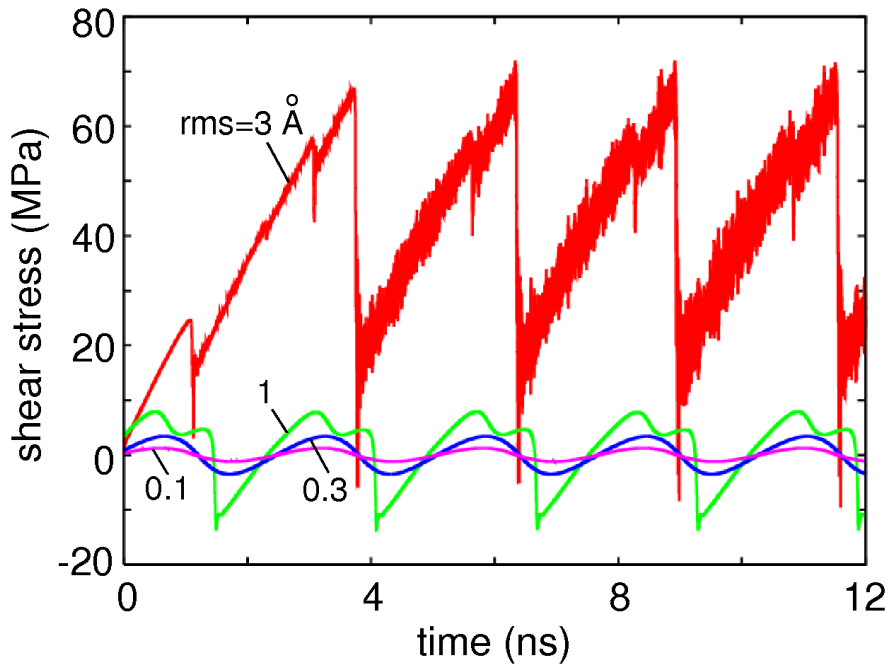


Figure 8.6: The shear stress as a function of time for the rough substrate with the root-mean-square roughness amplitudes $3, 1, 0.3$ and 0.1 \AA . The elastic modulus of the block is $E = 10 \text{ GPa}$. The transition from high friction to superlubricity is demonstrated clearly.

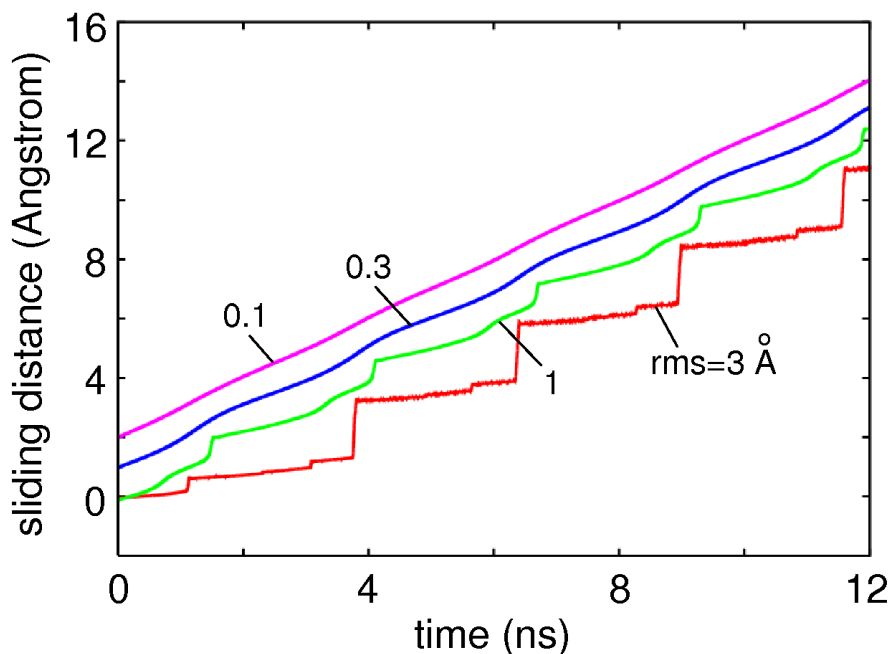


Figure 8.7: The average displacement of the interface block atoms (in the sliding direction) as a function of time for the rough substrate with the root-mean-square roughness amplitudes 3, 1, 0.3 and 0.1 Å. The elastic modulus of the block is $E = 10$ GPa. The transition from high friction (stick-slip) to superlubricity (steady sliding) is demonstrated clearly.

the (major) rapid slip events and not completely adsorbed by the thermostat.

The effect of the substrate root-mean-square (rms) roughness amplitude on the shear stress, as a function of time for the block with the elastic modulus $E = 10$ GPa, has been shown in Fig. 8.6. The root-mean-square roughness amplitude is varied from 3 to 0.1 Å. For the rms roughness amplitudes 0.3 and 0.1 Å the major slip is not as abrupt as for higher roughness amplitudes. In all cases, the time dependence of the shear stress remains periodic with the period 2.6 Å determined by the lattice spacing of the block. For the rms roughness 3 Å two small and a major slip events can be observed in each period, and the kinetic friction is high. For the case with the rms amplitudes 0.3 and 0.1 Å (almost) no elastic instability occurs, and the kinetic friction is very small.

The average displacement of the interface block atoms (in the sliding direction), has been shown in Fig. 8.7 as a function of time for the block with the elastic modulus $E = 10$ GPa, and for the rough substrate with various roughness amplitudes. The transition from high (stick-slip) friction for the most rough surface to very low friction (smooth sliding) for the surfaces with root-mean-square roughness 0.3 and 0.1 Å is demonstrated clearly.

8.3.2 Dependence of the friction on the load

Now let us study the dependence of the friction force on the load. Both flat surfaces and rough surfaces are considered. For flat surfaces the frictional shear stress is independent of the squeezing pressure p as long as p is smaller than the adhesion pressure p_{ad} which is of the order of 10^{10} Pa. For rough surfaces the situation is more complex and the frictional shear stress will depend on the squeezing pressure p even for very small p unless at least one of the solids is so compliant that the attractive interaction becomes important for the contact mechanics.

Flat surface

During sliding, the atoms at the sliding interface will experience energetic barriers derived from both the attractive interaction between the atoms on the two opposing surfaces, and from the applied load. Thus, let us define an *adhesion pressure* p_{ad} , and as long as $p_{\text{ad}} \gg p$, where p is the pressure in the contact area derived from the external load, the frictional shear stress will be nearly independent of the applied load. Let us first consider the limiting case where the elastic modulus of the block is extremely small. In this case, in the initial pinned state (before sliding) all the block atoms will occupy hollow sites on the substrate, as indicated by atom **A** in Fig. 8.8. During sliding along the x -direction, the atom **A** will move over the bridge position **B** and then “fall down” into the hollow position **C** (over-damped motion has been assumed). The minimum energy for this process is given by the energy barrier $\delta\epsilon$ (the energy difference between the sites **B** and **A**) plus the work $pa^2\delta h$ against the external load, where a is the block lattice constant and δh the change in the height between sites **B** and **A** (which depends on p). Thus the frictional shear stress σ_f is determined by $\sigma_f a^2 b = \delta\epsilon + pa^2\delta h$, or

$$\sigma_f = \delta\epsilon/(ba^2) + p\delta h/b = (p_{\text{ad}} + p)\delta h/b,$$

where the adhesion pressure has been defined $p_{\text{ad}} = \delta\epsilon/(a^2\delta h)$.

In our case $\delta\epsilon \approx 3$ meV and $\delta h \approx 0.008$ Å giving $p_{\text{ad}} \approx 10^{10}$ Pa. Thus, in the present case, only when the local pressure in the contact regions becomes of the order of ~ 10 GPa, or more, it will start to influence the shear stress. This result is in accordance with our simulation results. Thus, for smooth surfaces, the shear stress acting on the block with

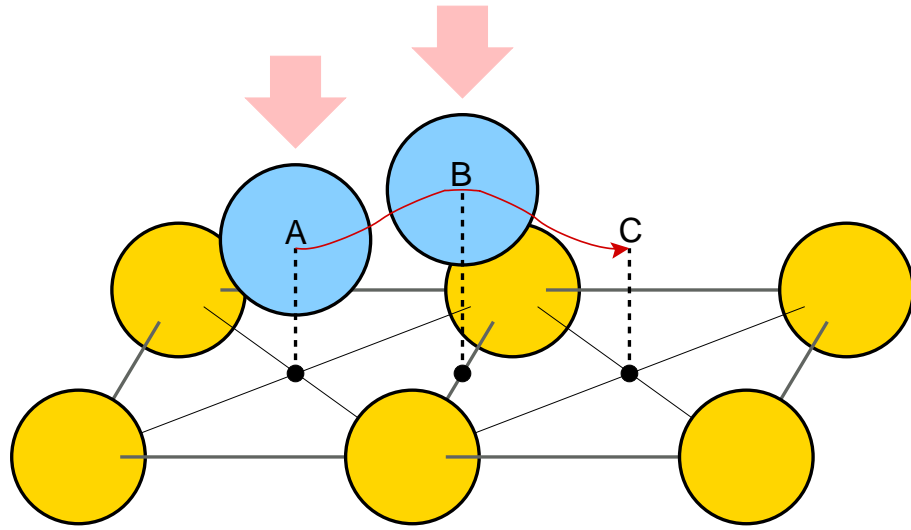


Figure 8.8: A block atom moving (or jumping) from the hollow site **A** over the bridge site **B** to the hollow site **C**. The maximum energy position along the trajectory is at site **B**.

the elastic modulus $E = 0.5$ GPa, squeezed against the substrate with the pressure $p = 50$ and 150 MPa, is identical (≈ 1 MPa) within the accuracy of the simulations.

Rough surface

In the absence of adhesion, contact mechanics theories predict that the area of real contact A between two elastic solids with randomly rough (but nominally flat) surfaces is proportional to the squeezing force (or load) F_N as long as $A \ll A_0$ (where A_0 is the nominal contact area). The law $A = \alpha F_N$ holds strictly only if the roughness occurs on many different length scales [60], but this is (almost) always the case for natural surfaces (e.g., a stone surface) or surfaces of engineering interest. For an infinite system (thermodynamic limit) not only A is proportional to F_N , but also the distribution of sizes of the contact regions and the stress distribution in the area of real contact, is independent of the squeezing force if $A \ll A_0$. The physical picture behind these results is that as the squeezing force increases, new contact regions are formed in such a way that the quantities referred to above remain unchanged. However, for any finite sized system this picture cannot hold exactly as it requires that some contact regions have infinite-size, which is possible only for an infinite sized system.

When the attractive interaction cannot be neglected, the area of real contact is often assumed [106] to be of the form $A \approx \alpha(F_N + F_{ad})$ where F_{ad} represents an adhesive load, but this relation is only approximate [4, 60]. If the friction force F_f is assumed to be proportional to the area of real contact, then one expects $F_f = \sigma_c A \approx \sigma_c \alpha(F_N + F_{ad})$ so that the nominal frictional shear stress

$$\sigma_f = F_f/A_0 \approx \sigma_c \alpha(F_N + F_{ad})/A_0 = \sigma_c \alpha(p + \sigma_a) \quad (8.3)$$

where $p = F_N/A_0$ is the (nominal) squeezing pressure and where the so called *detachment stress* [4, 60] σ_a gives a contribution to the frictional stress from the attractive wall-wall interaction. From (8.3) it also follows that the friction coefficient $\mu = \sigma_c \alpha(1 + \sigma_a/p)$ will diverge as the squeezing pressure p goes to zero.

The dependence of the frictional shear stress on the squeezing pressure for the system has been studied above, for the block elasticities $E = 10$ GPa and $E = 100$ GPa, and for

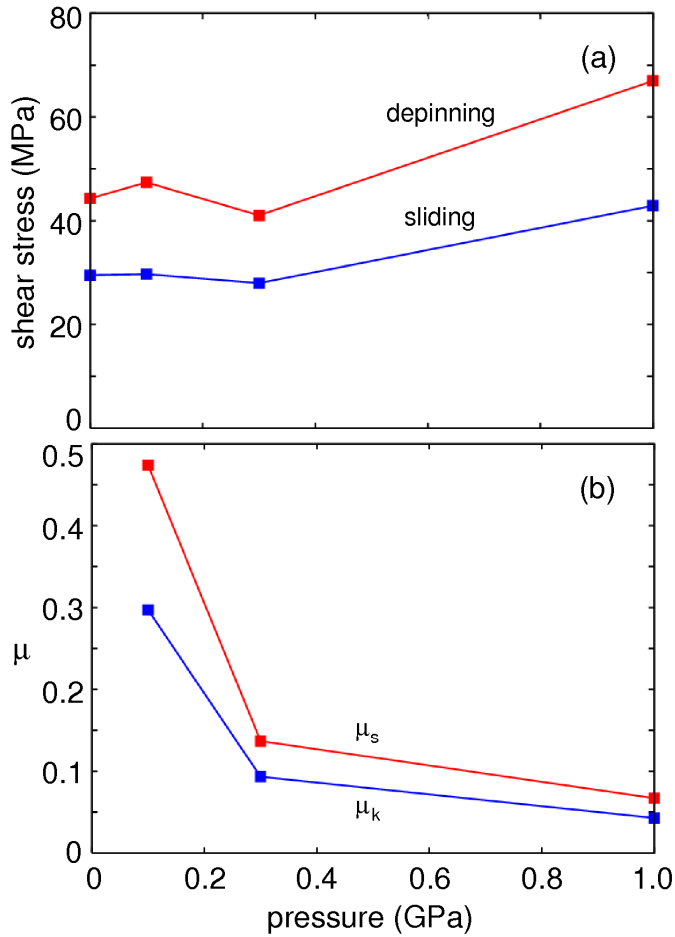


Figure 8.9: The shear stress at depinning (static friction) and during sliding (kinetic friction) (a) and the static and kinetic friction coefficients (b) as a function of the applied pressure, for an elastic block sliding on a rough substrate. For the substrate with the root-mean-square roughness amplitude 3 Å. The elastic modulus of the block is $E = 10$ GPa.

the rigid substrate with the rms roughness amplitude 3 Å. In Fig. 8.9 (a) the (nominal) frictional shear stress and (b) the friction coefficient, have been shown as a function of the squeezing pressure when $E = 10$ GPa. Note that, because of the attractive interaction, the frictional shear stress is constant for low squeezing pressures, while the friction coefficient diverges as $p \rightarrow 0$, in consistent with the theoretical analysis.

The adhesion contribution $\sigma_c \alpha \sigma_a$ to the frictional shear stress becomes important only when the elastic modulus of the block is small enough. The transition, with decreasing elastic modulus, from the case where the adhesion can be neglected to the case where it is important, is rather abrupt. To illustrate this, the interfacial atoms (the top atoms of the substrate and the bottom atoms of the block) for blocks with the elastic modulus $E = 1000, 100, 10$ and 5 GPa, and with the squeezing pressure $p = 0.1E$, have been shown in Fig. 8.10. In the absence of adhesion all the systems would exhibit virtually identical arrangement of atoms. Indeed the two stiffest solids exhibit very similar atom-arrangements, but there is a clear change when E decreases from 100 to 10 GPa; in the latter case the attractive interaction is able to pull the solids into intimate contact over most of the nominal contact area. Thus the bottom surface of the block is able to bend and fill out a substrate “cavity” with diameter D and height h if the gain in wall-wall

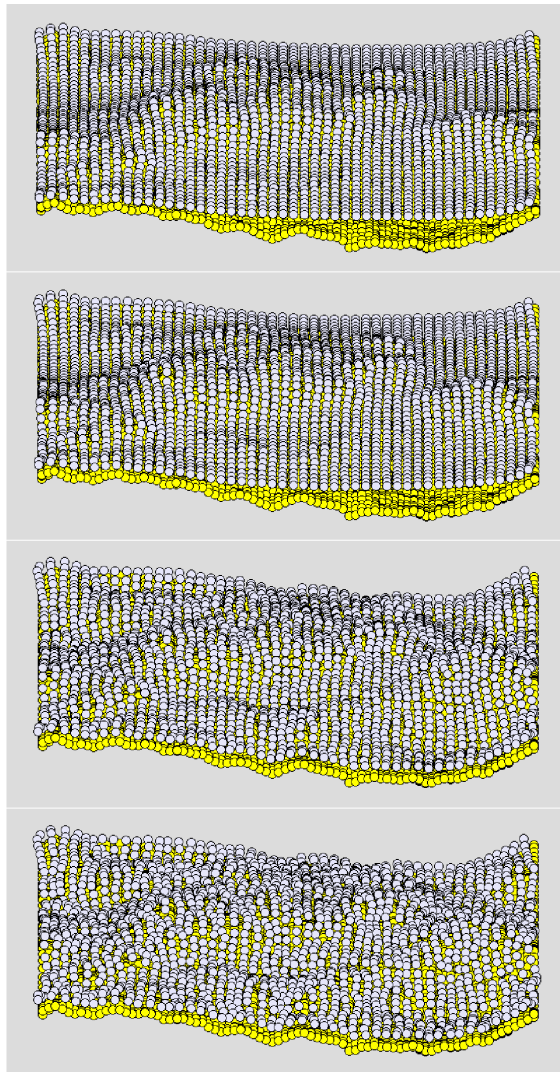


Figure 8.10: The contact between an elastic block with a flat surface and a rough *rigid* substrate. Only the interfacial layers of atoms are shown. The elastic modulus of the block is $E = 1000, 100, 10$ and 5 GPa (from top to bottom). The substrate is self-affine fractal with the root-mean-square roughness 3 \AA . The applied pressure $p = 0.1E$. Note the elastic deformation of the block, and that the real contact area is smaller than the nominal contact area for high values of the elastic modulus of the block.

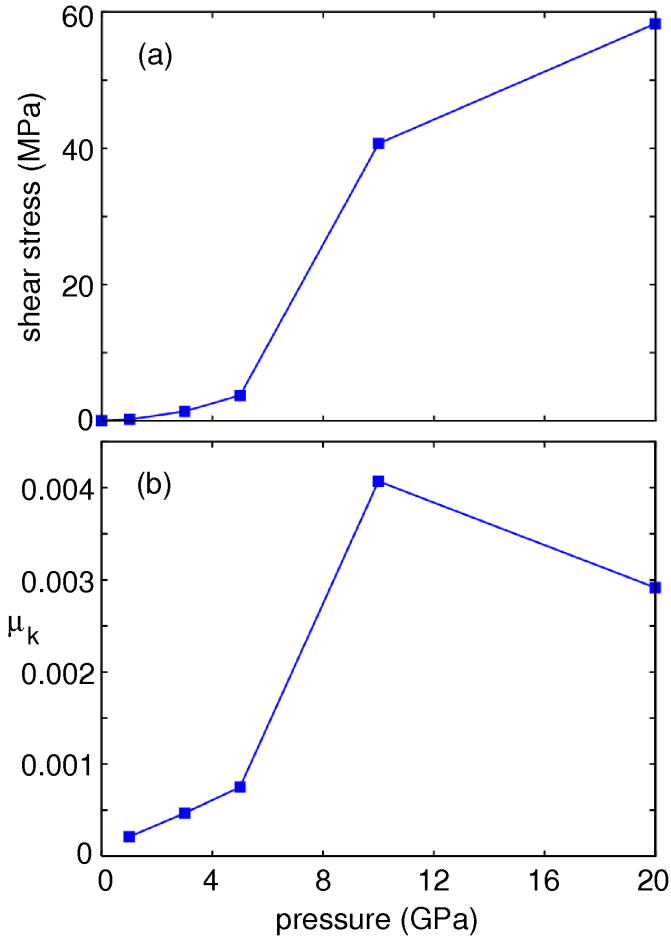


Figure 8.11: The shear stress during sliding (kinetic friction) (a) and the kinetic friction coefficient (b) as a function of the applied pressure, for an elastic block sliding on a rough substrate. For the substrate with the root-mean-square roughness amplitude 3 Å. The elastic modulus of the block is $E = 100$ GPa.

binding energy, which is of the order of $D^2\Delta\gamma$ (where $\Delta\gamma$ is the interfacial binding energy per unit surface area for flat surfaces), is equal to (or larger than) the elastic energy stored in the deformation field in the block, which is of the order of $ED^3(h/D)^2$. This gives the “critical” elasticity $E_c \approx D\Delta\gamma/h^2$. In the present case we have a distribution of roughness wavelength but one can obtain a rough estimate of E_c by taking $h^2 = \langle h^2 \rangle = 9$ Å² as the mean of the square of the roughness profile and $D \approx 100$ Å as a typical roughness wavelength. Using $\Delta\gamma \approx 4\epsilon/a^2 \approx 24$ meV/Å² this gives $E_c \approx 40$ GPa which is between 100 and 10 GPa. This change in the contact mechanics has a large influence on the sliding friction. Thus, as will be shown, for the block with elastic modulus $E = 100$ GPa there will be a negligible contribution to the friction from the attractive interaction and $\sigma_a \approx 0$.

Fig. 8.11 shows the frictional shear stress for the same system as in Fig. 8.9 except that the elastic modulus of the block is ten times higher. In this case the influence of the attractive interaction is *negligible*, and the frictional shear stress decreases continuously as the squeezing pressure decreases. However, the friction coefficient is not constant as expected from the arguments presented above related to the invariance of the pressure distribution and contact size distribution with the squeezing force. This fact must be related to the small size of the system used in our simulations. As the squeezing pressure

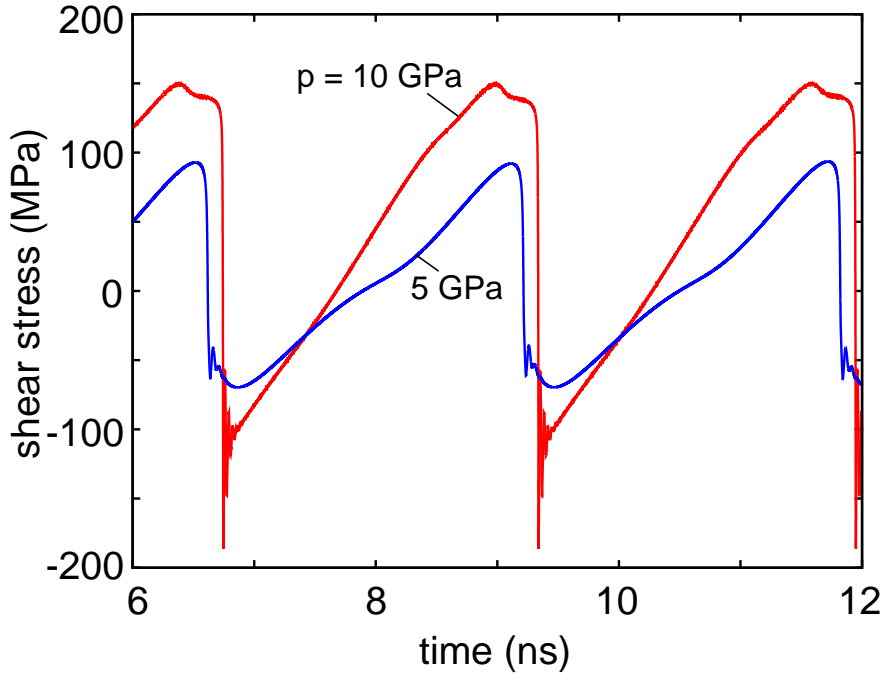


Figure 8.12: The shear stress as a function of time for the rough substrate with the root-mean-square roughness amplitude 3 \AA . The elastic modulus of the block is $E = 100 \text{ GPa}$ and the applied pressure $p = 5$ and 10 GPa .

increases the stress distribution at the interface and the average size of the contact regions will change in such a way that when p increases from $p = 5$ to 10 GPa there is a very rapid increase in asperity contact regions undergoing elastic instabilities during sliding. This can be directly demonstrated by comparing the time-variation of the shear stress for $p = 5$ and 10 GPa , see Fig. 8.12. Note that at the higher pressure some slip events take place before the main slip event, i.e., new elastic instabilities appear and the frictional shear stress increases much faster than linear with the nominal squeezing pressure as p increases from 5 to 10 GPa .

To illustrate the small influence of the adhesion on the contact mechanics for the block with the elastic modulus $E = 100 \text{ GPa}$, the interfacial atoms for the squeezing pressures $p = 10, 3, 1 \text{ GPa}$ and 0 have been shown in Fig. 8.13. When $p = 0$ only the adhesion pressure is acting and the area of real contact almost vanishes.

8.3.3 Role of adsorbates

Extremely low sliding friction is possible only in the absence of elastic instabilities. As shown above this is possible for stiff enough solids with incommensurate (or nearly incommensurate) surface structures. However, any types of imperfections may “lock” the surfaces together and introduce elastic instabilities during sliding. One type of “defect” discussed above is surface roughness. Another possibility is adsorbed molecules. Adsorbed molecules may arrange themselves at the interface between the two solids in such a way as to pin the solids together. A low concentration of (strongly bound) adsorbates is in many ways similar to nanoscale roughness and it is clear that if the perfect system (flat surfaces without adsorbates) were in a superlubric state, one would expect a strong increase in the friction already at low adsorbate coverage. We have performed an extensive

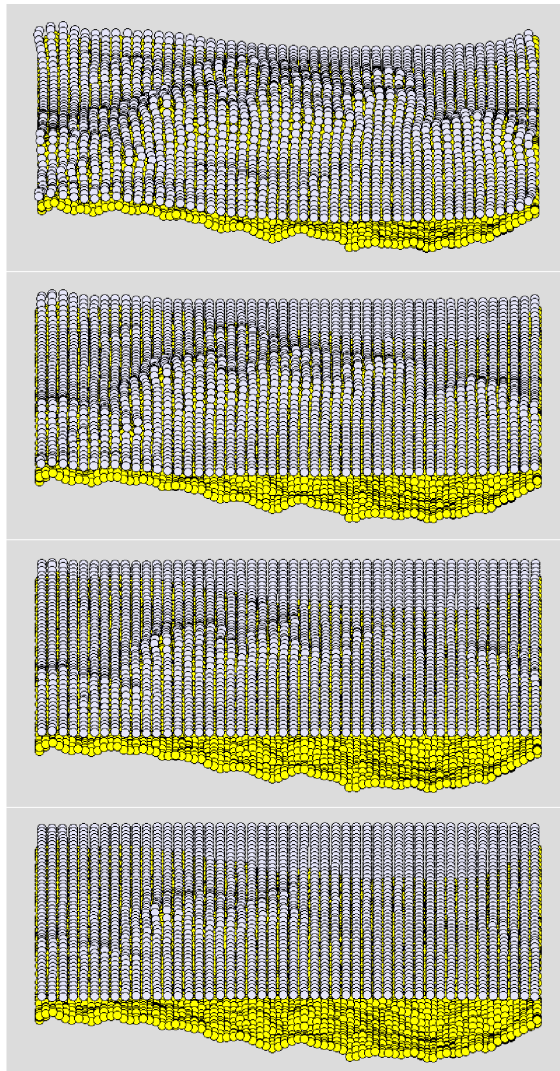


Figure 8.13: The contact between an elastic block with a flat surface and a rough *rigid* substrate. Only the interfacial layers of atoms are shown. The elastic modulus of the block is $E = 100$ GPa. The substrate is self-affine fractal with the root-mean-square roughness 3 Å. The applied pressure $p = 10, 3, 1$ GPa and 0 (from top to bottom). For the latter case only the adhesion pressure is acting. Note the elastic deformation of the block, and that the real contact area is smaller than the nominal contact area.

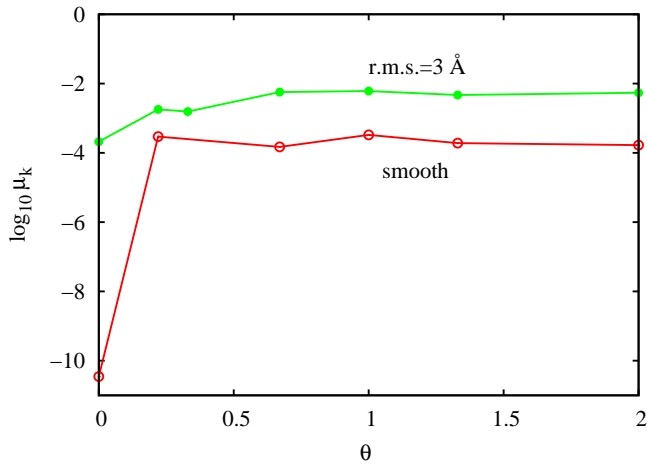


Figure 8.14: The kinetic friction coefficients for elastic block ($E = 100$ GPa) sliding both on smooth and on rough substrate, as a function of liquid coverage (octane, C_8H_{18}) θ confined between two walls [107]. The substrate has the root-mean-square (rms) roughness 3 \AA and the fractal dimension $D_f = 2.2$. The applied pressure $p = 1$ GPa.

set of computer simulations to illustrate this effect both for atomically smooth surfaces and for rough surfaces. In Fig. 8.14, the kinetic friction coefficients for elastic block ($E = 100$ GPa) sliding both on smooth and on rough substrate, have been shown as a function of liquid (octane, C_8H_{18}) coverage θ confined between two walls, for the applied pressure $p = 0.01E$ [107]. Note that for flat surfaces there is a very abrupt increase in the friction with increasing adsorbate coverage. In fact, the friction increases by a factor of $\sim 10^6$ as the coverage increases from zero to 0.22 monolayer. For $0.22 < \theta < 2$ the friction is nearly constant. For the rough surface the increase in the friction is much smaller. In this case the (small) increase in the friction results from octane molecules trapped in the asperity contact regions¹ – this results in an effectively increased surface roughness and enhanced friction.

8.4 Summary

To summarize, the sliding of elastic solids in adhesive contact with flat and rough surfaces has been studied. Firstly, the dependence of the sliding friction on the elastic modulus of the solids is considered. For elastically hard solids with planar surfaces with incommensurate surface structures extremely low friction (superlubricity) has been observed, which very abruptly increases as the elastic modulus decreases. Thus, at the superlubricity threshold, an increase in the elastic modulus by a factor of ~ 3 results in the decrease in the frictional shear stress by a factor $\sim 10^5$. Secondly, the dependence of friction on load has been studied both theoretically and numerically. Thirdly, even a relatively small surface roughness, or a low concentration of adsorbates, can eliminate the superlubricity.

¹In the simulations the C_8H_{18} bed-units interact with the solid wall atoms via the Lennard-Jones potential with the well-depth parameter $\epsilon = 40$ meV. This relatively strong interaction leads to lubricant molecules trapped in the asperity contact regions. Other studies (see Ref. [107]) with $\epsilon = 5$ meV result in the squeeze-out of the lubricant from the asperity contact regions into the “valleys” or “cavities” of the substrate height profile. In this case, any adsorbate-induced increase in friction is not expected.

Chapter 9

Nanodroplets on Rough Hydrophilic and Hydrophobic Surfaces

The behavior of liquid nanodroplets on rough hydrophobic and hydrophilic solid surfaces has been studied in this chapter. On hydrophobic surfaces, the contact angle for nanodroplets depends strongly on the root mean square roughness amplitude, but it is nearly independent of the fractal dimension of the surface. Since increasing the fractal dimension increases the short-wavelength roughness, while the long-wavelength roughness is almost unchanged, I conclude that for hydrophobic interactions the short-wavelength (atomistic) roughness is not very important. Results show that the nanodroplet is in a Cassie-like state. For rough hydrophobic surfaces, there is no contact angle hysteresis due to strong thermal fluctuations, which occur at the liquid-solid interface on the nanoscale. On hydrophilic surfaces, however, there is strong contact angle hysteresis due to higher energy barrier. These findings may be very important for the development of artificially biomimetic superhydrophobic surfaces.

9.1 Introduction

In the year of 1805, Thomas Young and Pierre Simon de Laplace proposed that an interface between two materials has specific energy, the so-called interfacial energy, which is proportional to the interfacial surface area [108–110]. This concept is the basis for the field of wetting, which has become an extremely hot topic in the last two decades [111, 112], thanks to biological and high-tech applications, ranging from self-cleaning surfaces, micro-electronics and thin film coatings, to image formation that involve the spreading of liquids on solid surfaces.

Wetting describes the contact between a fluid and a solid surface. Liquids with high surface tension (usually reflecting strong intra-molecular bonds), or liquids on low-energy solid surfaces, usually form nearly (complete) spherical droplets, whereas liquids with low surface tension, or liquids on high-energy surfaces, usually spread out on (or wet) the surfaces. This phenomenon is a result of minimization of interfacial energy. Thus, if a surface has a high free energy, most liquid will spread on the surface since this will usually lower the free energy.

Wetting phenomena have been widely studied both theoretically [113, 114] and experimentally [115, 116] in connection with the physics of surfaces and interfaces. The behavior of liquids on smooth solid surfaces is rather well understood. However, for rough solid

surfaces the situation is much less clear, even though roughness occurs on practically all real surfaces of engineering or biological interest. Studies (and classification) of disordered and inhomogeneous surfaces [117] should have significant impact on the problem of liquid contact angle and wetting of rough substrates [90, 107, 118–120]

The fascinating water repellents of many biological surfaces, in particular plant leaves, have recently attracted great interest for fundamental research as well as practical applications [15–17, 121–125]. The ability of these surfaces to make water beads off completely and thereby wash off contamination very effectively has been termed the “Lotus effect”, although it is observed not only on the leaves of the Lotus plant (Fig. 1.2), but also on many other plants such as strawberry, raspberry and so on. Water repellents are very important in many industrial and biological processes, such as prevention of the adhesion of snow, rain drops and fog to antennas, self-cleaning windows and traffic indicators, low-friction surfaces and cell mobility [126–128].

Most leaves that exhibit strong hydrophobicity have hierarchical surface roughness with micro- and nanostructures made of unwettable wax crystals, which maximize the contact angle with water and most other liquids. Fig. 1.3 shows epidermal cells (microscale roughness) covered with wax crystals (nanoscale roughness). The wax crystals exhibit a relative high contact angle with water, which is enhanced by the surface roughness. Water droplets on the rough wax surface tend to minimize the contact between the surface and the droplet by forming nearly spherical droplets, as approximately described by the two classical models due to Wenzel [129] and Cassie [130] (see below). As a result the leaves have also a self-cleaning property: because of the small adhesion energy (and small contact area) between contamination particles and the rough leaf [16], during raining water drops roll away removing the contamination particles from the leaf surface.

The hydrophobicity of solid surfaces is determined by both the chemical composition and the geometrical micro- or nanostructure of the surface [115, 131, 132]. Understanding the wetting of corrugated and porous surfaces is a problem of long standing interest in areas ranging from textile science [133] to catalytic reaction engineering [134]. Renewed interest in this problem has been generated by the discoveries of surfaces with small scale corrugations that exhibit very large contact angles for water and other liquids—in some cases the contact angle is close to 180°. Such surfaces are referred to as superhydrophobic [135].

In this chapter I present results of Molecular Dynamics (MD) calculations on the behavior of liquid nanodroplets on rough hydrophilic and hydrophobic solid surfaces. We find that for hydrophobic surfaces, the contact angle for nanodroplets depends strongly on the root mean square surface roughness amplitude, but is nearly independent of the fractal dimension D_f of the surface. For hydrophobic rough surfaces I do not detect any contact angle hysteresis. Both results can be explained by the strong thermal fluctuations which occur at the liquid-solid interface on the nanoscale. On hydrophilic surfaces, however, strong contact angle hysteresis has been found due to the higher energy barrier for interfacial liquid density fluctuations. These findings may be crucial for the development of artificial biomimetic superhydrophobic surfaces.

9.2 Theoretical background

In this section I briefly describe some results from the theory of the liquid-solid contact angle, which are necessary for the interpretation of the numerical results presented in Sec. 9.4. The importance of thermal fluctuations for the contact dynamics at the nanoscale is emphasized as compared to micrometer or macroscopic dimensions.

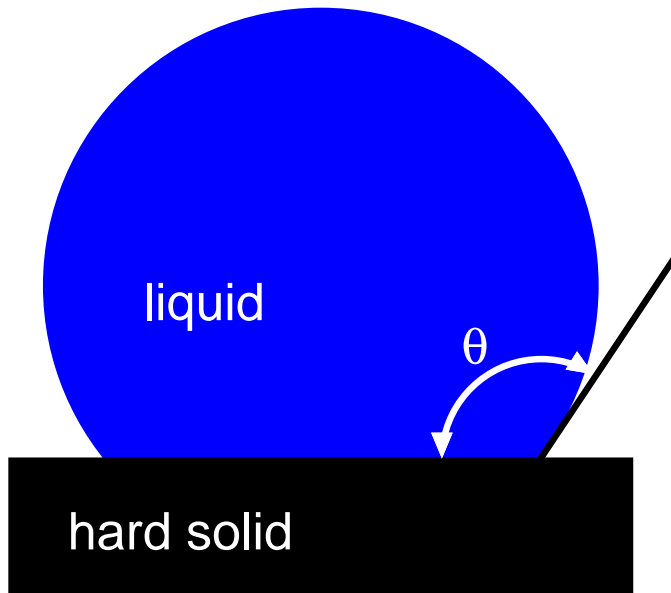


Figure 9.1: Liquid droplet on flat substrate. The contact angle θ is between 0 (complete wetting) and π .

9.2.1 Flat surfaces

If gravitational effects can be neglected, a liquid droplet on a flat substrate forms a spherical cap, see Fig. 9.1. The contact angle θ is determined by the minimization of the free energy and depends on the interfacial free energies per unit area: solid/liquid γ_{sl} , solid/vapor γ_{sv} and liquid/vapor γ_{lv} . Minimizing the surface free energy, with the constraint of fixed volume of the droplet, gives the Young's equation, first proposed by Thomas Young about two hundred years ago:

$$\gamma_{\text{sl}} + \gamma_{\text{lv}} \cos \theta = \gamma_{\text{sv}} \quad (9.1)$$

Complete wetting corresponds to $\theta = 0$, and typically happens for liquids with low surface tension γ_{lv} , and on solids with high surface energy γ_{sv} . Liquids with high surface tension on low energy surfaces tend to form droplets with high contact angle θ . Eq. 9.1 was deduced for a substrate which is assumed to be perfectly smooth, homogeneous, and rigid. However, in reality, structured or rough surfaces are quite common. So it is necessary to know how the contact angle behaves on rough surfaces.

9.2.2 Rough surfaces: minimum free energy state

Most surfaces of practical interest have roughness on many different length scales. For simple periodic surface profiles one may analytically develop accurate analytical treatments of the liquid droplet contact angle (see e.g., Ref. [136]), but for randomly rough surfaces the situation is much more complex. For surfaces with random roughness, e.g., self-affine fractal surfaces (see below), one may develop a general theory based on the study of the system at different magnifications ζ , see Fig. 9.2. Here $\zeta = D/\lambda$ where D is the diameter of the droplet-substrate (apparent) contact area and λ the resolution. One can introduce interfacial liquid-solid and solid-vapor free energies (per unit area) $\gamma_{\text{sl}}(\zeta)$

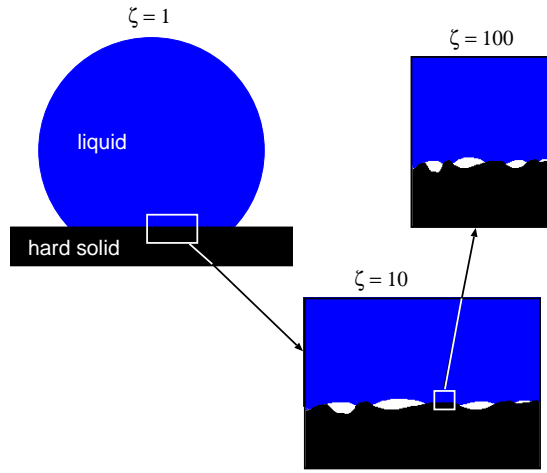


Figure 9.2: Liquid droplet on a rough substrate. At the lowest magnification ζ the surface appears flat and the liquid contact angle is θ_0 . At increasing magnification surface roughness is observed and the liquid will in general only make contact with the substrate in some asperity contact regions.

and $\gamma_{sv}(\zeta)$ which depend on the magnification ζ ¹. At the highest magnification ζ_1 , corresponding to nanoscale (or atomistic) resolution, these quantities reduce to those for the flat surface², $\gamma_{sl}(\zeta_1) = \gamma_{sl}$ and $\gamma_{sv}(\zeta_1) = \gamma_{sv}$. Since the substrate appears flat at the lowest magnification $\zeta = 1$, the macroscopic contact angle (corresponding to $\zeta = 1$) is obtained using the Young's equation with γ_{sl} and γ_{sv} replaced by $\gamma_{sl}(1)$ and $\gamma_{sv}(1)$, i.e.

$$\gamma_{sl}(1) + \gamma_{lv}\cos\theta_0 = \gamma_{sv}(1) \quad (9.2)$$

The change in the surface free energy (per unit area) when a liquid with a flat surface is brought in contact with the substrate is

$$\Delta F/A_0 = \gamma_{sl}(1) - \gamma_{sv}(1) - \gamma_{lv} = -\gamma_{lv}(1 + \cos\theta_0)$$

where A_0 is the (projected) surface area. Note that increasing contact angle θ_0 corresponds to an increasing interfacial free energy. Thus, if a liquid drop can occur in several metastable states on a surface, the state with the smallest contact angle corresponds to the (stable) minimal free-energy state.

Using Eq. 9.2 it is trivial to derive the results of the so called Wenzel [129] and Cassie [130] models. In the Wenzel model it is assumed that complete contact occurs at the liquid-solid interface. Thus

$$\gamma_{sv}(1) = r\gamma_{sv}(\zeta_1), \quad \gamma_{sl}(1) = r\gamma_{sl}(\zeta_1), \quad (9.3)$$

where $r = A/A_0$ is the ratio between the surface area A of the rough substrate, and the projected (or nominal) surface area A_0 . Substituting (9.3) in (9.2) gives the contact angle

¹The surface energy of a liquid does, in fact, also depend on the magnification because of thermally excited capillary waves which contribute to the surface energy of a liquid. However, the dependence of $\gamma_{lv}(\zeta)$ on the magnification ζ is rather weak and this effect in the present study is neglected.

²Here let us assume that the surface free energy per unit area does not depend on the orientation of the substrate surface, which may be a reasonable approximation for many amorphous materials, but which in general fails for crystalline materials.

θ_0 on the rough surface in terms of the contact angle θ on the microscopically flat surface of the same material (Wenzel equation):

$$\cos \theta_0 = r \cos \theta. \quad (9.4)$$

In the Cassie model [130] it is assumed that some air (or vapor) remains trapped between the drop and the cavities of the rough surface. In this case the interface free energy

$$\gamma_{sv}(1) = r\gamma_{sv}(\zeta_1), \quad (9.5)$$

$$\gamma_{sl}(1) = \phi r\gamma_{sl}(\zeta_1) + (1 - \phi)(r\gamma_{sv}(\zeta_1) + \gamma_{lv}), \quad (9.6)$$

where ϕ is the fraction of the (projected) area where the liquid is in contact with the solid. Substituting (9.5) and (9.6) in (9.2) gives

$$\cos \theta_0 = r \cos \theta - (1 - \phi)(1 + r \cos \theta) \quad (9.7)$$

Note that for $\phi = 1$, (9.7) reduces to (9.4). The Wenzel theory is exact if the liquid is in contact with the substrate everywhere within the nominal liquid-substrate contact area, the Cassie theory is always approximate and often not very accurate. This is easily understood from Fig. 9.3 which shows the interface between a liquid and a solid. $\phi < 1$ is the ratio between the projected liquid-solid contact area and the nominal (or apparent) contact area A_0 . Because the solid surface is curved, the actual liquid-solid contact area will be $A_0\phi s$ where $s > 1$. Similar, since in general the liquid-vapor interface is curved (in spite of the fact that the total curvature $1/R_1 + 1/R_2$ may vanish) and tilted (relative to the average surface plane), the total liquid-vapor interface area is $A_0(1 - \phi)s'$, with $s' > 1$. Similarly, the solid-vapor interface area equals $A_0(1 - \phi)s''$ with $s'' > 1$. In deriving (9.7) it is assumed that $s = s'' = r$ and $s' = 1$.

Comparing (9.4) and (9.7) shows that the Cassie state has the largest $\cos \theta_0$, and hence the lowest free (interfacial) energy if $1 + r \cos \theta < 0$ or

$$\cos \theta < -1/r \quad (9.8)$$

Since r is a measure of the magnitude of the surface roughness, I may qualitatively state that only for hydrophobic surfaces (with $\cos \theta < 0$ or $\theta > 90^\circ$) with large enough roughness (i.e., large enough $r = A/A_0$) will the Cassie state be the thermodynamically stable state.

The approach described above, where the interface is studied at different magnifications, is very general and a similar approach has recently been developed for the contact mechanics between elastic solids with randomly rough surfaces [4] (see also Ref. [137]).

It is well known that the roughness of a hydrophobic solid (with $\theta > 90^\circ$ on the flat substrate) enhances its hydrophobicity. If the contact angle of water on such flat solids is of the order of 100° to 120° , on a rough or micro-textured surface it may be as high as 150° to 175° [128, 137, 138]. Both the Wenzel model and the Cassie model can explain this effect.

Let us consider the most simple surface roughness consisting of a periodic rectangular roughness profile as illustrated in Fig. 9.4 (a) (xz -plane). The free energy (per unit surface area) for the Cassie state shown in the figure is

$$\gamma_C = [(a + 2h)\gamma_{sv} + a\gamma_{lv} + b\gamma_{sl}] / (a + b)$$

The free energy for the Wenzel state (complete contact) is

$$\gamma_W = (a + b + 2h)\gamma_{sl} / (a + b)$$

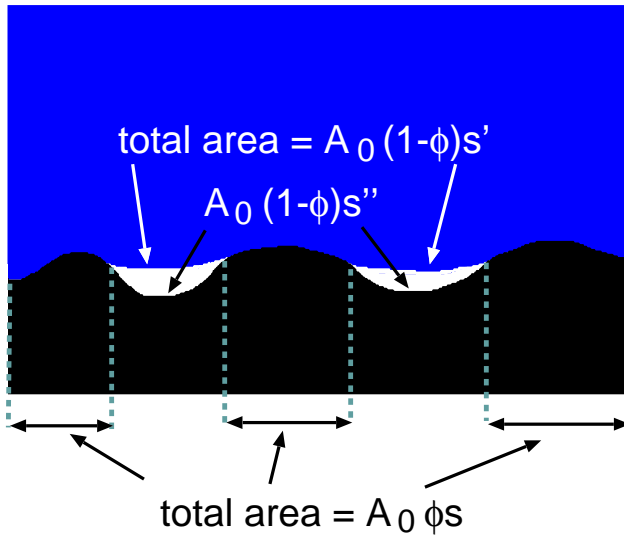


Figure 9.3: The interface between liquid and solid. $\phi < 1$ is the ratio between the projected liquid-solid contact area and the nominal (or apparent) contact area A_0 . Because the solid surface is curved, the actual liquid-solid contact area will be $A_0\phi s$ where $s > 1$. Similar, since in general the liquid-vapor interface is curved (in spite of the fact that the total curvature $1/R_1 + 1/R_2$ may vanish) and tilted (relative to the average surface plane) the total liquid-vapor interface area is $A_0(1 - \phi)s'$, with $s' > 1$. Similarly, the solid-vapor interface area equals $A_0(1 - \phi)s''$ with $s'' > 1$.

Using (9.1) The difference in free energy can be written as

$$\gamma_C - \gamma_W = \gamma_{lv}[a(1 + \cos \theta) + 2h\cos \theta]/(a + b)$$

Thus, the Cassie state has a lower free energy than the Wenzel state if

$$\cos \theta < - \left(1 + \frac{2h}{a}\right)^{-1} \quad (9.9)$$

which is satisfied only if for the flat surface $\theta > 90^\circ$, and if the ratio h/a is large enough. Note that in this case $r = A/A_0 = (a + b + 2h)/(a + b)$ so the (approximate) criteria (9.8) reduces to

$$\cos \theta < - \left(1 + \frac{2h}{a + b}\right)^{-1}$$

which is of similar general form as (9.9). In Nature strongly hydrophobic surfaces are often obtained by covering the surface with thin, long (so that $h/a \gg 1$) hydrophobic fibers. Thus, insects which move on top of water, e.g., water spiders (see Fig. 9.5) have a high density of thin wax coated hair on their legs. In addition, the hair fibers have nanoscale roughness which traps air and enhances the hydrophobicity [139]. In this case the water-leg contact will be in the Cassie state even when the insect is squeezed towards the water by the weight of the insect.

9.2.3 Rough surfaces: activation barriers and hysteresis

Consider a cylindrical cavity as in Fig. 9.4 (b) and assume first the Cassie state as in the figure. Let us apply a pressure p to the droplet. In this case the liquid will bend inwards

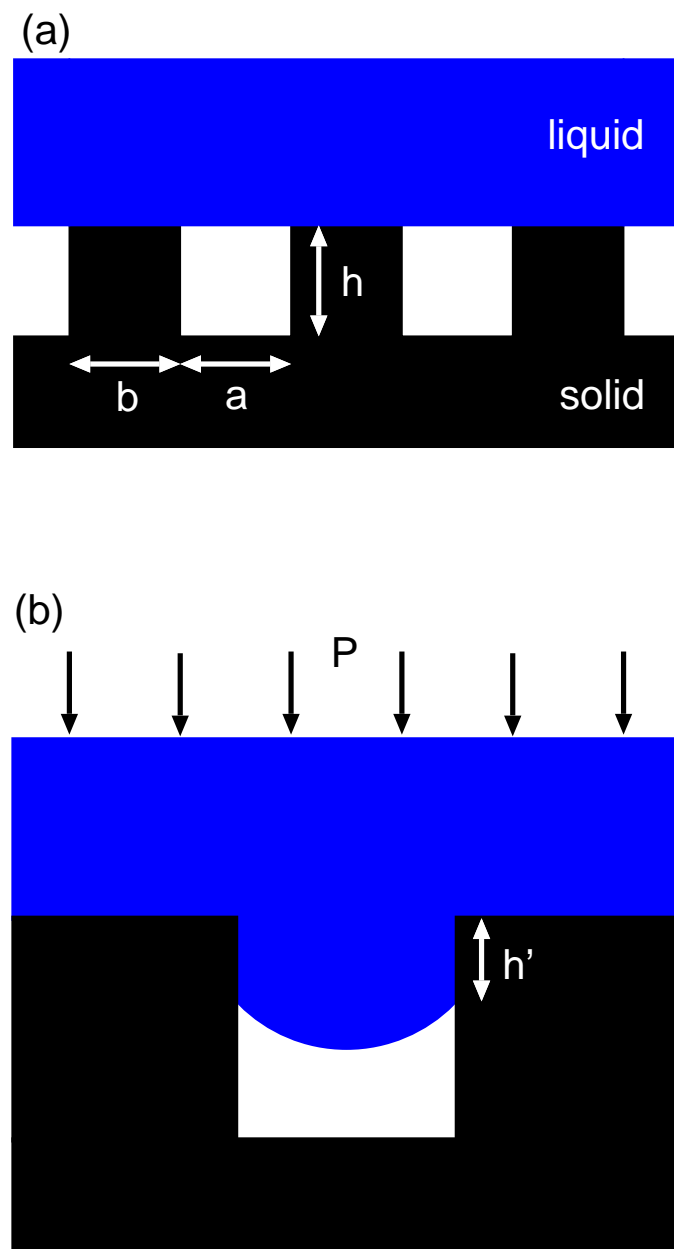


Figure 9.4: (a) Liquid drop (in the Cassie state) in contact with a surface with periodic surface roughness. (b) Even if the Cassie state (incomplete liquid-solid contact) is the ground state, with an applied pressure p one can squeeze the droplet into the Wenzel state.



Figure 9.5: Water spiders have thin hydrophobic (wax coated) hair with nanoscale roughness which traps air and enhances hydrophobicity.

in the cavity and if the applied pressure is larger than a critical value p_c , the liquid will be squeezed into the cavity (let us assume that the air in the cavity can leave the cavity, e.g., diffuse into the liquid). It is easy to show that the pressure

$$p_c = -2\gamma_{\text{sl}} \cos\theta / R \quad (9.10)$$

where R is the radius of the cavity. To prove this relation, note that the pressure work to squeeze the liquid a distance h' into the cavity (see Fig. 9.4) is given by $p_c \pi R^2 h'$ and this must be equal to the change in interfacial free energy which equals $2\pi R h' (\gamma_{\text{sl}} - \gamma_{\text{sv}})$. Using these equations and (9.1) gives (9.10).

From (9.10) it follows that if $\theta < 90^\circ$ (hydrophilic interaction), $p_c < 0$ and the liquid will be spontaneously sucked into the cavity and will fill out the cavity. If $\theta > 90^\circ$ (hydrophobic interaction), $p_c > 0$ and for nanometer sized cavities, the pressure $p_c \sim 100$ MPa, so very high pressure is necessary for squeezing the liquid into narrow cavities. However, if the liquid is squeezed into the cavity and completely fills the cavity, then the resulting Wenzel state is (at least) metastable. However, for nanometer sized cavities thermal fluctuations may give rise to strong local fluctuations between the Cassie (empty cavity) and Wenzel (filled cavity) states. This is easy to understand since the energetic barrier (for a hydrophobic system) for going from the Cassie state to the Wenzel state will be of order $\varepsilon \sim p_c \pi R^2 h \approx -2\pi R h \gamma_{\text{sv}} \cos\theta$ and strong fluctuations (on macroscopic time scales) will occur as long as $\varepsilon \approx 1$ eV or less. In a typical case this condition is satisfied as long as R and h are of order nanometer or less. In the computer simulations I do indeed observe very strong thermal fluctuations at the liquid-solid interface, in particular for rough hydrophobic surfaces, see Sec. 9.4.2.

The Wenzel droplets are highly pinned, and the transition from the Cassie to the Wenzel state results in the loss of the anti-adhesive properties generally associated with superhydrophobicity. However, for nanodroplets on rough hydrophobic surfaces, I find that the Wenzel state is unstable: if the droplet is pressed into contact with the substrate it quickly jumps back to the Cassie state due to strong thermal fluctuations. For a macroscopic droplet the energetic barrier towards flipping from the Wenzel to the Cassie state

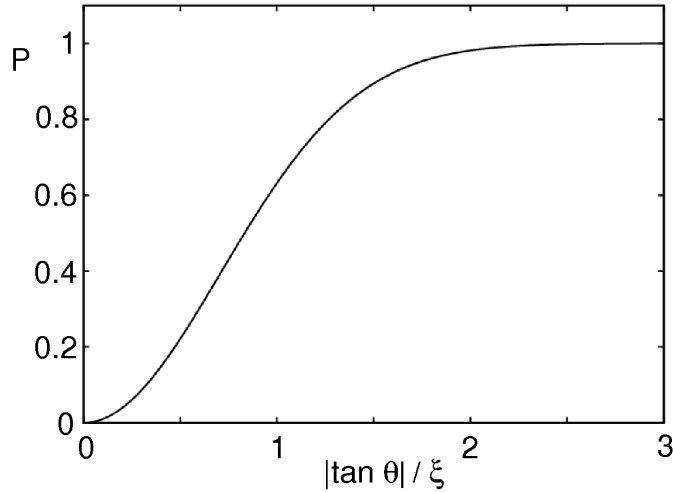


Figure 9.6: The fraction P of the surface area where the absolute value of the slope is smaller than $|\tan\theta|/\xi$ as a function of $|\tan\theta|/\xi$. See text for details.

may be so large that, even if the Cassie state is the minimum free energy configuration, the system remains trapped in the (metastable) Wenzel state for all time periods of physical relevance.

9.2.4 Cassie and Wenzel states for randomly rough surfaces

In this section I discuss under which condition one expects the Cassie state and the Wenzel state to prevail. Consider a rough surface and let $z = h(\mathbf{x})$ be the height of the surface at the point $\mathbf{x} = (x, y)$. For randomly rough surfaces the normalized surface area $r = A/A_0$ is given by (see Appendix C):

$$r = \int_0^\infty dx \left(1 + x\xi^2\right)^{1/2} e^{-x} \quad (11)$$

where

$$\xi^2 = \int d^2q q^2 C(q) = 2\pi \int_0^\infty dq q^3 C(q) = \langle (\nabla h)^2 \rangle \quad (12)$$

is the square of the average slope. The surface roughness power spectrum

$$C(q) = \frac{1}{(2\pi)^2} \int d^2x \langle h(\mathbf{x})h(\mathbf{0}) \rangle e^{i\mathbf{q}\cdot\mathbf{x}}. \quad (13)$$

Here $h(\mathbf{x})$ is the surface height profile and $\langle \dots \rangle$ stands for ensemble average. We have assumed that $\langle h(\mathbf{x}) \rangle = 0$.

The fraction of the surface where the surface slope $s < s_0$ is given by (see Appendix C):

$$P(s_0) = 1 - e^{-(s_0/\xi)^2}.$$

Note that as $\xi \rightarrow 0$ (corresponding to a flat surface) $P(s_0) \rightarrow 1$ which is expected because the slope of a flat surface is zero and hence smaller than any finite value s_0 . Assume that a liquid exhibits the contact angle θ on the perfectly flat substrate. The fraction of the surface where the slope $|\nabla h(\mathbf{x})| < |\tan\theta|$ is given by

$$P(\tan\theta) = 1 - e^{-(\tan\theta/\xi)^2}. \quad (14)$$

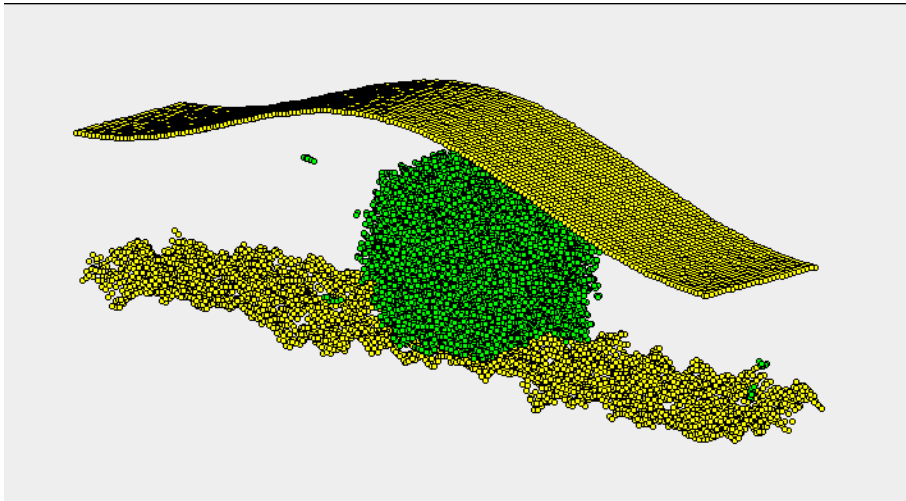


Figure 9.7: 3D side-view snapshot of a octane liquid droplet on a hydrophobic and rough substrate. The rigid substrate comprises 200×30 atoms disposed on a square lattice with lattice constant $a = 2.53 \text{ \AA}$. These atoms have been randomly displaced along the z coordinate, orthogonal to the wall, so to reproduce the desired roughness. The Lennard-Jones solid-liquid interaction potential $V(r) = 4\epsilon[(r_0/r)^{12} - (r_0/r)^6]$ with $r_0 = 3.28 \text{ \AA}$, $\epsilon = 4 \text{ meV}$ for hydrophobic substrate and $\epsilon = 8 \text{ meV}$ for hydrophilic substrate.

This function is shown in Fig. 9.6. Note that more than 90% of the surface area will have a slope below $|\tan\theta|$ if $|\tan\theta|/\xi > 1.5$ and in this case the Wenzel state will tend to prevail, while more than 90% of the surface will have a slope above $|\tan\theta|$ if $|\tan\theta|/\xi < 0.3$ and in this case the Cassie state will tend to prevail. For the system studied below $\xi < 2$ (see Fig. 9.10) and for the hydrophobic system $\theta \approx 103^\circ$ one gets $|\tan\theta|/\xi > 2.2$. Thus, one would expect the Wenzel state to prevail. However, the numerical data (see below) tend to suggest that the system is in a Cassie-like state. We attribute this to the strong fluctuations at the liquid-solid contact which occurs at the nanoscale, which are particularly important for nanoscale droplets.

9.3 Simulation Method

I have used Molecular Dynamics (MD) to study the contact angle and contact angle hysteresis. Here I briefly describe the system and how to generate the rough substrate surfaces.

9.3.1 Molecular dynamics model

MD calculations have been used to study the influence of surface roughness on liquid droplet contact angle and contact angle hysteresis. I have studied hydrocarbon liquid droplets on different self-affine fractal surfaces. The nano-droplet contains 2364 octane molecules C_8H_{18} at $T = 300 \text{ K}$, which is between the melting and boiling points of octane. The fractal surfaces are generated as in Ref. [140]. Different fractal surfaces are obtained by changing the root mean square (rms) roughness amplitude σ , and the fractal dimension D_f . The roll-off wave-vector for the rough surface is $q_0 = 2\pi/L$ with $L = 38 \text{ \AA}$, and the magnitude of the short-distance cut-off wave vector $q_1 = \pi/a$, where $a = 2.53 \text{ \AA}$ is the substrate lattice constant. The (non-contact) cylindrical droplet diameter is about 104

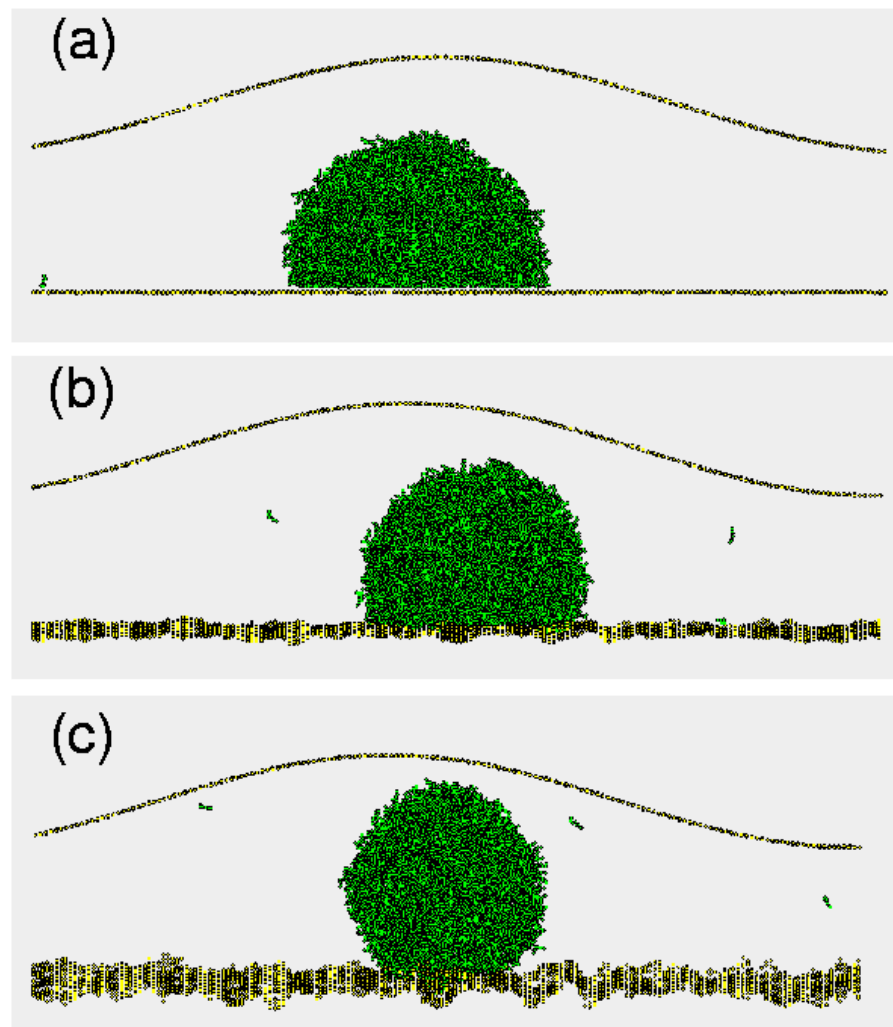


Figure 9.8: Snapshots for different root mean square roughness. (a) the droplet is in contact with the flat substrate. (b) and (c) are for rough substrates with the root mean square amplitude $\sigma = 2.3 \text{ \AA}$ and $\sigma = 4.8 \text{ \AA}$, respectively.

\AA , and the size of the droplet-substrate contact area varies (for the hydrophobic system) from $\approx 115 \text{ \AA}$ (case (a) in Fig. 9.8) to $\approx 60 \text{ \AA}$ (case (c)).

The lubricant molecules are described through the Optimized Potential for Liquid Simulation (OPLS) [26, 27]; this potential is known to provide density and viscosity of hydrocarbons close to the experimental one. We used the Lennard-Jones interaction potential between droplet atoms and substrate atoms. The L.-J. parameters for a hydrophobic surface are chosen in such a way that the Young contact angle is about 100° when a droplet sits on the flat surface. Because of the periodic boundary condition and the size of our system, the liquid droplet forms a cylinder with the central line along the y -axis, see Fig. 9.8. We fit the density profile of the droplet to a cylinder (see Fig. 9.9), and obtain the contact angle $\theta = 103^\circ$ for the droplet in contact with the flat hydrophobic substrate, while for the flat hydrophilic substrate $\theta = 39 \pm 3^\circ$.

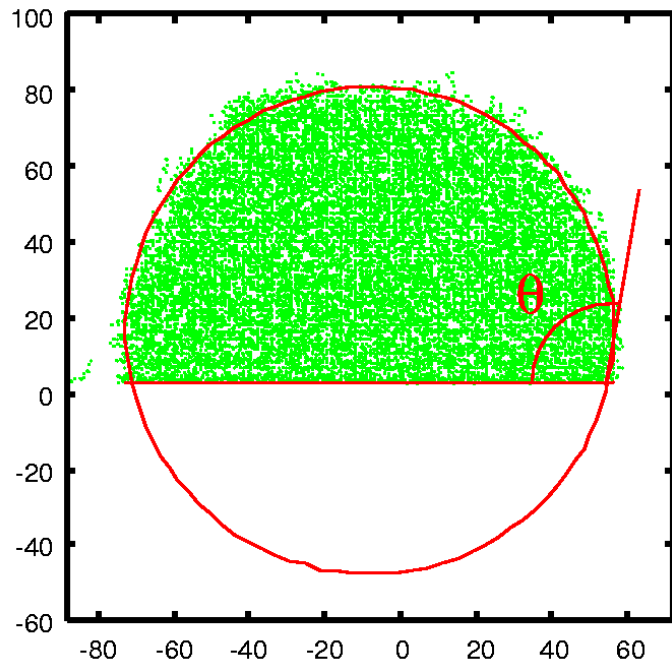


Figure 9.9: Determination of the contact angle θ for the flat substrate. Side view.

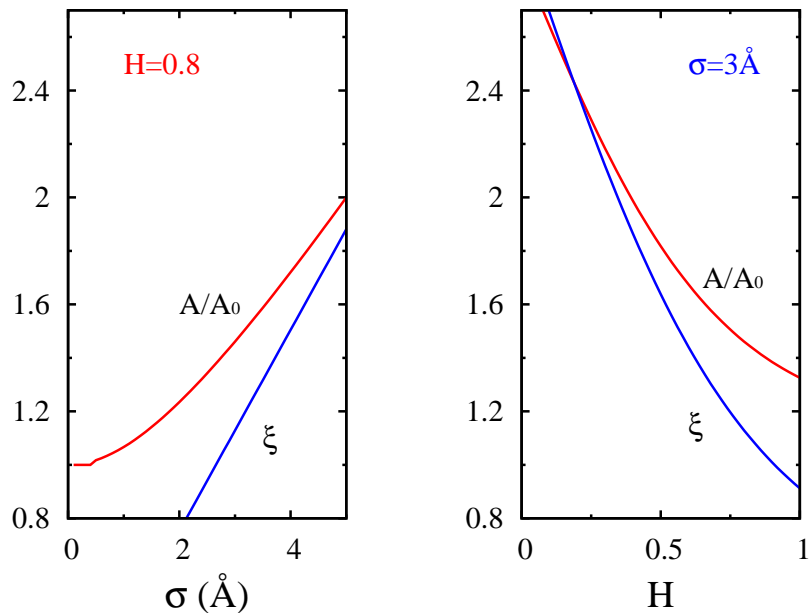


Figure 9.10: The average slope ξ and the ratio A/A_0 between the actual A and the nominal (or projected) A_0 surface area, as a function of the root mean square roughness σ when Hurst exponent $H = 0.8$, and as a function of Hurst exponent H for $\sigma = 3 \text{ \AA}$.

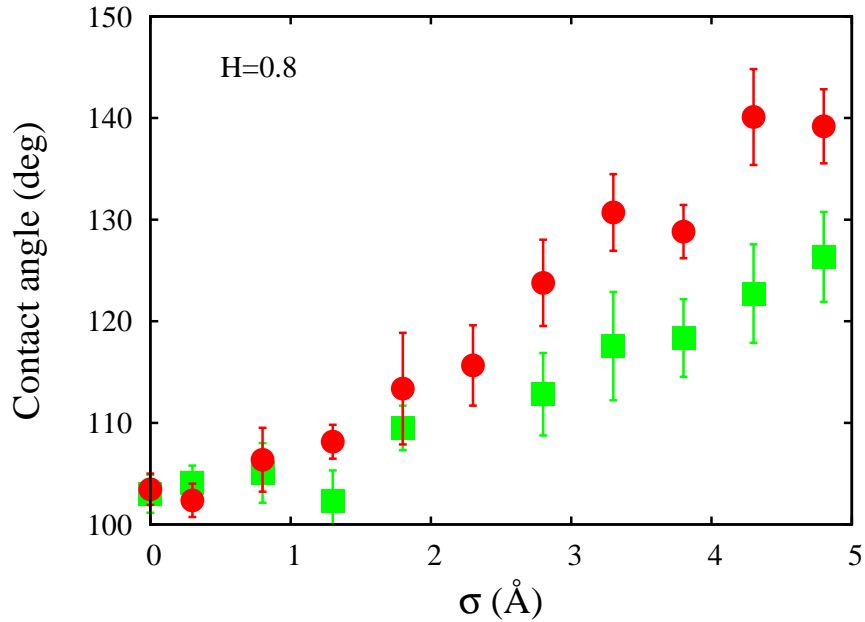


Figure 9.11: The contact angle as a function of the root mean square roughness σ . The circle points are numerical results from the simulations, while the square points are obtained from the Cassie model (see Eq. 9.7). Each data point is an average over several snap-shot configurations. The fractal dimension is $D_f = 2.2$.

9.3.2 Multiscale rough surfaces

Many solid surfaces in nature, e.g., surfaces prepared by fracture (involving crack propagation), tend to be nearly self-affine fractal. Self-affine fractal surfaces have multiscale roughness, sometimes extending from the lateral size of the surface down to the atomic scale. A self-affine fractal surface has the property that if part of the surface is magnified, with a magnification which in general is appropriately different in the directory perpendicular to the surface as compared to the lateral directions, the surface “looks the same” [1] i.e., the statistical properties of the surface are invariant under this scale transformation.

The most important property of a randomly rough surface is the surface roughness power spectrum defined $C(q)$. We assume that the statistical properties of the surface are translational invariant and isotropic so that $C(q)$ depends only on the magnitude $q = |\mathbf{q}|$ of the wave vector q . For a self-affine surface the power spectrum has the power-law behavior $C(q) \sim q^{-2(H+1)}$, where the Hurst exponent H is related to the fractal dimension $D_f = 3 - H$. Of course, for real surfaces this relation only holds in some finite wave vector region $q_0 < q < q_1$. Note that in many cases there is roll-off wavevector q_0 below which $C(q)$ is approximately constant. The self-affine fractal surfaces are generated by adding plane waves with random phases and appropriately chosen weights, as described in detail in Ref. [1, 6].

The average slope ξ and the ratio A/A_0 between the surface area A and the nominal (or projected) A_0 surface area, have been shown in Fig. 9.10 as a function of the root mean square roughness σ when Hurst exponent $H = 0.8$, and as a function of Hurst exponent H for $\sigma = 3 \text{ \AA}$.

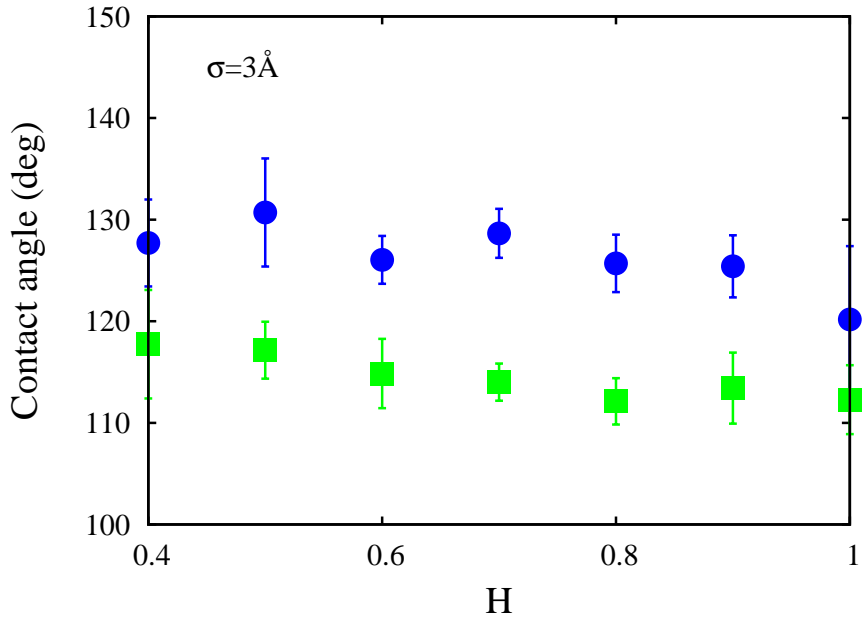


Figure 9.12: The contact angle θ as a function of Hurst exponent H for the rms roughness $\sigma = 3 \text{ \AA}$. The circles and squares have the same meaning as that in Fig. 9.11. The fractal dimension is $D_f = 3 - H$.

9.4 Numerical results

We present numerical results for the contact angle and contact angle hysteresis for both hydrophilic and hydrophobic systems. The substrate surfaces are assumed to be self-affine fractal, but the fractal dimension and the root-mean-square roughness amplitude have been varied.

9.4.1 Static contact angle on hydrophobic surface

The apparent contact angle, θ_0 , as a function of the root mean square roughness (rms), is shown in Fig. 9.11 with the fractal dimension $D_f = 2.2$. There is a strong increase in θ_0 with increasing rms-roughness amplitude. Fig. 9.12 shows how θ_0 depends on the Hurst exponent $H = 3 - D_f$. Note that θ_0 is almost independent of H .

Accordingly to the Wenzel equation, the apparent contact angle θ_0 depends only on the surface roughness via the ratio $r = A/A_0$. Fig. 9.10 shows that as H decreases from 1 to 0.4 (i.e., D_f increases from 2 to 2.6), A/A_0 increases by $\sim 50\%$. However, the MD-calculations show that the apparent contact angle θ_0 is almost independent of the fractal dimension, see Fig. 9.12. Thus the Wenzel equation cannot be used in the present situation. This is consistent with a visual inspection of the liquid-substrate interface which shows that on the rough substrates, the droplet is “riding” on the asperity tops of the substrate, i.e., the droplet is in the Cassie state. In order to quantitatively verify this, one need to calculate the distances $u(x, y)$ between the bottom surface of the liquid drop and the rough substrate surface in the (apparent) contact area. From the distribution

$$P(u) = \langle \delta[u - u(x, y)] \rangle$$

of these distances [see Fig. 9.13(a)] one obtains the fraction ψ of the (projected) surface

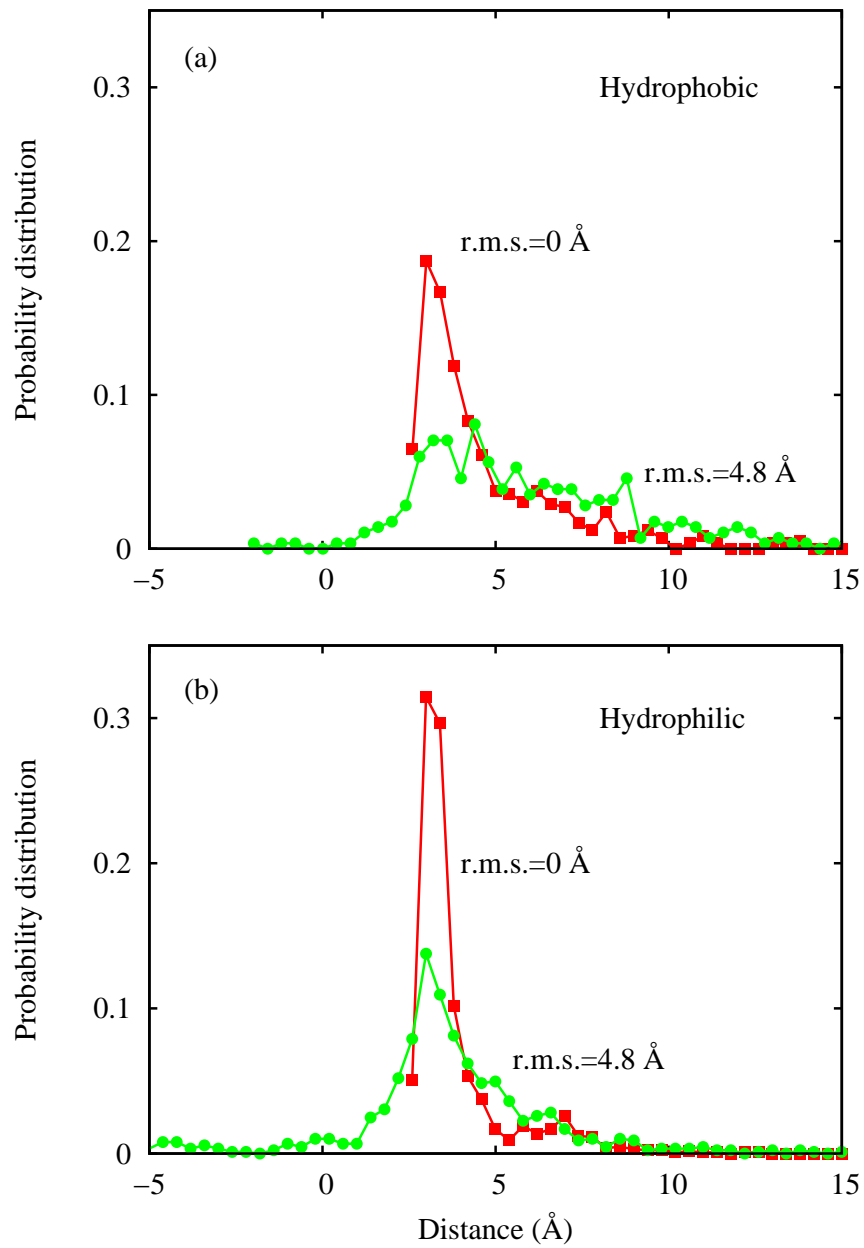


Figure 9.13: (a) The height probability distribution for hydrophobic surface both flat (squares) and rough (circles). (b) The height probability distribution for hydrophilic surface both flat (squares) and rough (circles).

area where contact occurs:

$$\psi = \int_0^{u_1} du P(u),$$

where u_1 is a cut-off distance to distinguish between contact and no-contact regions, which has to be comparable to the typical bond distance ($u_1 = 4\text{\AA}$ has been used). Note that due to the thermal fluctuations $\psi = \psi_0$ for flat surface is less than 1. Using the normalized $\phi = \psi/\psi_0$, the Cassie model (with $r = 1$) predicts the variation of the contact angle with σ and H given in Fig. 9.11 and 9.12 (square points).

Fig. 9.11 shows that the apparent contact angle θ_0 increases strongly with increasing rms-roughness amplitude, at fixed fractal dimension $D_f = 2.2$, while it is nearly independent of the fractal dimension D_f (see Fig. 9.12). Since increasing the fractal dimension at constant rms-roughness amplitude mainly increases the short-wavelength roughness, I conclude that the nanoscale wave length roughness doesn't matter so much in determining the contact angle for hydrophobic surfaces, while the long wavelength roughness plays an important role. We attribute this fact to the strong thermal fluctuations in the height (or width) u of the liquid-solid interface which occur at the nanoscale even for the flat substrate surface. Note also that in our model the wall-wall interaction is long-ranged, decaying effectively as $\sim 1/u^3$, so there will be a contribution to the interfacial energy also for non-contacting surfaces which, of course, is not rigorously included in the macroscopic Cassie model.

9.4.2 Dynamic contact angle: Contact angle hysteresis

The advancing contact angle θ_a is measured when the solid/liquid contact area increases, while the receding contact angle θ_r is measured when the contact area shrinks. If the difference $\theta_a - \theta_r$ is nonzero, the liquid-substrate system exhibits *contact angle hysteresis*.

Hydrophobic surfaces

Figs. 9.14 and 9.15 show the time-evolution of the advancing contact angle θ_a and receding contact angle θ_r , respectively, for a nanodroplet on a rough, hydrophobic substrate. The former has been obtained by placing the droplet close to the substrate, so that the drop will spontaneously spread under the adhesive interaction with the substrate. The contact angle evolves in time from $\theta = 180^\circ$ (non-contact) in panel 9.14(a) to its asymptotic value $\theta_a = 140^\circ$, reached after 3ns in panel 9.14(h).

The receding contact angle was simulated by squeezing the droplet into pancake-like shape with the upper wall. The interaction between the atoms of the upper wall and drop atoms is given by the repulsive term of a Lennard-Jones potential, i.e. $V(r) = 4\epsilon_0(r_0/r)^{12}$. The lack of attraction with the top surface allows us to suddenly pull the wall up, leaving the drop in the configuration of panel 9.15(a). Then the free drop increases the contact angle up to the asymptotic value θ_r . Fig. 9.16 shows the time evolution of the contact angle for these two cases: within spontaneous fluctuations of simulations, the two asymptotic contact angles coincide.

To be sure that in any system there is no contact angle hysteresis, the extensive simulations have been performed on various substrates with different Hurst exponent H (see Fig. 9.17(a)), and with different root-mean-square roughness amplitude(rms) (see Fig. 9.17(b)). The receding contact angle reaches its asymptotic value within about 2 or 3 nanoseconds. As the receding contact angle is concerned in Fig. 9.17, the contact angle variation at $t = 2\text{ns}$, as the rms increases from 0.3\AA to 4.8\AA , is much wider than that as Hurst exponent H increases from 0.4 to 1.0. The root-mean-square roughness is mainly determined by long wavelength roughness of the surface. Increasing the fractal dimension

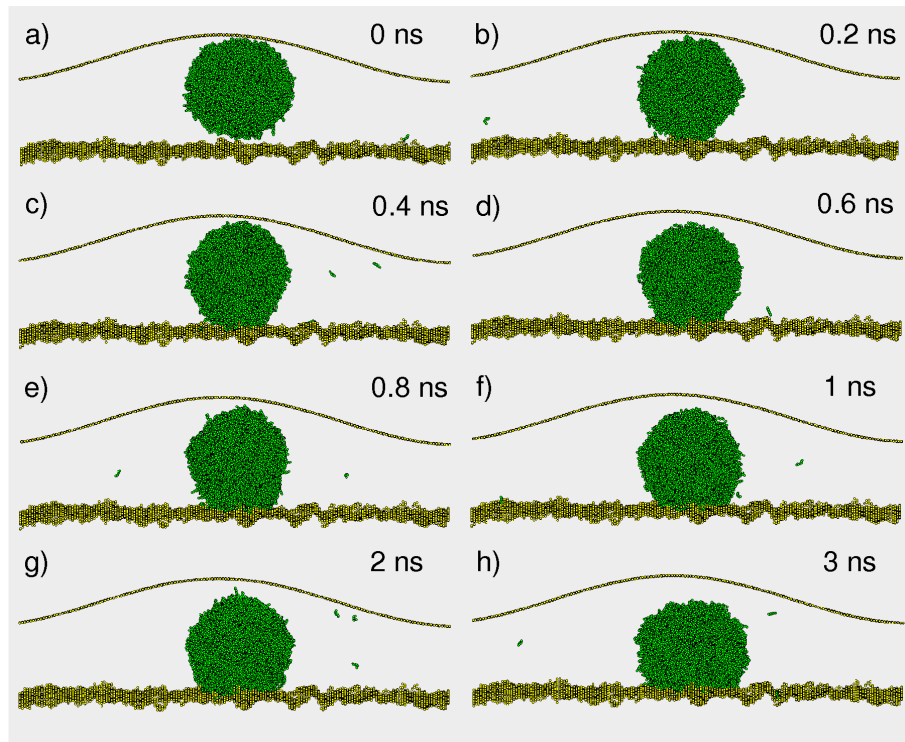


Figure 9.14: The advancing contact angle θ_a evolution for hydrophobic nanodroplet. θ_a is measured when the solid/liquid contact area increases.

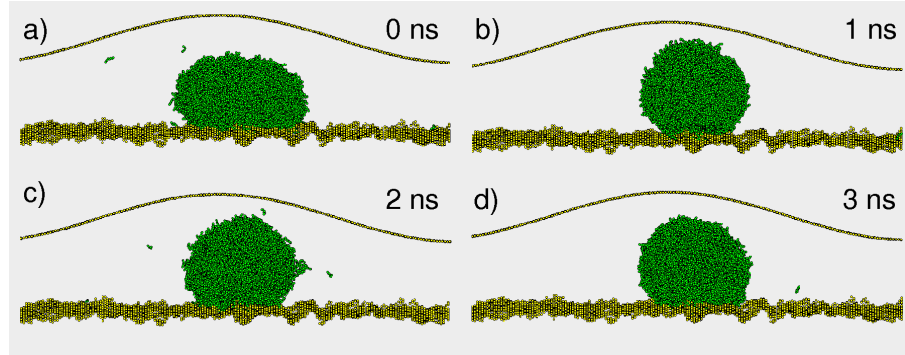


Figure 9.15: The receding contact angle θ_r evolution for hydrophobic nanodroplet. θ_r is measured when the solid/liquid contact area shrinks.

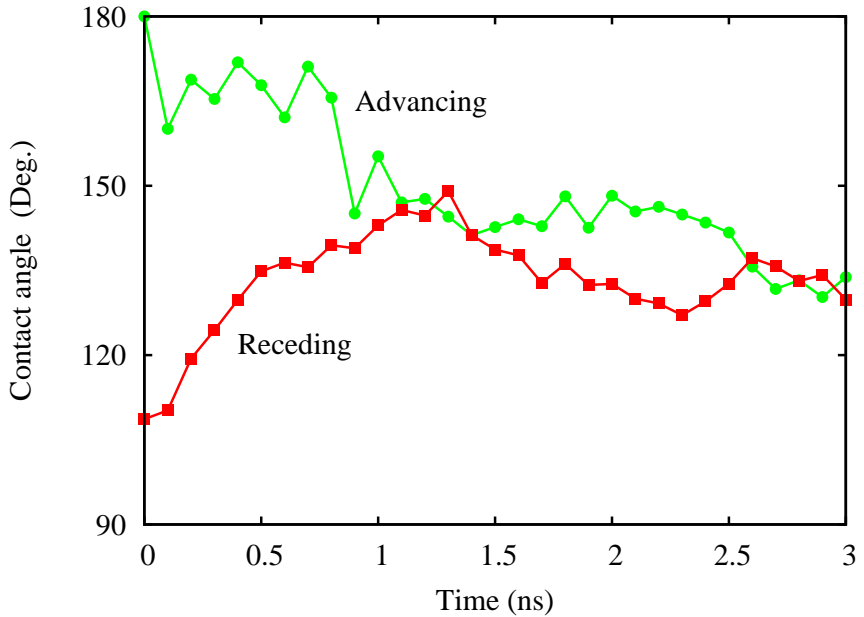


Figure 9.16: The advancing (circles) and receding (squares) contact angle θ , for hydrophobic substrate, as a function of time. The root-mean-square roughness of the substrate is $\text{rms} = 4.8 \text{ \AA}$. $\epsilon = 4 \text{ meV}$ and $r_0 = 3.28 \text{ \AA}$. The thermal equilibrium contact angle has been reached after a few nanoseconds, irrespective of whether the initial contact angle is larger or smaller than the equilibrium angle.

D_f signifies that the short wavelength roughness increases. Thus, one can see that the contact angle is more sensitive to the long wavelength roughness of the substrate than to the short wavelength roughness. This agrees with the results in Fig. 9.11 and Fig. 9.12.

A comparison of these results with those of the corresponding simulations for the advancing contact angle, confirms that there is no hysteresis. The difference between the data is unbiased due to the unavoidable thermal fluctuations on such a small scale (nanoscale). Thus, on *macroscopic* time scales, for hydrophobic systems the nano-scale roughness will not result in any hysteresis in the contact angle. This is in drastic contrast to simulation studies I have performed for hydrophilic surfaces (see below), where surface roughness results in strong pinning of the boundary line; for such surfaces it is therefore impossible to study static droplet contact angles (as observed on macroscopic time scales) using molecular dynamics.

Comparing the form of $P(u)$ for the flat and the most rough surfaces shows that the system is in the Cassie state, but at the nanoscale the difference between the Cassie state and the Wenzel state is not so large due to the thermal fluctuations. This also explains why no hysteresis is observed: The Wenzel state is probably the energy minimum state, but squeezing the droplet into a pancake shape does not push the system permanently into the Wenzel state because even if it would go into this state temporarily, the free energy barrier separating the Cassie and Wenzel states is so small that thermal fluctuations would quickly kick it back to the Cassie-like state.

Hydrophilic surfaces

Let us now consider the case where the liquid droplet contact angle on the flat surface $\theta < 90^\circ$ (hydrophilic system). We choose the energy parameter and the equilibrium

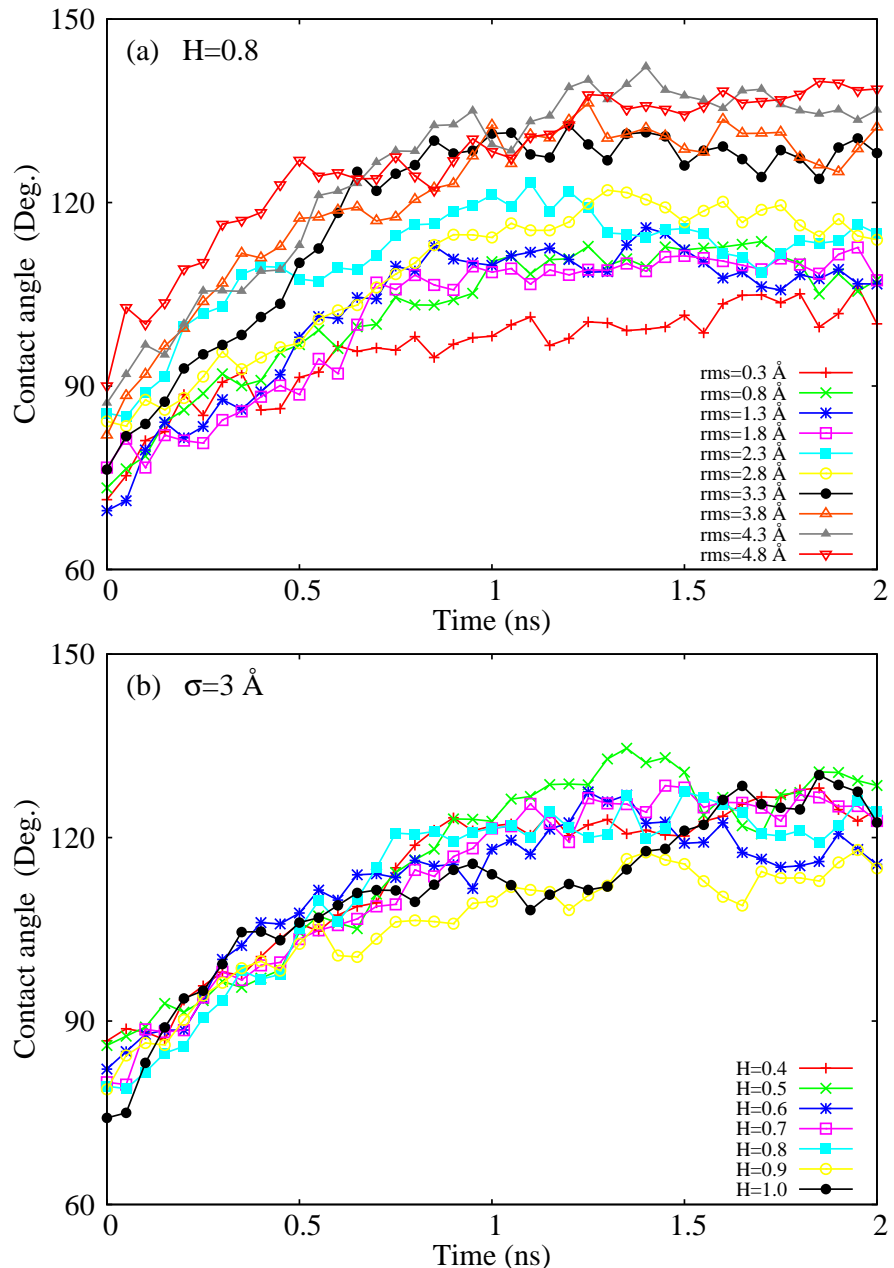


Figure 9.17: The time evolution of the receding contact angle for the hydrophobic droplets, on the substrates (a) with various values of root-mean-square (rms) roughness and fixed Hurst exponent $H = 0.8$, and (b) with various values of Hurst exponents H and fixed root-mean-square roughness $\text{rms} = 3 \text{ \AA}$.

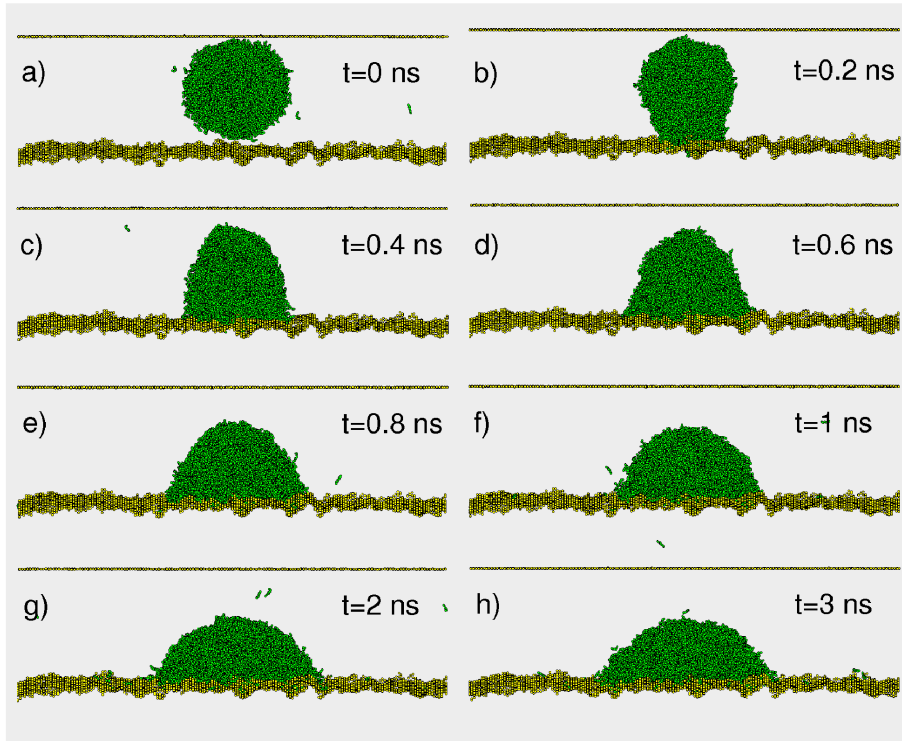


Figure 9.18: Advancing contact angle evolution for hydrophilic nanodroplet. The root-mean-square roughness of the substrate is $\text{rms} = 4.8 \text{ \AA}$. The energy parameter and the equilibrium distance in L.-J. potential are $\epsilon = 8 \text{ meV}$ and $r_0 = 3.28 \text{ \AA}$.

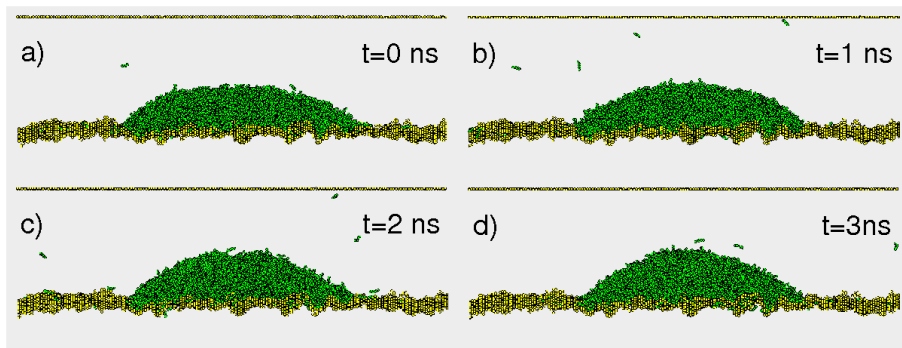


Figure 9.19: Receding contact angle evolution for hydrophilic nanodroplet. The root-mean-square roughness of the substrate is $\text{rms} = 4.8 \text{ \AA}$. The energy parameter and equilibrium parameter in L.-J. potential are $\epsilon = 8 \text{ meV}$ and $r_0 = 3.28 \text{ \AA}$.

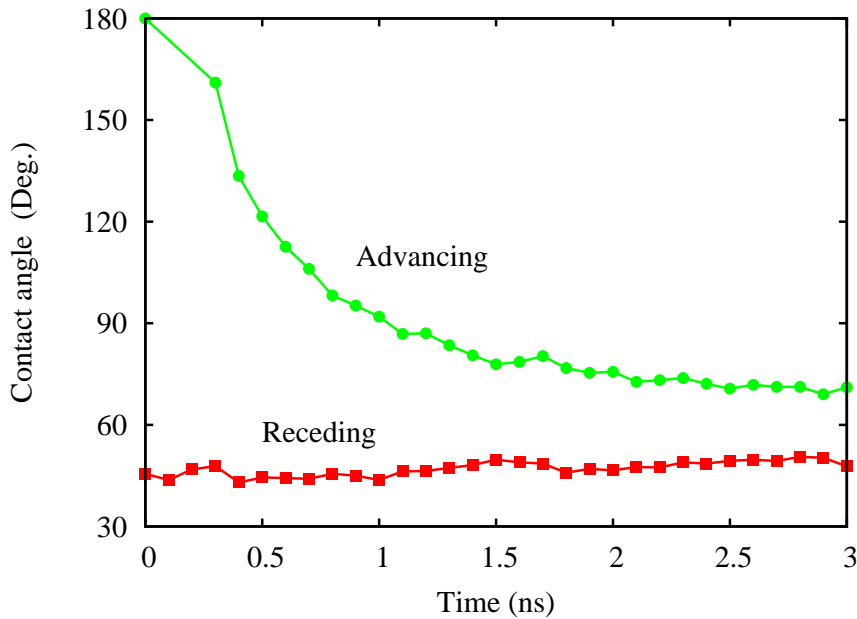


Figure 9.20: The advancing (circles) and receding (squares) contact angle θ , for the hydrophilic substrate, as a function of time. The root-mean-square roughness of the substrate is $\text{rms} = 3 \text{ \AA}$, and the L.-J. substrate-liquid interaction parameters $\epsilon = 8 \text{ meV}$ and $r_0 = 3.28 \text{ \AA}$.

distance in L.-J. potential, associated with the liquid-solid atom interaction, as $\epsilon = 8 \text{ meV}$, $r_0 = 3.28 \text{ \AA}$ respectively. This gives $\theta \approx 70^\circ$. Figs. 9.18, 9.19 and 9.20 for hydrophilic droplet, are analogous to Figs. 9.14, 9.15 and 9.16 respectively, for hydrophobic droplet. The time dependence of the advancing contact angle for the hydrophilic nanodroplet has been shown in Fig. 9.18. The root-mean-square roughness of the substrate is $\text{rms} = 4.8 \text{ \AA}$.

The time evolution of the receding contact angle for hydrophilic nanodroplet has been shown in Fig. 9.19.

Fig. 9.20 shows the advancing (circles) and receding (squares) contact angle θ , for the hydrophilic substrate, as a function of time, when the root-mean-square roughness of the substrate is $\text{rms} = 3 \text{ \AA}$. Note that the thermal equilibrium contact angle cannot be reached on the time-scale of the simulations.

Finally, the height probability distribution for the hydrophilic surface for both the flat (squares) and rough (circles) hydrophilic surface, has been shown in Fig. 9.13(b). Note that the fluctuations of liquid-solid separation at the interface are much smaller on the hydrophilic surface than on the hydrophobic surface [9.13(a)].

9.5 Discussion

In most practical cases it is not possible to modify the surface roughness without simultaneously affecting the chemical nature of the surface. This is obvious for crystalline materials, where surface roughening will result in the exposure of new lattice planes with different intrinsic surface energy, it may also hold for amorphous-like materials, where surface roughening may result in a more open atomic surface structure, with an increased fraction of (weak) unsaturated bonds. In our model a similar effect occurs, and some frac-

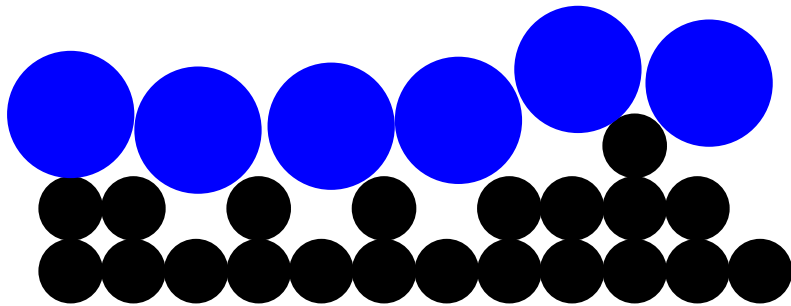


Figure 9.21: The natural separation between the molecules in a liquid is usually considerably larger than the atom-atom separation on the substrate surface. This implies that the fluid molecules cannot “follow” the atomic scale roughness so that the fluid molecules will naturally be in a Cassie-like state with respect to the shortest substrate roughness components determined by the substrate nearest neighbor atom-atom separation.

tion of the change in the contact angle with increasing root-mean-square amplitude may be associated with this effect. However, the most important result of our study, namely that the contact angle is mainly determined by the long-wavelength roughness, should not be affected by this fact.

Another reason for why the short-wavelength (atomic) roughness may influence the liquid contact state differently from long-wavelength roughness has to do with the fact that the natural separation between the molecules in a liquid is usually considerably larger than the atom-atom separation on the substrate surface. This implies that the fluid molecules cannot “follow” the atomic scale roughness (see Fig. 9.21) so that the fluid molecules will naturally be in a Cassie-like state with respect to the shortest substrate roughness wavelength components, determined by the substrate nearest neighbor atom-atom separation.

It is important to note that the discussion is also relevant for the contact between macroscopic liquid drops and rough substrates. That is, if the solid-liquid interface is studied with nanometer resolution λ , then the strong fluctuations (in time and space) at the liquid-solid interface discussed above will also be observed for a macroscopic droplet, and the interfacial energy $\gamma_{sl}(\zeta)$ for $\zeta = D/\lambda$ (where D is the diameter of the nominal contact area between the (macroscopic) liquid droplet and the substrate) will be the same as obtained above for nanodroplets at the same resolution λ .

9.6 Summary

In this chapter I have discussed under which condition the Wenzel or Cassie state is favorable on randomly rough surfaces. The contact angle and the contact angle hysteresis, on hydrophobic and hydrophilic surfaces, have been studied. We have found that thermal fluctuations play an important role at the nanoscale. The contact angle on hydrophobic surfaces depends strongly on the root-mean-square roughness of the substrate, but is nearly independent of the fractal dimension. For hydrophobic surfaces, there is no contact angle hysteresis due to the strong thermal fluctuations at the nanoscale. For hydrophilic surfaces, the contact angle hysteresis has been observed due to the pinning effect. This indicates that on randomly rough hydrophobic surfaces the Cassie-like state often prevails, at least for nanoscale droplets.

Chapter 10

Concluding Remarks

I summarize now the main new results of this thesis and discuss the prospects for future work.

I have been involved in developing a multiscale molecular dynamics (MD) approach that can properly describe the bulk property of the elastic solid and save much computer time.

I have used multiscale MD to study the contact between the elastic block and a rigid randomly rough surface. For small loads, in the absence of adhesion, the real contact area varies linearly with the load, in good agreement with the continuum contact mechanics theories, i.e. the theories of Bush et al. [49] and of Persson [2]. These theories predict that at small load, the real contact area is proportional to the load although the constants of proportionality differing by a factor of $2/\pi$. The real contact area from the MD calculation lies in between the two theories.

I have also studied the interfacial separation between two randomly rough surfaces. For small loads, the average interfacial separation depends logarithmically on the load or squeezing pressure, which agrees very well with the elegant theory developed by Persson [52] and with the finite element calculations of Robbins et al. [53] and with the experimental results of Israelachvili et al [58].

When adhesion is included, the logarithmic relation between squeezing pressure and the average interfacial separation no more holds. For the same squeezing pressure, the stronger the adhesion, the smaller the interfacial separation. Eventually, the interfacial separation will tend to a finite value, at least if the adhesion is strong enough, when the squeezing pressure approaches zero.

I have also studied the probability distribution of the interfacial separation at different squeezing pressures, which is very important for estimating the fluid leaking through seals. While studying the interfacial separation, I have surprisingly found that the contact mechanics theory of Persson can be applied to all ranges from small contact (small load) to full contact (high load) by introducing the “correction factor”. Persson’s theory is particularly accurate when full contact is reached.

A theory for leak-rate of seals, based on percolation theory and a recently developed contact mechanics theory, has been developed to study both static and dynamic seals. Molecular dynamics simulations show that when two elastic solids with randomly rough surfaces are squeezed together, with increasing magnification or decreasing squeezing pressure, a non-contact channel percolates when the relative projected contact area, A/A_0 , is about 0.4, in accordance with percolation theory.

I have simulated the sliding of elastic solids in adhesive contact with flat and rough interfaces. When the sliding material is hard, there is extremely low friction (superlubricity). The friction increases abruptly as the elastic modulus decreases, and a relatively small

surface roughness may kill the superlubric state. A small amount of lubricant molecules trapped in the asperity contact regions leads to increased friction. Qualitatively, a low concentration of adsorbates is equivalent to increased surface roughness and results in more instabilities and enhanced friction.

I have studied the behavior of liquid nanodroplet on rough hydrophobic and hydrophilic solid surfaces. On hydrophobic surfaces, the contact angle for nanodroplets strongly depends on the root mean square roughness amplitude, but it is nearly independent of the fractal dimension of the surface. For rough hydrophobic surfaces, there is no contact angle hysteresis due to strong thermal fluctuations that occur at the liquid-solid interface on the nanoscale. However, on hydrophilic surfaces, there is strong contact angle hysteresis due to higher energy barriers. These findings may be very important for the development of artificially bio-mimetic superhydrophobic surfaces.

I hope these “simulated experiments” will be followed by “real experiments” between randomly rough surfaces.

Acknowledgments

Almost four years have passed rapidly. Almost four years of intensive work, new experiences, routinely research, failures and successes. For me they were years of growth: my first conference, first poster, first talk, first article ... I want to express my gratitude to Forschungszentrum Jülich as a research center. Here I had the opportunity to work on modern computers, have access to recent research, study new things...

Of course, all these things would have been impossible without the people with whom I worked. I thank my supervisor Bo Persson for providing me such a good opportunity to study with him, for his encouragement, faith and patience, and for his ability to be at the frontier of our research field, for teaching me how to think and do research and live in physics, for providing me good environment to do research.

I thank Prof. Valentin Popov for providing me the possibility at the TU Berlin.

Great thanks to Ugo Tartaglino for opening me to the world of computers and molecular dynamics, and for his clear and patient criticism. I benefited much from his illuminating discussions.

Many thanks go to Vladimir Samoilov, Alexander Volokitin, and Ion Sivebaek for kind and useful discussions.

I express my gratitude to Robert Jones and Andreas Bringer: their support was very helpful in many situations, both in physics and in practical life. For instance, they gave me many good advices and patient criticism during the preparation of my first talk in an international conference.

I thank Stefan Blügel, the head of my research group in Jülich. Thanks to him the research center of Jülich provided me a doctoral position and financial support for my many trips to various conferences.

I thank Simon Woodford for his kindness in explaining me the ideas of quantum mechanics and for discussions before my talk at the APS March meeting.

These years would be certainly less colorful and advantageous without my group mates and friends, who shared humor and ideas especially in the coffee break. Many thanks to Ansgar Liebesch, Antonio Perroni, Luigi, Andreas Dolfen, Marcus Heide, David Bauer, Ute Winkler for their kind help. Before coming to Germany, I had no idea of the environment that I would have found. It turns out that most of the people are very friendly and warmhearted. There are too many people I should thank, but it is impossible to list them all.

Of course, special thanks to my mother Cangzhen Liu, my father Xihai Yang and my sister Lingling Yang.

Appendix A

Contact Mechanics Theories

Here I briefly review the history of continuum models of contact mechanics. I first consider the single asperity contact theories, dating back to the pioneering work of Hertz in 1881 [141]. Secondly I will review multi asperities contact theories, as used to describe the contact between randomly rough surfaces.

A.1 Single asperity contact

A.1.1 Hertz theory

The simplest force law to approximate the actual sphere-sphere surface interaction was chosen by Hertz. He neglected the attractive forces and modeled the repulsive part by a hard wall. Hertz theory predicts for the contact radius r_0 of the contact region

$$r_0 = \left(\frac{RF}{K} \right)^{1/3} \quad (\text{A.1})$$

where F is the external squeezing force, $R = (1/R_1 + 1/R_2)^{-1}$ the effective radius with R_1, R_2 as the radii of curvature of upper sphere and lower sphere, respectively, $K = (4/3) [(1 - \nu_1^2)/E_1 + (1 - \nu_2^2)/E_2]^{-1}$ the effective elastic modulus, with E_1, E_2 and ν_1, ν_2 as elastic moduli and Poisson ratios of upper sphere and lower sphere respectively. If the lower surface is flat, then $R_2 = \infty$, thus $R = R_1$.

The vertical displacement h of the two bodies in contact

$$h = \frac{r_0^2}{R} \quad (\text{A.2})$$

The pressure distribution in the contact area depends only on the distance r from the center of the circular contact area

$$\sigma(r) = \sigma_0 \left[1 - \left(\frac{r}{r_0} \right)^2 \right]^{1/2} \quad (\text{A.3})$$

where $\sigma_0 = \frac{3}{2} \langle \sigma \rangle = \frac{3}{2} \frac{F}{\pi r_0^2}$, $\langle \sigma \rangle$ is the average pressure.

A.1.2 JKR theory

Johnson, Kendall and Roberts in 1971 extended the Hertz theory to adhesive contacts, with the so called “JKR theory” [46]. The JKR theory introduces the attractive force which acts only inside the contact area. F_{JKR} denotes the effectively acting loading force

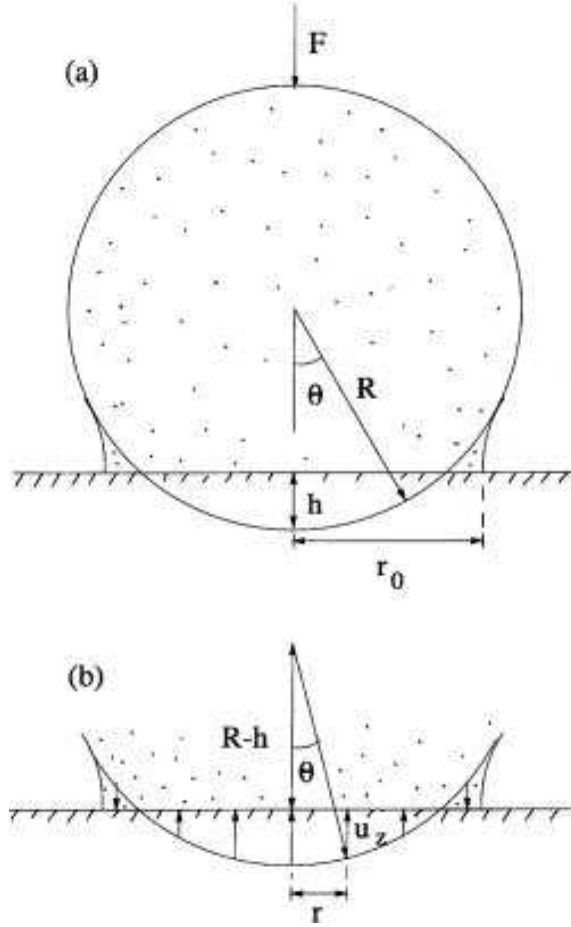


Figure A.1: where F is normal squeezing load and γ be adhesive energy per unit area. An elastic ball with radius R squeezed against a flat rigid substrate. Adapted from Ref. [3]

including the normal squeezing load F and the adhesive contribution inside the contact area. Consider an elastic ball with radius R squeezed with a flat rigid substrate, see Fig. A.1.

$$F_{JKR} = F + 3\pi R\gamma + \left(6\pi R\gamma F + ((3\pi R\gamma)^2)\right)^{1/2} \quad (\text{A.4})$$

Once the effective load is known, it is easy to get the radius of contact area r_{JKR} ,

$$r_{JKR} = \left(\frac{RF_{JKR}}{K}\right)^{1/3} \quad (\text{A.5})$$

vertical displacement h_{JKR} ,

$$h_{JKR} = \frac{r_{JKR}^2}{R} \quad (\text{A.6})$$

and the pressure distribution of σ_{JKR}

$$\sigma(r) = \sigma_0 \left[1 - \left(\frac{r}{r_{JKR}}\right)^2\right]^{1/2} + \sigma_1 \left[1 - \left(\frac{r}{r_{JKR}}\right)^2\right]^{-1/2} \quad (\text{A.7})$$

for $r < r_{JKR}$ and zero otherwise [3, 41]. In Eq. A.7,

$$\sigma_0 = \frac{E^*}{\pi} \frac{2r_{JKR}}{R} \quad (\text{A.8})$$

$$\sigma_1 = \frac{E^*}{\pi} \left(\frac{h_{JKR}}{r_{JKR}} - \frac{r_{JKR}}{R} \right) \quad (\text{A.9})$$

where $1/E^* = (1 - \nu_1^2)/E_1 + (1 - \nu_2^2)/E_2$. After minimizing the free energy of the system, one can get the pull-off force $F_s = -3/2\pi R\gamma$.

Furthermore, Derjaguin, Muller and Toporov in 1975 also extended the Hertz theory but this time they included adhesion outside the contact area by considering the long range attractive forces [142–145]. There is no analytical solution in original DMT theory [146]. In 1992, Maugis proposed the effectively acting loading force F_{DMT} including the normal load. DMT theory gets the pull-off force $F_s = -2\pi R\gamma$. The discrepancy between JKR theory and DMT theory was explained by Tabor by introducing a dimensionless number [147]

$$\mu = \left(\frac{R\gamma}{E^{*2}\epsilon^3} \right)^{1/3} \quad (\text{A.10})$$

where ϵ is the inter-atomic spacing. Tabor number μ can be explained as the ratio of elastic displacement of the surfaces at the point of separation to the effective range of the surface force [148]. When μ is quite large, JKR theory applies, e.g. large deformation with soft material; When μ is quite small, DMT theory applies, e.g. small deformation with hard material.

A.2 Multi asperities contact

In the previous section, I deal with the two simple models for a sphere in contact with a perfectly flat surface. Now let us consider the models for rough surfaces.

A.2.1 Greenwood-Williamson theory

Consider a surface with roughness on a single length scale, and approximate the asperities as spherical bumps with equal radius of curvature and with a Gaussian height distribution [50]

$$P_h = \frac{1}{(2\pi)^{1/2} h_{rms}^*} \exp \left(-\frac{h^2}{2h_{rms}^{*2}} \right) \quad (\text{A.11})$$

where h_{rms}^* is the root-mean-square amplitude of the summit height fluctuations, which is slightly smaller than the root-mean-square roughness amplitude h_{rms} of the surface profile $h(\mathbf{x})$. Assume that one can neglect the (elastic) interaction between the asperity contact regions. If the separation between the surfaces is denoted by d , an asperity with height $h > d$ will make contact with the plane and the penetration $s = h - d$. Thus, using the Hertz contact theory with $s = h - d$ the normalized area of real contact is

$$\frac{\Delta A}{A_0} = \pi n_0 R \int_d^\infty dh (h - d) P_h \quad (\text{A.12})$$

where A_0 is the nominal contact area and n_0 the number of asperities per unit area. The number of contacting asperities per unit area is

$$\frac{N}{A_0} = n_0 \int_d^\infty dh P_h \quad (\text{A.13})$$

and the nominal squeezing stress is

$$\sigma_0 = \frac{F_N}{A_0} = \frac{4E}{3(1-\nu^2)} n_0 \int_d^\infty dh (h-d)^{3/2} R^{1/2} P_h \quad (\text{A.14})$$

According to Ref. [60], the Greenwood-Williamson theory predicts that the contact area depends weakly non-linearly on the squeezing pressure, and the average contact patch area increases with squeezing pressure.

Fuller and Tabor have generalized the Greenwood-Williamson theory by introducing the adhesive interaction between randomly rough surfaces [48]. They applied JKR asperity contact model to each asperity contact area, instead of the Hertz model used in the original theory.

A.2.2 Bush-Gibson-Thomas theory

Bush et al. generalized the theory of Greenwood and Williamson, removing the assumption that all the asperities have to be spherical with the same radius [49,149]. The surface height profile $z(x, y)$ around the summit of an asperity can be expanded with a Taylor's series, up to the second order in Talor's expansion. All the asperities look like paraboloids. So the theory introduces the stochastic distribution of heights and curvature radii. This general theory still suffers the same problem of the original one from Greenwood and Williamson: All the asperities are treated as independent objects, while in reality they are elastically coupled together through the bulk. This theory assumes that the asperity contact regions are independent. For small load, the theory of Bush et al. predicts that the real contact area is proportional to the load $A = \alpha F$, where

$$\alpha = \kappa \frac{1-\nu^2}{E} \left(\int d^2q q^2 C(q) \right)^{-1/2} \quad (\text{A.15})$$

where $\kappa = (2\pi)^{1/2}$.

Bush et al. have developed a more general and accurate contact mechanics theory, where roughness is assumed to occur on many different length scales. It predicts that the real contact area is proportional to the load for small load, and the stress distribution at the interface and the average size a of an asperity contact region, are independent of the applied load. That is, as the load increases (but with $A \ll A_0$), existing contact areas grow and new contact regions form in such a way that the quantities referred to above remain unchanged.

A.2.3 Persson theory

Recently, Persson has developed a contact mechanics theory where the linear size of the system is studied at different magnification $\zeta = L/\lambda$, where L is some reference length and λ the shortest wavelength roughness which can be observed at the magnification ζ [2,4].

Persson defines the stress distribution at the magnification ζ in the following way

$$P(\sigma, \zeta) = \langle \delta(\sigma - \sigma(\mathbf{x}, \zeta)) \rangle \quad (\text{A.16})$$

where $\sigma(\mathbf{x}, \zeta)$ is the stress at the interface calculated when only the surface roughness components with wave-vector $q < \zeta q_L$ is included. $\langle \dots \rangle$ is ensemble average, which in most cases is equivalent to the average over the surface area

$$P(\sigma, \zeta) = \frac{1}{A_0} \int_A d^2x \delta(\sigma - \sigma(\mathbf{x}, \zeta)) \quad (\text{A.17})$$

where A is area of contact. The real contact area, projected on the xy plane, can be obtained directly from the stress distribution in Eq. A.17

$$\frac{A(\zeta)}{A_0} = \int d\sigma P(\sigma, \zeta) \quad (\text{A.18})$$

In Persson theory at complete contact, the stress distribution $P(\sigma, \zeta)$ at the interface between the block and substrate has been shown to obey a diffusion-like equation where time is replaced by the magnification and the spacial coordinate by the stress σ :

$$\frac{\partial P(\sigma, \zeta)}{\partial \zeta} = f(\zeta) \frac{\partial^2 P(\sigma, \zeta)}{\partial \sigma^2} \quad (\text{A.19})$$

where

$$f(\zeta) = \frac{\pi}{4} \left(\frac{E}{1 - \nu^2} \right)^2 q_L q^3 C(q) \quad (\text{A.20})$$

where $q_L = 2\pi/L$, $q = \zeta q_L$. It is assumed that Eq. A.19 holds locally also when partial contact occurs at the interface.

To solve Eq. A.19 one needs boundary conditions. If one assumes that, when studying the system at the lowest magnification $\zeta = 1$ (where no surface roughness can be observed, i.e., the surfaces appear perfectly smooth), the stress at the interface is constant and equal to $p = F_N/A_0$, where F_N is the load and A_0 the nominal contact area, then $P(\sigma, 1) = \delta(\sigma - p)$. In addition to this “initial condition” one needs two boundary conditions along the σ -axis. Since there can be no infinitely large stress at the interface one requires $P(\sigma, \zeta) \rightarrow 0$ as $\sigma \rightarrow \infty$.

For non-adhesive interaction (purely repulsive wall-wall interaction) there can be no tensile stress at the interface and $P(\sigma, \zeta)$ must vanish for $\sigma < 0$. In fact, one can show [1] that $P(\sigma, \zeta)$ vanishes continuously as $\sigma \rightarrow 0$ so that $P(0, \zeta) = 0$. Using this boundary condition the solution to diffusion-like equation gives the pressure distribution at the interface ($\sigma > 0$):

$$P(\sigma, \zeta) = \frac{1}{2(\pi G)^{1/2}} \left(e^{-(\sigma-p)^2/4G} - e^{-(\sigma+p)^2/4G} \right) \quad (\text{A.21})$$

where p is the nominal squeezing pressure, and where

$$G = \frac{\pi}{4} \left(\frac{E}{1 - \nu^2} \right)^2 \int_{q_L}^{\zeta q_0} dq q^3 C(q). \quad (\text{A.22})$$

The surface roughness power spectrum [1]

$$C(q) = \frac{1}{(2\pi)^2} \int d^2x \langle h(\mathbf{x})h(\mathbf{0}) \rangle e^{-i\mathbf{q} \cdot \mathbf{x}},$$

where $\langle \dots \rangle$ stands for ensemble average. The relative contact area

$$\frac{A}{A_0} = \int_0^\infty d\sigma P(\sigma, \zeta). \quad (\text{A.23})$$

Substituting (A.21) into (A.23) gives after some simplifications

$$\frac{A}{A_0} = \frac{1}{(\pi G)^{1/2}} \int_0^p d\sigma e^{-\sigma^2/4G} = \operatorname{erf} \left(\frac{p}{2G^{1/2}} \right). \quad (\text{A.24})$$

Thus, for small nominal squeezing pressure $p \ll G^{1/2}$ one obtains

$$\frac{A}{A_0} \approx \frac{p}{(\pi G)^{1/2}}. \quad (\text{A.25})$$

Persson theory predicts that the contact area depends linearly on the load at small load, $A = \alpha F$ with

$$\alpha = \kappa \frac{1 - \nu^2}{E} \left(\int d^2 q q^2 C(q) \right)^{-1/2} \quad (\text{A.26})$$

Persson theory predicts that $\kappa = (8/\pi)^{1/2}$, instead of $\kappa = (2\pi)^{1/2}$ predicted by Bush theory. Both the theory of Greenwood-Williamson and the theory of Bush et al. assume that the asperity contact regions are independent (no elastic coupling). This might be the origin of $2/\pi$ difference between the theory of Bush and the theory of Persson.

For adhesive contact, tensile stress occurs at the interface close to the boundary lines of the contact regions. In this case the correct boundary condition is instead $P(-\sigma_a, \zeta) = 0$, where $\sigma_a > 0$ is the largest tensile stress possible. The detachment stress $\sigma_a(\zeta)$ depends on the magnification and can be related to the effective interfacial energy (per unit area) $\gamma_{\text{eff}}(\zeta)$ using the theory of cracks

$$\sigma_a(\zeta) \approx \left(\frac{\gamma_{\text{eff}}(\zeta) E q}{1 - \nu^2} \right)^{1/2}, \quad (\text{A.27})$$

where

$$\gamma_{\text{eff}}(\zeta) A^*(\zeta) = \Delta \gamma A^*(\zeta_1) - U_{\text{el}}(\zeta), \quad (\text{A.28})$$

where $A^*(\zeta)$ denotes the total contact area at the magnification ζ , which is larger than the projected contact area $A(\zeta)$. $U_{\text{el}}(\zeta)$ is the elastic energy stored at the interface due to the elastic deformation of the solids on length scale shorter than $\lambda = L/\zeta$, necessary in order to bring the solids into adhesive contact (see below).

From Eq. A.19 it follows that the area of apparent contact (projected on the xy -plane) at the magnification ζ , $A(\zeta)$, normalized by the nominal contact area A_0 , can be obtained from

$$\frac{A}{A_0} = \int_{-\sigma_a(\zeta)}^{\infty} d\sigma P(\sigma, \zeta) \quad (\text{A.29})$$

We denote $A(\zeta)/A_0 = P_p(q)$, where the index p indicates that $A(\zeta)/A_0$ depends on the applied squeezing pressure p .

Persson theory is valid not only when the area of real contact is small compared to the nominal contact area, but also when the squeezing force is so high that nearly complete contact occurs within the nominal contact area. In Chapter 4, I have performed molecular dynamics calculations to test Persson theory from small to full contact.

Appendix B

Pressure Distribution between Randomly Rough Surfaces

Here the pressure distribution at the interface between two solids has been calculated in *complete contact* [6]. Assume that one solid is rigid and randomly rough and the other solid elastic with a flat surface. The pressure distribution

$$\begin{aligned} P(\sigma) &= \langle \delta(\sigma - \sigma(\mathbf{x})) \rangle = \frac{1}{2\pi} \int_{-\infty}^{\infty} d\alpha \langle e^{i\alpha(\sigma - \sigma(\mathbf{x}))} \rangle \\ &= \frac{1}{2\pi} \int_{-\infty}^{\infty} d\alpha e^{i\alpha\sigma} F(\alpha) \end{aligned} \quad (\text{B.1})$$

where

$$F(\alpha) = \langle e^{-i\alpha\sigma(\mathbf{x})} \rangle$$

where $\sigma(\mathbf{x})$ is the fluctuating pressure at the interface. Next, writing

$$\begin{aligned} \sigma(\mathbf{x}) &= \int d^2q \sigma(\mathbf{q}) e^{i\mathbf{q}\cdot\mathbf{x}} \\ &= \int d^2q \frac{Eq}{2(1-\nu^2)} h(\mathbf{q}) e^{i\mathbf{q}\cdot\mathbf{x}} \end{aligned}$$

where we have used the relation between $\sigma(\mathbf{q})$ and the Fourier transform $h(\mathbf{q})$ of the height profile $h(\mathbf{x})$ derived in Ref. [2], we get

$$F = \left\langle \exp \left(-i\alpha \int d^2q \frac{Eq}{2(1-\nu^2)} h(\mathbf{q}) e^{i\mathbf{q}\cdot\mathbf{x}} \right) \right\rangle$$

Next, using that $h(\mathbf{q})$ are independent random variables we get

$$F = e^{-\alpha^2 \xi^2 / 2} \quad (\text{B.2})$$

where

$$\xi^2 = \int d^2q d^2q' \left(\frac{Eq}{2(1-\nu^2)} \right)^2 q q' \langle h(\mathbf{q}) h(\mathbf{q}') \rangle e^{i(\mathbf{q}+\mathbf{q}')\cdot\mathbf{x}}$$

However (see Ref. [2])

$$\langle h(\mathbf{q}) h(\mathbf{q}') \rangle = C(q) \delta(\mathbf{q} + \mathbf{q}')$$

so that

$$\xi^2 = \int d^2q \left(\frac{Eq}{2(1-\nu^2)} \right)^2 C(q) \quad (\text{B.3})$$

Substituting (B.2) in (B.1) and performing the α -integral and using (B.3) gives

$$P(\sigma) = \frac{1}{(2\pi)^{1/2}\sigma_{\text{rms}}} e^{-\sigma^2/2\sigma_{\text{rms}}^2}$$

where the root-mean-square width σ_{rms} is determined by the power spectrum:

$$\sigma_{\text{rms}}^2 = \langle \sigma^2 \rangle = \frac{\pi}{2} \frac{E^2}{(1 - \nu^2)^2} \int_{q_0}^{q_1} dq q^3 C(q)$$

Appendix C

Distribution of Surface Slopes for Randomly Rough Surfaces

In this appendix the distribution of surface slopes for randomly rough surfaces has been derived. We discuss under which conditions one expects the Wenzel and Cassie states to prevail [140].

C.1 The surface area A and the average surface slope ξ

Consider a randomly rough surface and let $h(\mathbf{x})$ denote the height profile measured from the average plane so that $\langle h(\mathbf{x}) \rangle = 0$, where $\langle \dots \rangle$ stands for ensemble averaging, or (equivalently) averaging over the surface area. We assume that $h(\mathbf{x})$ is a Gaussian random variable characterized by the power spectra

$$C(q) = \frac{1}{(2\pi)^2} \int d^2x \langle h(\mathbf{x})h(\mathbf{0}) \rangle e^{-i\mathbf{q}\cdot\mathbf{x}}.$$

Note that if we write

$$h(\mathbf{x}) = \int d^2q h(\mathbf{q})e^{i\mathbf{q}\cdot\mathbf{x}}$$

where

$$h(\mathbf{q}) = \frac{1}{(2\pi)^2} \int d^2x h(\mathbf{x})e^{-i\mathbf{q}\cdot\mathbf{x}}$$

then

$$\langle h(\mathbf{q})h(\mathbf{q}') \rangle = \delta(\mathbf{q} + \mathbf{q}')C(q). \quad (\text{C.1})$$

Sometimes it is also convenient to use

$$\langle h(\mathbf{q})h(-\mathbf{q}) \rangle = \frac{A_0}{(2\pi)^2}C(q), \quad (\text{C.2})$$

where A_0 is the surface area. In deriving (C.2) we have used that

$$\delta(\mathbf{q} - \mathbf{q}) = \frac{1}{(2\pi)^2} \int d^2x e^{i(\mathbf{q}-\mathbf{q})\cdot\mathbf{x}} = \frac{A_0}{(2\pi)^2}.$$

If the surface roughness amplitudes $h(\mathbf{q})$ are assumed to be Gaussian random variables, one can show that the (normalized) surface area [3]

$$r = \frac{A}{A_0} = \int_0^\infty dx \left(1 + x\xi^2\right)^{1/2} e^{-x}$$

where

$$\xi^2 = \int d^2q q^2 C(q) = 2\pi \int_0^\infty dq q^3 C(q)$$

Let us calculate the rms surface slope. We get

$$\langle (\nabla h)^2 \rangle = \int d^2q d^2q' (iq_\alpha)(iq'_\alpha) \langle h(\mathbf{q})h(\mathbf{q}') \rangle e^{i(\mathbf{q}+\mathbf{q}') \cdot \mathbf{x}}$$

Using (C.1) this gives

$$\langle (\nabla h)^2 \rangle = \int d^2q q^2 C(q) = \xi^2$$

Thus, for a Gaussian random surface both the average slope and the increase in the surface area is determined by the parameter ξ . For non-random surfaces this is no longer the case.

C.2 Surface slope probability distribution

Let $h(\mathbf{x}, \zeta)$ denote the height profile after having smoothed out surface roughness with wavelength shorter than $\lambda = L/\zeta$. For example, we may define

$$h(\mathbf{x}, \zeta) = \int_{q < q_1} d^2q h(\mathbf{q}) e^{i\mathbf{q} \cdot \mathbf{x}},$$

where $q_1 = q_L \zeta$ (where $q_L = 2\pi/L$). We will refer to ζ as the magnification. Thus, when we study the surface at the magnification ζ we will only detect surface roughness with wavelength components larger than $\lambda = L/\zeta$.

We will now derive an equation of motion for the surface slope probability distribution function

$$P(\mathbf{s}, \zeta) = \langle \delta(\mathbf{s} - \nabla h(\mathbf{x}, \zeta)) \rangle.$$

We assume that the surface roughness amplitudes $h(\mathbf{q})$ are independent random variables. In this case, if we write

$$h(\mathbf{x}, \zeta + \delta\zeta) = h(\mathbf{x}, \zeta) + \delta h,$$

we get

$$\begin{aligned} P(\mathbf{s}, \zeta + \delta\zeta) &= \langle \delta(\mathbf{s} - \nabla h(\mathbf{x}, \zeta + \delta\zeta)) \rangle \\ &= \int d^2s' \langle \delta(\mathbf{s}' - \nabla \delta h) \rangle \langle \delta(\mathbf{s} - \mathbf{s}' - \nabla h(\mathbf{x}, \zeta)) \rangle \\ &= \int d^2s' \langle \delta(\mathbf{s}' - \nabla \delta h) \rangle P(\mathbf{s} - \mathbf{s}', \zeta). \end{aligned} \quad (\text{C.3})$$

But

$$\begin{aligned} \langle \delta(\mathbf{s}' - \nabla \delta h) \rangle &= \frac{1}{(2\pi)^2} \int d^2q \langle e^{i\mathbf{q} \cdot (\mathbf{s}' - \nabla \delta h)} \rangle \\ &= \frac{1}{(2\pi)^2} \int d^2q \left(1 - \frac{1}{2} \langle (\mathbf{q} \cdot \nabla \delta h)^2 \rangle \right) e^{i\mathbf{q} \cdot \mathbf{s}'} \\ &= \delta(\mathbf{s}') + \frac{1}{2} \langle (\nabla_\alpha \delta h) (\nabla_\beta \delta h) \rangle \frac{\partial}{\partial s'_\alpha} \frac{\partial}{\partial s'_\beta} \delta(\mathbf{s}'). \end{aligned}$$

Substituting this result into (C.3) and expanding the left-hand-side to linear order in $\delta\zeta$ gives

$$\frac{\partial P}{\partial \zeta}(\mathbf{s}, \zeta) = \frac{1}{2\delta\zeta} \langle (\nabla_\alpha \delta h) (\nabla_\beta \delta h) \rangle \frac{\partial}{\partial s_\alpha} \frac{\partial}{\partial s_\beta} P(\mathbf{s}, \zeta). \quad (\text{C.4})$$

But

$$\begin{aligned} \langle (\nabla_\alpha \delta h) (\nabla_\beta \delta h) \rangle &= \int_{q_L \zeta}^{q_L(\zeta+\delta\zeta)} d^2 q d^2 q' \\ &\times (iq_\alpha)(iq'_\beta) \langle h(\mathbf{q}) h(\mathbf{q}') \rangle e^{(\mathbf{q}+\mathbf{q}') \cdot \mathbf{x}} \\ &= \int_{q_L \zeta}^{q_L(\zeta+\delta\zeta)} d^2 q q_\alpha q'_\beta C(q) \\ &= \frac{1}{2} \delta_{\alpha\beta} \int_{q_L \zeta}^{q_L(\zeta+\delta\zeta)} d^2 q q^2 C(q) \\ &= \pi \delta_{\alpha\beta} q_L \delta \zeta q^3 C(q). \end{aligned}$$

Thus

$$\frac{1}{2\delta\zeta} \langle (\nabla_\alpha \delta h) (\nabla_\beta \delta h) \rangle = \frac{\pi}{2} \delta_{\alpha\beta} q_L q^3 C(q)$$

Substituting this result in (C.4) gives the following diffusion-like equation for $P(\mathbf{s}, \zeta)$:

$$\frac{\partial P}{\partial \zeta} = D(\zeta) \nabla_s^2 P \quad (\text{C.5})$$

where

$$\nabla_s^2 = \frac{\partial}{\partial s_\alpha} \frac{\partial}{\partial s_\alpha}$$

where the “diffusivity”

$$D(\zeta) = \frac{\pi}{2} q_L q^3 C(q), \quad (\text{C.6})$$

with $q = q_L \zeta$.

C.3 Solution of the diffusion equation

The function $P(\mathbf{s}, \zeta)$ describes the probability to observe a surface slope or gradient $\mathbf{s} = \nabla h(\mathbf{x})$ when the system is studied at the magnification ζ . When the system is studied at the lowest magnification $\zeta = 1$ the surface appears flat and smooth so that the gradient vanishes, i.e.,

$$P(\mathbf{s}, 1) = \langle \delta(\mathbf{s} - \nabla h(\mathbf{x}, 1)) \rangle = \delta(\mathbf{s}). \quad (\text{C.7})$$

We also require that there is no infinite high slopes, i.e.,

$$P(\mathbf{s}, \zeta) \rightarrow 0 \quad \text{as} \quad |\mathbf{s}| \rightarrow \infty. \quad (\text{C.8})$$

Let us determine the solution to (C.5) which obeys the “initial” condition (C.7) and the boundary condition (C.8). It is clear that the solution is given by

$$P(\mathbf{s}, \zeta) = \frac{1}{\pi s_1^2} e^{-(s/s_1)^2}, \quad (\text{C.9})$$

where the width parameter $s_1(\zeta)$ depends on the magnification:

$$s_1^2 = 4 \int_1^\zeta d\zeta' D(\zeta') = 2\pi \int_{q_L}^{\zeta q_L} dq q^3 C(q) = \xi^2(\zeta).$$

Note that P is normalized,

$$\int d^2 s P(\mathbf{s}, \zeta) = 1,$$

and that the width of the Gaussian distribution P increases with increasing resolution, i.e., when the surface is studied at higher and higher resolution, steeper and steeper surface slopes will be detected.

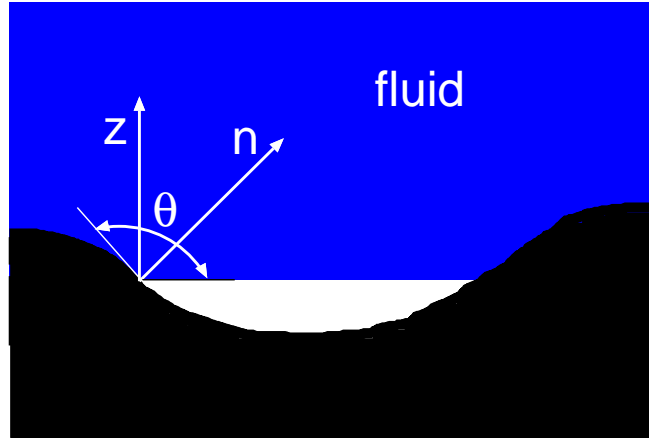


Figure C.1: A fluid in contact with a rough substrate. The contact angle θ is determined by Young's equation.

C.4 Distribution function $P(s_0, \zeta)$

In what follows we will need the fraction $P(s_0, \zeta)$ of the total surface area where the slope $s < s_0$, where s_0 is a fixed number between zero and infinite. Let $A_\perp(\zeta)$ be the surface area, projected on the xy -plane, where the surface slope $s < s_0$. We then have

$$P(s_0, \zeta) = A_\perp(\zeta)/A_0.$$

Using the definition

$$\begin{aligned} P(\mathbf{s}, \zeta) &= \langle \delta(\mathbf{s} - \nabla h(\mathbf{x}, \zeta)) \rangle \\ &= \frac{1}{A_0} \int d^2x \delta(\mathbf{s} - \nabla h(\mathbf{x}, \zeta)) \end{aligned}$$

we get

$$P(s_0, \zeta) = \int_{s < s_0} d^2s P(\mathbf{s}, \zeta).$$

Using (C.9) this gives

$$P(s_0, \zeta) = 1 - e^{-(s_0/s_1)^2}. \quad (\text{C.10})$$

C.5 Surface area with slope below $\tan\theta$

Consider a liquid in contact with a rough substrate. The contact angle θ is determined by Young's equation:

$$\cos\theta = \frac{\gamma_{sv} - \gamma_{sl}}{\gamma_{lv}}$$

where γ_{sl} , γ_{sv} and γ_{lv} are the solid-liquid, solid-vapor and liquid-vapor interfacial energies, respectively. Note that if \mathbf{n} is the normal to the solid surface and \mathbf{z} the normal to the liquid surface (see Fig. C.1) then $\cos\theta = -\mathbf{z} \cdot \mathbf{n}$. Since

$$\mathbf{n} = \frac{(-\nabla h, 1)}{(1 + (\nabla h)^2)^{1/2}}$$

we get

$$\cos\theta = -\left(1 + (\nabla h)^2\right)^{-1/2}, \quad |\tan\theta| = |\nabla h|.$$

Thus, using (C.10) the fraction of the surface where the surface slope is below $\tan\theta$ is

$$P(\tan\theta) = 1 - e^{-(\tan\theta/\xi)^2}. \quad (\text{C.11})$$

Bibliography

- [1] B.N.J. Persson, O. Albohr, U. Tartaglino, A.I. Volokitin, and E. Tosatti. On the nature of surface roughness with application to contact mechanics, sealing, rubber friction and adhesion. *J. Phys. Condens. Matter*, 17:R1, 2005.
- [2] B.N.J. Persson. Theory of rubber friction and contact mechanics. *J. Chem. Phys.*, 115:3840, 2001.
- [3] B.N.J. Persson and E. Tosatti. The effect of surface roughness on the adhesion of elastic solids. *J. Chem. Phys.*, 115:5597, 2001.
- [4] B.N.J. Persson. Adhesion between an elastic body and a randomly rough hard surface. *Eur. Phys. J. E*, 8:385, 2002.
- [5] S. Hyun, L. Pei, J.-F. Molinari, and M.O. Robbins. Finite-element analysis of contact between elastic self-affine surfaces. *Phys. Rev. E*, 70:026117, 2004.
- [6] C. Yang, U. Tartaglino, and B.N.J. Persson. A multiscale molecular dynamics approach to contact mechanics. *Eur. Phys. J. E*, 19:47, 2006.
- [7] C. Campana and M.H. Muser. Contact mechanics of real vs. randomly rough surfaces: A green's function molecular dynamics study. *EPL*, 77:38005, 2007.
- [8] E. Rabinowicz. *Friction and wear of materials*. Number 2nd Edition. Wiley, New York, 1995.
- [9] B.N.J. Persson. *Sliding Friction: Physical Principles and Applications*. Number 2nd Edition. Springer, Heidelberg, 2000.
- [10] B. Bhushan. *Micro/Nanotribology and its applications*. Number 1st Edition. Kluwer Academic Publishers, 1997.
- [11] D. Dowson. *History of tribology*. Number 2nd Edition. Professional engineering publishing limited London and Bury St Edmunds, UK, 1998.
- [12] F.P. Bowden and D. Tabor. *The friction and lubrication of solids*. Number 5th Edition. Oxford University Press, 2001.
- [13] B. Bhushan, J.N. Israelachvili, and U. Landman. Nanotribology - friction, wear and lubrication at the atomic scale. *Nature*, 374:607, 1997.
- [14] J.P. Gao, W.D. Luedtke, D. Gourdon, M. Ruths, J.N. Israelachvili, and U. Landman. Frictional forces and amontons'law: From the molecular to the macroscopic scale. *J. Phys. Chem. B*, 108:3410, 2004.
- [15] <http://www.lotus-effect.com>.

- [16] W. Barthlott and C. Neinhuis. Purity of the sacred lotus, or escape from contamination in biological surfaces. *Planta*, 202:1, 1997.
- [17] C. Neinhuis and W. Barthlott. Characterization and distribution of water-repellent, self-cleaning plant surfaces. *Annals of Botany*, 79:667, 1997.
- [18] K. Autumn, Y.A. Liang, S.T. Hsieh, W. Zesch, W.P. Chan, T.W. Kenny, R. Fearing, and R.L. Full. Adhesive force of a single gecko foot-hair. *Nature*, 405:681, 2000.
- [19] Y.P. Zhao, L.S. Wang, and T.X. Yu. Mechanics of adhesion in mems - a review. *J. Adhes. Sci. Technol.*, 17:519, 2003.
- [20] C. Gui, R.E. Oosterbroek, J.W. Berenschot, S. Schlautmann, T.S.J. Lammerink, A. Ven den Berg, and M.C. Elwenspoek. Selective wafer bonding by surface roughness control. *J. Electrochem. Soc.*, 148:G225, 2001.
- [21] C. Gui, M. Elwenspoek, N. Tas, and J.G.E. Gardeniers. The effect of surface roughness on direct wafer bonding. *J. Appl. Phys.*, 485:7448, 1999.
- [22] D.C. Rapaport and D. Rapport. *The art of molecular dynamics simulations*. Number Reprint. Cambridges university press, 2001.
- [23] M.P. Allen and D.J. Tildesley. *Computer simulation of liquids*. Clarendon Press, Oxford, 1989.
- [24] T. Zytkova-Timan. *High temperature physics and nanofriction properties of alkali halide surfaces*. PhD thesis, Sissa, 2006.
- [25] G. Ciccotti and W.G. Hoover (Eds.). *Molecular dynamics simulation of statistical-mechanical system*. Amsterdam: North-Holland Elsevier Science Publisher, 1987.
- [26] W.I. Jorgensen, J.D. Madura, and C.J. Swenson. Optimized intermolecular potential functions for liquid hydrocarbons. *J. Am. Chem. Soc.*, 106:6638, 1984.
- [27] D.K. Dysthe, A.H. Fuchs, and B. Rousseau. Fluid transport properties by equilibrium molecular dynamics. iii. evaluation of united atom interaction potential models for pure alkanes. *J. Chem. Phys.*, 112:6638, 2000.
- [28] F. Ercolessi. <http://www.fisica.uniud.it/~ercolessi/>.
- [29] B. N. J. Persson and P. Ballone. Squeezing lubrication films: Layering transition for curved solid surfaces with long-range elasticity. *J. Chem. Phys.*, 112:9524, 2000.
- [30] J. Gao, W. D. Luedtke, and U. Landman. Origins of solvation forces in confined films. *J. Phys. Chem. B*, 101:4013, 1997.
- [31] L. D. Landau and M. E. Lifshitz. *Theory of Elasticity*. Number 3rd Edition. 1981.
- [32] R. Feynman. *The Feynmann lectures on physics*, volume 2. 1960.
- [33] C. Kittel. *Introduction to Solid State Physics*, volume 2. John Wiley & Sons, New York, 1996.
- [34] J. Krim, I. Heyvaert, C. Van Haesendonck, and Y. Bruynseraeede. Scanning tunneling microscopy observation of self-affine fractal roughness in ion-bombarded film surface. *Phys. Rev. Lett.*, 70:57, 1993.

- [35] R. Buzio, C. Boragno, F. Biscarini, F.B. de Mongeot, and U. Valbusa. The contact mechanics of fractal surfaces. *Nature Mat.*, 2:233, 2003.
- [36] S. Curtarolo and G. Ceder. Dynamics of an inhomogeneously coarse grained multi-scale system. *Phys. Rev. Lett.*, 88:255504, 2002.
- [37] X.B. Nie, S.Y. Chen, E. WN, and M.O. Robbins. continuum and molecular dynamics hybrid method for micro- and nano-fluid flow. *Fluid Mech.*, 500:55, 2004.
- [38] W. E and Z. Huang. Matching conditions in atomistic-continuum modeling of materials. *Phys. Rev. Lett.*, 87:135501, 2001.
- [39] W.A. Curtin and R.E. Miller. Atomistic/continuum coupling in computational materials science. *Modelling Simul. Mater. Sci. Eng.*, 11:R33, 2003.
- [40] W. Cai, M. de Koning, V.V. Bulatov, and S. Yip. Minimizing boundary reflections in coupled-domain simulations. *Phys. Rev. Lett.*, 85:3213, 2000.
- [41] K.L. Johnson. *Contact Mechanics*. Cambridge University Press, Cambridge, 1985.
- [42] J. Israelachvili. *Intermolecular and Surface Forces*. Academic Press, London, 1992.
- [43] B. Luan and M.O. Robbins. The breakdown of continuum models for mechanical contacts. *Nature*, 435:929, 2005.
- [44] B.N.J. Persson, F. Bucher, and B. Chiaia. Elastic contact between randomly rough surfaces: Comparison of theory with numerical results. *Phys. Rev. B*, 65:184106, 2002.
- [45] M. Borri-Brunetto, B. Chiaia, and M. Ciavarella. Incipient sliding of rough surfaces in contact: a multiscale numerical analysis. *Comput. Methods Appl. Mech. Eng.*, 190:6053, 2001.
- [46] K.L. Johnson, K. Kendall, and A.D. Roberts. Surface energy and contact of elastic solids. *Proc. R. Soc. London Ser. A*, 324:301, 1971.
- [47] K. Kendall. *Molecular Adhesion and its Applications*. New York, Kluwer, 2001.
- [48] K.N.G. Fuller and D. Tabor. Effect of surface-roughness on adhesion of elastic solids. *Proc. Roy. Soc. A*, 345:327, 1975.
- [49] A.W. Bush, R.D. Gibson, and T.R. Thomas. Elastic contact of a rough surface. *Wear*, 35:87, 1975.
- [50] J.A. Greenwood and J.B.P. Williamson. Contact od nominally flat surfaces. *Proc. Roy. Soc. London, Ser. A*, 295:300, 1966.
- [51] J.N. Israelachvili. Engineering - skimming the surface. *Nature*, 435:893, 2005.
- [52] B.N.J. Persson. Relation between interfacial separation and load: A general theory of contact mechanics. *Phys. Rev. Lett.*, 99:125502, 2007.
- [53] L. Pei, S. Hyun, J.F. Molinari, and M.O. Robbins. Finite element modeling of elasto-plastic contact between rough surfaces. *J. Mech. Phys. Solids*, 53:2385, 2005.
- [54] G. Carbone and F. Bottiglione. Asperity contact theories: Do they predict linearity between contact area and load. 2008. to be published.

- [55] A.I. Volokitin and B.N.J. Persson. Near-field radiative heat transfer and noncontact friction. *Rev. Mod. Phys.*, 79:1291, 2007.
- [56] E. Rabinowicz. *Friction and Wear of Materials*. Number 2nd Edition. Wiley, New York, 1995.
- [57] N. Patir and H.S. Cheng. Average flow model for determining effects of 3-dimensional roughness on partial hydrodynamics lubrication. *Transactions of the ASME*, 100:12, 1978.
- [58] M. Benz, K.J. Rosenberg, E.J. Kramer, and J.N. Israelachvili. The deformation and adhesion of randomly rough and patterned surfaces. *J. Phys. Chem. B*, 110:11884, 2006.
- [59] J.F. Archard. Elastic deformation and the laws of friction. *Proc. Roy. Soc. London, Ser. A*, 243:190, 1957.
- [60] B.N.J. Persson. Contact mechanics for randomly rough surfaces. *Surf. Sci. Rep.*, 61:201, 2006.
- [61] C. Yang and B.N.J. Persson. Contact mechanics: Contact area and interfacial separation from small contact to full contact. *J. Phys.: Condens. Matt.*, 20:215214, 2008.
- [62] S. Hyun and M.O. Robbins. to be published.
- [63] A. Honig, 2007. Julich report.
- [64] N.G. Stanley-Wood (Ed.). *Enlargement and Compaction of Particulate Solids*. Butterworth-Heinemann, Cambridge, 1983.
- [65] A.R.G. Alig, M. Akbulut, Y. Golan, and J. Israelachvili. Forces between surfactant-coated zns nanoparticles in dodecane: Effect of water. *Adv. Funct. Mater.*, 16:2127, 2006.
- [66] C. Yang and B.N.J. Persson. Molecular dynamics study on contact mechanics: contact area and interfacial separation from small to full contact. *Phys. Rev. Lett.*, 100:024303, 2008.
- [67] J.A. Greenwood. Adhesion of elastic spheres. *Proc. R. Soc. Lond. A*, 453:1277, 1997.
- [68] R. Flitney. *Seals and sealing handbook*. Elsevier, 2007.
- [69] M. Mofidi, B. Prakash, B.N.J. Persson, and O. Albohr. Rubber friction on (apparently) smooth lubricated surfaces. *J. Phys.: Condens. Matt.*, 20:085223, 2008.
- [70] B.N.J. Persson, O. Albohr, C. Creton, and V. Peveri. Contact area between a viscoelastic solid and a hard, randomly rough, substrate. *J. Chem. Phys.*, 120:8779, 2004.
- [71] D. Stauffer and A. Aharony. *An introduction to percolation theory*. CRC press, 1991.
- [72] E. Widder. 2004. ASME B46 seminar, April 15.
- [73] M. Schmidt, H. Murrenhoff, H. Lohrberg, and F.J. Korber. page 8779. to be published.

- [74] B. Zappone, K.J. Rosenberg, and J. Israelachvili. Role of nanometer roughness on the adhesion and friction of a rough polymer surface and a molecularly smooth mica surface. *Trib. Lett.*, 26:191, 2007.
- [75] B.N.J. Persson. Capillary adhesion between elastic solids with randomly rough surfaces. *J. Phys: Condens. Matt.*, 20:315007, 2008.
- [76] F. Deleau, D. Mazuyer, and A. Koenen. *Triboogy International*, 2008. to be published.
- [77] B.N.J. Persson and C. Yang. Theory of leak-rate seals. *J. Phys: Condens. Matt.*, 2008. in press.
- [78] M. Scherge and S. Gorb. *Biological Micro- and Nano- tribology*. Springer, Berlin, 2000.
- [79] B.N.J. Persson and F. Mugele. Squeeze-out and wear: fundamental principles and applications. *J. Phys. Condens. Matter*, 16:R295, 2004.
- [80] I.L. Singer and H.M. Pollock (Ed.). *Fundamentals of Friction: Macroscopic and Microscopic Processes*. Kluwer, Dordrecht, 1992. Series E: Applied Science.
- [81] E. Arzt, S. Gorb, and R. Spolenak. From micro to nano contacts in biological attachment devices. *Proc. Natl. Acad. Sci.*, 100:10603, 2003.
- [82] M. Heuberger, M. Zach, and N.D. Spencer. Density fluctuations under confinement: When is a fluid not a fluid? *Science*, 292:905, 2001.
- [83] <http://adam.about.com/encyclopedia/19698.htm>.
- [84] <http://www.britannica.com/eb/article-9022138>.
- [85] S.J. Lai-Fook. Pleural mechanics and fluid exchange. *Physiol. Rev.*, 84:385, 2004.
- [86] G. Huber, H. Martin, R. Spolenak, K. Mecke, K. Jacobs, S.N. Gorb, and E. Arzt. Evidence for capillarity contributions to gecko adhesion from single spatula nanomechanical measurements. *Proc. Natl. Acad. Sci.*, 102:16293, 2005.
- [87] G. Huber. Nanoscale adhesion of individual gecko spatula explored by atomic force microscopy. Master's thesis, Stuttgart Universit, 2006.
- [88] S. Chandra and C. Batur. Manipulation of capillary force by electrowetting for micromanipulation. volume 3, page 578, 2006. Technical proceedings of the 2006 NSTI nanotechnology conference and trade show.
- [89] V.N. Samoilov, I.M. Sievebaek, and B.N.J. Persson. The effect of surface roughness on the adhesion of solid surfaces for systems with and without liquid lubricant. *J. Chem. Phys.*, 121:9639, 2004.
- [90] C. Yang, U. Tartaglino, and B.N.J. Persson. Influence of surface roughness on superhydrophobicity. *Phys. Rev. Lett.*, 97:116103, 2006.
- [91] B.N.J. Persson. Nanoadhesion. *Wear*, 254:832, 2003.
- [92] B.N.J. Persson and S. Gorb. The effect of surface roughness on the adhesion of elastic plates with application to biological systems. *J. Chem. Phys.*, 119:11437, 2003.

- [93] J. Aubry. *J. Phys. (Paris)*, 44:147, 1983.
- [94] B.N.J. Persson and E. Tosatti. Theory of friction: elastic coherence length and earthquake dynamics. *Solid State Communications*, 109:739, 1999.
- [95] B.N.J. Persson and E. Tosatti (Ed.). *Physics of Sliding Friction*. Kluwer, Dordrecht, 1996.
- [96] B.N.J. Persson, O. Albohr, F. Mancosu, V. Peveri, V.N. Samoilov, and I.M. Sivebaek. On the nature of the static friction, kinetic friction and creep. *Wear*, 254:835, 2003.
- [97] B.N.J. Persson. Theory of friction - stress domains, relaxation, and creep. *Phys. Rev. B*, 51:13568, 1995.
- [98] C. Caroli and P. Nozieres. Hysteresis and elastic interactions of microasperities in dry friction. *Eur. Phys. J. B*, 4:233, 1998.
- [99] T. Baumberger and C. Caroli. Solid friction from stick-slip down to pinning and aging. *Advances in Physics*, 55:279, 2006.
- [100] K. Shinjo and M. Hirano. Dynamics of friction - superlubric state. *Surf. Sci.*, 283:473, 1993.
- [101] M.H. Muser. Structural lubricity: Role of dimension and symmetry. *Europhys. Lett.*, 66:97, 2004.
- [102] E. Riedo and H. Brune. Young modulus dependence of nanoscopic friction coefficient in hard coatings. *Appl. Phys. Lett.*, 83:1986, 2003.
- [103] M. Dienwiebel, G.S. Verhoeven, N. Pradeep, J.W.M. Frenken, J.A. Heimberg, and H.W. Zandbergen. Superlubricity of graphite. *Phys. Rev. Lett.*, 92:126101, 2004.
- [104] V.N. Samoilov, C. Yang, U. Tartaglino, and B.N.J. Persson. *Effect of Surface roughness and adsorbates on superlubricity*. Elsevier, 2007. a chapter in Superlubricity, edited by A. Erdemir and J.-M. Martin.
- [105] J.B. Sokoloff. Theory of the effects of multiscale surface roughness and stiffness on static friction. *Phys. Rev. E*, 73:016104, 2006.
- [106] B.V. Derjaguin. Mechanical properties of the boundary lubrication layer. *Wear*, 128:19, 1988.
- [107] C. Yang, U. Tartaglino, and B.N.J. Persson. How do liquids confined at the nanoscale influence adhesion? *J. Phys.: Condens. Matter*, 18:11521, 2006.
- [108] T. Young. An essay on the cohesion of fluids. *Phil. Trans. R. Soc. Lond.*, 95:65, 1805.
- [109] P.S. Laplace. *OEUVRES*. Paris: Imprimerie Royale, 1847.
- [110] J. Rowlinson and B. Widom. *Molecular Theory of Capillarity*. Oxford University Press, 1982.
- [111] P.G. de Gennes. Wetting: static and dynamics. *Rev. Mod. Phys.*, 57:827, 1985.
- [112] D. Quere. Non-sticking drops. *Rep. Prog. Phys.*, 68:2495, 2005.

- [113] T.S. Chow. Wetting of rough surfaces. *J. Phys.: Condens. Matter*, 10:L445, 1998.
- [114] N.A. Patankar. On the modeling of hydrophobic contact angles on rough surfaces. *Langmuir*, 19:1249, 2003.
- [115] W. Chen, A.Y. Fadeev, M.C. Hsieh, D. Oner, J. Youngblood, and T.J. McCarthy. Ultrahydrophobic and ultralyophobic surfaces: Some comments and examples. *Langmuir*, 15:3395, 1999.
- [116] M. Callies and D. Quere. On water repellency. *Soft Matter*, 1:55, 2005.
- [117] L.W. Schwartz and S. Garoff. Contact angle hysteresis on heterogeneous surfaces. *Langmuir*, 1:219, 1985.
- [118] C.W. Extrand, S.I. Moon, P. Hall, and D. Schmidt. Superwetting of structured surfaces. *Langmuir*, 23:8882, 2007.
- [119] S.L. Ren, S.R. Yang, Y.P. Zhao, T.X. Yu, and X.D. Xiao. Preparation and characterization of an ultrahydrophobic surface based on a stearic acid self-assembled monolayer over polyethyleneimine thin films. *Surf. Sci.*, 546:64, 2003.
- [120] M. Nosonovsky and B. Bhushan. Roughness optimization for biomimetic superhydrophobic surfaces. *Microsystem Technologies-Micro- and Nanosystem-Information storage and Processing Systems*, 11:535, 2005.
- [121] A. Otten and S. Herminghaus. How plants keep dry: A physicist's point of view. *Langmuir*, 20:2405, 2004.
- [122] S. Shibuichi, T. Onda, N. Satoh, and K. Tsujii. Super water-repellent surfaces resulting from fractal structure. *J. Phys. Chem.*, 100:19512, 1996.
- [123] R. Blossey. Self-cleaning surfaces - virtual realities. *Nature Mat.*, 2:301, 2003.
- [124] N.A. Patankar. Mimicking the lotus effect: Influence of double roughness structures and slender pillars. *Langmuir*, 20:8209, 2004.
- [125] Y.T. Cheng and D.E. Rodak. Is the lotus leaf superhydrophobic? *Appl. Phys. Lett.*, 86:144101, 2005.
- [126] A. Nakajima, K. Hashimoto, and T. Watanabe. Recent studies on super-hydrophobic films. *Monatsh. Chem.*, 132:31, 2001.
- [127] S.R. Coulson, L. Woodward, J.P.S. Badyal, S.A. Brewer, and C. Willis. Superrepellent composite fluoropolymer surfaces. *J. Phys. Chem. B*, 104:8836, 2000.
- [128] H.Y. Erbil, A.L. Demirel, and O. Mert Y. Avci. Transformation of a simple plastic into a superhydrophobic surface. *Science*, 299:1377, 2003.
- [129] R.N. Wenzel. Resistance of solid surfaces to wetting by water. *Ind. Eng. Chem.*, 28:988, 1936.
- [130] A.B.D. Cassie and S. Baxter. Wettability of porous surfaces. *Trans. Faraday Soc.*, 40:546, 1944.
- [131] R.E. Johnson and R.H. Dettre. Contact angle hysteresis .3. study of an idealized heterogeneous surface. *J. Phys. Chem.*, 68:1744, 1964.

- [132] A. Dupuis and J.M. Yeomans. Modeling droplets on superhydrophobic surfaces: Equilibrium states and transitions. *Langmuir*, 21:2624, 2005.
- [133] M. Suzuki. Activated carbon-fiber - fundamentals and applications. *Carbon*, 32:577, 1994.
- [134] T.J. Barton. Tailored porous materials. *Chem. Mater.*, 11:2633, 1999.
- [135] J. Bico, C. Marzolin, and D. Quere. Pearl drops. *Europhys. Lett.*, 47:220, 1999.
- [136] G. Carbone and L. Mangialardi. Hydrophobic properties of a wavy rough substrate. *Eur. Phys. J. E*, 16:67, 2005.
- [137] S. Herminghaus. Roughness-induced non-wetting. *Europhys. Lett.*, 52:165, 2000.
- [138] A. Lafuma and D. Quere. Superhydrophobic states. *Nature Mat.*, 2:457, 2003.
- [139] X. Gao and L. Jiang. Water-repellent legs of water striders. *Nature*, 432:36, 2004.
- [140] C. Yang, U. Tartaglino, and B.N.J. Persson. Nanodroplet on rough hydrophobic and hydrophilic surfaces. *Eur. Phys. J. E*, 25:139, 2008.
- [141] H. Hertz. On the contact of elastic solids. *J. Reine Angew. Math*, 92:156, 1881.
- [142] B.V. Derjaguin, V.M. Muller, and Y.P. Toporov. Effect of contact deformation on adhesion of particles. *J. Colloid Interface Sci.*, 53:314, 1975.
- [143] B.V. Derjaguin, V.M. Muller, and Y.P. Toporov. Role of molecular forces in contact deformations. *J. Colloid Interface Sci.*, 73:378, 1978.
- [144] B. Derjaguin, V. Muller, and Y. Toporov. Different approaches to the contact mechanics. *J. Colloid Interface Sci.*, 73:293, 1980.
- [145] V.M. Muller, B.V. Derjaguin, and Y.P. Toporov. On 2 methods of calculation of the force of sticking of an elastic sphere to a rigid plane. *Colloids Surf.*, 7:251, 1983.
- [146] U.D. Schwarz. A generalized analytical model for the elastic deformation of an adhesive contact between a sphere and a flat surface. *J. Colloid Interface Sci.*, 261:99, 2003.
- [147] D. Tabor. Surface forces and surface interaction. *J. Colloid Inter. Sci.*, 58:2, 1977.
- [148] T. Geike and V.L. Popov. Reduction of three-dimensional contact problems to one-dimensional ones. *Tribology international*, 40:924, 2007.
- [149] A.W. Bush, R.D. Gibson, and G.P. Keogh. Limit of elastic deformation in contact of rough surfaces. *Mech. Res. Commun.*, 3:169, 1976.